DEVELOPMENT OF HIGH EFFICIENCY HIGH SPEED PERMANENT MAGNET GENERATOR

Prepared by:

Colin Richmond
RCHSIQ001

Prepared for

Professor Ramesh Kuppuswamy

Thesis submitted to the Department of Mechanical Engineering, University of Cape Town, in complete fulfilment of the requirements for the degree of Master of Science.

July 2019

Department of Mechanical Engineering

Faculty of Engineering & Built Environment

University of Cape Town

DECLARATION

This dissertation is submitted to the Department of Mechanical Engineering, University of Cape Town, in complete fulfilment of the requirements for the degree of Master of Science. It has not been submitted before for any degree or examination at this or any other university. The author confirms that this thesis is based on his own work. Portions of this work have been published in peer-reviewed journals and at refereed international conferences.

“I know the meaning of plagiarism and declare that all the work in the document, save for that which is properly acknowledged, is my own. This thesis/dissertation has been submitted to the Turnitin module (or equivalent similarity and originality checking software) and I confirm that my supervisor has seen my report and any concerns revealed by such have been resolved with my supervisor.”

Signed by candidate

C. RICHMOND

01 June 2019

ACKNOWLEDGMENTS

I would like to start by returning all the glory to God for giving me the strength, courage, determination and faith I needed throughout this journey. It was through believing that 'all things are possible through you who gives me strength' that has made it possible to complete this work.

To my amazing mother, I thank you endlessly for your support and comfort throughout my academic journey. You have groomed me into the man I am today, and I thank you for the sacrifices you have made along the way to ensure that I received the best education.

To my Supervisor, Professor Ramesh Kuppuswamy, words cannot even begin to express my gratitude. From a young final year student, you took me under your wing and taught me many life lessons outside of the project, some of which you may not have realized. I would to say thank you for your invaluable guidance throughout the project and for the many opportunities and doors you unlocked for me during this time. Your insight and wealth of knowledge into this research work was crucial. Thank you and may you continue to inspire other students in academia/research as you have done for me.

And to my Co-Supervisor, Professor Azeem Khan, I would like to thank you for your guidance and insight throughout the project.

Finally, to all my friends I made in Cape Town, thank you for making this beautiful city home away from home. I would also like to thank my colleagues in the Advanced Manufacturing and AMES research groups at the University of Cape Town. Each one of you played a major role in realizing this entire project.

It is impossible to mention everyone who contributed to my development during this time and ultimately the completion. However, to those not mentioned I am eternally grateful and humbled by the kind acts of support throughout my Journey.

ABSTRACT

Renewable energy technology is steadily gaining importance in the energy market because of the limited nature of fossil fuels, as well as the political pressures to reduce carbon emissions. To ensure sustainable development, adequate and affordable energy should be made available to satisfy the demand of electric energy. The High Speed Permanent Magnet (HSPM) generator is designed and developed and is expected to deliver 10 kW output power as well as to achieve a speed of 30000 RPM, however, to achieve a compact and efficient design with lower excitation losses, magnetizing currents and rotor losses requires the HSPM generator to be operated at high rated speeds of approximately 30000 RPM. However, at high speeds these machines produce a substantial amount of heat. This makes the thermal management of these machines difficult and complicated, which leads to demagnetization and the reduction of the output power and shortens the lifetime of the critical components such as the bearings. This thesis presents the design and development of the HSPM generator. It also identifies the heat generated by means of electromagnetic, mechanical and core losses. The development of an adequate cooling system (cooling jacket) is presented to avoid hot spots in the generator and thermal damage to the magnets, resulting in demagnetization. The use of pressurized oil air particles as a lubrication method for the bearings of the generator is also considered to avoid: thermal damage and starvation at the rolling element and to address the predominant concern of effectively cooling the HSPM generator ball bearings at elevated speeds. The HSPM generator is designed and developed to operate at a maximum speed of 30000 RPM to deliver 10 kW output power and is subjected to 80~92°C temperature rise with an idle power consumption of ~2kW, enough to cause hot spots on the generator, demagnetization of the magnets and severe impact to the rolling elements of the bearings. The developed cooling jacket and the newly developed oil air mist lubrication arrangement enables the control of the temperature rise of the generator and the temperature rise at the rolling element, respectively. A steady state analysis was also carried out at motor maximum power output to determine its safe operation with the objective of finding an optimal operating condition by performing a parametric study on the effect of cooling. A 3D steady state model of a 10-kW electric permanent magnet machine was generated and investigated with one cooling jacket layout. The end windings and bearings were not considered to simplify the motor model. Numerical analysis is performed with two different coolant flow rates, no flow and maximum flow (3.5 m^3/h) with special emphasis on the maximum motor temperature. The analytical calculations for the role of coolant flowrate on heat transfer characteristics for a high speed generator, showed that the convection heat transfer coefficient increases with an increase in flowrate (0.3 – 3.5 m^3/hr), while the numerical simulations showed that the maximum coolant flowrate conditions achieved lower temperature generation (27.9°C at the front bearing) throughout the generator compared to no coolant flowrate (43.7°C at the front bearing). The detailed understanding of the effects of these parameters on the generator's temperature field will help in validating the performance of the generator with actual results.

LIST OF PUBLICATIONS

- Ramesh Kuppuswamy, Colin Richmond, Azeem Khan, (2019) “A Study on the role of Oil-Air Mist Lubrication on an Ultrahigh-Speed Bio-Generator”, Procedia Manufacturing, 33(107-114), ISSN 2351-9789

- Colin Richmond, Kerry Anne Airey, Ramesh Kuppuswamy, and Azeem Khan, (2016) “Role of Coolant Flow Rate on Heat Transfer Characteristics for a High Speed Generator”, SAIMechE Conference on Mechanical, Manufacturing and Materials Engineering – showcasing postgraduate research at local universities – 4 November 2016, Cape Town, South Africa

- Colin Richmond, (2018) “Design and Development of a High Speed Generator”, Mechanical Engineering Pecha Kucha - University of Cape Town Postgraduate Showcase – 7 May 2018, Cape Town, South Africa

- Colin Richmond, Ramesh Kuppuswamy, and Azeem Khan, “ Effect of Coolant Velocity to Enhance High Speed Permanent Magnet Generator Efficiency” (In preparation 2019)

TABLE OF CONTENTS

LIST OF FIGURES

LIST OF TABLES

LIST OF ABBREVIATIONS

UCT	University of Cape Town
HSPM	High Speed Permanent Magnet
EED	Electrical Engineering Department
IPM	Interior Permanent Magnet
SPM	Surface-Mounted Permanent Magnet
PM	Permanent Magnet
PMSM	Permanent Magnet Synchronous Motor
HS	High-Speed
GE	General Electric
EV	Electric Vehicle
HSEMs	High Speed Electric Machines
TEFC	Totally Enclosed Fan-Cooled
LPTM	Lumped Parameter Thermal Model
SRM	Switched Reluctance Motor
SMPMM	Surface Mounted Permanent Magnet Machine
FE	Finite Element
TENV	Totally Enclosed Non-Ventilated
HEV	Hybrid Electric Vehicle
ZEV	Zero Emission Vehicle
AFPM	Axial-Flux Permanent Magnet
CFD	Computational Fluid Dynamics
FEA	Finite Element Analysis
4QT	Four-Quadrant Transducer
CAE	Computer Aided Engineering
PCD	Pitch Circle Diameter
EMC	Electro Chemical Machining
QC	Quality Control
CNC	Computer Numerical Control
IEC	International Electro Technical Commission
NEMA	National Electrical Manufacturers Association
RMxprt	Rotating Machine Expert
FEM	Finite Element Method

LIST OF SYMBOLS

Symbol	**Unit**	**Definition**
A	m^2	Contact area
A_w	m^2	Winding cross-sectional area
B	T	Maximum flux density
B_o		Raceway geometric factor
B_i		Raceway geometric factor
C	N	Dynamic load rating
$C_{a\text{-}f}$		Coefficient moment for air friction
C_p	kJ/kg K	Specific heat
C_{PM}	m	Radii of mass centres of magnets
C_o	J/kgK	Specific heat capacity of oil
C_a	J/kgK	Specific heat capacity of air
C_{SL}	m	Radii of mass centres of sleeve
D	m	Diameter of dog clutch
D_b	m	Pitch circle diameter of the bearing
d	m	Oil mist nozzle diameter
D_r	m	Laminated rotor diameter
d_b	m	Rolling element diameter
d_c	m	Minimum/critical diameter
d_s	m	Diameter of the shaft
E	GPa	Modulus of elasticity
E	V/m	Electric field
$F_{c,PM}$	N	Centrifugal Force
f	Hz	frequency
f_s		Coefficient of sliding friction
g	m/s^2	Acceleration due to gravity
g_b	kg/m^3	Density of the rolling element
h	W/m^2°C	Heat transfer coefficient
H_f	W	Heat developed
i	m/m	Interference rate
I	A	Armature current
J	A/m^2	Eddy current density
k	kW/mK	Thermal conductivity
L	hrs	Life in 10^6 revolutions
L_a	m	Axial length of rotor
l_c	m	Length of the conductor

L_{cj}	m	Coolant jacket length
l	m	Distance between oil mist nozzle and rolling element
L_h	J/kg	Latent heat of evaporation
L_{PM}	m	PM length in axial direction
l_b	m	Length of the laminated rotor bore
l_{SL}	m	Sleeve thickness
M_a	kg/s	Mass flow rate of air particles
M_b	Nm	Maximum bending moment
M_{ds}	Nm	Friction Torque due to sliding
M_{gr}	Nm	Gyroscopic torque
M_m	kg/s	Mass balance of evaporating liquid
M_o	kg/s	Mass flow rate of oil particles
M_s	Nm	Twisting moment
m	Kg	Mass of the magnets
m_1		Number of phases
m_{PM}	kg	Mass of magnet
N	RPM	Rotor shaft speed
N_{PM}		PM no. of magnets
N_u		Nusselt number
n		Safety factor
P	N	Radial force
P_t	W	Power
p	N/m^2	Contact pressure
P_R	W	Rotor loss
P_{cen}	N	Centrifugal effect
P_{EQ}	N	Equivalent dynamic load
	W	Total Loss
P_{Cu1}	W	Copper loss of the Stator Winding
P_{Cu2}	W	Rotor Copper loss
P_{Fe}	W	Iron-core Loss
P_i	W	Idle power/mechanical loss
P_{Δ}	W	Stray loss
P_h	W/m^3	Hysteresis loss per unit volume
P_e	W/m^3	Eddy current loss per unit volume
P_r		Prandtl number
Q	m^3/s	Volumetric flow
Q_c	J/s	Convective rate heat transfer
Q_l	J/s	Dissipation of latent heat due to evaporation
Q_{s-o}	J/s	Sensible heat due to colliding of oil particles

$Q_{s\text{-}a}$	J/s	Sensible heat due to colliding of air particles
r	m	Radius of the rotor magnets
r_s	m	Sum of the outer radius and magnet height
r_{SL}	m	Radius of the rotor
R_a	Ω	Resistance of the Windings
R	Ω	DC armature resistance
R_s	m	Radius of the rotor shaft
R_e		Reynolds number
r_o	m	Radius of bearing outer raceway
r_i	m	Radius of bearing inner raceway
S	m^2	Transversal section of flow
S_y	N/m^2	Yield strength
T	Nm	Torque
T_{tm}	Nm	Twisting moment
Teq	Nm	Equivalent twisting moment
T_f	Nm	Torque transmission through interference fit
t	m	Thickness of the material
T_b	°C	Rolling element temperature
T_m	°C	Mist temperature
T_o	°K	Inlet oil Temperature
T_a	°K	Incoming air temperature
V	m/s	Average speed
V	m^3	Volume of the material
v_c	m/s	Coolant velocity
V_b	m/s	Velocity of rotating rolling element
y	m	Deflection
Z		Number of balls/rolling elements
σ_x	N/m^2	Bending stress
τ_{xy}	N/m^2	Torsional stress
τ_{max}	N/m^2	Maximum Shear stress
μ		Coefficient of friction
ω	rad/s	Angular velocity of the magnets
ω_{max}	rad/s	Maximum rotating speed of machine
σ_H	N/m^2	Hoop Stress
ρ	Kg/m^3	Density of the material
σ	S/m	Electrical conductivity
$\sigma_{t,PM}$	N/m^2	Centrifugal force on the sleeve due to the magnets
$\sigma_{t,SL}$	N/m^2	Inertial stress of sleeve

η	kg/ms	Dynamic viscosity
η_m		Material constant
ρ_r	Ωm	Resistivity of the material
ρ_c	kg/m^3	Coolant density
α	°	Contact angle
Υ_{SL}	Kg/m^3	Specific density of sleeve material

Chapter 1

INTRODUCTION

1.1 Background

Renewable energy technology is steadily gaining importance in the energy market because of the limited nature of fossil fuels, as well as the political pressures to reduce carbon emissions. To ensure sustainable development, adequate and affordable energy should be made available to satisfy the demand of electric energy. The University of Cape Town (UCT) collaborated with the International Research Institute Stavanger, Vrije Universiteit Brussel, Faith University, and Ain Shames University to develop a scaled down prototype of an advanced power generation system with minimum carbon emission. The upscaled model would be decentralized with a target plant size of 10 MW to serve a small industrial community with drinking water production of 1000 m^3/d. UCT was tasked with the design and development of the High Speed Permanent Magnet (HSPM) Generator subsystem, in collaboration with the UCT Electrical/Mechanical Engineering Department, to be coupled to a micro-gas turbine with a blended fuel mix which includes hydrogen, biogas and biodiesel. The main specifications of the HSPM generator are a rated speed of 30000 RPM and a power output of 10 kW. However, HSPM generators produce substantial heat especially at high operating speeds and make the thermal management of these machines difficult and complicated resulting in temperature rise which leads to demagnetization, damaged insulation, bearing starvation and reduced power output and efficiency. This thesis presents the design and development of the HSPM generator and focuses on both the mechanical and electrical aspects for the Interior Permanent Magnet (IPM) and Surfaced-Mounted Permanent Magnet (SPM) topologies of the HSPM generator. In particular, it is the effect of coolant velocity to enhance the HSPM generator efficiency that makes it the subject of this research.

1.2 High Speed Permanent Magnet Machines

A HSPM generator is a machine that converts mechanical energy into electrical energy and works based on the principle of Faraday’s law of electromagnetic induction. These machines consist of electric conductors that are wound onto the stator and large magnets that are fixed onto the rotor shaft that rotates to induce a flow of electrical current in the conductors. A classic HSPM generator includes, a rotor, stator, shaft, bearings, and a generator housing. Other electric generator configurations may include more components. These machines are used in an array of industrial drives and servo applications, mainly due to their superior power density, high torque-to -inertia ratio and efficiency, and availability of high density permanent magnet (PM) material [1,2]. HSPM generators are designed with different types of rotor configuration. Two types of rotor are generally used in the construction of these machines: The more popular type is the surface mounted configuration where the magnets are mounted on the rotor surface and the interior type where magnets are buried inside the rotor, shown in Figure 1.1 respectively. The rotor and stator design of the SPM topology specific to this thesis are shown in Figure 1.2 and Figure 1.3. The dimensions of these designs were supplied by the EED and the drawings were done on Solidworks. The stator core is the stationary part of an electric generator made of silicon steel, with slots for the current-carrying conductors. To minimize eddy currents the core is laminated with laminations punched from 0.3-0.5 mm steel sheet. The slots of the stator in most designs tend to be skewed and this is because the slots take up a large part of the total area of the lamination which disrupts the uniformity of the path of the flux, thus skewing the slots presents an overlapping slot pattern and a less irregular path to the flux which enters and leaves the core radially, which results in better performance [3, 4]. The interaction of the PM rotor shaft, rotating at high speeds and the stationary stator induces a voltage related to the rate of change of magnetic flux linked with the coil. The increase in speed of the PM rotor shaft will result in the magnetic flux linked with the coils to be changed faster thus inducing a larger voltage. The high speeds are associated with eddy currents being developed which results in temperature rise in the rotor stator interface which could result in demagnetization of the magnets and damage to the insulation of the wires [5]. Past research has attempted to improve the problem pertaining to heat generation and temperature rise in HSPM machines. A novel attempt was made to minimize the eddy current loss and maximize the critical speed of a permanent magnet synchronous motor (PMSM) which was rated at 15 kW, 120 krpm for an air blower by varying the sleeve thickness from 4mm to 5mm, the eddy current loss increased with increasing sleeve thickness [6]. In [7], the research focused on the loss analysis and thermal performance evaluation for a rotor of 100 kW, 32 km/min high speed PM motor. Using finite element method, and a coupling simulation of fluid-temperature field the rotor design for the minor thrust collar and less outer diameter was found to be crucial to reduce the losses and the temperature rise for the high-speed motor. Past research in [8], summarizes and discusses the electrical and mechanical aspects involved in high-speed (HS) machine design by highlighting the main issues and tradeoffs that need to be considered. The mechanical aspects focus on the shaft dimensions, bearings and lubrication, and cooling system to enhance the performance of the machines. In [9], a holistic 3D FEM thermal model of a high speed motor spindle is presented. The model characterizes quantitatively the major heat sources, the heat transfer between spindle parts and allows for a precise transient analysis of the thermal behaviour. The comparison between measured and simulated results showed a very good agreement. Past research shows numerous scientific developments and techniques to improve the heat generated and temperature rise in HSPM machines, however no research in the last 10 years (2008-2018) focuses on the effect of coolant velocity, in the designed cooling jackets, to enhance the HSPM machine efficiency.

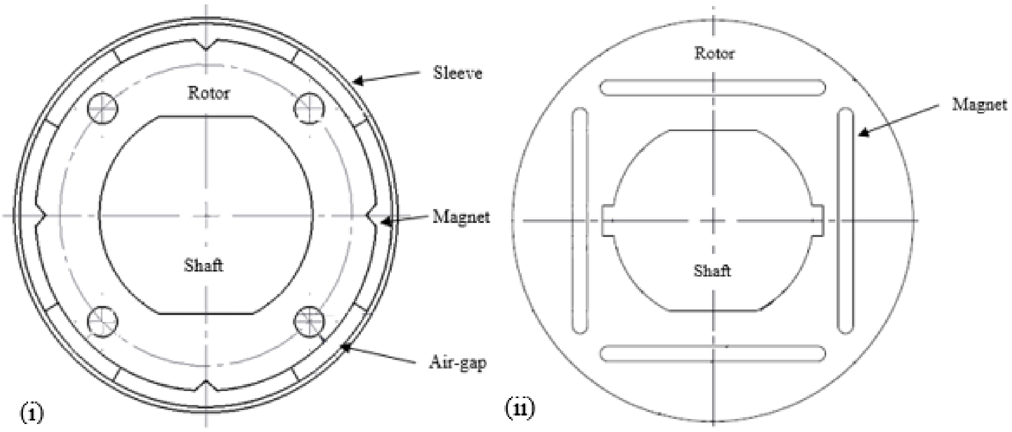

Figure 1.1: (i) Surface mount and (ii) interior mount Rotor configuration design for HSPM generator

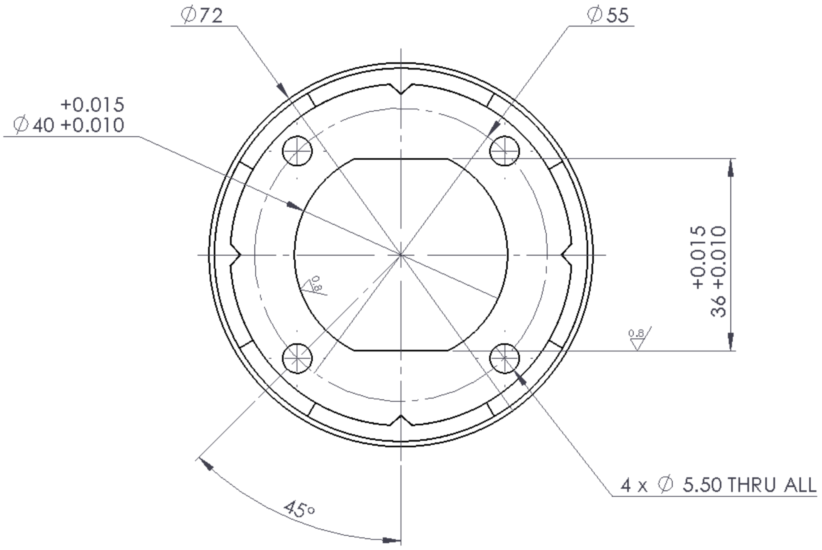

Figure 1.2: Solidworks surface permanent magnet rotor configuration

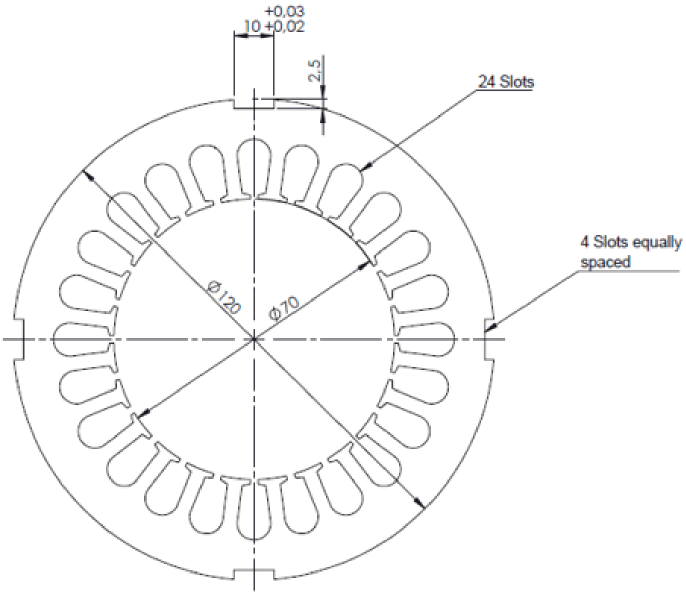

Figure 1.3: Solidworks stator design

1.3 Generator Power Losses

In a HSPM generator, not all the transmitted power is transformed into electrical energy and that is defined as generator power loss. Most of the power losses transform to heat energy which leads to the formation of extreme internal temperature inside the generator especially at high speeds. Power losses could cause an increase in the temperature of the windings and the PM magnets which reduces the efficiency of the generator. Past research [10], shows that the lifetime of the winding insulation is inversely proportional to the temperature. The higher the winding insulation temperature is, the less the winding insulation life time is.

Two studies have been released by Benhaddadi and General Electric (GE) concerning two power losses type's [11, 12]. The following Figure 1.4 is showing a comparison between the two different power losses investigation from Benhaddadi and GE [11, 12]. The results from these studies revealed that most of the power losses are due to the load losses (resistive losses from stator and rotor), and specifically from the stator winding, 35% and 33% for Benhaddadi and GE, respectively. Therefore, approximately 30% of the total power losses is the no load losses, which includes magnetic losses and mechanical losses. Magnetic losses consist of two types of losses, which are hysteresis losses and eddy losses, while mechanical losses include windage and friction losses.

Past research [13] has also shown that there is a relation to loss and the frequency of the generator, which is directly proportional to the speed of the generator. Figure 1.5 shows the variation of total loss with flux density for different operating frequencies obtained from the manufacturers' data sheet. From Figure 1.5 it can be seen that the iron loss increases with frequency and the loss as a result of eddy currents is proportional to the second power of frequency and flux density and therefore accounts for a larger percentage of the total Iron loss at higher frequencies. It is also evident that a linear model of the Iron loss would only be applicable at lower frequencies. At higher frequencies, the iron loss adopts a more exponential curve with an increase in flux densisty.

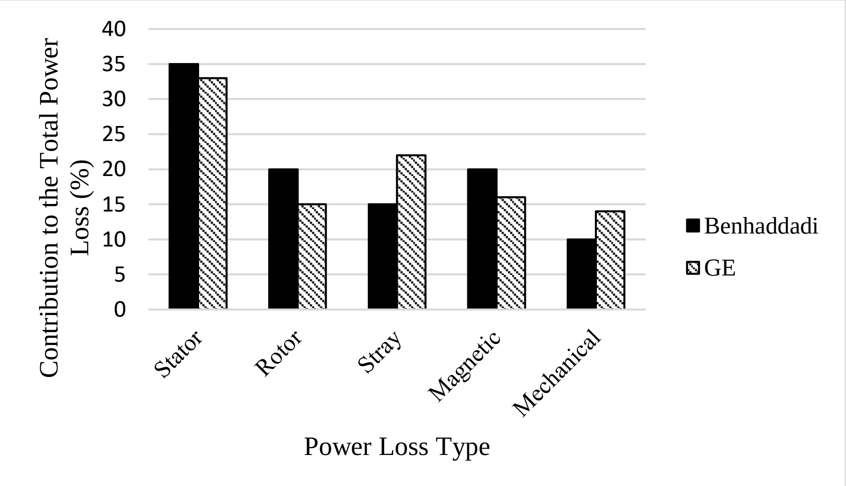

Figure 1.4: Distribution of Power Losses in Electric Motors

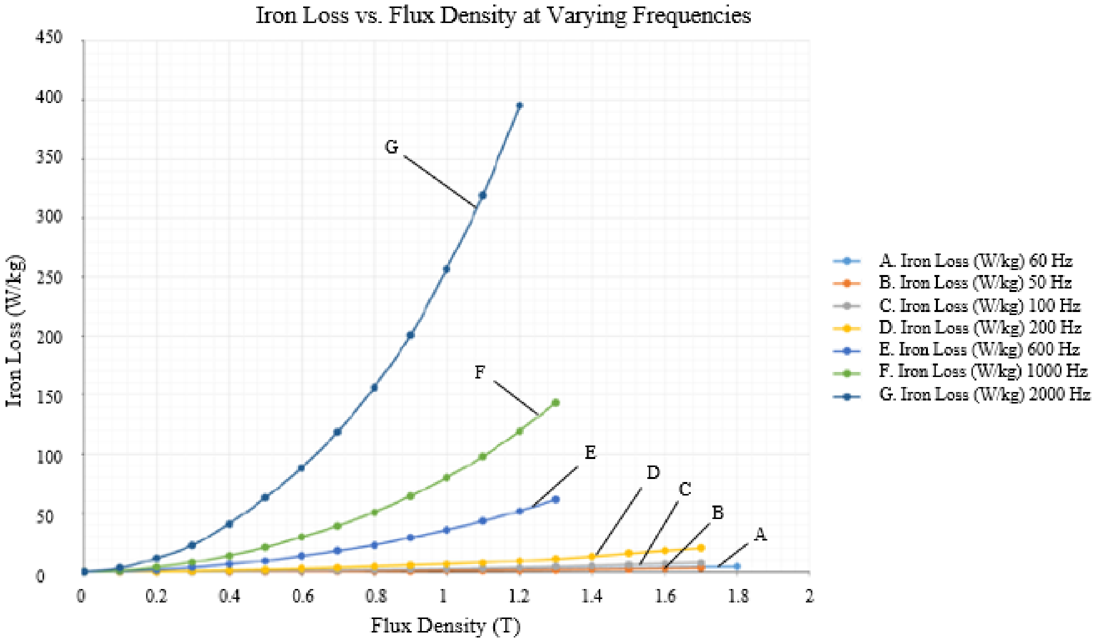

Figure 1.5: Iron loss vs. Flux density at Varying Frequencies [Appendix D]

1.4 Generator Cooling

Thermal management is one of the key aspects in HSPM generator design and has been one of the primary interest areas in advanced heat transfer research and development due to the need of producing more efficient, more compact, and less energy consuming generators. Heat transfer inside the generator is complex, as heat is dissipated from the windings, conducted into the housing, and then transferred to the annulus of the generator by a combination of thermal conduction and convection. Thus, all the power losses generated, mentioned in section 1.3, must be released from the generator to cooling medium, usually air, to assure better performance and reliability of the generator. As a result, innovative heat removal techniques have been considered in the thermal management of HSPM generators, in various applications, to keep the temperature of the stator and the rotor below the maximum prescribed limit. Air-cooling is often used due to its abundance, economical, safe and readily available. Liquid and phase-change cooling are two noble examples, but it is very hard to implement these ways in generators. However, the use of liquid can be very effective.

Increasing the coolant flowrate over the component and/or increasing the surface area across which convection occurs may achieve enhancement in heat transfer by liquid cooling. However, increasing the coolant flow requires larger water pumps which often leads to greater costs. The employing of fins with a high thermal conductivity on the generator housing is used to augment the total surface area for heat dissipation. The cost of constructing the heat sinks increases the overall cost of the system based on the machining that must be implemented. The presence of a heat sink in the system often poses an increased resistance to the flow, and pressure drop associated with the flow must be considered in the design. In general, it is more effective and economical to increase the surface area than the velocity. However, in high speed applications, such as the HSPM generator, a substantial amount of heat is generated which could have an adverse effect on the generator performance as well as critical components, and so coolant velocity is an important consideration to optimise the cooling of the generator.

A variety of applications utilize the coolant flowrate to achieve thermal management, and past research has shown that there is a relationship between coolant flowrate and the rate of heat transfer. One of the most common applications are heat exchangers. A heat exchanger is a device in which heat is transferred from one medium to another medium across a corrugation plate surface. In past research a study was done to find ‘the effect of mass flow rate on the enhanced heat transfer characteristics in a corrugated plate type heat exchanger [13]. In this study, the heat transfer and flow characteristics of water, and sodium chloride (NaCl) were tested in corrugated plate type heat exchanger. The flow of cold and hot fluid was varied using control valves. Comparison of the heat transfer coefficient of NaCl-water and water-water system at different flowrates is shown Figure 1.6 The study showed that the increase of mass flow rate with subsequent increase in the flow velocity leads to an increase in the overall heat transfer coefficient as well the individual heat transfer coefficient. In high pressure die casting processes, the cooling water flow rate plays a major role in controlling thermal pattern of the die. High pressure die casting is a manufacturing process for producing accurately net-shape, smooth-surface metal components. It is accomplished by forcing molten metal into a reusable metal mould, which is called the die. In past research, a study was done on the ‘effect of cooling water flow rates on local temperatures and heat transfer of casting dies’ [14]. In this study two sets of experimental setups and procedures were developed to answer three questions presented in the research on i) how the temperature of the die changes when varying cooling water flow rates in the internal cooling waterlines, ii) how the heat flux changes along the internal waterline when varying cooling water flow rate, and iii) how the overall heat removal rates change when different cooling water flow rates are applied to the internal cooling waterline. The objective of Experiment A was to acquire temperature signals from three locations inside the die inserts and the cooling water flowrate signal simultaneously, while the objective of Experiment B was to acquire the data necessary to estimate the overall heat removal rates. The instantaneous heat removal rates with different water flow rates are shown in Figure 1.7. it shows that the total heat removal rate of the internal waterline varies with cooling time. It decreases rapidly during the first 3s, then, gradually decreases with further cooling time. Thus, heat removal rate is also a function of cooling water flow rate.

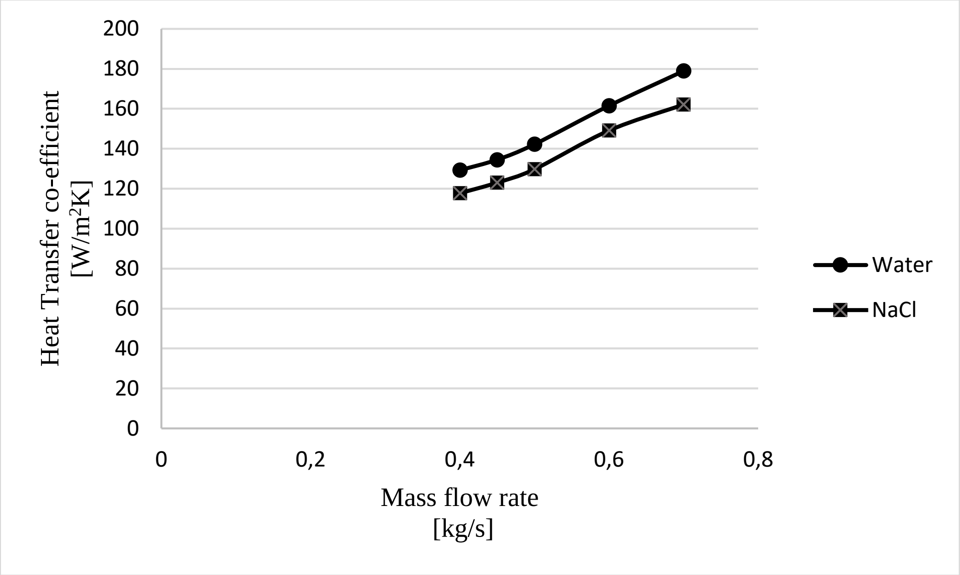

Figure 1.6: Comparison of Heat Transfer Coefficient of NaCl and Water at different flow rates

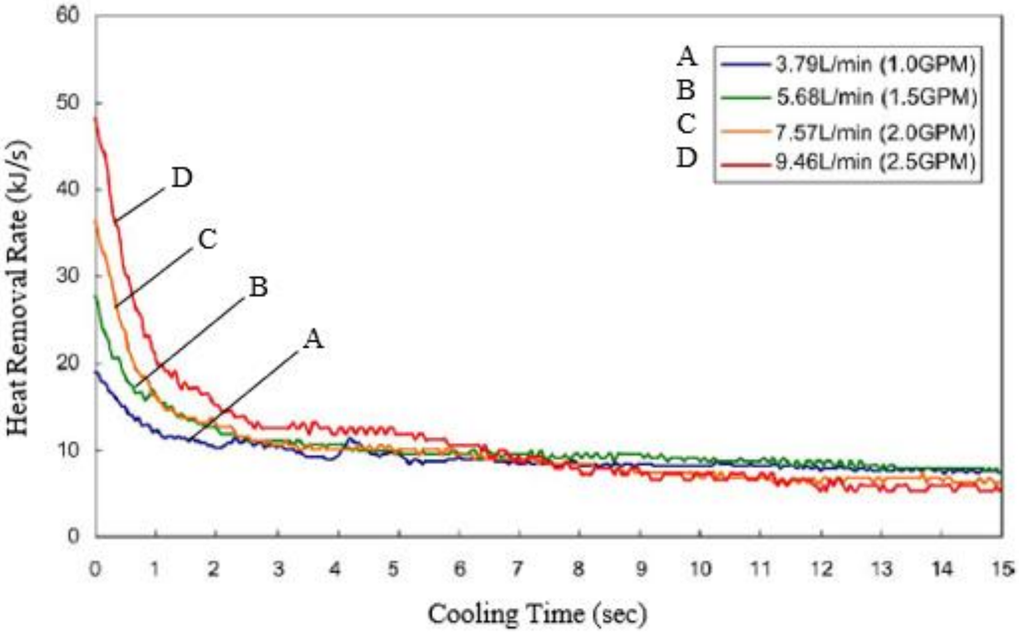

Figure 1.7: Heat removal rates with varying flow rates [14]

In another study, a three-dimensional steady state numerical method is used to investigate the performance of a cooling jacket using water as the primary coolant of a three-phase induction motor with special emphasis on the maximum temperature and the required pumping power [15]. For the study, a 3-D steady state model of a 90 kW electric induction motor for electric vehicle (EV) is generated and investigated with three different cooling jacket cooling layouts and four different numbers of coolant flow passes. The end windings and bearings were not considered to simplify the motor model which can show hotspots in the windings. Numerical analysis on each scenario was performed with five different flowrates with special emphasis on the maximum motor temperature and the pumping power. In this study, it was found that an increase in the flow rate increases the heat transfer coefficient improving the heat transfer rate from the motor. Thus, for this study a cooling jacket with six water passes and one inlet and one outlet port configuration with a flowrate of 10 L/min was used to effectively lower the maximum motor temperature while keeping coolant pumping power to a minimum value.

1.5 Problem Description

The continued need to make PM machines for power generation compact and efficient with lower excitation losses, magnetizing currents and rotor losses requires these machines to be operated at high rated speeds. However, at high speeds these machines produce a substantial amount of heat. The high speeds make the thermal management of these machines difficult and complicated as the temperature rise facilitates demagnetization which creates a cascading effect towards the reduction of the output power. Past findings also suggest that the lifetime of insulation shortens exponentially with the temperature rise of the machine [16]. A rise of 10°C cuts the lifetime of the insulation by as much as 50% [10]. The shortening of lifetime also applies to critical components such as the bearings due to lubrication starvation which is a major issue for the rolling element type bearing mounting. While cooling can add some cost, the cost can be offset by higher output performance. There are important factors that can determine how much additional performance can be extracted from a generator which includes [17]:

- Type of coolant
- Temperature of coolant
- Flow rate
- Coolant viscosity
- Thermal resistance from winding to case

However, no study in the past 10 years specifically focuses on the effect of coolant velocity (flow rate) to enhance HSPM generator efficiency. The literature reviewed in the past decade has focused on air as the cooling medium and in instances where water was used as the cooling medium, the aim was to optimize the cooling jacket configuration, optimization of the water flow through the cooling jacket, or a completely different application altogether.

1.5.1 Project Objective

To summarize the problem description, this thesis aims to achieve the following:

The development of the HSPM generator, focusing on the mechanical design in particular, to meet the specifications presented such as, high operational frequencies. Thus, a suitable cooling system needs to be implemented by means of analytical calculations and Numerical analysis, using ANSYS.

A study needs to be conducted on the role of oil-air mist lubrication on the HSPM generator to determine the temperature distribution of the high speed of the generator by using the theory of hydraulics and thermal analysis using ANSYS Maxwell simulation and ANSYS mechanical thermal steady state.

Analytical calculations need to be performed for the role of coolant flow rate on the heat transfer characteristics of the HSPM generator. Numerical simulations on the effect of the coolant velocity to enhance the HSPM generator efficiency also needs to be performed using ANSYS Fluent. Two coolant flowrates are to be considered, no flowrate and maximum flowrate (3.5 m^3/hr).

As a basis for future work which is beyond the scope of this thesis, basic no-load tests need to be conducted to validate the analytical calculations and numerical simulations.

1.5.2 Test Setup: An Ultra High Speed PM Generator

The testing of the HSPM machine consists of a vibration test and temperature (heat generation and effect of coolant flowrate) test. While two machines were designed and developed for this thesis, the testing was only considered for the SPM machine and not the IPM machine. The vibration test measured the vibration generated by the machine at different speeds. The test measured the heat developed in the SPM machine, close to the front and rear bearings, using thermocouples which were fitted into holes located close to these bearings. Throughout the testing, the SPM machine was operated with the assistance of the cooling jacket. Thus, there are two conditions that were considered for the testing; which is when there was no flow in the cooling jackets, zero coolant velocity, and the second condition was when the cooling jacket operated at maximum flow, maximum coolant velocity. A chiller was used to circulate the coolant through the cooling jackets. Only two velocities were considered due to the limited resources. The SPM machine was also designed to operate at 30000 RPM however, the test was only done up to 8000 RPM. This was due to the limitations of speed and temperature experienced by the aircraft motor that was used to drive the HSPM generator.

1.6 Thesis Outline

The structure and flow of this thesis is presented below and gives an overview of how each chapter is connected

Chapter 2 – Literature Review

Beyond this introductory chapter, Chapter 2 presents the literature review of work done in the last decade regarding the cooling of high speed machines

Chapter 3 – Design and development of the HSPM Generator

Chapter 3 concerns the design and development of the HSPM generator by introducing the generator and the specifications required. A detailed design of the HSPM generator, together with all the major parts of the generator are presented and discussed in detail, with the complete technical drawings found in Appendix A. The chapter then focuses on the manufacturing process of all the parts of the generator.

Chapter 4 – Analysis of Designed HSPM Generator

Chapter 4 concerns the analysis of the designed HSPM generator by summarizing the material properties used in the HSPM generator. The rotor shaft twisting and bending moments are also determined as well as the critical diameter of the rotor shaft of the HSPM generator. The rotor shaft design of the HSPM generator uses friction to transmit torque from the shaft to the rotor itself and the pressure to avoid slip between the rotor and the rotor shaft at high speeds is determined. This chapter also focuses on the bearing life and bearing selection of the HSPM generator as well as the deflection and rigidity of the rotor which is supplemented by the precise design of the housing. This chapter also focuses on the various components which make up the housing. Emphasis is made on the design of the cooling jackets of the HSPM generator and the design of the bearing lubrication system. This chapter also establishes the cause of the heat generated in the HSPM generator by considering the electromagnetic losses (stator loss and rotor loss), the idle power/mechanical loss and core losses and their effects on the HSPM generator. The Chapter then looks at the thermal analysis of the HSPM generator as well as the effects of coolant flow rate on heat transfer characteristics of the generator.

Chapter 5 – Numerical Calculations

Chapter 5 focuses on the Numerical calculations performed using ANSYS. The introduction classifies the HSPM generator and looks at the type of Permanent magnets used in the generator as well as the insulation class selected for the wiring. The chapter then looks at the heat transfer theory focusing on conduction and forced convection heat transfer in conjunction with ANSYS numerical analysis theory. Furthermore, the chapter focuses on ANSYS Maxwell and its familiarization as well as the simulations performed. The coupling of Maxwell designs with ANSYS Thermal via workbench as well as the computational Fluid Dynamics (ANSYS Fluent) are also covered in this chapter.

Chapter 6 – Experimental Results and Discussion

Chapter 6 concerns the test setup used for the temperature and vibration for the HSPM generator as well as the procedure and data acquisition for the respective tests. The chapter also presents the test results by first looking at the data analysis performed for both the vibration test and the thermal test, then the results for the respective tests are presented and discussed.

Chapter 7 – Conclusions and Recommendations

Chapter 7 concludes the thesis report based on factors of the design and development of the HSPM generator, the heat generated and how the heat generated was countered through cooling. Recommendations for further work are also presented.

Chapter 2

LITERATURE REVIEW

2.1 Introduction

In the last decade, thermal analysis and thermal management of high speed electric machines (HSEMs) has become a major concern for both scientists and researchers. For heat transfer augmentation, there are several important factors that can enhance the performance of HSEMs through the selection of an adequate machine topology and bearings, the design of the rotor, stator, housing as well as the lubrication system, and by implementing cooling such as: type of coolant, temperature of coolant, flowrate, coolant viscosity, and thermal resistance from winding to case [17].

2.2 High Speed Electric Machine Topologies

The selection of the topology for high speed machine design is dependent on the application, speed as well as the desired power output. Thus, according to past research [18], topologies pertaining to high speed applications include; Permanent Magnet (PM) Machines, Induction Machines (IM), Synchronous Machines, Switched Reluctance (SR) Machines, Claw Pole Machines, Homo-Polar Machines and Synchronous Reluctance (SyR) Machines.

In [19], switched reluctance machines are found to have numerous advantages in high speed applications such as fault tolerance, robustness and low cost. On the other hand SR machines have major drawbacks such as vibration, noise, drive topology and torque ripple which hinders the use of these machines for less specific applications Furthermore, research conducted in [20] shows that SR machines are able to operate under the loss of one phase and display better fault tolerance in designs with more than three phases, making these machines favourable in the aerospace industry.

In synchronous reluctance machines the rotor and the stator have a similar construct to that of IPM machines but differs from the IPM machine in that it is completely free of magnets. This makes SyR machines inexpensive to manufacture and capable of operating at much higher temperatures and speeds than PM machines [21]. In [21], SyR machines are found to have similar advantages as SR machines except that they possess lower torque ripple and can operate from simple P.W.M. converters. Further research [22] suggests that the performance of SyR machines reduces due to structural limitations at speeds over 70 krpm. Furthermore, the use of SyR machines in high-speed applications is usually discouraged due to their low structural integrity caused by the presence of multiple flux barriers. In [23-26] new mechanically robust construction techniques were used which includes, a 100 kW 20,000 rpm motor, a 10 kW 10,000 rpm, 20 kW 20,000 rpm and a 5 kW 50,000 rpm SyR machine, respectively.

In [27], Synchronous homopolar machines have been commonly used in high-speed flywheel energy storage systems. They are also similar to the wound-field synchronous machine however, differs in that the field winding is fixed to the stator rather than the rotor, which results in a simplified rotor construction, elimination of slip rings and better cooling of the field winding. Further research is ongoing on the design and development of synchronous homopolar machines for HS applications. Still in [27], a 30 kW 100,000 rpm machine was designed, constructed and tested. Furthermore, the development of a homopolar machine with a slotless stator was suggested which would eliminate slotting induced rotor losses and bring about the realization of higher airgap flux densities. In [28], a 8 kW 60,000 rpm machine was proposed for use in a flywheel energy storage system.

In applications where higher power and speeds are desirable, the solid rotor induction machines are preferred based on their robust construction. In [29] it is recorded that the smooth solid rotor design is the most robust however, this design is inefficient as it exhibits low conductivity paths for the induced rotor currents. Other designs of induction machines include the slitted solid rotor, coated solid rotor and caged solid rotor. Figure 2.1, shows the different rotor designs of the induction machines. In [30] the coated solid rotor design is an improvement over the standard solid rotor design. The introduction of a coated copper layer over the rotor provides enhanced mechanical robustness and higher efficiencies. Furthermore, [30] shows that the axially slitted solid rotor induction machine enables the fundamental flux component to be guided into the rotor and also provides a path of high resistance for eddy currents travelling on the rotor surface which is due to the construct of this topology which has an axially slitted rotor. Research conducted in [31] revealed that the caged solid rotor had a blend of features from both the solid rotor topology and squirrel cage rotor topology and in turn achieves higher efficiency levels and utilization factor compared to copper coated solid rotor topology. In [32] a comparative study is done and concludes that from the four topologies of induction machines for high speed applications, the order of preference in terms of mechanical performance is; solid rotor induction machine, slitted solid rotor induction machine, solid rotor with coated conducting sheet induction machine and finally, solid cage rotor induction machine. However, the result is reverse in terms of electromagnetic performance with the first choice being the solid cage rotor induction machine.

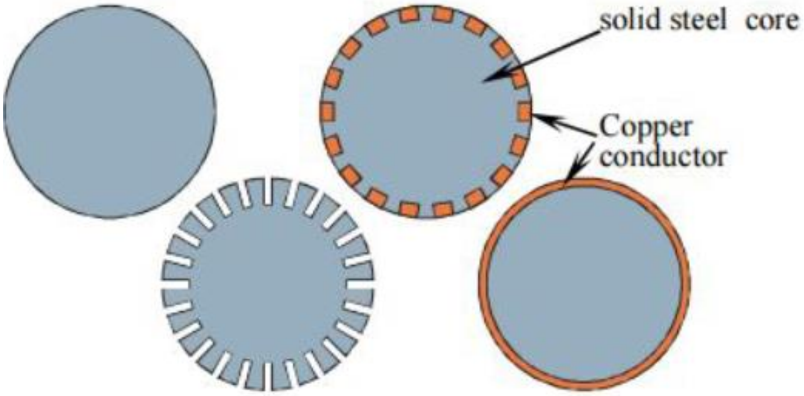

Figure 2.1: Induction Machine Rotor Structure

HSPM machines have increasingly become more popular over the years particularly in high speed applications due to their high efficiency levels and the design of novice configurations. As previously mentioned the two most common topologies in high speed applications are the Interior Permanent Magnet (IPM) and the Surface Permanent Magnet (SPM) machine.

[30] reveals that the SPM machines are the dominant choice in industry with evidence from various technical papers reviewed. This is due to the fact that SPM machines show a greater robustness over other configurations such as the IPM machines, as the use of the sleeve proves to be better at retaining magnets at high speeds than embedding them in the rotor as with IPM machine [33]. In [34] research done on IPM machines in high speed applications showed that these machines are limited primarily by mechanical constraints. This is due to the strength of conventional electrical steels that these machines ae limited to surface speeds less than 80 m/s. However, in [35] the use of high-strength electrical steels makes it possible to achieve peripheral speeds in excess of 230 m/s in IPM machines. In [36], permanent magnet machines are compared to induction machines as shown in Figure 2.2 which shows the rated powers and speeds of high speed machines, permanent magnet machines and induction machines.

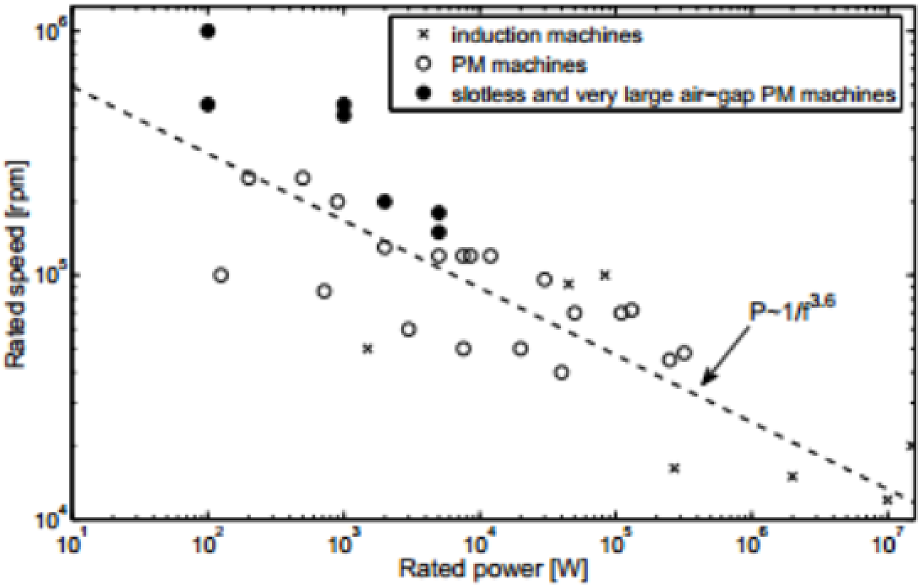

Figure 2.2: Rated powers and speeds of existing high-speed machines

From the various topologies that have been reviewed from literature, the less common topologies used for high speed applications include; the Switched Reluctance machine, Synchronous Reluctance machine and the Synchronous Homopolar machine. While the induction machine and the permanent magnet machine show clear dominance in high speed applications. In particular, the PM machine was seen as suitable for higher speed, low power applications whereas the IM was favourable for lower speeds and higher power applications [30]. According to [34], permanent magnet machines limited to applications where the required surface speed of the rotor does not exceed 250 m/s.

2.3 PM Rotor Structure

In HSPM generators, the rotor is responsible for providing the stator winding with rotational magnetic field but at the same time, the revolving rotor at high speeds produces large centrifugal forces. Thus, both electromagnetic and mechanical considerations have significant meaning for the rotor design of a HSPM generator. However, the PM rotor is preferred compared to other structures due to its simple structure and high power density.

A. Determination of Rotor Diameter

Literature shows that the centrifugal force is proportional to the square of the rotor speed. Thus, to reduce the centrifugal force, the rotor diameter needs to be chosen to be as small as possible. However, the rotor diameter cannot be too small due to the required electromagnetic torque and output power which means the rotor should have enough space to contain the permanent magnets, and the stator should also have enough size to contain the windings. The rotor also needs to have enough strength and rigidity. Therefore, the rotor cannot be too long and too thin, and a proper ratio of length to diameter needs to be considered.

B. Choice of Pole Number

The choice of pole number affects the machine structure and performance of the HSPM generator. There are usually two options of the pole number: 2 or 4 poles and either option has its own set of advantages and disadvantages. In a 2-pole generator, the rotor has a simpler structure as shown in Figure 2.3 (a). The PM ring is easy to build and has good strength and rigidity even without the use of a sleeve on the surface of the PM ring. Furthermore, the frequency of the magnetic flux in the stator core and the frequency of the stator current are much lower in the 2-pole generator compared to the 4-pole generator, which could result in reduced stator and copper losses. Despite these advantages, the main disadvantage of this structure is in the length of the machine. This is due to the long endings of the 2-pole stator windings. In contrast to the 2-pole machine, one of the advantages of the 4-pole generator is that the length of the machine is shorter in the axial direction due to the smaller endings of the 4-pole windings. However, this structure will succumb to larger stator core and copper losses as well as less strength of the rotor due to the assembling of the 4-pole permanent magnets. Furthermore, a sleeve is required as shown in Figure 2.3 (b) for safety considerations based on the high centrifugal forces. Literature shows that there are two methods to build the sleeve. One of the methods is using a thin ring made of non-magnetic alloy steel and the other method is using a carbon-fibre bandage. A thin ring made of non-magnetic alloy steel has good mechanical performance but relatively poor electrical behaviour due to the eddy losses caused by the harmonic component of the airgap magnetic field. A carbon-fibre bandage has good mechanical and electric characteristics without eddy losses [37-38]. However, carbon-fibre material has poor thermal conductivity which could cause the heat generated in the rotor not be transferred efficiently.

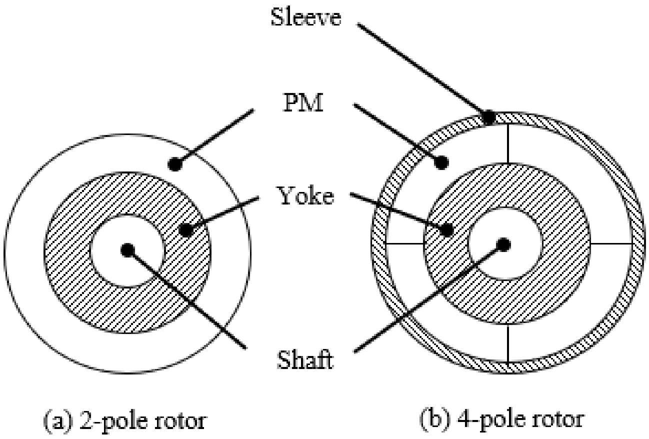

Figure 2.3: Rotor structure of high-speed PM generator

C. Choice of PM Material

The PM material properties contribute significantly to the size and performance of the HSPM generator. The factors listed below are considered for choosing PM material and rotor design [39]:

- To get the high power density and high efficiency of the generator, the PM material should have good magnetic properties normally including remanence B_r, coercive force H_c and maximum energy product $(BH)_{\text{max}}$.
- The magnetic properties of the PM should be stable, and the demagnetization curve is expected to be linear within the operation temperature range. An important issue is to ensure that the rotor never reaches a temperature, which would de-magnetize the magnets. So, the PM material should withstand high temperature.
- The price of the PM material and the cost of the PM rotor manufacture should be reasonable.

Considering the aforementioned considerations, the sintered Nd-Fe-B material would typically be the best candidate [39]. The magnetic properties and working temperature of some sintered Nd-Fe-B materials are as shown in Table A.

Table A: Magnetic Properties and working Temperatures

Grade	Remanence B_r (T)	Coercive force H_c (kA/m)	Energy Product $(BH)_{\text{max}}$ (kJ/m^3)	Working temperature (°C)
N35	11.8	859	263	80
N35M	1.09	875	263	100
N35H	1.18	875	263	120
N30SH	1.09	812	223	150
N30UH	1.09	812	223	180
N28UH	1.05	780	207	180
N28EH	1.05	780	207	220

It can be seen from Table A that the magnetic properties of the PM material will decrease if the working temperature increases. The choice of the PM material should be a compromise between the considerations of magnetic properties and working temperature.

2.4 Stator Design

The design of the stator requires careful attention to avoid high losses and overheating. Literature [39], shows that if the rotor speed of a HSPM generator is above 50000 rpm, the variation frequency of magnetic flux in the stator teeth and yoke will be more than 800 Hz (for 2-pole machine) or 1600 Hz (for 4-pole machine). Consequently, the current frequency in the stator winding is much higher than the conventional machine.

A. Stator Core

Based on the design theory of AC machines, the stator core is subject to losses, which is governed by the frequency and magnetic flux in the stator core, the loss coefficient per kg of the stator core material tested under the condition of a specific frequency and flux density, and the stator core weight. In [39], it can be seen that the stator core losses per kg of the high-speed generator will be much higher in comparison to normal machines due to the high frequency. Literature shows that there are two approaches to reduce the stator core losses. The first approach entails reducing the flux density in the stator teeth and yoke, and the second approach would be to reduce the loss coefficient by using thinner high quality cold-roll silicon steel sheet to make the stator core. The flux density in the stator teeth and yoke for the high-speed generator should be much less than that of a normal low speed machine and the thickness of the stator core silicon steel should be less than 0.3 mm. The thinner the stator core silicon steel sheets, the less the losses of the stator core.

B. Stator winding

If the frequency of the stator winding is more than 1 kHz, then the skin-effect should be considered in the stator winding design. Literature [39] shows that in order to use the stator winding efficiently, the wire should be divided into individually insulated small sized strands (referred to as Litz wire). The radius of the of the conductor is governed by the angular frequency of the winding current, as well as the permeability and conductivity of the wire. Furthermore, the filling-factor of the stator slots is relatively low when the Litz wire is used due to the insulation between the individual wires. Therefore, high quality wires with thinner insulation should be used. The advanced vacuum pressure impregnation (VPI) process can ensure good heat dispatching and a long time life of the winding.

2.5 Design of Housing

The housing design is of utmost importance because it holds all the components together. Therefore, it is vital that all the components (particularly the bearings) and housings are accurately and precisely mated in order to take full advantage of the cooling jackets, lubrication system, and precision bearings capabilities, which include rotational accuracy, high speed performance, and low heat generation. When the inner or outer ring of a bearing is mounted onto a shaft or into a housing with some interference, the shape of the shaft or housing (out of roundness) is transferred to the bearing raceway surfaces and affects running accuracy. The NSK (bearing manufacturer) catalogue shows that when multiple angular contact ball bearings are used, cylindricity affects the distribution of preload for each bearing. Therefore, the mating parts should be as accurate as possible. Inaccurate mating of parts can cause the formation of peaks and ridges. Tolerances and surface finishes for the housing and other components also need to be considered in the design of the housing.

2.6 Lubrication

The main purposes of lubrication are to reduce friction and wear inside the bearing that may cause premature failure. The effects of lubrication may be briefly explained as follows: reduction of friction and wear, extension of fatigue life, dissipation of heat, prevention of foreign material entering the bearings, and protection against corrosion or rusting. For high speed machines in which high accuracy is important, it is necessary to prevent excessive temperature rise of the rotor to reduce thermal deformation. Bearing heat generation is divided into a load term determined by the bearing type and load, and a speed term determined by the lubricating method and speed. Generally, the speed term is greater, but if a lubricating method resulting in a small speed term is selected, the influence of the load term cannot be disregarded. Therefore, it is important to select a low heat generating bearing and lubricating method. The lubrication method and quantity of lubricant have important effects on the heat generation. Lubrication using a small amount of grease is common since this method is economical, maintenance free, and there is little heat generation. At high speeds, to maintain a constant low temperature, the oil-air lubrication method, which requires a minimum quantity of oil, should be considered. Table B, compares the various lubricating methods.

Table B: Comparison of Lubricating methods

Lubricating Methods	Advantages	Disadvantages
Grease Lubrication	▪ Cost is low. ▪ Limitation of temperature rise is possible. ▪ Maintenance free.	▪ If packed grease deteriorates, seizure may occur. ▪ May allow penetration of dust or cutting fluid
Oil Mist Lubrication	▪ Since new oil is always fed, no fear of oil deterioration. ▪ Dust and cutting fluid cannot easily enter	▪ Pollution of environment. ▪ Oil supply quantity varies depending on oil viscosity and temperature, so control of a small flow rate is difficult. ▪ It is difficult to confirm that oil is actually fed.
Jet Lubrication	▪ Since the oil flow rate is high, dust and cutting fluid cannot enter and seizure hardly ever occurs. ▪ Because of cooling by oil, the bearing temperature can be controlled to some degree.	▪ Frictional loss is high. ▪ Since oil leaks, it is difficult to use for vertical configurations. ▪ Cost is high.

Oil-Air Lubrication	▪ Since oil quantity control is possible, the optimum quantity of oil is fed, and heat generation is low. ▪ Besides little heat-generation, there is a cooling effect of the air, so the temperature is low. ▪ Since new oil is always fed, no fear of oil deterioration. ▪ Dust, cutting fluid cannot easily enter. ▪ Environmental pollution mist is slight.	▪ Cost is rather high. ▪ Confirmation of whether oil is actually fed to bearing is difficult.

2.6.1 Oil Mist Lubrication and Oil-Air Lubrication

Spray oiling is a method of spraying oil by turning it into a mist using compressed air. It is also called oil mist lubrication. Oil-air lubrication is a method of feeding oil continuously by injecting oil into a compressed air stream by means of a mixing valve that intermittently discharges the minimum quantity of oil using a constant-quantity piston. Table B shows the recommended oil quantity for the lubrication methods described, each quantity is for one bearing. In the case of oil mist lubrication, it is necessary to adjust the oil quantity to accommodate for the effects of the branches in path tubing, and leakage from the gaps around the spacers. In cases where the $d_m n$ value is higher than 1 800 000, the oil quantity should be increased. For bearings operating under normal speed, proper lubrication can be achieved by positioning the nozzle bore along the side of the bearing and aiming directly into the bearing interior at the level of the inner ring. For constant high speed operations, it is advantageous to position the nozzle bore so that the lubricant is directed into the bearing interior at angle of about 15° or 20°. An appropriate means of draining the oil sump is necessary to prevent severe oil shear friction, which can result in bearing damage at the sliding section. Furthermore, a maximum 5-micron filter is recommended to provide filtration of oil entering the lubricating system. In a study done in [40], on the role of oil-air mist lubrication on an ultrahigh-speed generator, the output portrays the use of pressurized oil-air particles as a lubrication method on an ultrahigh speed generator in order to avoid: thermal damage and starvation at the rolling element and to address the predominant concern which is effective cooling of ultra-precision ball bearings even at elevated speeds. The ultrahigh-speed generator was designed and developed to operate at a maximum speed of 30000 RPM to deliver 10kW output power and expected to reach a temperature rise of 80~92°C, with approximately 2 kW idle power consumption, enough to cause severe impact to the rolling elements of the bearing. The newly developed oil-air mist lubrication arrangement was able to control the temperature rise at the rolling element and ensured the use of ultrahigh speed conditions for the generator.

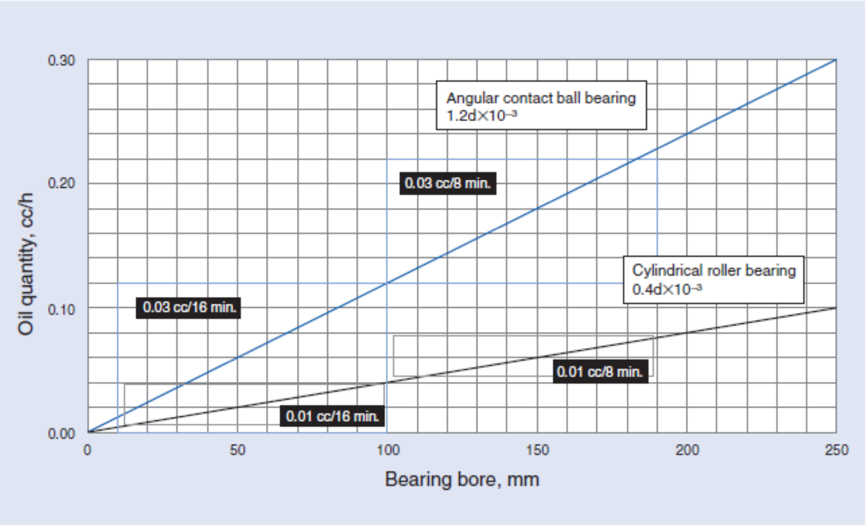

Figure 2.4:Recommended Oil Quantity for Each Bore Size of Bearing (Minimal Oil quantity Lubrication)

2.7 Bearings

Bearings serve as one of the critical components in high speed machines, which can cause major problems if not dealt with correctly. Some of the challenges encountered include friction loss, mechanical strength and reduced reliability, which all become pronounced as the rotational speed of the machine increases. The options available for high speed machines bearing selection include, ball bearings, static and dynamic fluid bearings, foil bearings and magnetic bearings. Figure 2.5 shows data from past research [41] for bearings used in HS machines.

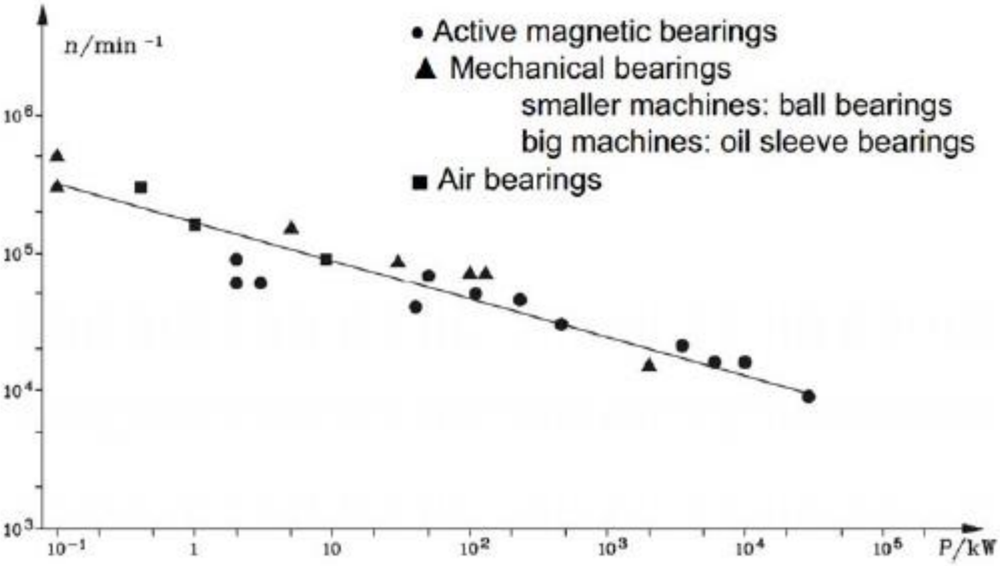

Figure 2.5: Bearings Considered for High Speed Machine Application

Ball bearings are the most commonly used and simplest option for HS applications. In [42], research shows that the main advantages of ball bearings include simple construction, small size and high robustness. Furthermore, the lifetime of ball bearings can be estimated using Equation (4.21). It can be concluded that the lifetime of ball bearings is highly dependent on load. Doubling the load reduces its life by up to 10 time, while doubling the speed, reduces it by half.

Air bearings levitate the rotor shaft during operation by using air pressure. The air pressure is often generated externally or by the rotor through a unique design [42]. In [43], research shows that it is usual for air bearings to be designed much smaller than magnetic bearings for the same load capacity and stiffness, which allows for the realization of more compact machines for high speed applications. However, one of the main disadvantages is their poor dynamic stability. Experiments done in [44] show that air bearings can operate up to speeds of about 700 krpm and temperatures of up to 650°C.

Magnetic bearings also use levitation to support the rotor shaft through the use of magnetic forces. However, research conducted in [42] shows that the complex auxiliary control system of magnetic bearings inevitably increases their capital outlay as compared to other bearings. In [45] the precise position control and vibration damping of magnetic bearings make them particularly appropriate and desirable in high speed rotating machines. Presented in [46] is the design and analysis of a permanent magnet bearingless high speed motor. The bearingless technology was capable of being used for high speeds applications. The bearingless design is an improved modification of the active magnetic bearings but it has not yet been completely realized in high applications as research is still on-going [47-48]. Research conducted in [49] revealed that magnetic bearings cannot be stable due to the fact that they only make use of permanent magnet interactions or reluctance forces, which is in accordance with Earnshaw theorem. Furthermore, in [43, 50] several developments have been made in hybrid magnetic bearings which combine both air and magnetic bearing properties, in order to achieve better stability. Table C displays a summary of the pros and cons of different bearing types for high-speed machines.

Table C: Pros and Cons of different Bearing types

	Bearing Type	Pros	Cons
	Magnetic	No Wear Lifetime Controllability	Complexity
	Ball	Small size Availability	Losses Noise Lifetime/wear
Film Bearings	Static	Exact positioning Lifetime	External pressure System
	Dynamic	Small size	Instabilities Wear at start/stop
	Foil	Small size	Availability Wear at start/stop

Of the aforementioned types of bearings, only the ball bearings
have a simpler design process. The rest require more intricate design methods and analysis.

2.8 Previous Work

Thermal management play an important role in the design of electrical machines and in the quest for better overall economics it is found that high speed operation of electrical machines is limited by their operating temperatures. Therefore, the heating and cooling of electrical machines operating at high speeds are the decisive elements for the progression of output power, size, weight, cost, etc. A better cooling design can improve the motor efficiency, as well as the motor operational reliability [51, 52]. Thus, it is imperative to optimize thermal management and electrical machines cooling systems to enhance the longevity and reliability of the motor [53].

In [54], a lumped parameter approach is proposed for prediction of the steady-state and transient thermal behaviour of a prototype multiple teeth per stator pole switched reluctance motor of totally enclosed fan-cooled (TEFC) design and experimentally demonstrated its application to the induction motor. While a study in [55] used a lumped parameter thermal model (LPTM) to study the temperature rise of a 1 kW motor. The thermal model employed considered just a stator, rotor, and environment representative temperatures so that parameter estimation could be carried out. However, their model was unable to find the temperature change of a position in the motor. However, while a lumped parameter model has advantages in computational effort, parameterization, and interpretation of steady-state results, it lacks the accuracy and 3-D capability needed to support a good design tool.

The study done in [56] reported on the thermal analysis carried out on a switched reluctance motor (SRM) by finite element (FE) methods. In their study, thermal flux plot, the isothermal distribution, thermal gradients in different parts of SRM at its different rotor positions and the respective governing equation are presented. While FEA possesses respectable accuracy, it has drawbacks in computational effort, 3-D capability, and parameterization.

The need of a sustainable clean future has paved the way for environmentally friendly technology which is reliant on the electric machines for various applications such as electric vehicles and power generation. With the development of these motors, thermal analysis becomes more and more important due to the influence of heat generation during power transmission on the performance and safety issues of electric motor particularly in high speed applications. In [57], the research investigated the capabilities of the switched reluctance motor (SRM) for electric vehicle and hybrid electric vehicle applications.

The study in [58] experimentally and numerically investigates the thermal performance of a large-scale motor with a capacity of 2350 kW. Their models of the fan and motor have been implemented in a Fluent software package to predict the flow and temperature fields inside the motor.

Paper [59] established a thermal prediction model to estimate for the temperature rise of a 30-kW reluctance motor in order to obtain quickly thermal information on some sensitive components of an electrical motor in a short lapse of time. In their model, two model reduction techniques are used: the Eitelberg method and the reduction by modal identification. The thermal characteristics of the system is modelled and validated.

Heat transfer in electrical machines is complicated because all the phenomena which includes, conduction, natural convection, forced convection and radiation are all present depending on the motor cooling system such a natural convection, fan cooling, and liquid cooling. In addition to this, many heat sources are active at the same time. Therefore, it is difficult to separate the cause and effects in thermal exchange phenomena.

A study done [18], analyses the role of coolant velocity towards the transfer of the heat generated at the rotor-stator interface by using mathematical modelling to enhance the performance of a 10 kW high speed generator operating at 30000 RPM. The mathematical model showed that an increase in coolant flowrate increased the convection heat transfer coefficient which makes it possible to characterize the role of coolant flow rate on enhancing the convection co-efficient for a high speed generator.

Research presented in [60] shows thermal fluid analysis on the air cooling of a permanent magnet electric motor with a centrifugal impeller numerically and experimentally. It was found that the cooling flowrate is proportional to the motor rotation speed and cooling is a determining factor for the motor torque rating. Further, the increase of coolant flowrate did not have a significant effect on the convection heat transfer coefficient.

In [61], the study numerically discussed the convective heat transfer coefficients in a motor under different cooling conditions based on empirical data. These cooling conditions are totally enclosed non-ventilated system (TENV), totally enclosed fan-cooled system (TEFC) and external liquid cooling system of the motor housing.

The study done in [62] presented the characterization of forced cooling channels using oil as the working fluid with three different shapes which are applied in traction motors mounted in hybrid vehicles (HEVs) or Zero Emission Vehicles (ZEVs). Both heat transfer coefficient and pumping power were estimated. Further, the dimensionless parameters Nusselt number and Darcy friction factor are evaluated with the aim to understand the characterizations for different channels.

The study in [63] investigated the optimization of the shape of the channel in the hollow shaft for the oil spray cooling of a high capacity 35 kW in-wheel motor and the evaluation of the thermal performance of the motor both numerically and experimentally. The thermal flow was analysed by evaluating the thermal performance of two conventional cooling models of in-wheel motors under conditions of continuous rating base speed. The model was designed and enhanced for in-wheel motors, and evaluated its thermal performance under continuous rating conditions, and the maximum temperatures of the coil at the base and maximum speeds, which were set as the design points, being 138.1°C and 137.8°C, respectively.

The research in [64] addresses the evaluation of the heat transfer capability of a finned frame for different velocities of the cooling fan and different numbers and dimensions of the fins. For each frame, each sector was thermally isolated and evenly heated. The experimental results presented local transfer coefficient on each axial sector in terms of the fin dimensions and cooling air velocity and used the empirical coefficients to evaluate the thermal capability of the frames and to compute the temperature gradient needed to dissipate certain losses. The research was able to propose a simple and accurate method to size finned frames.

Research in [65] focuses on the steady-state modelling and laboratory testing of an axial-flux permanent-magnet (AFPM) electrical machine intended for a traction application. The proposed hybrid cooling arrangement consists of a frame cooling circuit with a water flow inside, a set of copper bars inserted in the teeth, and a segment of potting material around the end windings. Computational fluid dynamics (CFD) and finite-element-analysis (FEA) are applied for the preliminary design. The test results of the… show that the stator winding temperature reduces by 20°C in the case of copper bars and by 25-35°C in the case of copper bars and potting material.

The study in [66] presents a new IPM motor using rotor cooling to enhance motor power per specific weight. The IPM motor employs a forced cooling by providing channels for housing cooling a hollow shaft for rotor cooling for the study. The coolant circulates in the entire motor from the housing to the rotor through the proposed coolant paths. This type of cooling system forces the coolant to circulate inside an IPM motor, providing superior cooling effect compared with conventional cooling methods. It was found that the proposed cooling system can increase motor efficiency because high motor speed can be achieved with a superior cooling effect of the IPM motor.

The research in [67] presents the analysis of 3D steady-state temperature field distribution of air-cooled and water-cooled MW high speed permanent magnet motor with 1120 kW, 18000 RPM under the rated load. It was found that the results provided a theory basis for the cooling system design of this type of high speed permanent magnet motor. The cooling structure with both air and water-cooling structures ensured that the temperature rising of the motor was in the allowable range, which proved the rationality of the cooling structure. Furthermore, the modelling and meshing of the motor could be simplified significantly via making a reasonable equivalent insulation layer.

[68] aims to find the hot spot and investigate the cooling system of the four-quadrant transducer (4QT), the calculated thermal field is calculated using finite-element method (FEM). The impact of different water-cooling channel is discussed, and 12-water-channels distribution is employed. It was found that the stator winding maximum temperature decreases by approximately 13°C as compared to that in the original cooling system, which validated the improvement of cooling performance.

The work done in [69] consists in optimizing the water flow inside a water-cooled frame of a newly designed electrically excited synchronous machine for automotive industry by considering the boundary conditions intrinsic to both the manufacturing process and the electric motor itself. With the support of the CFD technique it was possible to foresee the water flow behaviour inside the frame channel.

In [70], the finite element model of the three-dimensional steady state temperature field for a miniature water-cooled induction motor was established. It was found that the change of flowrates had more effects on the stator yoke and motor case, and little effect on the stator winding and the rotor. The numerical simulation results were consistent with the experimental results.

The extended survey done in [71] represents the evolution and modern approaches in the thermal analysis of electrical machines. The improvements and the new techniques proposed are analysed in depth and compared to highlight the qualities and defects of each.

From [40-71], it is shown that the motor performance is influenced significantly by the heat generation during operation. Thus, the estimation of heat generation for cooling of a motor is of importance as well as the design of an adequate cooling system. The motor performance is strongly reduced by the temperature rise of the motor as well. In designing a motor, establishing a model with appropriate cooling methods is required. However, it is noted that in the last decade, no literature has specifically focused on the effect of coolant velocity on the performance of generators, more specifically HSPM generators, which has been validated by experimental results. The literature reviewed mainly focused on the accuracy of various computational techniques and computational analysis pertaining to the heat generated, and the investigation of coolant flowrates, air used as the cooling medium, on motors and other different applications. In instances where literature stated that experimental analysis was performed, this was done for the optimisation of the cooling jacket configuration, thermal fluid analysis on the air cooling of a permanent magnet electric motor with a centrifugal impeller. Furthermore, where water was used as the cooling medium, the aim was to find the hotspots and investigate the cooling system of the four-quadrant transducer by considering the impact of different water-cooling channels. In another investigation the aim was to optimize the water flow inside a water-cooled frame. However, in this study computer aided engineering (CAE) was employed to estimate the HSPM generator temperature and the effect of different liquid (water) coolant velocities on the thermal performance of a 10 kW HSPM generator by coupling electromagnetic and thermal analysis. The physical three-dimensional design of the HSPM generator was established first with Solidworks, a 3D graphical software. Then the electromagnetic performance of the generator was analysed using ANSYS-Electromagnetic (Maxwell). Finally, the velocity and temperature field of the generator were simulated through ANSYS-Fluent with heat source generated from the loss of the generator. The highest value loss is used in the thermal analysis for cooling design to ensure that a suitable temperature is maintained at high speed operation of 30000 RPM. Furthermore, experimental tests were performed and presented.

[1-8, 10] shows that there are many factors that need to be considered for the design and development of a HSPM generator. While there is a wide selection of machine topologies, this is narrowed down due to the application of the machine, speed, and the desired output. Thus, the PM machine structure was identified as a suitable consideration for higher speed, low power applications. Furthermore, it was found that the determination of the rotor diameter, choice of pole number, choice of PM material are important factors in the design of the PM rotor to ensure rigidity. [9] shows that the stator core is susceptible to high losses and overheating due to the variation frequency of magnetic flux in the stator teeth and yoke at high rotor speeds. Thus, losses in high speed machines are expected to be much more than in conventional machines. However, the use of thin high quality cold-roll silicon steel laminations to make the stator core can reduce the loss coefficient. Furthermore, Litz wire for the stator windings should be used for efficiency. Presented in literature, is also a wide selection of bearings which differ in application, load, and speed requirements. While magnetic bearings are an attractive option based on speed capabilities and flexibility on controlling radial error during operation, they do however increase the capital

outlay of the project significantly. For this reason, rolling element type bearings offer a much cheaper option and high speeds with specially manufactured high precision bearings available in the market. However, lubrication starvation is a major issue for rolling element type bearing, particularly in high speed applications. Thus, the design of the housing should be tailored to effectively cool the bearings. Oil-air mist lubrication is also commonly used in high speed applications because it continuously feeds oil to the bearings, ensures oil quantity control, provides a cooling effect, prevents oil deterioration and dust from effecting the operability of the bearings. Furthermore, the heat generated by the rotor-stator interface at high speeds makes the thermal management of high speed machines difficult and complicated since the temperature rise could lead to demagnetization of the permanent magnets. The temperature rise is also responsible for shortening the lifetime of the insulation of the windings and so an effective cooling method needs to be considered. Literature shows that forced convection by means of air is popular and economically viable in smaller machines and less strenuous applications. However, in larger machines and in high speed applications other forms of cooling or a combination of cooling needs to be considered. Water/liquid cooling is an effective and efficient method of cooling for high speed machines and its implementation despite the extra costs is justified by the heat generated at high speeds and the enhanced heat transfer capabilities achieved with certain coolants. Literature shows that heat transfer analysis by means of forced convection, justifies the effectiveness of coolant velocity, since the convection heat transfer coefficient of a high speed generator was found to increase with increasing coolant flow rate. Further research can be done with the support of CFD to validate the mathematical model and the experimental results. While there is literature available on the effectiveness of water cooling in various applications despite the extra cost. Almost no literature focused on the effectiveness of coolant velocity on high speed machines. Thus, based on the literature reviewed, this thesis will focus on the effect of coolant velocity to enhance the efficiency of the HSPM generator, with the aid of CFD (ANSYS) and experimental results.

Chapter 3

DESIGN AND DEVELOPMENT OF THE HSPM GENERATOR

3.1 Introduction

For this project two generators were designed and developed namely, the interior permanent magnet (IPM) high speed generator and the surface mounted permanent magnet (SPM) high speed generator. While majority of the design between the two machines remained the same, they differed in their rotor and stator stamping design and magnet design. However, this thesis only considers the SPM high speed generator. The high speed permanent magnet (HSPM) generator was designed and developed following literature reviewed in Chapter 2. This Chapter considers the detailed design and development of the HSPM generator to meet the specifications of the capacity, main features and rigidity required. The following section gives a description on the design of the HSPM generator, including important features. Sect. 3.3 gives detail on the development of the HSPM generator.

3.2 Detailed design of HSPM Generator

The HSPM generator was designed using Solidworks and the detailed section view is shown in Figure 3.1, and the front and side (drive and non-drive end) views together with the overall dimensions of the HSPM generator are shown in Figure 3.2, while the detailed parts list corresponding to Figure 3.1 and Figure 3.2, is shown in Table D.

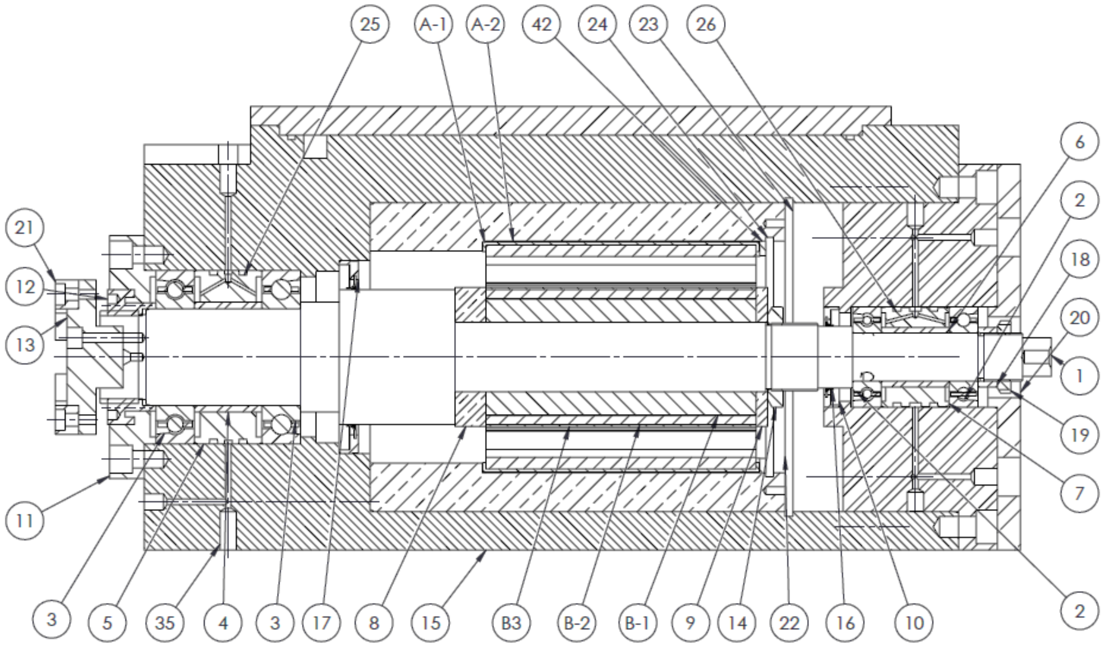

Figure 3.1: Detailed section view of the HSPM generator

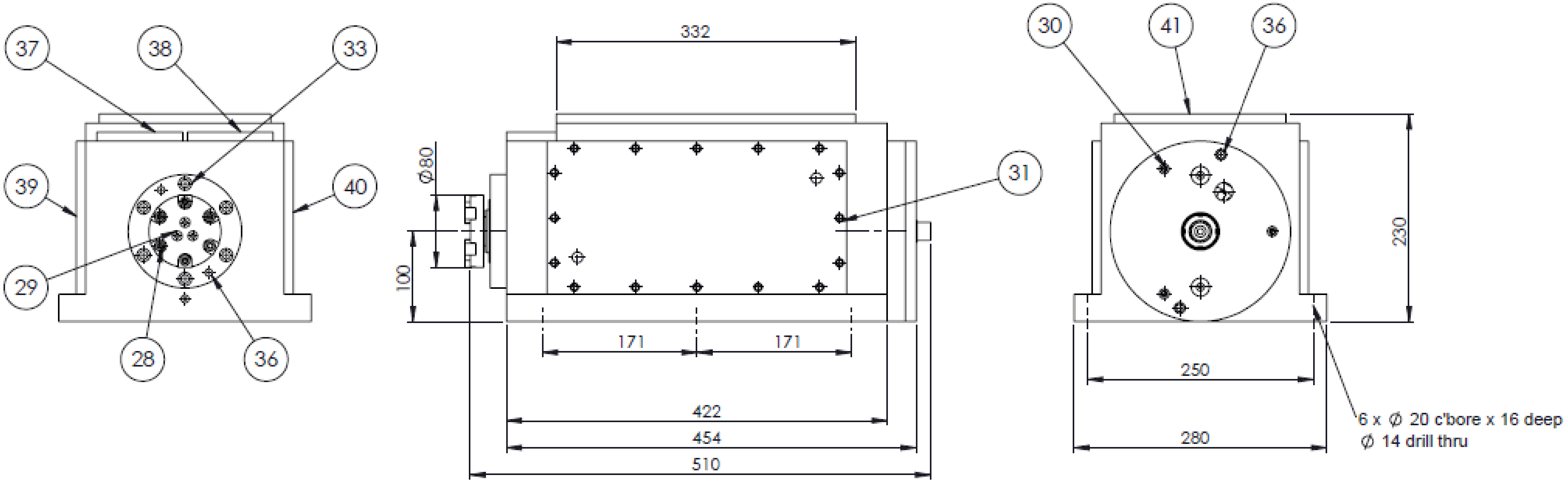

Figure 3.2: Front and side (drive and non-drive end) views and the overall dimensions of the HSPM generator

Table D: Parts list of the designed surface mounted HSPM generator

ITEM NO.	PART	DESCRIPTION	QTY.
1	Shaft	En 24	1
2	High Precision Angular Contact Ball Bearing	7205C SN24 TYNDBLP4	2
3	High Precision Angular Contact Ball Bearing	7210C SN24 TYNDBLP4	2
4	Inner spacer	S45C	1
5	Outer spacer	S45C	1
6	Inner spacer-rear BRG S45C	S45C	1
7	Outer spacer rear brg	S45C	1
8	Front Brass Spacer	Bronze	1
9	Rear Brass Spacer	Bronze	1
10	Rear Housing	En24	1
11	Front labrinth	En24	1
12	Front brg Nut	En24	1
13	Clutch Plate	En24	1
14	Lock Nut	KM7 (SKF)	1
15	Housing_rev1	FC20	1
16	Turcon varlip PDR seal (Trelleborg)	TJA3B0320-T251	1
17	Turcon varlip PDR seal (Trelleborg)	TJA3B0700-T251	1
18	Preload Rear Spacer	S45C	1
19	Lock Nut	KM 5 (SKF)	1
20	Rear cover	S45C	1
21	Clutch tooth	SKC43	6
22	Brass cooling cartridge	Brass	1
23	Inner circlip	Dia 160	1
24	Inner circlip	Dia 120	1
25	O-ring	OD: 90 C/S ϕ: 3	2
26	O-ring	OD: 52 C/S ϕ: 3	2
27	Hex socket Head cap screw	M6 X 10	16
28	Hex socket Head cap screw	M6 X 15	6
29	Hex socket Head cap screw	M6 X 20	3
30	Hex socket Head cap screw	M6 X 10	3
31	Hex socket Head cap screw	M8 X 12	32
32	Hex socket Head cap screw	M8 X 12	18
33	Hex socket Head cap screw	M10 X 16	6
34	Hex socket Head cap screw	M12 X 15	6

35	Hex socket Head cap screw	M16 X 30	6
36	Taper Pin	ϕ 8 X 24	4
37	Front bearing cooling cover left	S15C	1
38	Front bearing cooling cover right	S15C	1
39	Cooling system cover_side_left	S15C	1
40	Cooling system cover_side_right	S15C	1
41	Cooling system cover	S15C	1
A-1	Stator Spring Clamp (SMPMM)	SCM 420	4
A-2	Stator Stamping (SMPMM)	M19	400
B-1	Rotor Stamping (SMPMM)	M19	400
B-2	Rotor Magnet (SMPMM)	Neodymium (NdFeB30)	4
B-3	Rotor Sleeve (SMPMM)	Epoxy/PEEK	1
B-4	Rotor Clamp Rod	Nylon 66	4
B-5	Rotor Stamp Nut	Nylon 66	8
42	Spring Clamp Spacer	Bronze	1

The main rotor shaft, item no. 1, which has the magnets mounted on the rotor core laminations as shown previously in Figure 1.1 (i) is suspended with Silicon Nitride, Si_3N_4, ceramic high precision angular contact ball bearings located in the front and rear portion. The final diameters for the front and rear bearings were selected based on the diameter calculations performed in Chapter 5 to determine the minimum shaft diameter possible, the final PM rotor design, and the bearing catalogue supplied by bearing manufacturer, NSK. The final PM rotor diameter that was supplied by the electrical engineering department (EED) was ϕ 40 mm as shown in Figure 3.3. Instead of using a key to transmit speed form the shaft to the roto laminations, flat surfaces were used as shown section c-c of Figure 3.3 and an interference fit to avoid slip between the shaft and rotor laminations. The diameters for the front and rear bearings were ϕ 50 mm and ϕ 25 mm, respectively. These diameters also corresponded with the standard bore sizes of the desired bearings, which met the speed specification of the 30000 RPM. The designed clutch plate, item no. 13, is responsible for coupling the HSPM generator to the power source (aircraft motor) and is fitted on the drive end as shown in Figure 3.3, Detail B. A detailed Solidworks drawing of both the shaft and clutch can be seen in Appendix A, drawing no 1 and 13, respectively.

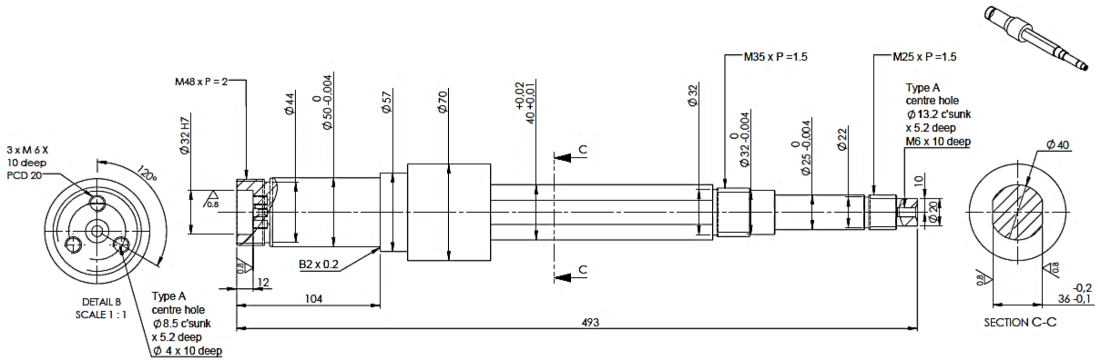

Figure 3.3: Detailed Solidworks drawing of the HSPM Generator Shaft

The complete rotor assembly of the HSPM generator is shown in Figure 3.4 and consists of: (B-1) rotor stamping, (B-2) rotor magnet, (B-3) rotor sleeve, (B-4) Rotor clamp rod, (B-5) rotor stamp nut, (8) front brass spacer, and (9) rear brass spacer. The rotor assembly is press fitted onto the shaft along with the selected bearings, shown in Sect. 4.3. The stator stamping design is shown in Figure 3.5, and the final dimensions were supplied by the EED which was used to design the main housing of the HSPM generator (Housing_rev1). The stator assembly is also featured stator spring clamps which are used to hold the stator stampings in place. A complete design of the stator assembly and stator stamping can be seen in Appendix A, drawing A and drawing A-2, respectively.

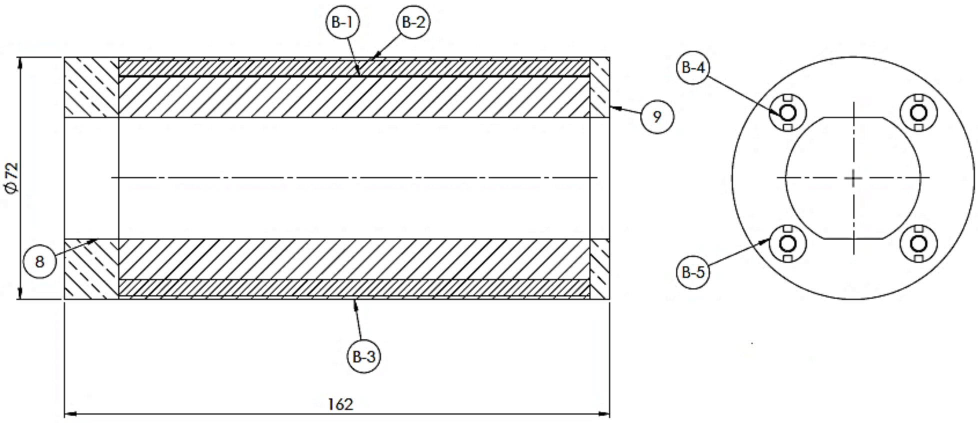

Figure 3.4: Rotor Assembly of the Surface mounted HSPM Generator

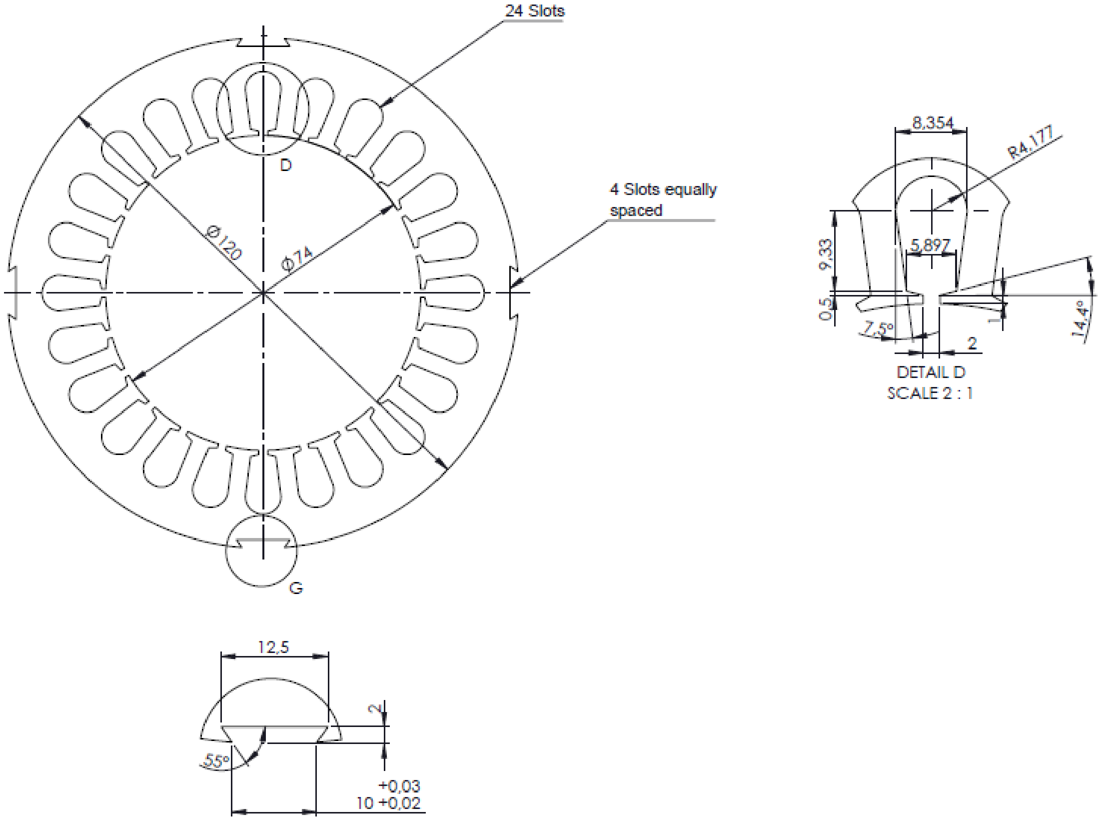

Figure 3.5: Solidworks Stator Stamping Design for HSPM Generator

The designed housing of the HSPM generator is shown in Figure 3.1. The housing is responsible for containing all the components of the HSPM generator and thus the geometric tolerances and surface finishes of each component that is in contact with the housing needed to be considered to achieve a good runout, precision, and to minimize vibrations in the generator. A detailed design of the housing and the housing geometric tolerances and surface finishes can be seen in Appendix A, drawing no. 15. The housing design is also featured with cooling jackets and bearing lubrication channels for the front bearing arrangement which can be seen in the detailed housing drawing in Appendix A, drawing 15. The design of the lubrication system for the front bearings consists of the inner spacer and outer spacer, item 4 and 5 in Table D, and the complete arrangement of the front bearing lubrication system design can be seen in Figure 3.6. The lubrication method employed was oil-air mist lubrication, which sprays oil by turning it into a mist using compressed air. Thus, the design for the position of the spray nozzle was critical for effective lubrication and cooling effect. Since the generator operates at high speeds, literature provided by NSK, showed that it was advantageous to position the nozzle bore so that the lubricant is directed into the high precision angular contact ball bearing interior. The angle of the nozzle selected was 30° as shown in Figure 3.7. Also shown in Figure 3.6, is the oil lubricant outlet for draining into the oil sump to prevent severe oil shear friction, which could damage the bearing. Detailed drawings of the inner and outer spacer can be seen Appendix A, Drawing 4 and 5, respectively.

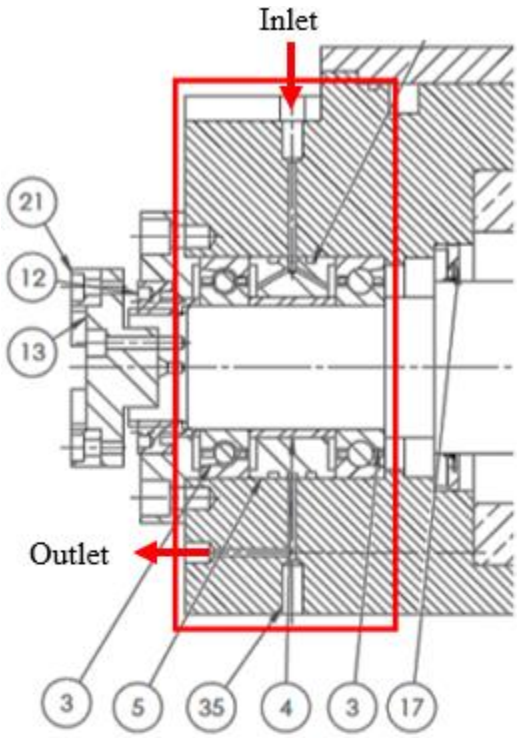

Figure 3.6: Complete Arrangement of the Front Bearing Lubrication System of the HSPM Generator

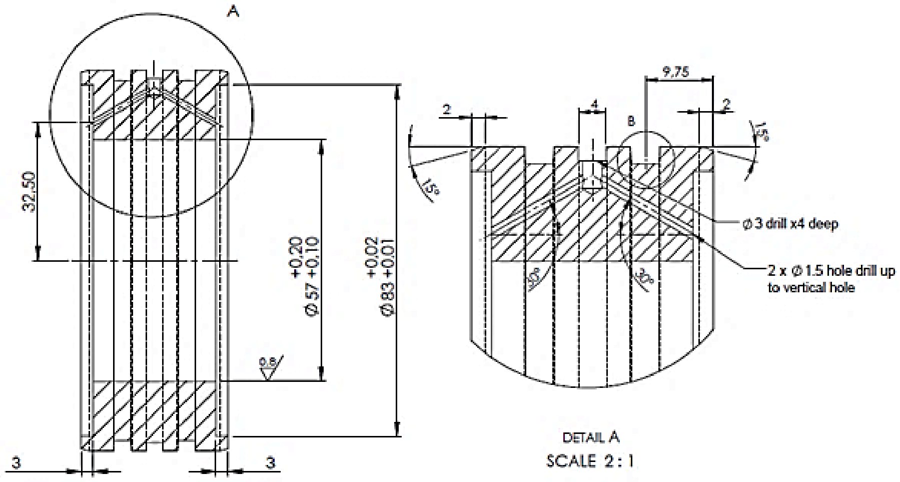

Figure 3.7: Outer Spacer for the Front Bearing Arrangement for the HSPM Generator

The design for the lubrication system and positioning, for preload purposes, for the rear bearings was unique in that the lubrication to the bearings could not be supplied from the top since the cooling jacket occupied most of the housing area on top of the housing. Therefore, a rear housing was designed, item 10, as shown in Figure 3.8. The inlet and outlet for the lubrication enters and exits from the rear end of the housing and the outlet empties into a sump. A through hole of ϕ 3 mm was drilled and was plugged at either end to complete the lubrication system. As previously mentioned, the rear housing is also responsible for the positioning of the rear bearings as well as the inner spacer-rear BRG S45C, and the outer spacer rear brg which is shown in Figure 3.9. Thus, the geometric tolerances and surface finish of the rear housing were carefully considered as shown in Figure 3.8. A rear spacer and locknut (supplied by SKF) arrangement was used to preload the rear bearings.

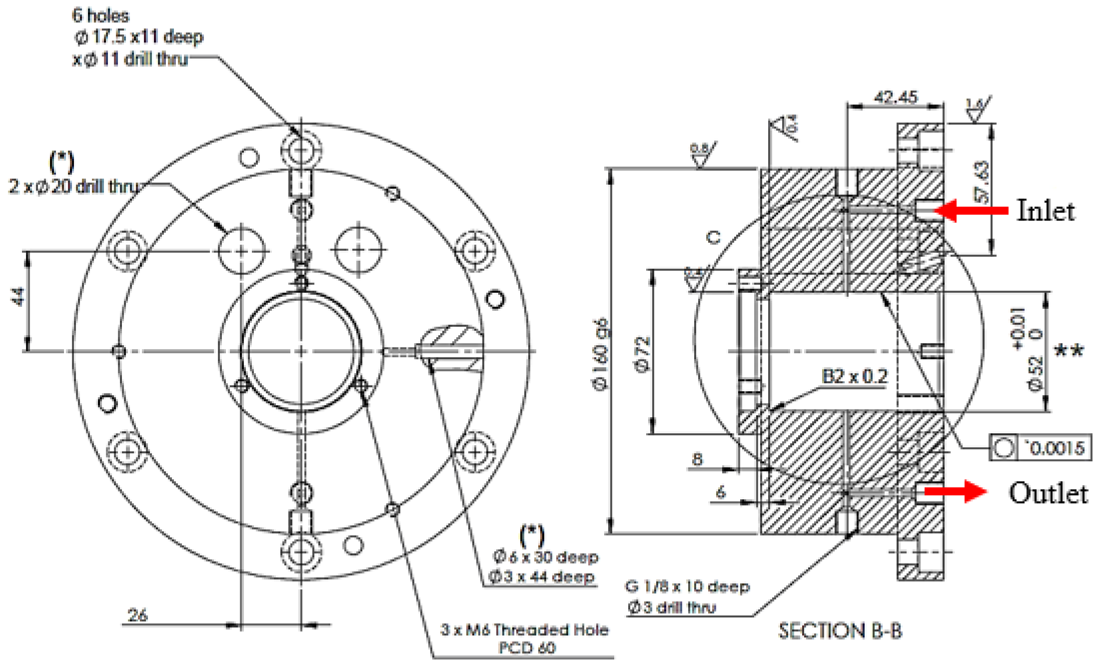

Figure 3.8: Design of the Rear Housing for the HSPM Generator

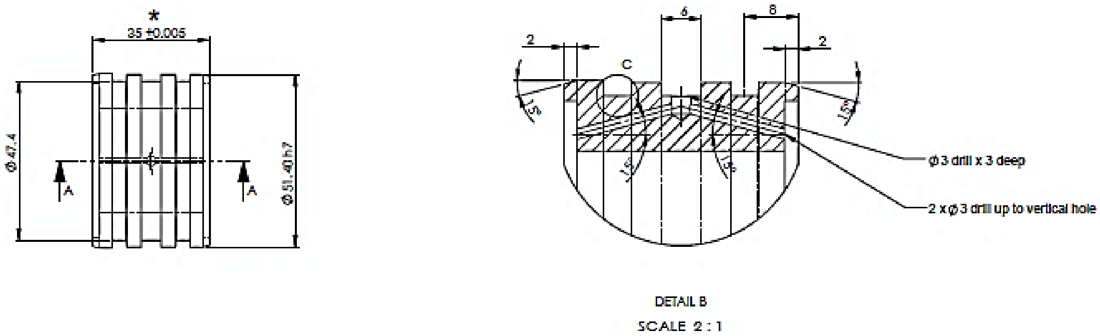

Figure 3.9: Outer Spacer for the Rear Bearing Arrangement for the HSPM Generator

The design of the Front Labrinth, item no. 11, is shown in Figure 3.10. The front Labrinth was used to preload the front bearings using a specially designed front bearing nut, item 12, shown in Figure 3.11. The NSK bearing catalogue was used to determine the preload required for the both the front and rear bearings. The complete detailed Solidworks drawing pack of the HSPM generator design can be found in Appendix A.

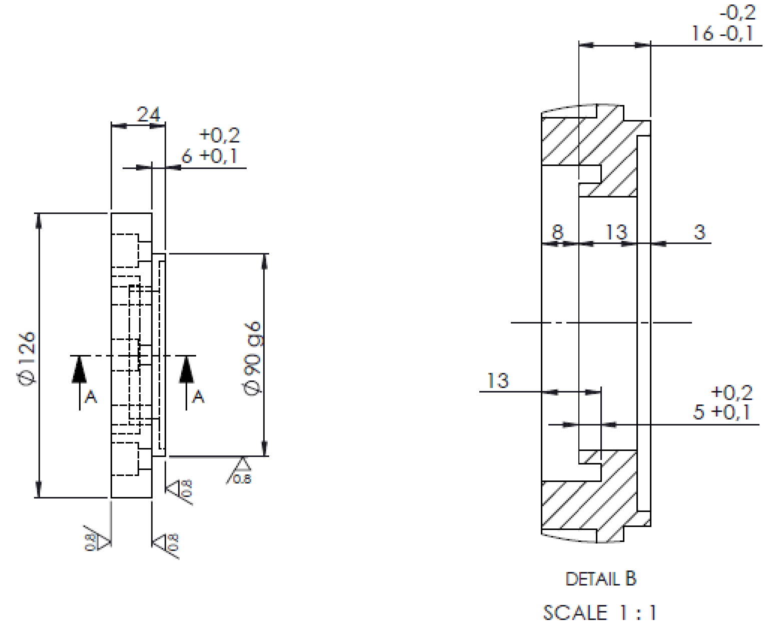

Figure 3.10: Front Labrinth for preload of the front bearings of the HSPM generator

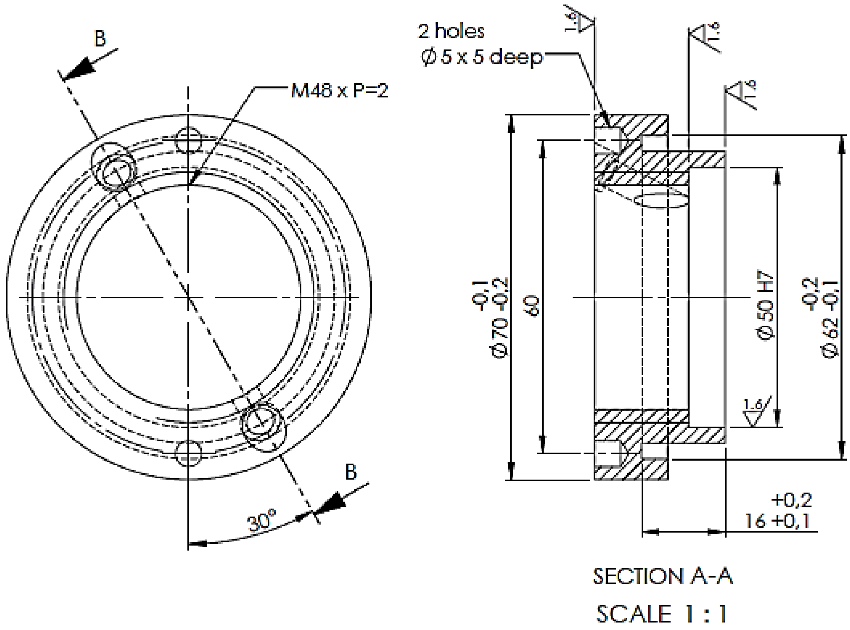

Figure 3.11: Front Bearing Nut of the HSPM Generator

3.3 Manufacturing of the HSPM Generator

This section presents the manufacturing of the HSPM generator. Here the manufacturing methods, material, sizing and technical aspects for the critical components are discussed which include: the rotor, magnets, retaining sleeve, stator, winding and housing.

3.3.1 Stator and Rotor Laminations

The rotor and stator of the HSPM generator are made from M19 29G Silicon steel. Electro chemical machining (ECM) method is used to cut the rotor and stator laminations to a thickness of 0.36 mm, before they are stacked and clamped to a total length of 140 mm. The EMC method is preferred over laser cutting due to its high precision and accuracy. The magnets used are graded N33 NdFeB permanents magnets (PMs) with parallel magnetization and are radially shaped. They can withstand temperatures of 180°C and are segmented to reduce eddy current losses. A thin layer of epoxy glue was used to fix the PMs onto the rotor core. The assembled rotor core and fixed PMs are shown in Figure 3.12.

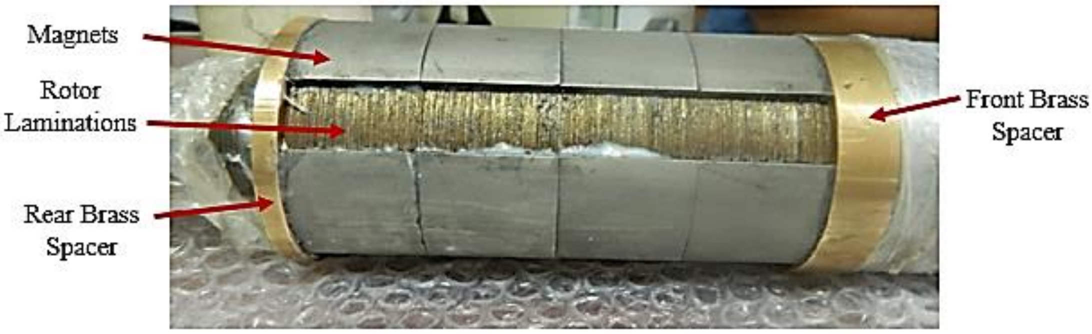

Figure 3.12: Assembled rotor core for SPM configuration of the HSPM generator

3.3.2 Stator Winding

Stranded litz wire was used for the winding of the HSPM generator, which employed an overlapping double layer winding configuration. The stranded litz wire was used to limit high frequency AC losses due to skin and proximity effects. To get the prevailing effects of the stranded litz wire, the coils were twisted and hand-wound whilst maintaining uniformity of the winding and minimization of the length by using an assembly tool to twist the coils which contribute to the final inductance of the HSPM generator. The twisted coils consist of 15 strands copper wire, insulation class H, of diameter 0.776mm. The stator has 24 slots and consists of 8 coils per phase and 2 turns per coil. It is to be noted that reason for the low number of turns is due to the high operating frequency of the HSPM generator. Thermocouples were placed on the three phase windings, in position 17, 19, and 21 of the stator core, and on the end windings. Figure 3.13 shows the STAR connected stator winding of the 3 phase HSPM generator, which consists of six terminal points (3 phase connections and a star/neutral point).

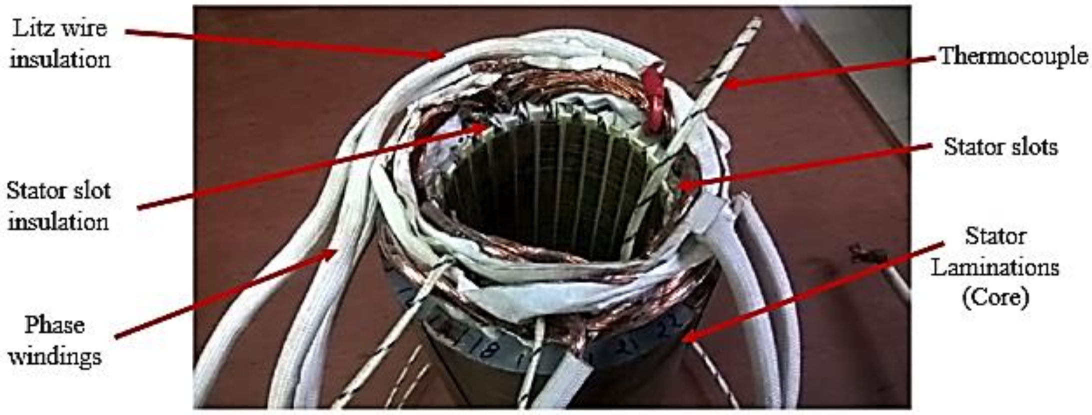

Figure 3.13: STAR connected stator winding for HSPM generator

3.3.3 Machine Shaft

High-grade stainless steel 415, a non-magnetic material, was used to manufacture the shaft of the HSPM generator to avoid interference with the active magnetic circuit between the rotor and the stator which is shown in Figure 3.14. High precision was maintained throughout the manufacturing process of the shaft and Quality Control (QC) reports were issued at each stage. To provide extra retaining strength, epoxy was added in between the magnets and the retaining sleeve. The temperature capabilities of the epoxy were considered due to the possible high operating temperatures of the HSPM generator. Figure 3.15 shows the assembled rotor with the retaining sleeve. The shaft of the HSPM generator was dynamically balanced to G2.5, an ISO balancing quality grade, where G is the balance quality grade and 2.5 is the vibration velocity in mm per second. The balancing of the shaft was performed in stages, which considered the shaft alone, until the completed rotor assembly. The dynamic balancing of the rotor shaft is shown in Figure 3.16.

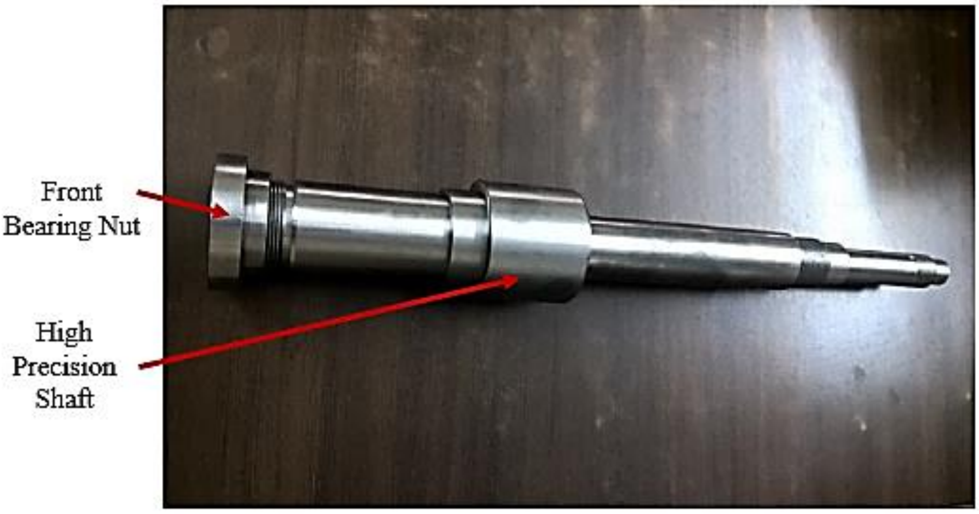

Figure 3.14: High precision shaft of the HSPM generator

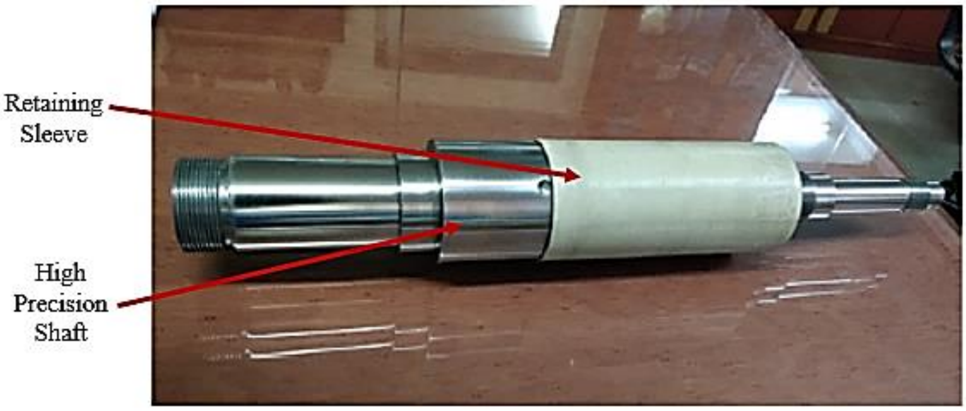

Figure 3.15: Rotor assembly with high precision shaft and retaining sleeve

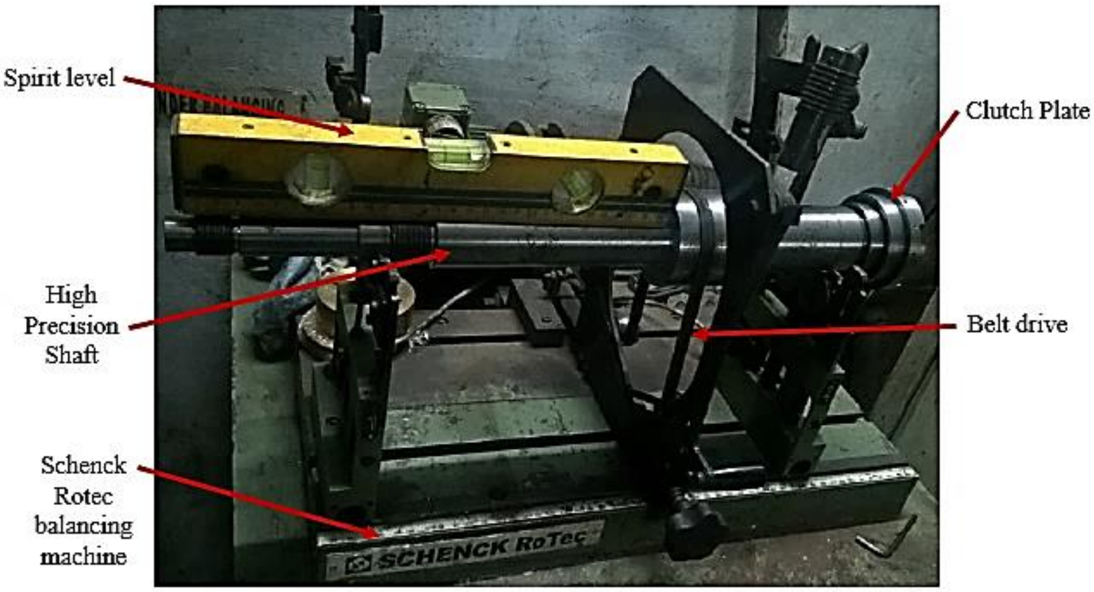

Figure 3.16: Dynamic balancing of the rotor shaft using the SCHENCK RoTec balancing machine at 1000 RPM

3.3.4 Housing Structure

The main frame (Housing) of the HSPM generator was cast at a foundry from FC20 Cast Iron. According to the design of the housing, certain surface finishes were required to accommodate the stator, bearings and seals. These surface finishes were achieved using boring and reaming processes, to smooth, enlarge and accurately size existing holes. The housing structure post casting is shown in Figure 3.17. The cooling jackets on the housing as shown in Figure 3.17 were manufactured using a Computer Numerical Control (CNC) machine. A hydraulic pressure test was conducted on the housing as shown in Figure 3.18 to check for cracks, which is a common occurrence due to a poor casting process. The test was conducted at a maximum of 15 bars for a period of 4-5 hours and the pressure was incrementally increased at 5 bars throughout the testing period. 3 to 4 bars is the standard specification for pressure tests conducted on low speed motors.

The housing of the HSPM generator developed a crack across the cooling jacket after an applied pressure of 8 Bars, which can be associated with a poor casting process and exacerbated by the CNC machining of the coolant jacket. To rectify the problem, a cold-welding compound, base material filling epoxy, was filled in the cracks and the excess was ground down to sit flush with the housing surface. It is recommended that a new housing be developed to conduct tests at rated conditions, due to safety concerns.

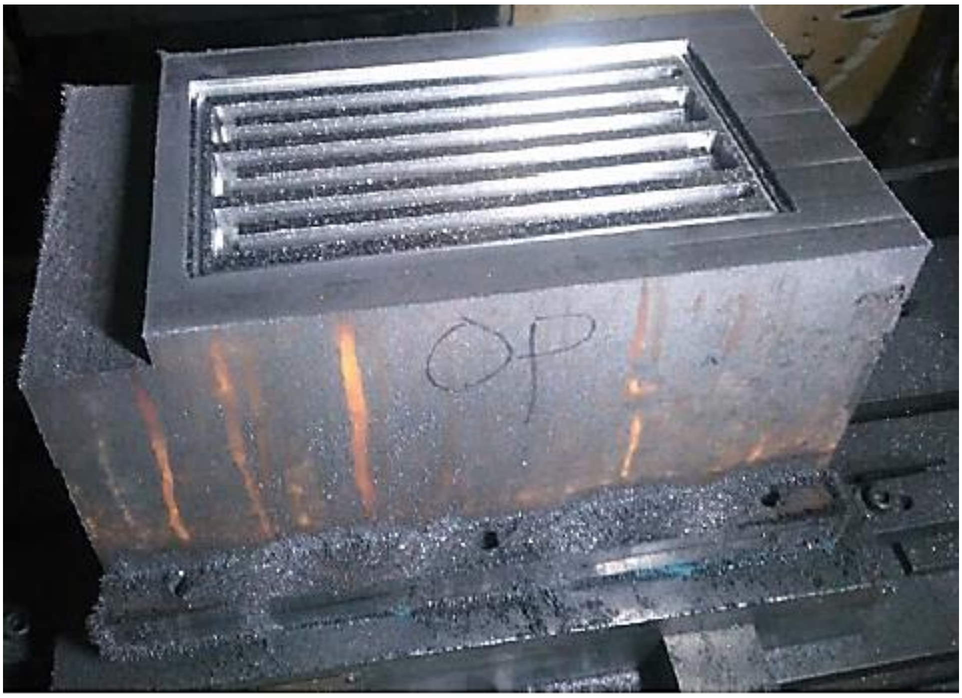

Figure 3.17: Main housing for the HSPM generator

Figure 3.18: Pressure test of the HSPM generator housing

Chapter 4

ANALYSIS OF DESIGNED HSPM GENERATOR

4.1 Introduction

The HSPM generator design is featured with several design challenges such as high DN values of approximately 1.5 X 10^6 and above (where D, N are the maximum diameter of the rotor shaft and speed (RPM) of the rotor respectively) and a high power to speed (kW/speed) rating. In general, an HSPM generator is to be featured with essential components which include but not limited to the following:

- Effective lubrication even at high rotor speeds of 30000 RPM
- Preload control to achieve a stiffness value of 75~150 N/µm
- Hybrid bearings
- Effective cooling
- Dynamic balancing of value G2.5 and below
- Precision manufacturing and assembly

As a result, the HSPM generator design would offer; low radial and axial error of values less than 0.005 mm, high rigidity, high temperature withstanding, stable dynamic characteristics, ease of maintenance and economy. The dimensions of the rotor and stator shown in Figure 1.2 and Figure 1.3, were critical to the overall design of the HSPM generator based on the required technical specifications presented in Table E. The schematic of the HSPM generator as well the overall dimensions are shown in Figure 4.1 and Figure 4.2 shows the complete layout of the HSPM generator system.

Table E: Technical Specifications of the HSPM Generator

Detail	**Value**
Physical size	510 mm x 280 mm x 230 mm
Maximum Speed	30000 RPM
Power to be generated	10 kW
Operating Speed	30000 RPM
Coolant	Water based coolant
Coolant pressure	15 ~ 20 bar
Coolant flow rate	0.3 to 3.5 m^3/hr.
Oil-air Mist ratio	1:10 ~ 1:13
Mist pressure	2 ~ 5 bar

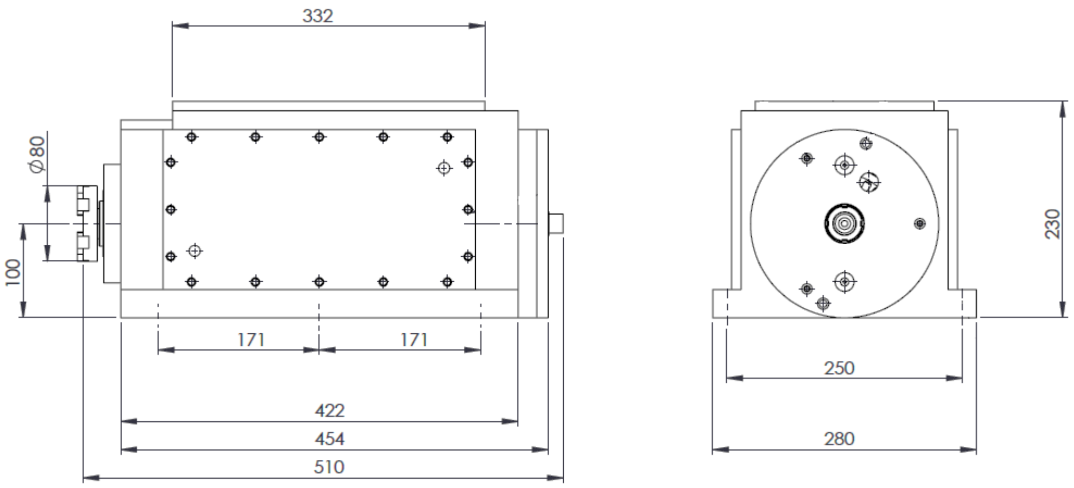

Figure 4.1: Schematic of the HSPM generator and the overall dimensions

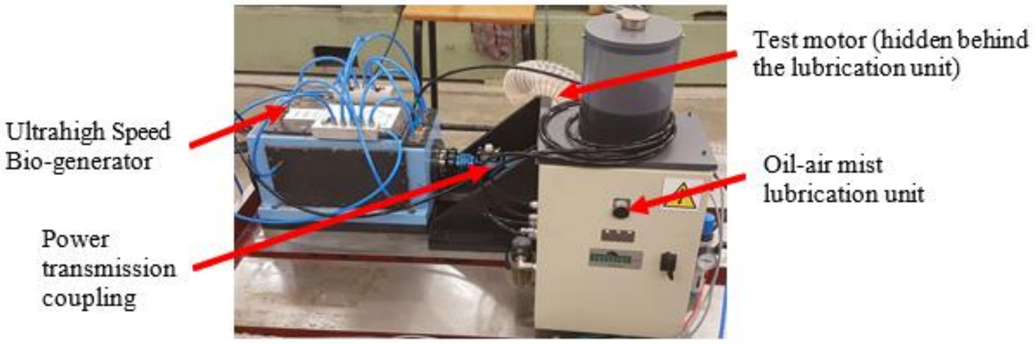

Figure 4.2:complete layout of the HSPM generator system

4.1.1 Summary of Material Properties

The material properties used in the design analysis and finite element analysis presented in this thesis are summarised in Table F, Table G, and Figure 4.3, respectively. Figure 4.3 shows the nature of the mild steel (magnetic material) based on the shape and size of the hysteresis loop (hysteresis loss). The shape and size of the hysteresis loop determines the suitable application of the mild steel in the HSPM generator. Thus, the smaller the hysteresis loop area, the less is the hysteresis loss while a large hysteresis loop area indicates that the material has high retentivity and coercivity. The sectioned technical drawing of the HSPM generator with a list of materials for each of the parts can be found in Appendix A.

Table F: Summary of material properties used for rotor shaft analysis

Material	**Density (kg/m^3)**	**Yield Strength (MPa)**	**Tensile Strength (MPa)**	**Young's Modulus (GPa)**	**Poisson's Ratio**
S45C	7700	343	569	200	0.28
Bronze	8820	125	255	93	0.334
En24	7840	680	900	207	0.3

FC20	7500	130	240	180	0.29
Brass	8470	135	345	105	0.346
Peek	1310	116	116	4.2	

Table G: Summary of material properties used in 2D and 3D finite element analysis

Material	**Mass Density (kg/m^3)**	**Electrical Conductivity (kS/m)**	**Thermal Conductivity (W/mK)**	**Relative Magnetic Permeability**	**Magnetic Coercivity (kA/m)**
Air	1.29	0	0.025	1	
Copper	8960	58,000	392.9	0.999991	-
Mild Steel	7849	10,000	61.0	Non-linear, refer Figure 4.3	-
NdFeB Magnets	7438	625		1.09978	965

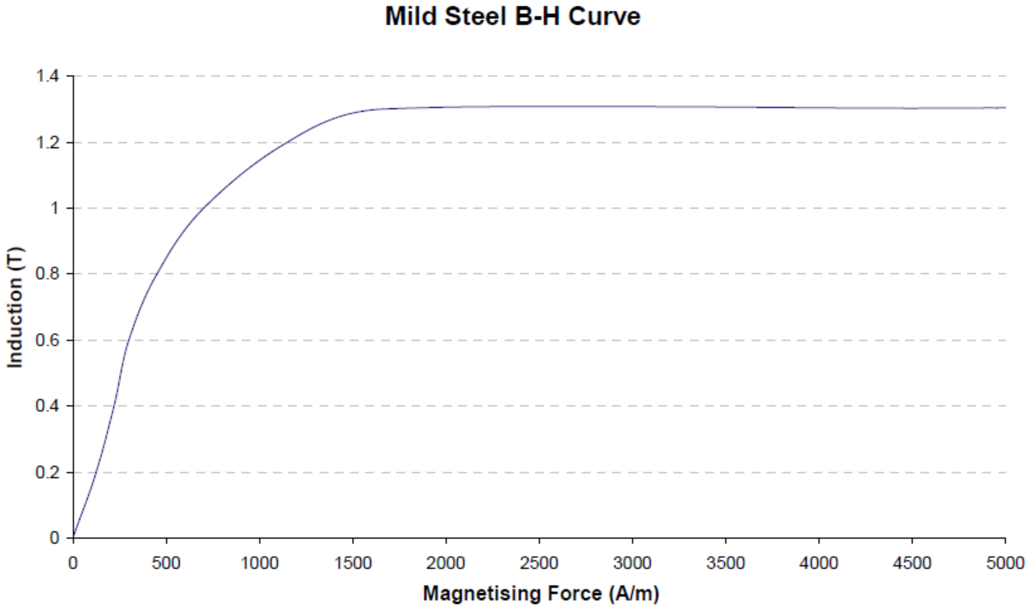

Figure 4.3: B-H curve used to simulate mild steel components of the HSPM generator.

The following section explains the rotor shaft design of the HSPM generator by defining rotor shaft twisting and bending moments to determine a suitable diameter for the shaft, 50 mm, as well as the transmission of torque from the shaft to the rotor. In Sect. 3.3 the bearing life is determined, and the bearing selections are made. Sect. 3.4 focuses on the deflection and rigidity of the shaft on the design, while Sect. 3.5 presents the housing and cooling system design of the HSPM generator. Furthermore, the Sect 3.6 looks at the type of configuration selected for the cooling jackets and Sect. 3.7 focuses on the design of the bearing lubrication system (oil air mist lubrication unit). Sect. 3.8 establishes the heat generated in the HSPM generator, while Sect. 3.9, Sect. 3.10 and 3.11 focuses on the electromagnetic losses, induced in the rotor and stator, idle power/mechanical loss, and core losses respectively. Sect. 3.12 then focuses on the thermal analysis and Sect. 3.13 and Sect. 3.14 focus on the coolant flow rate on heat transfer characteristics and quantitative analysis for heat generation and heat dissipation of oil-air mist lubrication, respectively. Finally, Sect. 3.15 presents the manufacturing of the HSPM generator.

4.2 HSPM Generator Rotor Shaft Design

The design of shafts is a basic design problem and utilizes the fundamentals of stress analysis, deflection and stiffness considerations, materials as well as fatigue strength. Depending on the design of the shaft the implementation of these fundamentals will vary. The shaft design for the HSPM generator is a rotating member, having mounted upon it a dog-clutch plate as shown in Figure 4.4 which transmits power from the gas turbine to the HSPM generator. This action could subject the shaft to bending, tension, compression, or torsional loads, acting singly or in combination with one another. When they are combined, it is important that both static and fatigue strength are considered for the design, since a single shaft may be subjected to static stresses, completely reversed stresses, and repeated stresses, all acting at the same time [11].

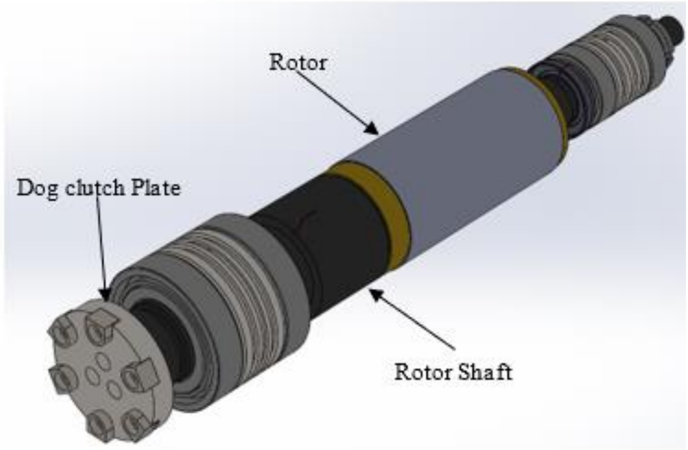

Figure 4.4: Rotor shaft and dog clutch plate used for power transmission

4.2.1 Rotor Shaft Twisting and Bending Moments

The HSPM generator is driven by a gas turbine which transmits power through the dog clutch plate. Because the rotor shaft is constantly rotating, and experiences load from the rotor and the drive of the gas turbine, the rotor shaft is subjected to both twisting (Torsion) and bending. Therefore, the shaft should be designed based on twisting moment and bending moment.

Twisting Moment:

The power transmitted by the rotor shaft of the HSPM generator is given by:

$$P_t = \frac{2\pi NT}{60} \tag{4.1}$$

$$\therefore T = \frac{P_t \times 60}{2\pi N}$$

The torque was computed by applying data from the technical specifications where, P_t is the power transmitted by the shaft (10 kW); N is the rotor shaft speed (30000 RPM). Substituting the above values, the T value for the HSPM generator is 3 Nm.

Bending Moment:

To determine the bending moments of the HSPM generator the reaction forces acting on the rotor shaft must be determined. The rotor shaft is assumed to be a simply supported (load on the bearings) beam with an overhanging load (load on the dog clutch plate). The depiction of the loads acting on the shaft is shown in Figure 4.5, where 'a', is the location of the load (F_n) on the dog clutch plate end of the HSPM generator. The points 'b' and 'c' are the locations of the reaction loads R_1 and R_2, acting on the bearings of the HSPM generator respectively.

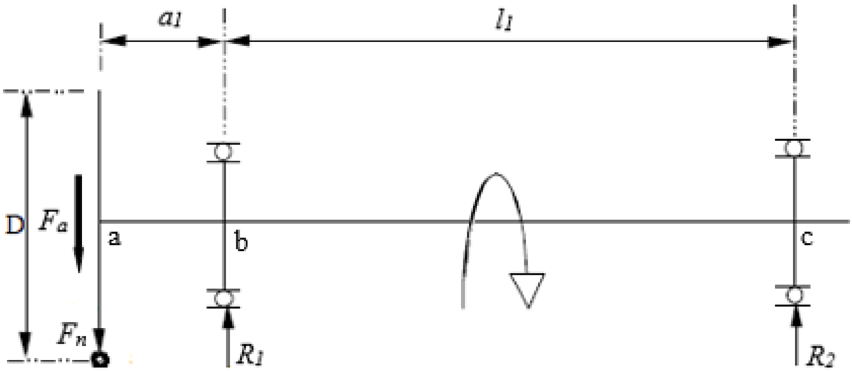

Figure 4.5: Reaction force diagram of a simply supported beam with an overhanging load (HSPM generator)

The load F_a is given by:

$$T = F_a \times \frac{D}{2} \qquad (4.2)$$

$$\therefore F_a = T \times \frac{2}{D}$$

$$F_a = 3 \times \frac{2}{0.08}$$

$$F_a = 75 \text{ N}$$

Where D is the diameter of the dog clutch plate (80mm). The F_a value is approximately 75 N as shown above. To determine the reaction forces R_1 and R_2, the load F_a is assumed to be 30% [72] of F_n, and thus F_n is 250 N.

$$F_a = 30\% \times F_n$$

$$\therefore\ F_n = \frac{F_a}{30\%}$$

$$F_n = \frac{75}{30\%}$$

$$F_n = 250\ \mathrm{N}$$

The reaction forces are determined by assuming that the sum of the loads acting on the rotor shaft are zero as well as the moments acting on the bearings located at ‘b’ and ‘c’. By using Figure 4.5 the reaction forces at each supported end can be expressed by:

$$R_1 = \frac{F_n(l_1 + a_1)}{l_1} \tag{4.3}$$

$$R_2 = \frac{F_n \times a_1}{l_1} \tag{4.4}$$

Where l_1 (270mm) and a_1 (56mm) are the distances between the load F_n and the reaction forces which can be seen in Figure 4.5. The values for R_1 and R_2 are determined to be 302 N and 52N, respectively. The maximum bending moment for the rotor shaft was determined by taking moments at each load point of the rotor shaft and was found to be a maximum at point ‘b’. The maximum bending moment can be determined by:

$$M_b = F_n \times a_1 \tag{4.5}$$

The M_b value of the HSPM generator rotor shaft is 14 Nm.

Equivalent twisting moment:

An equivalent twisting moment of the HSPM generator rotor shaft can be determined by combining T (twisting moment) and M_b (bending moment) of the rotor shaft as follows:

$$T_{eq} = \sqrt{M_b^2 + T^2} \tag{4.6}$$

T_{eq} was determined to be approximately 14 Nm. T_{eq} will be used in the next sub-section which shows how the critical diameter of the HSPM generator rotor shaft was determined.

4.2.2 HSPM Generator Rotor Shaft Diameter

Since the HSPM generator rotor shaft is subjected to combined loading, the stresses at the surface of the rotor shaft are subjected to the same combined loads and these stresses are:

$$\sigma_x = \frac{32\,M_b}{\pi d_s^3} \tag{4.7}$$

$$\tau_{xy} = \frac{16\,T}{\pi d_s^3} \tag{4.8}$$

Where σ_x is the bending stress; τ_{xy} is the torsional stress and d_s (mm) is the rotor shaft diameter. Using a Mohr's circle, it is found that maximum shear stress is

$$\tau_{max} = \sqrt{\left(\frac{\sigma_x}{2}\right)^2 + \tau_{xy}^2} \tag{4.9}$$

Thus, by eliminating σ_x and τ_{xy} from Equation (4.9) gives

$$\tau_{max} = \frac{16}{\pi d_s^3}\sqrt{{M_b}^2 + T^2} \tag{4.10}$$

Where the square root of M_b^2 and T^2 is the Equivalent twisting moment T_{eq}, shown in Sect. 2.2 The maximum-shear-stress theory of static failure states that $S_{sy} = S_y/2$ [73]. Where S_y is the yield strength of the En24 material, rotor shaft (680 MPa, Table F). A factor of safety, n (1.5) is also employed and thus Equation (4.9) can be re-written and the rotor shaft diameter can be determined by:

$$d_s = \left[\left(\frac{32n}{\pi S_y}\right) T_{eq}\right]^{\frac{1}{3}} \tag{4.11}$$

The minimum/critical diameter, d_c was determined and is approximately 6 mm. This is the minimum rotor shaft that can be used, and anything below this would result in elastic failure of the rotor shaft. However, for practical reasons the shaft is expected to be much larger due to the intermittent load from the turbine experienced by the shaft during operation. Thus, the duty cycle considered was 8, and the minimum diameter for the drive end of the shaft was determined to be 48 mm (8 X 6 mm). Other reasons were based on the bearing life and bearing selection, the desired deflection and rigidity of the rotor shaft, covered in Sect. 3.3 and Sect. 3.4, respectively, as well as the bearing requirements to achieve the desired speed (30000 RPM). Once suitable bearings had been identified the diameter used was 50 mm (standard manufacturing size, 48 mm was not available). Equation (4.11**)** can be used to determine whether the stress of the 50 mm rotor shaft is suitable to avoid elastic failure. A detailed technical drawing which was done on Solidworks can be found in Appendix A, drawing 1.

4.2.3 Transmission of Torque to Rotor Laminations

The transmission of torque to the laminated rotor of the HSPM generator was efficiently accomplished using friction. Assembling a cylindrical body over a shaft by an interference fit (press fit) is a very old art [74]. However, the advantages of this system over a keyed connection are: (1) the significant reduction of stress concentrations in the shafts and laminated rotor, (2) an increase in the torque that can be transmitted, and (3) the ease of the laminated rotor removal [75]. The laminated rotor with a bore slightly smaller than the shaft is expanded radially through heating. Once the laminated rotor is sufficiently expanded, the laminated rotor can slide on the shaft and can cool down and resume its original diameter. Since the shaft has a slightly bigger diameter than the laminated rotor, a high contact pressure is created at the interface. It is this pressure, the contact area and the coefficient of friction that generate the tangential force which permits the torque transmission which is given as:

$$T_f = Ap\mu\left(\frac{d_s}{2}\right) \qquad \textbf{(}4.12)$$

Where T_f is the torque transmission through interference fit (Nm), A is the contact area (m^2), p is the contact pressure (N/m^2) and d_s is the diameter of the shaft (m), and μ is the coefficient of friction. The contact area, A is defined as:

$$A = \pi d_s l_b \qquad \textbf{(}4.13)$$

$$A = \pi\ (0.04)(0.12)$$

$$A = 0.015\ \text{m}^2$$

While it is tempting to use the effective area, it should be noted that any reduction in Area (within reason) will result in an equivalent increase in the contact pressure and thus the total length of the laminated rotor bore, l_b (120 mm) of the HSPM generator should be used in the calculations. The theoretical area, as expressed in Equation (4.13), does not account for certain factors, such as imperfect contact between the bore and the shaft [75]. For the rotor shaft design of the HSPM generator, flat surfaces are made on the rotor shaft as seen in Figure 4.6 to increase the contact pressure despite using the theoretical contact area for calculations.

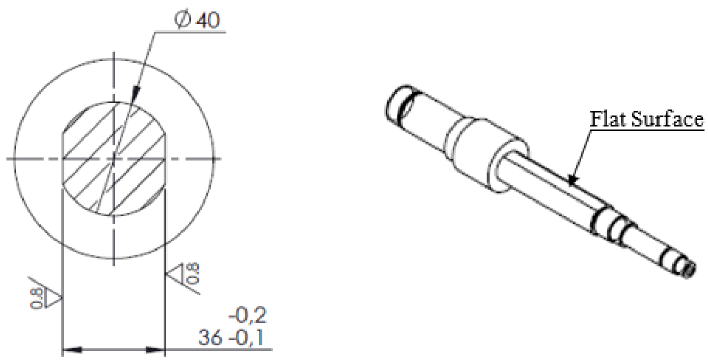

(a) (b)

Figure 4.6: Cross section of the HSPM generator rotor shaft with flat surfaces

The contact pressure, p (N/m^2) is determined by:

$$p = iE\,\frac{(D_r^2 - d_s^2)}{2D_r^2} \tag{4.14}$$

$$p = \left(\frac{0.02}{0.04}\right)(207 \times 10^9)\,\frac{(0.08^2 - 0.04^2)}{2(0.08)^2}$$

$$p = 38\,812\,500\,000 \text{ N/m}^2$$

$$p \approx 39 \text{ GPa}$$

$$\therefore T_f = Ap\mu\left(\frac{d_s}{2}\right)$$

$$T_f = (A)(p)(\mu)\left(\frac{d_s}{2}\right)$$

$$T_f = 2341114 \text{ Nm}$$

$$T_f = 2.34 \text{ MNm}$$

Where i is the interference rate (m/m), (diametral interference/shaft diameter). The diametral interference is 0.02mm which is the max interference between the rotor shaft diameter and the laminated rotor diameter. The technical drawings for these components and their dimensions can be found in Appendix A, drawing 1 and B-1. The rotor shaft diameter, d_s is 40mm shown in Figure 4.6. E is the modulus of elasticity, 207 GPa for En24 steel. D_r (80 mm) and d_s (40 mm) are shown in Figure 4.7, and are the laminated rotor diameter and rotor shaft diameter respectively. If the two mating surfaces (the rotor shaft and the laminated rotor) could indeed make perfect contact, there would be total molecular adhesion and the two parts would fuse together. Practical values for coefficients of friction have been determined [76]. The coefficient of friction for heat shrunk hubs (300°C), for normal cleanliness is; μ = .14 and heat shrunk hubs (300°C), for very clean parts is; μ = .20 [76]. The shaft of the HSPM generator is assumed to be a very clean part. Using the above formulae, the transmission of torque, T_f from the shaft to the laminated rotor was determined to be 2.34 MNm.

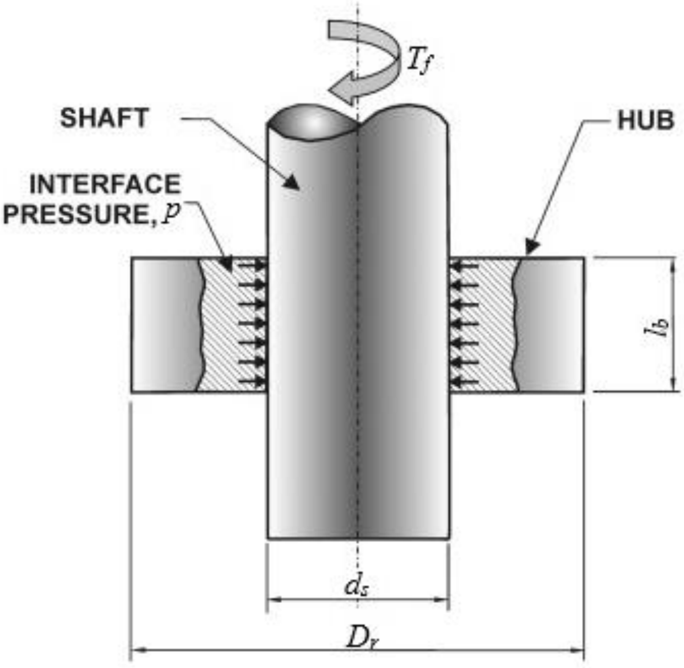

Figure 4.7: Basic Configuration of an Interference Fitted Hub

4.2.4 Preload and Rigidity

The bearings of the HSPM generator can be thought of as a spring, with regards to the rigidity of the spindle. Axial displacement, when an axial load is applied to the spindle, is determined by the axial rigidity of the fixed end bearings. Axial loads are usually sustained by angular contact ball bearings. The bigger the contact angle of the angular contact ball bearings, the higher the axial rigidity. Bearings of the same bore size, which have more rolling elements have higher rigidity, even though the diameter or rolling element is smaller. Preload is typically applied to bearings to increase rigidity of the machine. However, if the preload is excessively high, it may result in flaking and possible seizure. The rigidity could also be increased by using a combination of two or more angular contact ball bearings. Thus, the amount of preload should be carefully studied and selected to avoid excessive preload while taking into consideration the type of application and the operating conditions. The design of the HSPM generator uses a combination of two angular contact ball bearings located at the drive end and rear end as shown in Figure 3.1. The bearing manufacturer of the selected bearings have supplied a table of the suggested preload (N) and axial rigidity (N/µm) as shown in Figure 4.8. The values shown in the table are for the 72 series bearings, C angle, with a nominal contact angle of 15°. For the HSPM generator a light (L) preload is assumed due to the high speed application and excessive heat generated. The table is calculated for steel balls. However, when a ceramic ball is used, the Preload and axial rigidity value becomes 1.2 times the value of the steel ball. Furthermore, calculation of preload and axial rigidity for combination bearings can be obtained by multiplying factors in Table H, which is for the DBD and DBB configurations shown in Figure 4.9. To determine the radial rigidity, the axial rigidity should be multiplied by factors as shown in Table I. Thus, the Preload, axial rigidity and radial rigidity of the front and rear bearings were calculated as shown below:

Front bearing

Preload:

$$250 \times 1.2 = 300\ N$$

Axial rigidity:

$$69 \times 1.2 = 83\ N/\mu m$$

Radial rigidity:

$$69 \times 1.2 \times 6 = 497\ N/\mu m$$

Rear bearing

Preload:

$$78 \times 1.2 = 94\ N$$

Axial rigidity:

$$36 \times 1.2 = 43\ N/\mu m$$

Radial rigidity:

$$36 \times 1.2 \times 6 = 259\ N/\mu m$$

The Preload and axial rigidity for the front and rear bearings was determined to be 300 N, 83 N/µm and 94 N, 43 N/µm, respectively.

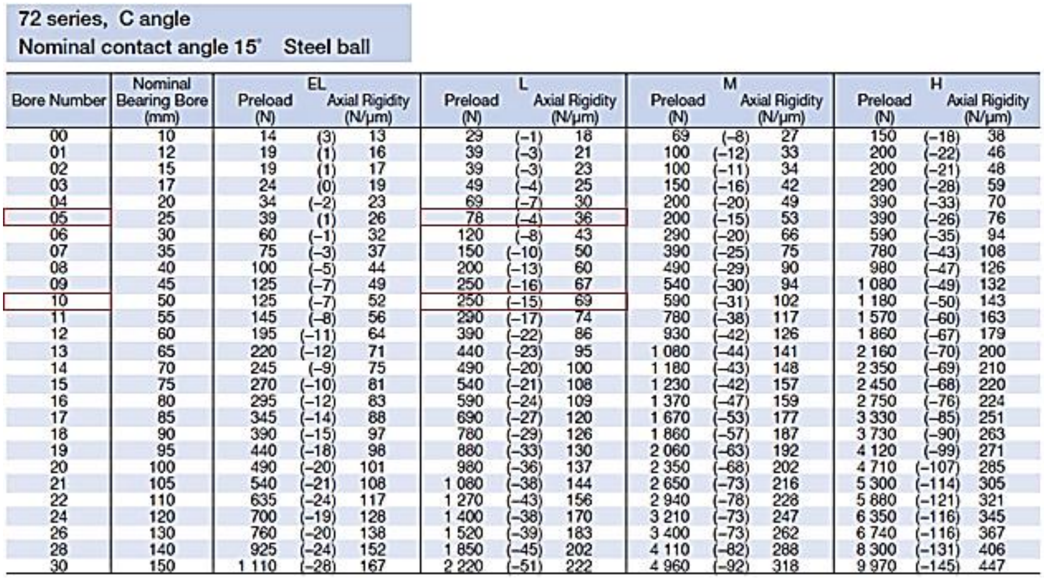

72 series, C angle
Nominal contact angle 15° Steel ball

Bore Number	Nominal Bearing Bore (mm)	EL		L		M		H	
		Preload (N)	Axial Rigidity (N/µm)	Preload (N)	Axial Rigidity (N/µm)	Preload (N)	Axial Rigidity (N/µm)	Preload (N)	Axial Rigidity (N/µm)
00	10	14	(3) 13	29	(–1) 18	69	(–8) 27	150	(–18) 38
01	12	19	(1) 16	39	(–3) 21	100	(–12) 33	200	(–22) 46
02	15	19	(1) 17	39	(–3) 23	100	(–11) 34	200	(–21) 48
03	17	24	(0) 19	49	(–4) 25	150	(–16) 42	290	(–28) 59
04	20	34	(–2) 23	69	(–7) 30	200	(–20) 49	390	(–33) 70
05	25	39	(1) 26	78	(–4) 36	200	(–15) 53	390	(–26) 76
06	30	60	(–1) 32	120	(–8) 43	290	(–20) 66	590	(–35) 94
07	35	75	(–3) 37	150	(–10) 50	390	(–25) 75	780	(–43) 108
08	40	100	(–5) 44	200	(–13) 60	490	(–29) 90	980	(–47) 126
09	45	125	(–7) 49	250	(–16) 67	540	(–30) 94	1 080	(–49) 132
10	50	125	(–7) 52	250	(–15) 69	590	(–31) 102	1 180	(–50) 143
11	55	145	(–8) 56	290	(–17) 74	780	(–38) 117	1 570	(–60) 163
12	60	195	(–11) 64	390	(–22) 86	930	(–42) 126	1 860	(–67) 179
13	65	220	(–12) 71	440	(–23) 95	1 080	(–44) 141	2 160	(–70) 200
14	70	245	(–9) 75	490	(–20) 100	1 180	(–43) 148	2 350	(–69) 210
15	75	270	(–10) 81	540	(–21) 108	1 230	(–42) 157	2 450	(–68) 220
16	80	295	(–12) 83	590	(–24) 109	1 370	(–47) 159	2 750	(–76) 224
17	85	345	(–14) 88	690	(–27) 120	1 670	(–53) 177	3 330	(–85) 251
18	90	390	(–15) 97	780	(–29) 126	1 860	(–57) 187	3 730	(–90) 263
19	95	440	(–18) 98	880	(–33) 130	2 060	(–63) 192	4 120	(–99) 271
20	100	490	(–20) 101	980	(–36) 137	2 350	(–68) 202	4 710	(–107) 285
21	105	540	(–21) 108	1 080	(–38) 144	2 650	(–73) 216	5 300	(–114) 305
22	110	635	(–24) 117	1 270	(–43) 156	2 940	(–78) 228	5 880	(–121) 321
24	120	700	(–19) 128	1 400	(–38) 170	3 210	(–73) 247	6 350	(–116) 345
26	130	760	(–20) 138	1 520	(–39) 183	3 400	(–73) 262	6 740	(–116) 367
28	140	925	(–24) 152	1 850	(–45) 202	4 110	(–82) 288	8 300	(–131) 406
30	150	1 110	(–28) 167	2 220	(–51) 222	4 960	(–92) 318	9 970	(–145) 447

Figure 4.8: Preload and axial Rigidity table for the selected front and rear bearings of the HSPM Generator

Table H: Factors for the calculation of preload and axial rigidity for combination bearings (DBD and DBB configuration)

	DBD	DBB
Preload factor	1.36	2
Axial rigidity	1.48	2
Radial rigidity	1.54	2

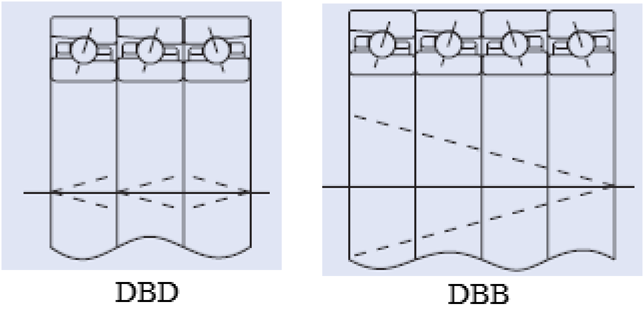

Figure 4.9: DBD and DBB combinations of angular contact ball bearings

Table I: Factors for the calculation of radial rigidity

	EL	L	M	H
15°	6.5	6.0	5.0	4.5
18°	4.5			
25°	2.0			
30°	1.4			
40°	0.7			

4.2.5 HSPM Generator Rotor Retaining Sleeve

The sizing (dimensions) and material selection for the retaining sleeve of the HSPM generator is a critical consideration to meet the specifications presented. To determine the dimensions and material of the retaining sleeve, it is imperative to consider the centrifugal force induced by the magnets because of the high speeds of the HSPM generator. These forces can cause damage if the magnets and rotor are not restrained, and thus the rotational components can be strengthened by using a retaining sleeve. In order to properly select the sleeve thickness, the overall tangential stress (hoop stress) acting on the sleeve has to be calculated and the sleeve thickness has to be selected to ensure that the total hoop stress does not exceed the yield stress limit of the sleeve material. The total hoop stress acting on the retaining sleeve is due to three effects, namely the centrifugal force exerted by the magnets during the rotation, the inertial stress due to the sleeve mass itself, and the stress due to the rotor-shaft cylinder. Manufacturing tolerances, thermal deformation and interference fit for rotor parts fastening should be considered before manufacturing for a proper dimensioning. However, in [77] this phenomenon was neglected during the initial sleeve sizing because the main aim was to have an approximate but simple estimation of the sleeve thickness to predict its impact on machine electromagnetic performances. The centrifugal stress on the sleeve due to the magnets can be calculated as:

$$\sigma_{t,PM} = \frac{\frac{F_{c,PM}}{2\pi C_{PM}} \times C_{SL}}{L_a l_{SL}} \tag{4.15}$$

Where $F_{c,PM}$ is the centrifugal force due to the magnets and is calculated as:

$$F_{c,PM} = N_{PM} \times m_{PM} C_{PM} \omega_{max}^2 \tag{4.16}$$

N_{PM} is the PM number, m_{PM} is the mass of each magnet, and ω^2_{max} is the maximum rotating speed of the machine, C_{PM} and C_{SL} are the radii of the mass centres of magnets and sleeve respectively, L_{PM} is the PM length in the axial direction, and l_{SL} is the sleeve thickness in the radial direction.

The inertial stress due to the sleeve mass itself has, again, a centrifugal nature, i.e., it is proportional to the square of the speed. With the assumption of the sleeve thickness being much smaller than the diameter, the inertial stress of the sleeve can be calculated as:

$$\sigma_{t,SL} = \gamma_{SL} \times C_{SL}^2 \times \omega_{max}^2 \tag{4.17}$$

With Υ_{SL} being the specific density of the sleeve material.

The total stress on the sleeve due to the rotor-shaft part is composed of three contributions: the centrifugal stress due to the iron mass ($\sigma_{\mathrm{c,RT}}$); the shear stress (τ_{RT}), which is proportional to the torque; and the tangential stress generated by the mechanical interference of the rotor-shaft coupling ($\sigma_{\mathrm{p,RT}}$). The latter depends on the minimum interference that is required to ensure the torque transmission from the rotor of the machine to the shaft, which has been calculated to avoid slipping between the parts during motion. The resulting hoop stresses have been then increased considering the mechanical tolerances and the effect of temperature. To evaluate the resulting hoop stress on the sleeve, the equivalent Von Mises stress has been calculated as:

$$\sigma_{VM} = \sqrt{\sigma_{c,RT}^2 + \sigma_{p,RT}^2 + 3\tau_{RT}^2} \tag{4.18}$$

The total Von Mises stress has been referred to as the sleeve radius and compared with the two aforementioned contributions from the PMs and from the sleeve itself. As stated above, the total hoop stress on the sleeve is the sum of the three contributions. Since the contribution from the rotor-shaft part is much lower than the other two, with the aim of finding a closed-form expression for the sleeve dimensioning, the detailed calculations of the rotor hoop stress have been neglected. An increased security factor

Ks was also employed, in order to reduce the risk of a bandage failure as presented in [78]. By imposing the total sleeve hoop stress (σ_{SL}) to be less than the yield stress of the material ($\sigma_{y,SL}$) divided by the security factor Ks

$$\sigma_{SL} = \frac{\frac{F_{c,PM}}{2\pi C_{PM}} \times C_{SL}}{L_{PM} l_{SL}} + \gamma_{SL} \times C_{SL}^2 \times \omega_{max}^2 < \frac{\sigma_{y,SL}}{K_s} \tag{4.19}$$

The sleeve thickness is given by:

$$l_{sl} = \frac{N_{PM} \times m_{PM} \times r_{SL} \times \omega_{max}^2}{\pi L_a \left[\gamma_{SL} \times r_{SL}^2 \times \omega_{SL}^2 - \frac{\sigma_{y,SL}}{K_s}\right]} \tag{4.20}$$

Where r_{SL} is the radius of the rotor comprising the sleeve, and L_a the rotor axial length.

For the HSPM generator a carbon-fibre composite i.e. PEEK (~ 200 MPa) was selected based on calculations that were done on Excel using Equation (4.19) and Equation (4.20). Table J, shows the correlation between the sleeve thickness and the achievable hoop stress. A safety factor of 1.1 was also considered for the design, while a sleeve thickness of 1.5 mm was selected for the HSPM generator, since the calculated hoop stress was lower than the yield stress of the PEEK material. The yield stress of the PEEK material divided by the safety factor was 182 MPa. The complete excel spreadsheet for the retaining sleeve calculation can be seen in Appendix B.

Table J: Retaining sleeve hoop stress calculation

Sleeve Thickness, l_{SL} (mm)	Hoop Stress (MPa)	Yield Stress with SF (MPa)
0.5	359	395
1.0	188	206
1.5	131	144
2.0	102	112
2.5	85	93
3.0	73	81
3.5	65	72

4.3 HSPM Generator Bearing Life and Bearing Selection

There is a vast selection of bearings that could be considered for the design of high speed machines depending on the design specifications and application. However, these bearings each have their own advantages and limitations. Thus, for the design of the HSPM generator this was narrowed down to three types of bearings; *Magnetic Bearings, Rolling Element Bearings* and *Foil/Journal Bearings.* Magnetic bearings offer flexibility on controlling the radial error but would increase the capital of the project [79, 80]. Foil bearings have reduced weight due to the elimination of the oil system, stable operation at higher speeds and temperatures, low power loss at high speeds and long life with little maintenance, however, they have low load capacities at low speed and modest stiffness and damping values [81]. Bearings are manufactured to take pure radial loads, pure thrust loads, or a combination of these two. Rolling bearings are widely used in many applications because of their wide range of load capacity and low capital outlay on projects. Some of the various types of standardized bearings are shown in Figure 4.10. However, wear and bearing life is a major concern for rolling bearings especially at high speeds and thorough bearing life calculation needs to be considered. The angular contact bearing, shown in Figure 4.10 (c), was selected because of its potential to provide greater thrust capacity coupled with the desired speed.

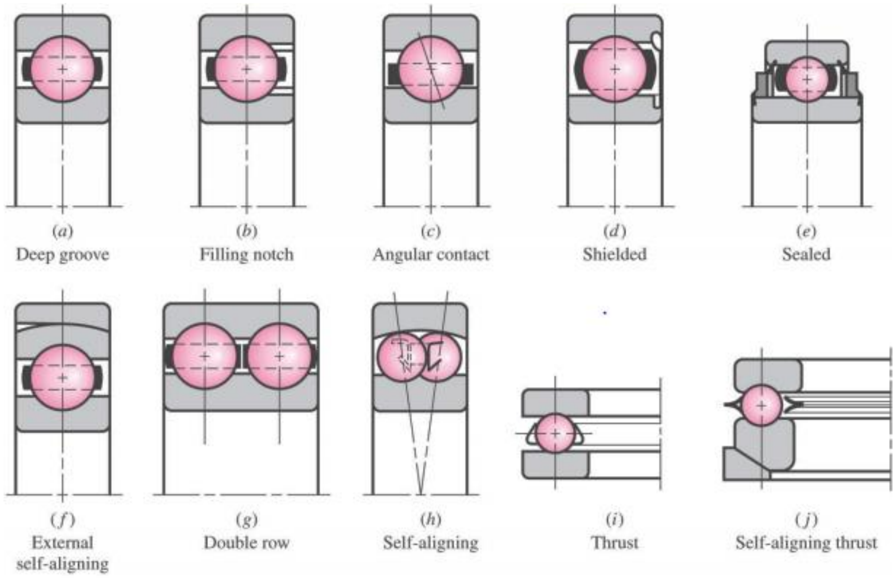

Figure 4.10: Various types of ball bearings

4.3.1 Bearing Life

The normal fatigue life of angular contact ball bearings that experience point contact is governed by the following:

$$L = \left(\frac{C}{P_{EQ}}\right)^3 \quad (4.21)$$

Where, L is the life in 10^6 revolutions; C is the dynamic load rating of the bearing and P_{EQ} is the equivalent dynamic load which is calculated by:

$$P_{EQ} = XF_r + YF_a \quad (4.22)$$

$$P_{EQ} = (0.72)(302 \times 1.5) + (2.11)(300 \times 1.5)$$

$$P_{EQ} = 326 + 950$$

$$P_{EQ} = 1276 \text{ N}$$

$$L = \left(\frac{43000}{1276}\right)^3$$

$$L = 38270 \text{ hrs}$$

Where X is 0.72 and Y is 2.11 for the front bearing of the HSPM generator, Figure 4.11 shows the value of factors X and Y, where the normal contact angle was given as 15° in the bearing catalogue, see Appendix C. The maximum value for P_{EQ} was 1276 N, and C was given as 43000 N (from the bearing catalogue, see Appendix C) for the front bearing, located at ‘b’ in Figure 4.5. A safety factor of 1.5 was assumed and the life of the bearing was estimated to be 38270 hrs, approximately 4 years. The schematic of the front and rear angular contact bearings of the HSPM generator is shown Figure 4.12 and the specifications of the selected bearings have been highlighted in red in Figure 4.13. The numbering system of the ‘high precision angular contact ball bearings’ for the front and rear bearings are:

- 7210CSN24TYN (front bearing)
- 7205CSN24TYN (rear bearing)

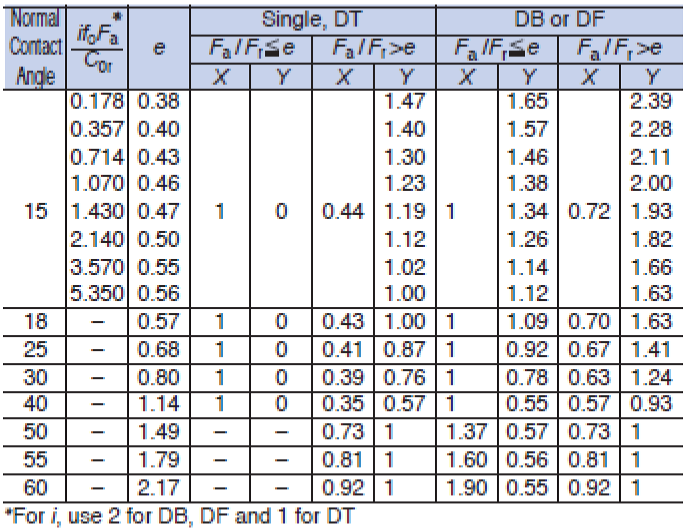

Normal Contact Angle	$\frac{if_0F_a}{C_{0r}}$*	e	Single, DT				DB or DF			
			$F_a/F_r \leq e$		$F_a/F_r > e$		$F_a/F_r \leq e$		$F_a/F_r > e$	
			X	Y	X	Y	X	Y	X	Y
15	0.178	0.38	1	0	0.44	1.47	1	1.65	0.72	2.39
	0.357	0.40				1.40		1.57		2.28
	0.714	0.43				1.30		1.46		2.11
	1.070	0.46				1.23		1.38		2.00
	1.430	0.47				1.19		1.34		1.93
	2.140	0.50				1.12		1.26		1.82
	3.570	0.55				1.02		1.14		1.66
	5.350	0.56				1.00		1.12		1.63
18	–	0.57	1	0	0.43	1.00	1	1.09	0.70	1.63
25	–	0.68	1	0	0.41	0.87	1	0.92	0.67	1.41
30	–	0.80	1	0	0.39	0.76	1	0.78	0.63	1.24
40	–	1.14	1	0	0.35	0.57	1	0.55	0.57	0.93
50	–	1.49	–	–	0.73	1	1.37	0.57	0.73	1
55	–	1.79	–	–	0.81	1	1.60	0.56	0.81	1
60	–	2.17	–	–	0.92	1	1.90	0.55	0.92	1

*For *i*, use 2 for DB, DF and 1 for DT

Figure 4.11: Value of Factors X and Y

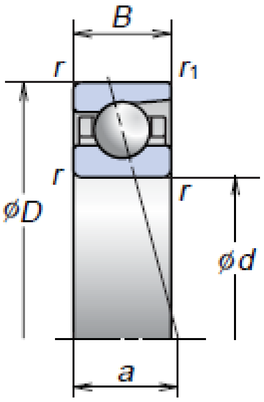

Figure 4.12: Schematic of Angular Contact Bearing and Associated Dimensions

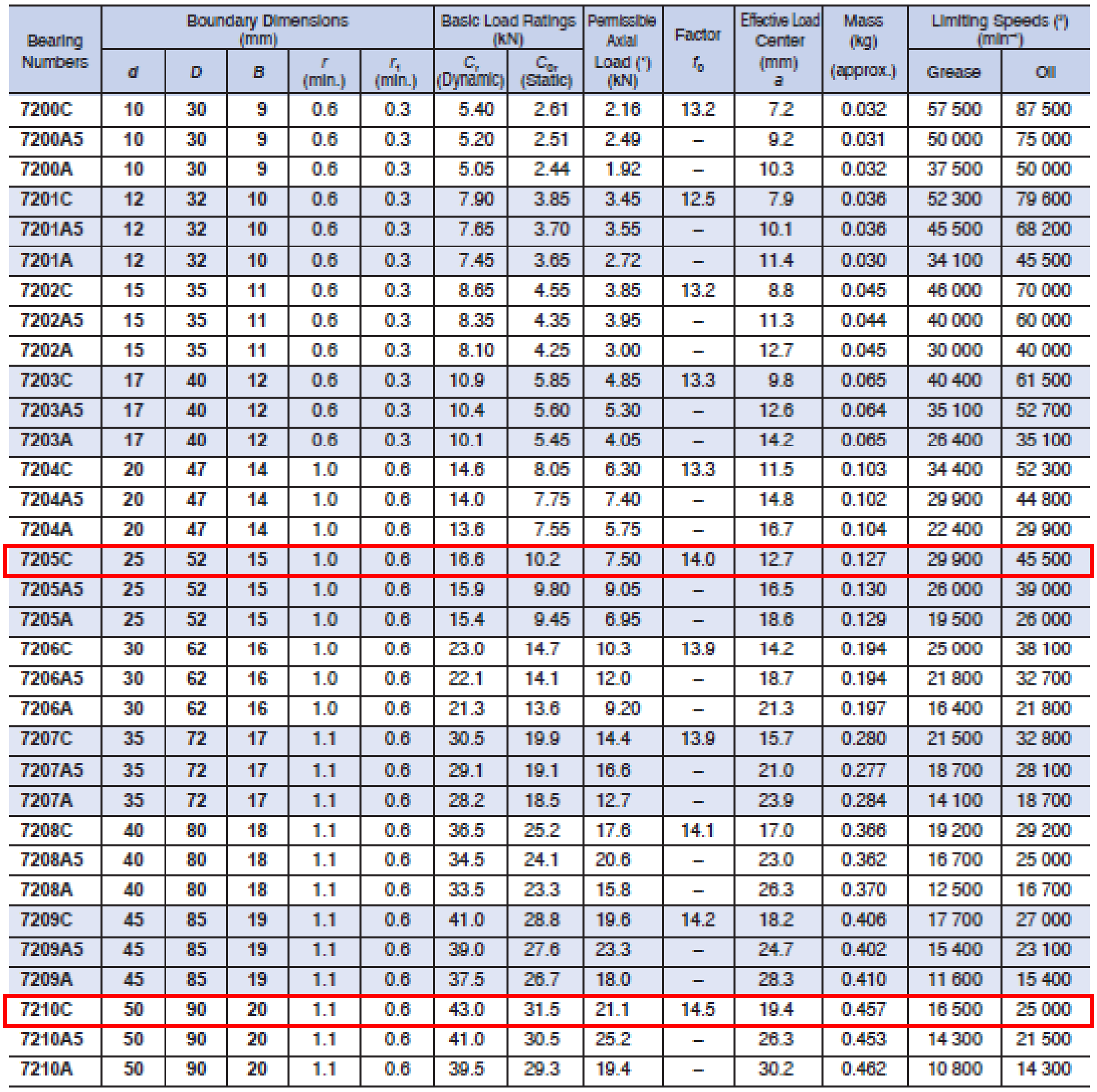

Bearing Numbers	Boundary Dimensions (mm)					Basic Load Ratings (kN)		Permissible Axial Load (*) (kN)	Factor f_0	Effective Load Center (mm) a	Mass (kg) (approx.)	Limiting Speeds (*) (min^{-1})	
	d	D	B	r (min.)	r_1 (min.)	C_r (Dynamic)	C_{0r} (Static)					Grease	Oil
7200C	10	30	9	0.6	0.3	5.40	2.61	2.16	13.2	7.2	0.032	57 500	87 500
7200A5	10	30	9	0.6	0.3	5.20	2.51	2.49	–	9.2	0.031	50 000	75 000
7200A	10	30	9	0.6	0.3	5.05	2.44	1.92	–	10.3	0.032	37 500	50 000
7201C	12	32	10	0.6	0.3	7.90	3.85	3.45	12.5	7.9	0.036	52 300	79 600
7201A5	12	32	10	0.6	0.3	7.65	3.70	3.55	–	10.1	0.036	45 500	68 200
7201A	12	32	10	0.6	0.3	7.45	3.65	2.72	–	11.4	0.030	34 100	45 500
7202C	15	35	11	0.6	0.3	8.65	4.55	3.85	13.2	8.8	0.045	46 000	70 000
7202A5	15	35	11	0.6	0.3	8.35	4.35	3.95	–	11.3	0.044	40 000	60 000
7202A	15	35	11	0.6	0.3	8.10	4.25	3.00	–	12.7	0.045	30 000	40 000
7203C	17	40	12	0.6	0.3	10.9	5.85	4.85	13.3	9.8	0.065	40 400	61 500
7203A5	17	40	12	0.6	0.3	10.4	5.60	5.30	–	12.6	0.064	35 100	52 700
7203A	17	40	12	0.6	0.3	10.1	5.45	4.05	–	14.2	0.065	26 400	35 100
7204C	20	47	14	1.0	0.6	14.6	8.05	6.30	13.3	11.5	0.103	34 400	52 300
7204A5	20	47	14	1.0	0.6	14.0	7.75	7.40	–	14.8	0.102	29 900	44 800
7204A	20	47	14	1.0	0.6	13.6	7.55	5.75	–	16.7	0.104	22 400	29 900
7205C	25	52	15	1.0	0.6	16.6	10.2	7.50	14.0	12.7	0.127	29 900	45 500
7205A5	25	52	15	1.0	0.6	15.9	9.80	9.05	–	16.5	0.130	26 000	39 000
7205A	25	52	15	1.0	0.6	15.4	9.45	6.95	–	18.6	0.129	19 500	26 000
7206C	30	62	16	1.0	0.6	23.0	14.7	10.3	13.9	14.2	0.194	25 000	38 100
7206A5	30	62	16	1.0	0.6	22.1	14.1	12.0	–	18.7	0.194	21 800	32 700
7206A	30	62	16	1.0	0.6	21.3	13.6	9.20	–	21.3	0.197	16 400	21 800
7207C	35	72	17	1.1	0.6	30.5	19.9	14.4	13.9	15.7	0.280	21 500	32 800
7207A5	35	72	17	1.1	0.6	29.1	19.1	16.6	–	21.0	0.277	18 700	28 100
7207A	35	72	17	1.1	0.6	28.2	18.5	12.7	–	23.9	0.284	14 100	18 700
7208C	40	80	18	1.1	0.6	36.5	25.2	17.6	14.1	17.0	0.366	19 200	29 200
7208A5	40	80	18	1.1	0.6	34.5	24.1	20.6	–	23.0	0.362	16 700	25 000
7208A	40	80	18	1.1	0.6	33.5	23.3	15.8	–	26.3	0.370	12 500	16 700
7209C	45	85	19	1.1	0.6	41.0	28.8	19.6	14.2	18.2	0.406	17 700	27 000
7209A5	45	85	19	1.1	0.6	39.0	27.6	23.3	–	24.7	0.402	15 400	23 100
7209A	45	85	19	1.1	0.6	37.5	26.7	18.0	–	28.3	0.410	11 600	15 400
7210C	50	90	20	1.1	0.6	43.0	31.5	21.1	14.5	19.4	0.457	16 500	25 000
7210A5	50	90	20	1.1	0.6	41.0	30.5	25.2	–	26.3	0.453	14 300	21 500
7210A	50	90	20	1.1	0.6	39.5	29.3	19.4	–	30.2	0.462	10 800	14 300

Figure 4.13: Bearing Specifications of the Selected Bearings

4.3.2 Angular Contact Ball Bearing Combinations

The rotor shaft design of the HSPM generator uses the 2 rows (DB) configuration also referred to as the back to back arrangement shown in Figure 4.14. For the back to back arrangement, axial loads in both directions and radial loads can be sustained. Since the distance between the effective load centres of the rotor shaft of the HSPM generator is large, the DB type arrangement is suitable since the rotor shaft approximates a supported beam with an overhanging load which creates a moment. Care is taken to ensure high accuracy of the housing and precision alignment of the spindle is achieved to avoid large internal loads on the bearings which could result in premature failure due to greater moment stiffness.

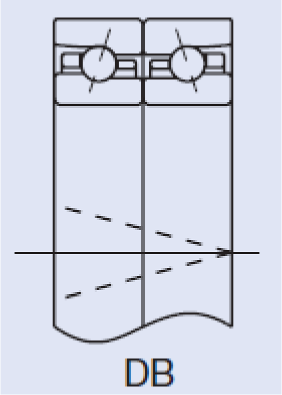

Figure 4.14:Selected Combination of Angular Contact Ball Bearing

4.4 Rotor Deflection and Rigidity

The bending of shafts is an important consideration especially in high speed applications such as the HSPM generator. By applying deflections by use of singularity functions. The maximum spindle deflection in the simply supported beam with an overhang load, shown in Figure 4.5, the deflection occurs in the overhang zone and the deflection, y is given as:

$$y = \frac{F(x - l_1)}{6E_2 I}\left[(x - l_1)^2 - a_1(3x - l_1)\right] \qquad (4.23)$$

The maximum deflection occurs when, '$x = l_1 - a_1$' which is 326 mm. Where, E_2 is the modulus of elasticity (2.08 x 10^5 N/mm^2), and I is the moment of inertia for the equivalent diameter (306796 mm^4). The deflection of the simply supported rotor shaft with an overhang load from the gas turbine, is shown in Figure 4.15 with increasing radial load, *Fn.*

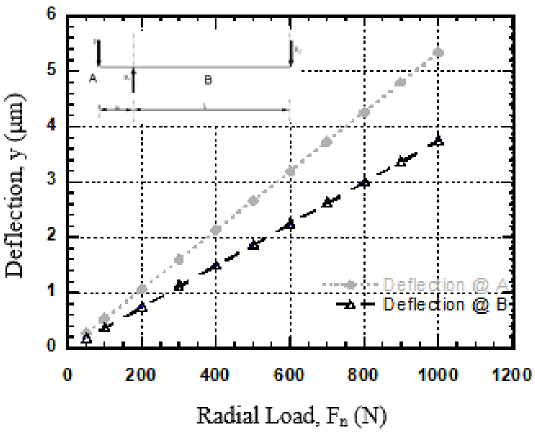

Figure 4.15: Deflection of the rotor shaft of the HSPM generator

4.5 Housing and Cooling System Design

The housing of any high speed machine plays an integral role in ensuring that the machine operates at an optimal and safe standard. Thus, it is critical to select suitable materials and ensure that the correct dimensions and tolerances are specified for the smooth operation of the machine. The material used for the housing of the HSPM generator is FC20, which is a Japanese standard cast iron. A detailed drawing of the Housing can be seen in Appendix A, drawing 15. Figure 4.16 shows the 3D Solidworks model of the HSPM generator, which includes the housing and the positioning of the cooling jackets on the housing. Studies on thermal effects of electric motors have reported that the heat generation developed in the motor decreases the efficiency of the motor and even threatens its safe operation. By implementing principles of heat transfer, the heat developed can be moved from a high heat sink to a lower one, resulting in heat transfer.

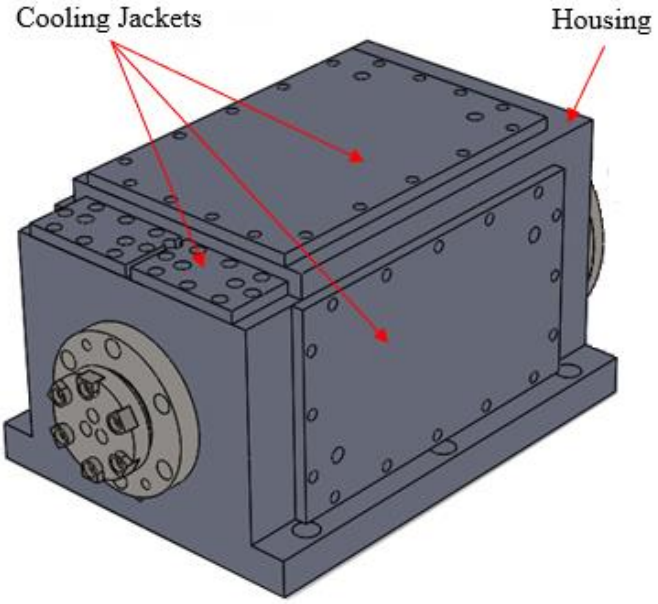

Figure 4.16: 3D Solidworks model of the HSPM generator

The removal of heat from the rotor and stator interface is achieved by introducing a brass cooling cartridge, shown in Figure 4.17, which was selected based on its thermal capabilities to quickly transfer the heat into the housing of the HSPM generator. The brass cooling cartridge is positioned between the stator and the housing. The detailed drawings for this component can be seen in Appendix A, drawing 21. In general practice the heat transferred to the housing is usually dissipated through the finned outermost surface. The lubrication system of the bearings is shown in Figure 4.18 as well as the assembly of the HSPM generator. A complete parts list can be found in Appendix A, drawing M1.

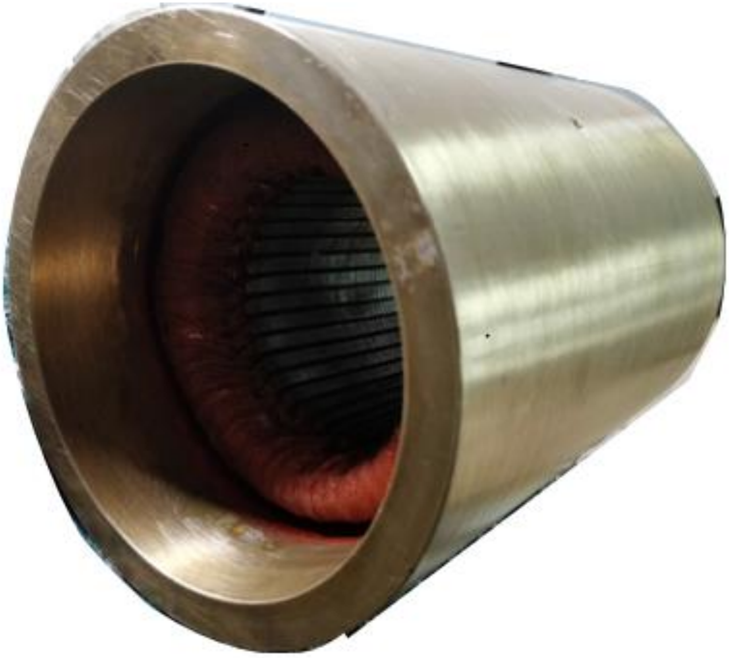

Figure 4.17: Brass cooling cartridge

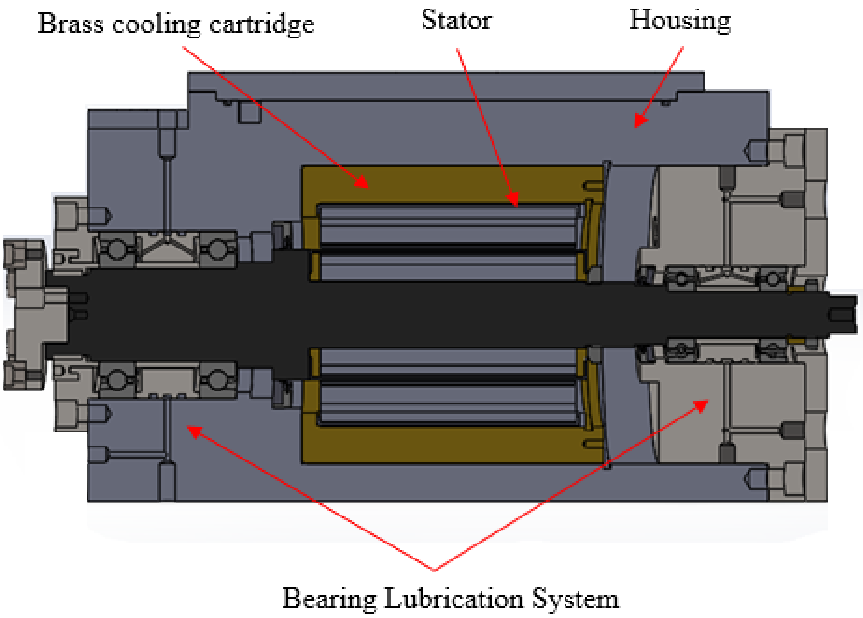

Figure 4.18: Sectioned Solidworks model of the HSPM generator

The following section explains the design of the cooling jackets of the HSPM generator to most effectively remove the heated generated by increasing the number of passes on the housing to increase the surface area of the heat transferred. Sect.3.3 explains the bearing lubrication system for the front and rear bearings and its associated components.

4.6 Design of the Cooling Jackets of the HSPM Generator

One of the main objectives is to ensure that the temperature rise of the HSPM generator is below critical operating conditions which could cause failure. In general practice, the heat generated by the motor is usually dissipated through the finned outermost surface of the motor [82-85]. However, to enhance the cooling of an HSPM generator would require more dissipation of heat through its housing by increasing the diameter of the HSPM generator, which in most cases is neither possible nor desirable. Thus, other methods to achieve a higher cooling rate for a fixed diameter of the HSPM generator need to be considered. One of the ways to do this is by utilizing an optimized cooling jacket configuration [73, 86]. Many researchers have focused on totally enclosed fan-cooled machines to understand the complex heat exchange phenomenon and its influence in motors and to identify the most important thermal parameters in the motors to achieve high performance and robust design [82-84]. However, in applications such as power generation, the electric motor must withstand loads exceeding its rated value for short periods of time. This is limited by the maximum temperature rise allowed which can be relaxed when more heat is removed, which has led to the implementation of cooling jackets [73,79, 86]. Thus, cooling by means of water circulation is frequently used in large motors and justification for its use in smaller motors is hindered by its higher cost compared to air cooling systems, provided that its use presents some technical and/or economic viability, then water cooling can also be used in smaller frame sizes [73]. While the design of the HSPM generator is compact, the justification of using water circulation for cooling is technically motivated, as it will be operating at speeds of 30000 RPM. The design of the cooling system is based on the premise of constant fluid flow and heat transfer coefficient. Then the volumetric rate is given by:

$$Q = V\,S \tag{4.24}$$

Where Q is the volumetric flow [m^3/s], V is the average speed [m/s] and S is the transversal section of flow [m^2]. To keep the speed constant, the ratio Q/S must be kept constant. In the case of the HSPM generator, as the flow is constant the area can also be kept constant throughout the cooling system. Past research shows three types of cooling jacket configurations for a water circuit geometry that has a basic shape of a cylinder [73]. Configuration I, II, and III are shown in Figure 4.19, Figure 4.20, and Figure 4.21, respectively.

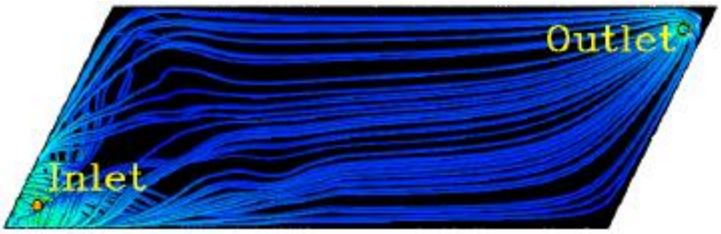

Figure 4.19: Configuration I of the Cooling Jacket

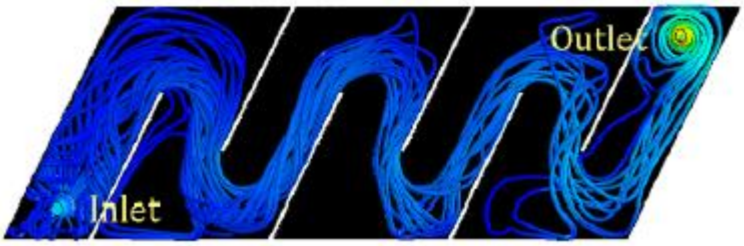

Figure 4.20: Configuration II – Intercalated opposite guides of the Cooling Jacket

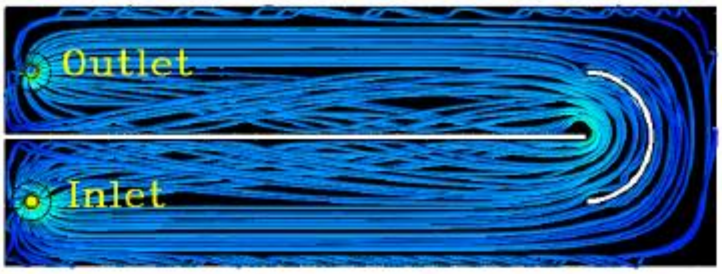

Figure 4.21: Configuration III – central guide with curved guide of the Cooling Jacket

In accordance with the Figure 4.19, configuration I presented a good flow, but the absence of guides inside the circuit could compromise the frame stiffness. While configuration II, Figure 4.20, incorporates guides in the circuit, it did not present good results because it caused low speeds in the back of the guides. Based on the poor results of configuration II, configuration III, Figure 4.21, was proposed. In this configuration, double the water speed of the initial configuration I water speed was obtained and it also presented good flow and low load loss. The cooling jackets in the design of the HSPM generator are positioned on the flanks and on the top of the HSPM generator as shown in Figure 4.16. The cooling jackets of the HSPM generator employ a configuration like configuration II, Figure 4.20, however, more channels are introduced, which further decreases the transversal section of flow, *S* [m^2], and increases the coolant speed. The 3D schematic which was done on Solidworks in Figure 4.22 Shows the configuration of the HSPM generator cooling jacket. The channels of the cooling jacket are further optimized by including a 10 mm copper pipe, wound into the shape of the configuration in Figure 4.22 for the coolant to flow inside, and the copper pipe is attached to the housing by a thermal paste. The actual housing of the HSPM generator and the cooling configuration can be seen in Figure 4.23. The front bearings of the HSPM generator experience the greatest load as previously shown in Sect. 2.2.1, which means there is a significant amount of heat generated by these bearings during operation. Thus, a cooling jacket for the front bearings was also considered and because of space limitations the design of the cooling system configuration for the bearings was limited to the one like configuration I, shown in Figure 4.19. The cooling jackets for the front bearings are shown in Figure 4.23 located on the far left of the housing.

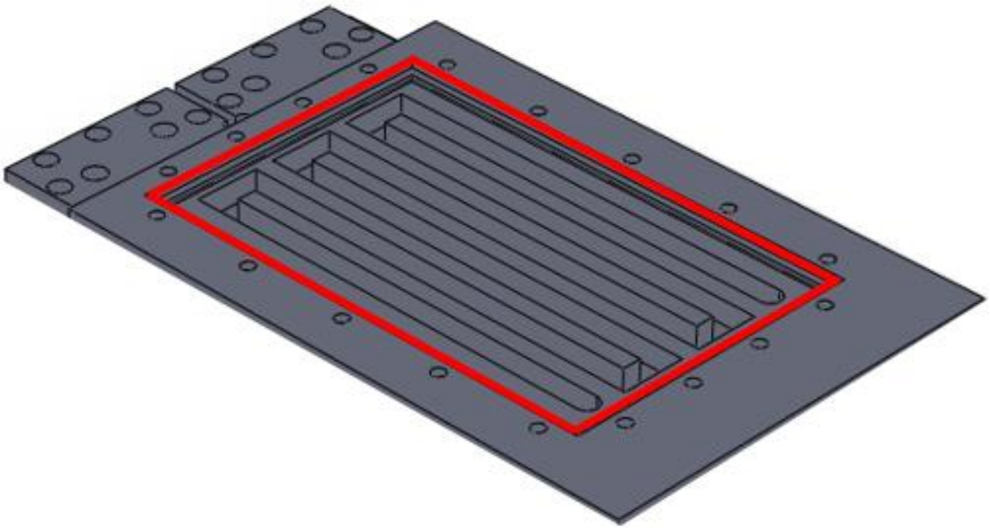

Figure 4.22: Cooling jacket configuration of the HSPM generator

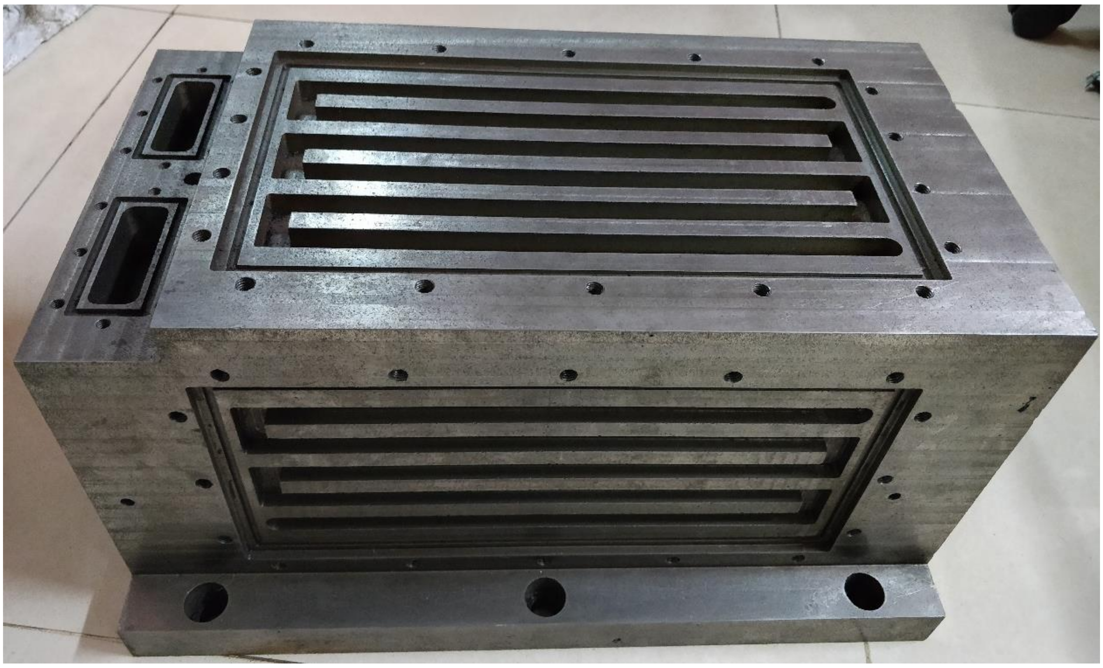

Figure 4.23: HSPM generator housing and cooling jacket configurations, front bearing cooling jacket configuration (far left)

4.7 Design of the Bearing Lubrication System of the HSPM Generator

The HSPM generator uses rolling element type bearings and at ultra high speeds lubrication starvation becomes a major issue. Most bearings typically use grease to lubricate bearings. However, the process of constantly having to ensure there is enough grease available for the bearings becomes tedious and on the onset of human error, such as applying too little grease or forgetting to top up the grease at the appointed time could well lead to bearing starvation and ultimately failure. The use of grease is also limited by high speeds, and as the speeds increase it is favourable to use oil as a lubricant, based on its properties to cope with higher speeds. Prior research shows the use of pressurised oil mist lubrication on the rolling elements using a piezo-electric nozzle and observed lesser fluctuations [87]. In other research, oil air mist lubrication was supplied through specially drilled holes at the outer races so that the oil-air mist could be directly applied to the rolling element and overcome the turbulence that occurs at the bearing cages [88]. The lubrication system design used for the HSPM generator is shown in Figure 4.24. The outer spacer, shown in Figure 4.25, has specially drilled holes that allows the oil air mist lubrication to flow to the back-back arrangement of the bearings for effective lubrication to take place. A detailed drawing of the inner spacer can be seen in Appendix A, drawing 5.

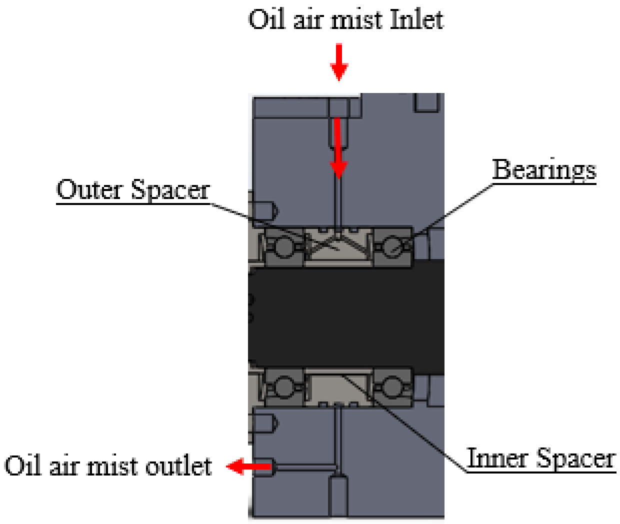

Figure 4.24: Lubrication system for front bearings of HSPM generator

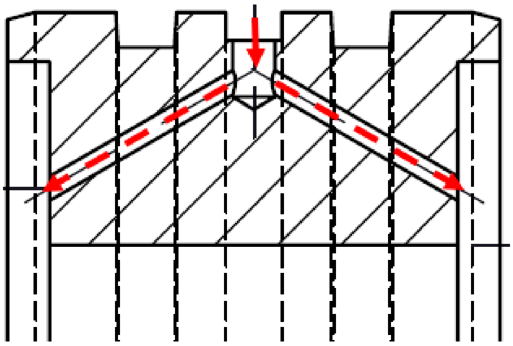

Figure 4.25: Outer spacer and the path of oil air mist lubrication to the bearings of the HSPM generator

The rear bearings of the HSPM generator also uses oil air mist lubrication and the lubrication system for the rear bearings is shown in Figure 4.26. The oil air mist flows through specially drilled holes in the rear housing and flows into the rear outer spacer where the oil air mist flow is channelled to the back-back bearing arrangement of the rear bearings. Detailed drawings of the rear housing and the rear outer spacer, can be seen in Appendix A, drawing 10 and drawing 7, respectively.

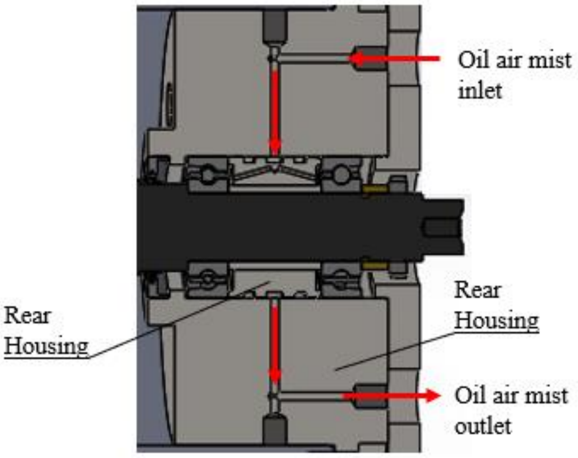

Figure 4.26: Lubrication system for rear bearings of HSPM generator

4.7.1 Oil Air Mist Lubrication Unit

The oil air system shown in Figure 4.27 supplies the oil air mist to the ceramic ball bearings. A specially designed mixing valve performs lubrication and cooling through intermittent feeding of 0.03~0.05 cc of VG-68 oil every 8 minutes into a stream of compressed air supplied by a compressor. The process is shown in Figure 4.28.

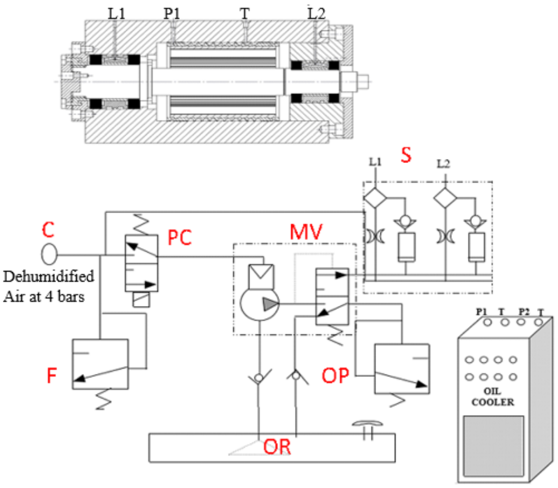

Figure 4.27: Lubrication and cooling of the developed HSPM generator

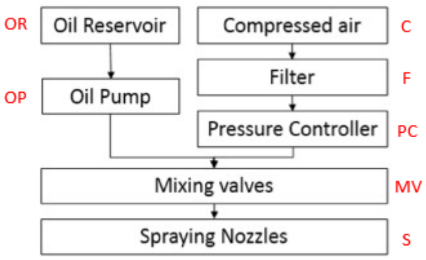

Figure 4.28: Process of the oil air mist lubrication system

4.8 Heat Generation

The severity of the thermal damage in the HSPM generator initiates the necessity of a comprehensive thermal analysis. In general, if the magnets are exposed to high temperatures the magnets will be demagnetized over time. In the HSPM generator the temperature rise occurs at the rotor-stator interface, and if the temperature exceeds the curie temperature of the magnets this could lead to demagnetization at a far more rapid rate which could have an adverse effect on the performance of the HSPM generator if adequate cooling is not supplied [89, 90]. However, to proceed with the thermal analysis of the HSPM generator, the heat generated in the HSPM generator must be understood and thoroughly investigated to make informed decisions regarding the cooling of the HSPM generator. The heat sources leading to the temperature rising of the HSPM generator come from all losses when it is running. These losses include electromagnetic losses (winding loss of the stator and rotor, and iron-core loss), mechanical loss /idle power and additional loss (stray loss). The total loss is given by:

$$P_{\Sigma} = P_{\mathrm{Cu1}} + P_{\mathrm{Cu2}} + P_{\mathrm{Fe}} + P_i + P_{\Delta} \tag{4.25}$$

Where P_{Σ} is the, P_{Cu1} is the copper loss of the stator winding, P_{Cu2} is the rotor copper loss, P_{Fe} is the iron-core loss, P_i is the idle power/mechanical loss, and P_{Δ} is the stray loss. The power flow diagram of the HSPM generator is shown in Figure 4.29.

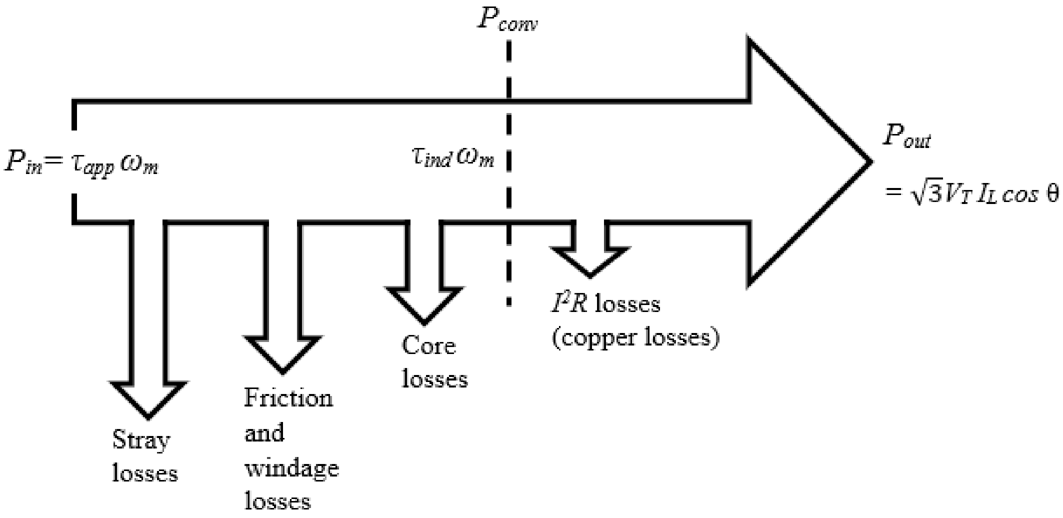

Figure 4.29: Power flow diagram of the HSPM generator

The following section discusses the heat generated in the HSPM generator because of electromagnetic losses. Sect. 4.3, discusses the mechanical loss (Idle power) of the HSPM generator and its effect on the machine performance.

4.9 Electro Magnetic Losses

The electromagnetic losses in the HSPM generator are grouped into (a) *stator loss*, and (b) *rotor eddy current loss.*

4.9.1 Copper Loss (Stator Winding Loss)

The copper loss arises from the current flowing in the stator windings. The resistance of the windings is calculated using Equation (4.26), where l_c is the length of the conductor, σ is the winding conductivity, and A_w is the winding cross-sectional area. The stator loss is found using the traditional power equation for a resistance, given by Equation (4.27). Where m_1 is the number of phases, I (15.8A) is the armature current, and R_a (0.014 Ω) is the dc armature resistance. Figure 4.30 shows the copper loss for the HPSM generator.

$$R_{\mathrm{a}} = \frac{l_c}{\sigma A_w} \tag{4.26}$$

$$P_{\mathrm{Cu}} = m_1 I^2 R_a \tag{4.27}$$

$$P_{\mathrm{Cu}} = 3 \times 15.8^2 \times 0.014$$

$$P_{\mathrm{Cu}} = 10.48\ W$$

$$P_{\mathrm{Cu}} \approx 10.5\ W$$

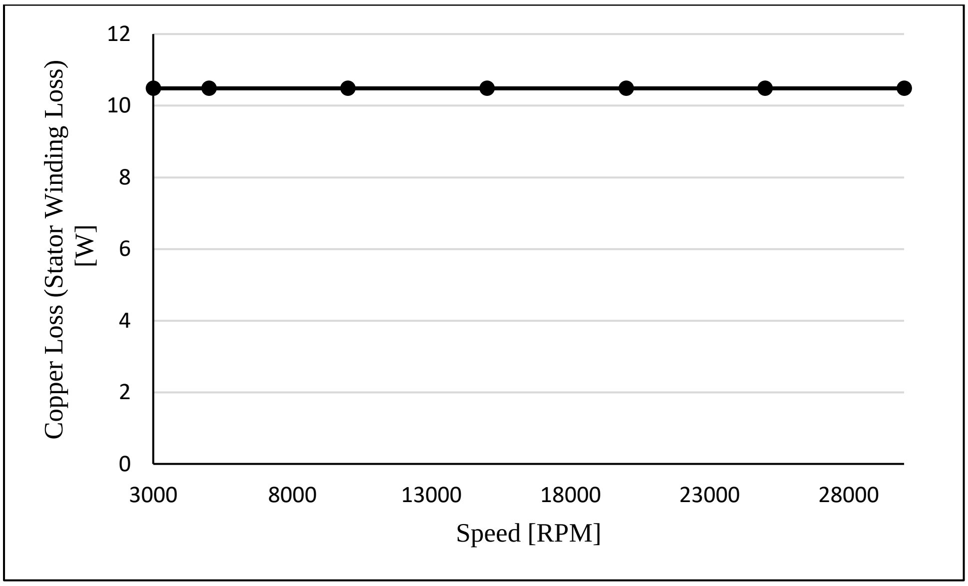

Figure 4.30: Copper loss/stator winding loss for the HSPM generator

4.9.2 Rotor Loss

The permanent magnets used in the HSPM generator are electrically conductive and therefore support eddy currents. In the case of the SPM, the retaining sleeves are sometimes made from electrically conductive material that can also carry eddy currents. Eddy currents are primarily caused by fluctuations in the magnetic flux density produced by time and space harmonics of the winding currents [91]. The currents produce losses which can cause excessive heating or demagnetization of the permanent magnets. The loss due to eddy current, in general, can be expressed by:

$$P_{\mathrm{R}} = \int_{v} \sigma \boldsymbol{E}^2 dV = \int_{v} \boldsymbol{J}^2/\sigma dV \tag{4.28}$$

Where σ is the material conductivity, $\boldsymbol{E}$ is the electric field, $\boldsymbol{J}$ is the eddy current density, and V is the volume of the material. Figure 4.31, shows the rotor loss for the HSPM generator. ANSYS Maxwell was used to determine the rotor loss.

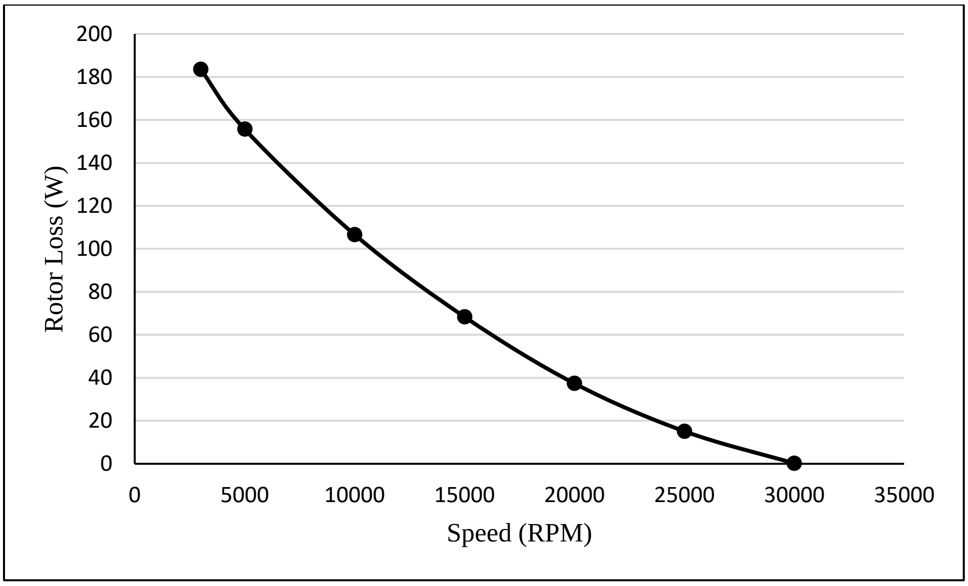

Figure 4.31: Rotor loss for the HSPM generator

4.10 Idle Power/Mechanical Loss

Several past findings reveal that the heat generated especially at the ultrahigh speed rolling elements has a direct relation to the rotor speed and the magnitude of the idle power was found to be nearly 50% of the total capacity of the HSPM generator [92]. Using the theory of hydraulics, the idle power (P_i) required to run the rotor shaft to overcome the: air friction, mechanical friction and preload was theoretically computed and is given by [93];

$$P_i = \frac{\rho \omega^3 R_s^5 C_{a-f}}{2} \tag{4.29}$$

Where ρ is the density of air (1.21 kg/m^3); ω is the angular velocity of the rotor shaft of the HSPM generator; R_s is the radius of the rotor shaft (ϕ 32.5 mm); $C_{a\text{-}f}$ is the coefficient moment for air friction. The rotor shaft of the HSPM generator which consists of permanent magnets, end caps and a dog clutch, is expected to create a turbulent boundary especially at ultrahigh speeds. Hence the coefficient of air friction ($C_{a\text{-}f}$) was computed using an empirical relation given by;

$$C_{a-f} = 0.146 R_e^{-\frac{1}{5}} \tag{4.30}$$

Where R_e is the Reynolds number at the boundary layer of the rotor shaft given by;

$$R_e = \frac{R_s^2 \omega \rho}{\eta} \tag{4.31}$$

Where η is the dynamic viscosity of air (1.98 X 10^{-5} kg/ms). By combining Equations (4.29), (4.30), and (4.31) the idle power required is recomputed and given by;

$$P_i = 0.073 \rho^{0.8} \omega^{2.8} R_s^{4.6} \eta^{0.2} \tag{4.32}$$

The properties of air and the rotor shaft were incorporated into Equation (4.32) and the idle power was determined to establish the behaviour of idle power against the rotor shaft speed shown in Figure 4.32.

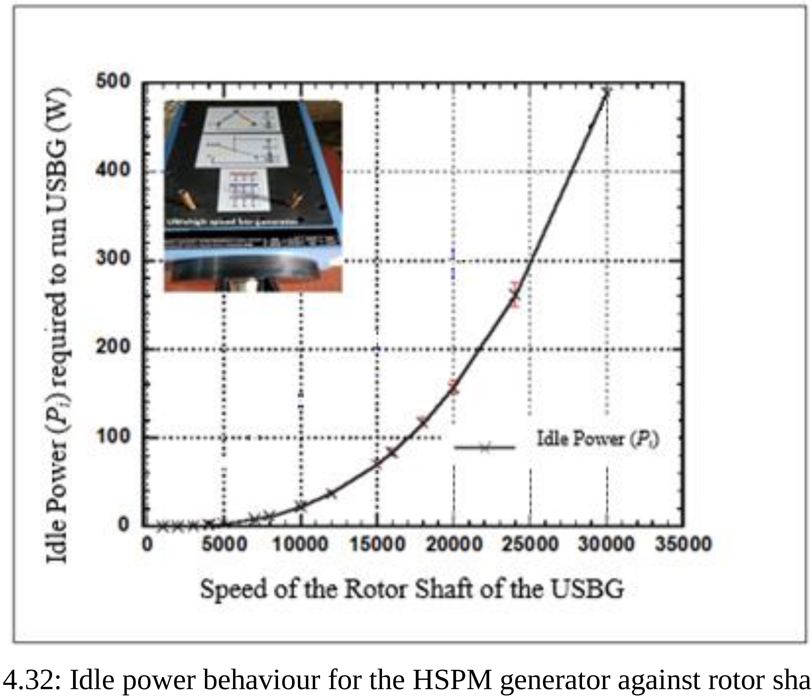

Figure 4.32: Idle power behaviour for the HSPM generator against rotor shaft speed

4.11 Core Losses

The stator core losses of the HSPM generator can be greater than normal machines because of the higher frequencies. Past research shows that these losses are minimized by using laminated steels in the stator and by not generating frequencies that are too high. Core losses consist of hysteresis losses, which results from the steel not wanting to change magnetic state, and Eddy current loss which is caused by the variation in flux density. The empirical formula expressing the hysteresis loss per unit volume, P_h (W/m^3), in terms of the maximum flux density, B (T) and frequency, f (Hz) is by:

$$P_h = \eta_m B^n f \tag{4.33}$$

Where η is a material constant and n is an exponent, which depends on the lamination material. The eddy current loss per unit volume, P_e (W/m^3), at frequencies which are low enough for the inductive effects to be neglected is given by:

$$P_e = \frac{\pi^2 B^2 t^2 f^2}{\rho_r \beta_e} \tag{4.34}$$

Where t is the thickness of the material (m), B is the peak flux density (T), ρ_r is the resistivity of the material (Ωm), and β is a coefficient that is related to the geometric structure. Because there are usually various imperfections in materials, the best way to approximate core losses is to use empirical loss data. If the flux density is estimated for each part of a machine and the mass of the steel calculated, the empirical core loss data can be used to estimate the total loss. Empirical data for M-19, 29-gauge material is shown in Figure 4.33.

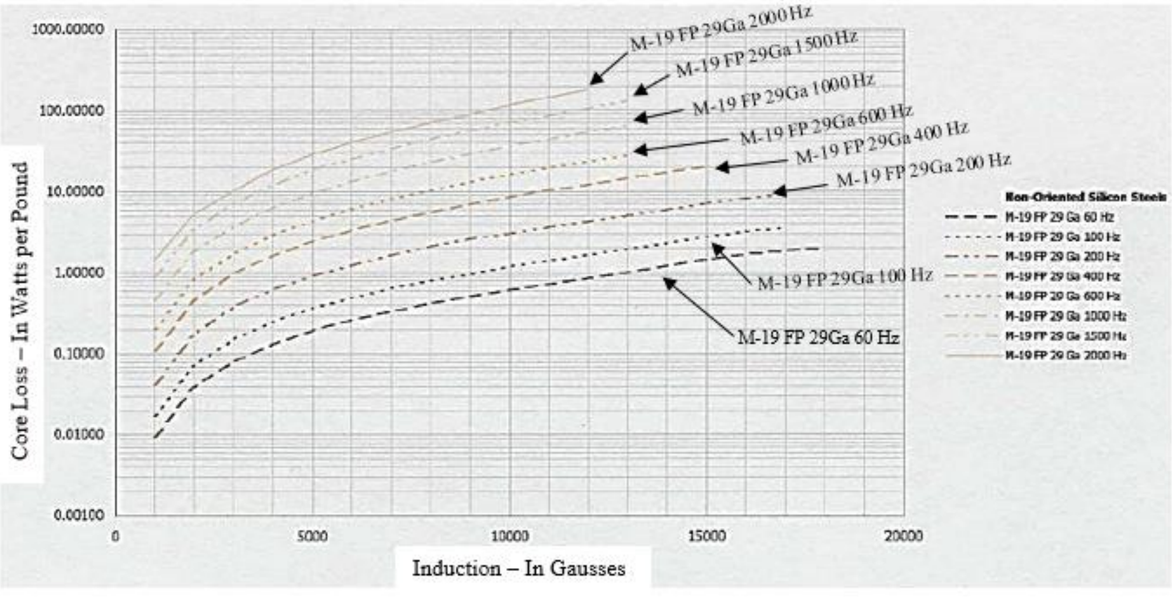

Figure 4.33: Core loss data for M-19, 29-gauge material used for rotor and stator laminations

Figure 4.34 shows the core loss data for the HSPM generator which was generated using ANSYS Maxwell and Figure 4.35 shows the total power loss for the HSPM generator at varying speeds. The total power loss was determined by summing all the losses (Core loss, Idle/Mech loss, Copper loss, and Rotor loss).

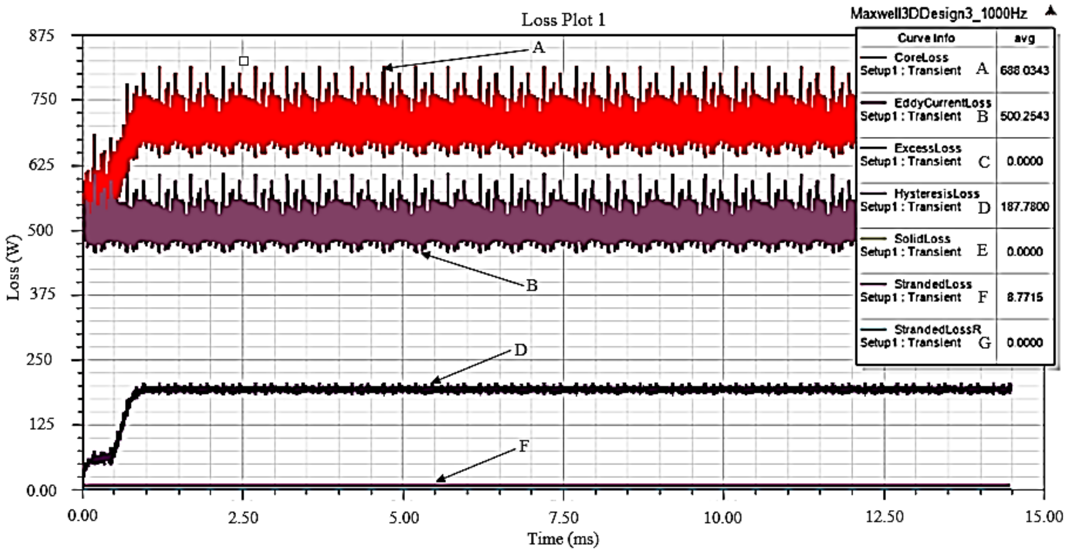

Figure 4.34: Core loss data for the HSPM generator

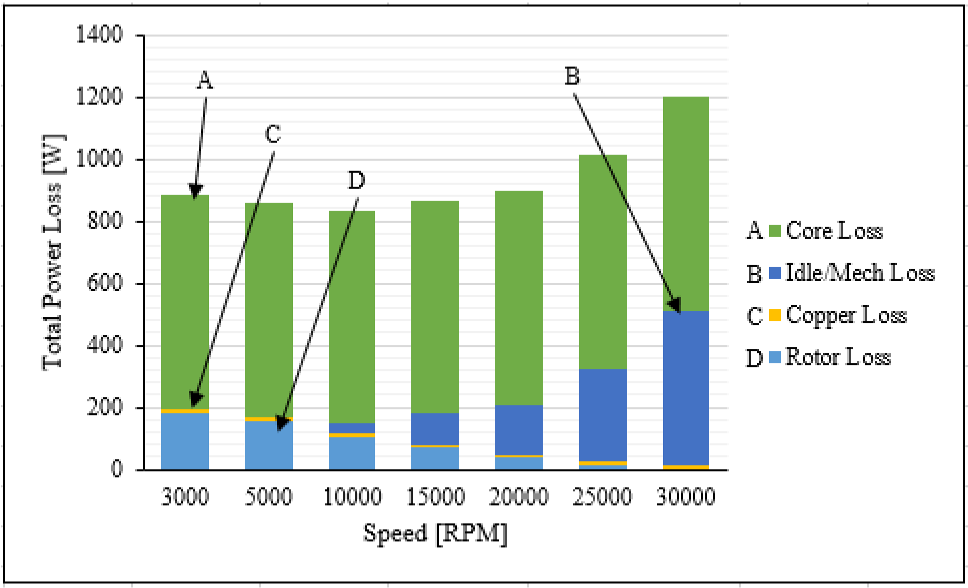

Figure 4.35: Total power loss at varying speeds for the HSPM generator

4.12 Thermal Analysis of the HSPM Generator

The HSPM generator is expected to generate a substantial amount of heat, as presented in Chapter 4, because of the high operating speeds; which would have an adverse effect on the performance of the HSPM generator. Thus, it is important to ensure that a suitable cooling system is employed. Chapter 3 presented the design of the cooling and lubrication system of the HSPM generator and bearings, respectively. However, the cooling jackets can be further optimized by manipulating the velocity of the coolant used, and while the newly developed oil air mist lubrication arrangement enables the control of the temperature rise at the rolling element of the HSPM generator and ensures the use of ultrahigh speed conditions for the HSPM generator, it still must be quantified.

The next section describes the role of the coolant velocity towards the transfer of the heat generated at the rotor-stator interface by using mathematical modelling to enhance the performance of the HSPM generator. Sect. 5.3, establishes the tribological behaviour between the rolling element and bearing races using a sphere and plane method of contact mechanics to understand the lubrication function particularly at ultrahigh speeds. It also presents the study of the liquid droplet; which quantifies the heat transfer components and its behaviour with the rotor speed as well as the gyroscopic speed of the silicon nitride rolling elements of the bearings.

4.13 Coolant Flow Rate on Heat Transfer Characteristics of the HSPM Generator

The generated heat at the rotor-stator interface is transferred to the cooling jackets, shown in Figure 4.23, and the coolant. This section analyses the role of coolant velocity towards the transfer of the heat generated by the HSPM generator. The following assumptions are made to establish a quantitative relation between the coolant velocity and its heat transfer characteristics:

- Fluid motion is characterized by average velocities.
- Convection is the major mode of heat transfer.

The cooling system of the HSPM generator employs forced convection and thus the heat transfer coefficient is determined based on semi-empirical relations and the type of flow of the coolant. The flow type of the coolant was assessed through the computation of the Reynolds number given by:

$$R_e = \frac{\rho_c l_{cj} v_c}{\eta} \tag{4.35}$$

Where ρ_c is the coolant density (998.2 kg/m^3), v_c is the coolant velocity (3.6 – 5 m/s), l_{cj} is the coolant jacket length (150 mm) and η is the dynamic viscosity (1.002 X 10^{-3} kg/ms). Substituting the coolant properties in Equation (4.35), the Reynolds number was computed, and the value was found to be between 358634 ~ 498103. It is well accepted that when "$R_e < 5 \text{ X } 10^5$", the coolant flow is predominantly laminar [94]. Therefore, the heat transfer coefficient, 'h' is computed using the semi-empirical equation of the theory of forced convection given by:

$$N_u = R_e^{\frac{1}{2}} P_r^{\frac{1}{3}} \tag{4.36}$$

Where N_u is the Nusselt number; R_e is the Reynolds number, from (4.35); and P_r is the Prandtl number defined given by:

$$N_u = \frac{hl_{cj}}{k} \tag{4.37}$$

$$P_r = \frac{\mu C_p}{k} \tag{4.38}$$

Where k is the thermal conductivity of the coolant media (6.3 X 10^{-4}kW/mK) and C_p is the specific heat of coolant (4.183 kJ/kg K). Substituting the coolant properties and combining Equation (4.36), (4.37), and (4.38), the convection coefficient 'h' was simplified as:

$$h = 0.759\sqrt{\frac{v_c}{l_{cj}}} \tag{4.39}$$

The convection heat transfer coefficient was computed, using Equation (4.39), to establish the behaviour of the convection heat transfer coefficient against the coolant velocity, as shown in Figure 4.36, and was found to have a near linear relation against the coolant velocity. Thus, it is expected that as the coolant velocity of the HSPM generator increases more heat is removed from the HSPM generator.

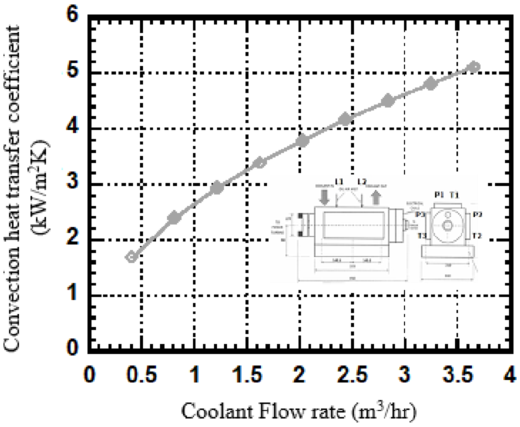

Figure 4.36: Influence of the coolant flow rate on the convection coefficient of the HSPM generator

4.14 Oil-Air Mist Lubrication on the HSPM Generator

The heat generated at the rolling element of the bearing is due to frictional torque and gyroscopic torque. This analysis will show the relationship between the rotor shaft speed and the angular spin velocity of the ceramic rolling element. An analysis on the heat dissipated will be done which has three components; the convective heat transfer, latent heat due to evaporation and sensible heat due to colliding and leaving droplets. Figure 4.37 shows the front and rear bearing configuration of the HSPM generator which is featured with ceramic rolling elements of diameter (d_b). The rolling elements rotate at a velocity (V_b) about a pitch circle diameter (PCD), 'D_b'. The rolling element spins with its own axis at a velocity (u_b). The pressurised oil mist is applied from a nozzle having diameter (d) from a distance (l) from the rolling element shown in Figure 4.38.

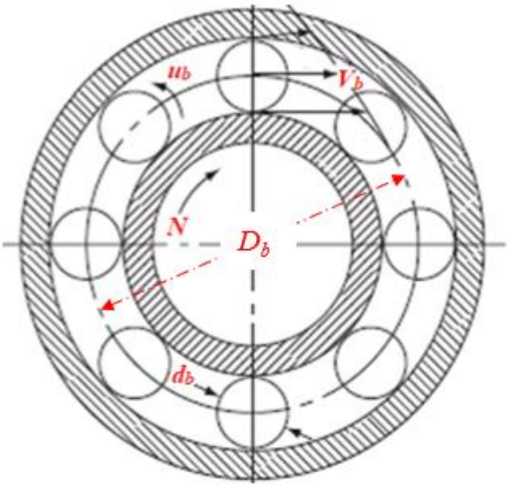

Figure 4.37: Front and rear bearing configuration of the HSPM generator

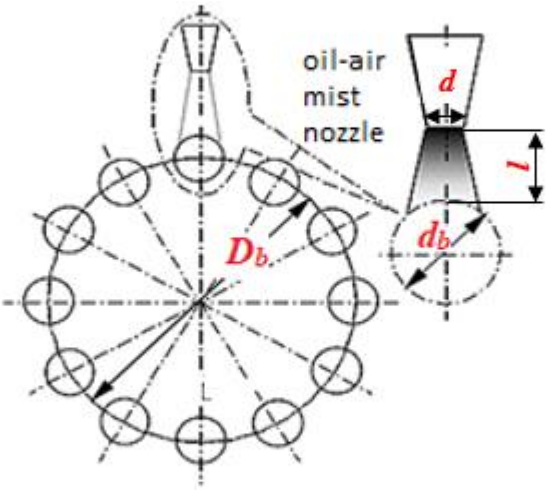

Figure 4.38: Oil-air mist lubrication to the ceramic rolling element

4.14.1 Quantitative Analysis for Heat Generation

Previous research has reported that a significant amount of heat generated at the rolling element is largely vested in [93];

I. *Frictional torque*

Which is:

a. Induced between the rolling element and the bearing outer races.

b. A result of the pre-load design of the bearing arrangement

II. *Gyroscopic torque of the ceramic rolling element used in hybrid bearings*

Which is the required external torque to produce precession motion. This can be explained as the axis of rotation of the ceramic rolling element is itself rotating about a second axis, the PCD.

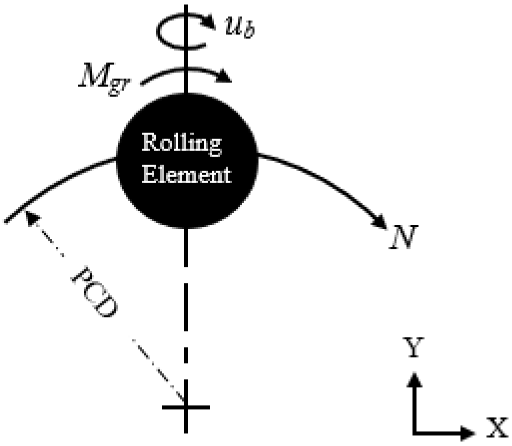

Figure 4.39:2D representation of precession motion of the ceramic rolling element on XY axis

In general, the magnitude of the heat developed (H_f) at the interface of the rolling element and bearing races is given by:

$$H_f = u_b M_s \tag{4.40}$$

Where u_b is the angular spin velocity of the ceramic rolling element used in the hybrid bearings, M_s is the twisting moment required to cause slip. It should be noted that the rolling element would slip when the applied twisting moment overcomes the vectoral summation of frictional and gyroscopic induced moments and is given by:

$$M_s = M_{ds} + M_{gr} \tag{4.41}$$

Where M_{ds} is the friction torque due to sliding, and M_{gr} is the gyroscopic torque for ball spin. Applying the principles of contact mechanics, the frictional torque was computed, and the generic equation is given by [95]:

$$M_{ds} = \frac{PD_bZ}{4d_b}\left[1 - \frac{d_b^2}{D_b^2}(cos^2\alpha)(r_0B_0 - r_iB_i)\right]f_s \tag{4.42}$$

Where P is the radial force, D_b is the PCD of the bearing, Z is the number of balls, d_b is the diameter of the ceramic rolling elements (D_b, and d_b are shown in Figure 4.38), α is the contact angle, r_o and r_i are the radii of the outer and inner raceway, respectively, f_s is the coefficient of sliding friction, and B_o and B_i are factors based on the geometric conditions of the raceway. Figure 4.40, shows the ceramic rolling element and the associated input dimensions to Equation (4.42).

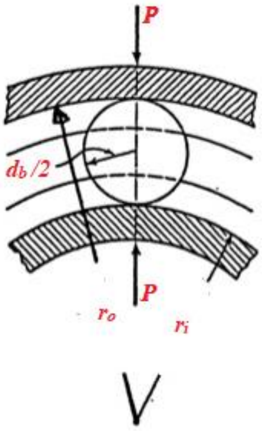

Figure 4.40: Ceramic rolling element and the load acting on the bearing and its associated dimensions

The gyroscopic torque of the rolling element M_{gr} is induced by the difference in the circumferential velocity of the inner and outer races and is given by [95]:

$$M_{gr} = \frac{\pi}{60} d_b^2 \frac{g_b}{g} u_b Z sin(\alpha) \qquad (4.43)$$

Where g_b is the density of the rolling element, and g is the acceleration due to gravity. The components of the HSPM generator were manufactured with built-in precision features; having tolerances with values less than 5 μm and higher surface integrity and hence the moment due to other effects such as *errors in manufacturing* and *stacked tolerances at the assembly* are assumed to be negligible. Using the geometrical details of the used ultra-precision hybrid angular contact ball bearing geometry, the inner and outer raceway values are given by:

$$r_o B_o = \frac{D_b}{2} + \frac{d_b}{2} \qquad (4.44)$$

$$r_i B_i = \frac{D_b}{2} - \frac{d_b}{2} \qquad (4.45)$$

The twisting moment that is required to cause slip at the rolling element was computed after substituting the raceway dimensions in terms of the ball diameter, PCD of the rolling element, contact angle and combining Equations (4.42) and (4.43). The twisting moment M_s is re-written and given by:

$$M_s = \frac{PD_bZ}{4d_b}\left[1 - \frac{d_b^2}{D_b^2}(cos^2\alpha)(d_b)\right]f_s + \frac{\pi}{60}d_b^2\frac{g_b}{g}u_bZsin(\alpha) \qquad (4.46)$$

The total slip moment at the front bearing of the HSPM generator was computed by applying the data provided by the bearing manufacturer (FAG). The data of the hybrid super-precision specifications are shown in Table K.

Table K: Data from FAG of the hybrid super precision bearing specifications

	Parameter	**Value**	**Unit**
i.	d_i	50	mm
ii.	Z	15	
iii.	d_o	80	mm
iv.	d_b	10	mm
v.	PCD	ϕ65	mm
vi.	α	15	degrees

Because of the data substituted into Equation (4.46), the twisting moment is simplified, and is given as:

$$M_s = 0.2381f_sP + 0.00688u_b \qquad (4.47)$$

Hence, the total heat developed at the rolling element, given in Equation (4.40), is re-written and given by:

$$H_f = u_b(0.2381f_sP + 0.00688u_b) \qquad (4.48)$$

Thus, the extensive analysis suggests that the heat generation for a fixed geometry hybrid ultra-precision ball bearing used in the HSPM generator is proportional to the square of the rolling element speed (u_b) and has a linear relation with the contact forces and the friction between the ceramic rolling element and the outer races of the hybrid bearings. The angular speed of the rolling element has a credible relation to the rotor shaft speed, '*N*', which is given by:

$$u_b = \frac{2\pi}{60}N\frac{\left(D_b^2 - d_b^2cos^2(\alpha)\right)}{2D_bd_b} \qquad (4.49)$$

Hence, H_f, in Equation (4.48) can be re-written by substituting Equation (4.49). By further substituting the physical conditions of the developed HSPM generator, H_f is simplified is simplified and given by:

$$H_f = 3.32N(0.2381f_sP + 0.022N) \tag{4.50}$$

Thus, Equation (4.50) suggests that there is a second order effect of the rotor shaft speed and a linear effect of the contact forces and frictional factor values on the heat generated at the ceramic rolling elements. Furthermore, effective heat management is a key issue to avoid the early failure of the bearings especially at the ceramic rolling elements.

4.14.2 Quantitative Analysis for Heat Dissipation

It is expected that the application of a pressurized impingement of oil-air mist on ceramic rolling elements of the ultrahigh speed hybrid bearings would manage the temperature rise at the rolling elements. The heat generated at the ceramic rolling element would be absorbed and transferred to the oil-air mist as well as to enhance the internal energy of the front and rear bearings. The rate at which the thermal energy is absorbed and transferred is dependent on the following components:

i. *Convective rate heat transfer,* Q_c;

$$Q_c = hA(T_b - T_m) \tag{4.51}$$

Where h is the convection coefficient (3000 to 200,000 W/m^2°C), T_b is the rolling element temperature, T_m is the mist temperature, A is the surface area of the rolling element (0.0003 m^2). Substituting the oil-air mist properties and the ceramic rolling element geometrical features, the convective rate heat transfer, Q_c is simplified and given by:

$$Q_c = 0.0003h(T_b - T_m) \tag{4.52}$$

ii. *Dissipation of latent heat due to evaporation,* Q_l

$$Q_l = M_mL_h \tag{4.53}$$

Where M_m is the mass balance of evaporating liquid (3.8×10^{-8} kg/s), L_h is the latent heat of evaporation for oil-air mist vapor (333.4 kJ/kg). Substituting these values, the value of Q_l for the front bearing portion of the HSPM generator is 12.67 J/s.

iii. *Sensible heat due to colliding and leaving droplet*

The interaction between the pressurized oil-air mist particles and the hot ceramic rolling elements is likely to bring changes to the system heat and this portion is computed separately for oil and air particles. They are:

- *Sensible heat due to colliding of oil particles, Q_{s-o}*
- *Sensible heat due to colliding of air particles, Q_{s-a}*

The total sensible heat is the summation of these components and given by:

$$Q_{s-o} + Q_{s-a} = M_o C_o (T_b - T_o) + M_a C_a (T_b - T_a) \quad (4.54)$$

Where C_o is the specific heat capacity of oil (1762 J/kg K), M_o is the mass flow rate of oil particles (2.5×10^{-6} kg/s), T_b is the ceramic rolling element temperature (°K), M_a is the mass flow rate of air particles (3.5×10^{-8} kg/s), and T_o is the inlet oil temperature (°K). The density of the lubrication oil and air is 826 kg/m^3 and 1.176 kg/m^3, respectively. C_a is the specific heat capacity of air (1005.6 J/kg K), T_a is the incoming air temperature (°K). The total rate of thermal energy transfer by the pressurized oil-air mist is the summation of the convective heat transfer, Q_c, the dissipation of latent heat due to evaporation, Q_l, and the sensible heat due to colliding and leaving droplet, $Q_{s-o}+Q_{s-a}$, which is given by:

$$Q = 0.0003h(T_b - T_m) + 12.67 + 0.00445(T_b - T_0) + 0.0000362(T_b - T_a) \quad (4.55)$$

From the analysis above, it is understood that the heat transfer primarily depends upon two factors; which are the convection coefficient and the temperature difference of the mist and the spinning element as shown in Figure 4.41. As the rotor shaft speed rises the relative velocity between the outer race and inner race of the bearing changes and increases the ball spin velocity. This was further checked through the measurement of the front and rear bearing temperatures at the nearest point of the hybrid bearing outer races and the results are shown in Figure 4.42. It is observed that when the oil-air mist pressure increases from 2 to 5 bar, a proportional increase on convection co-efficient was seen and hence the thermal management at the ceramic rolling element of the hybrid bearings was well maintained.

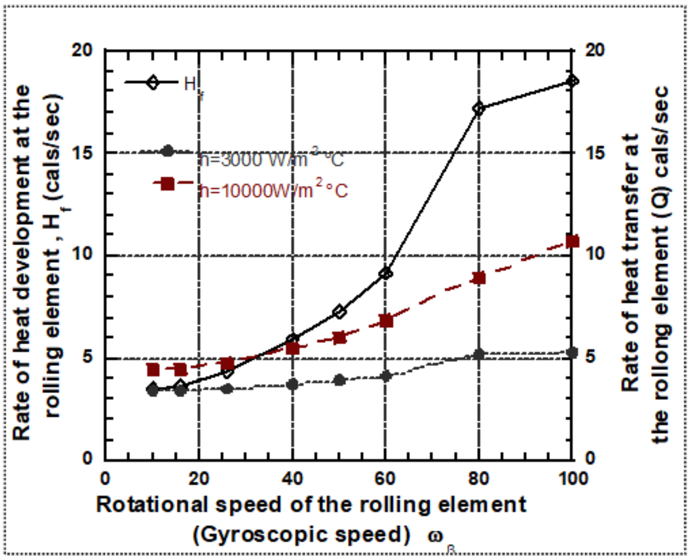

Figure 4.41: Thermal analysis at the rolling element of the HSPM generator

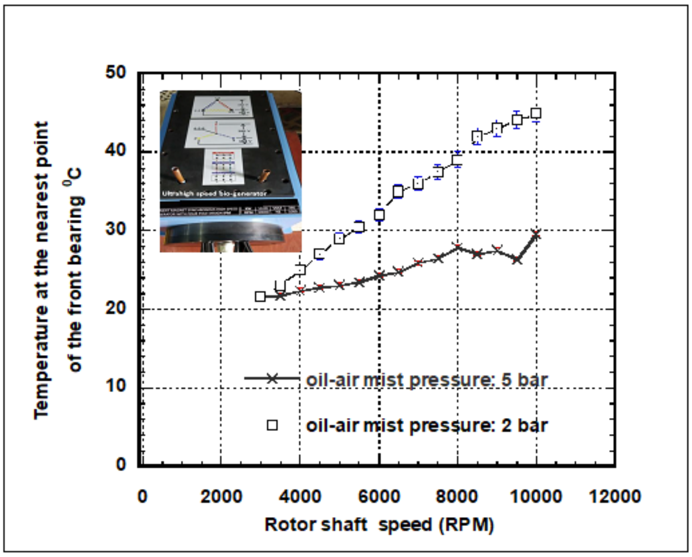

Figure 4.42: Temperature behaviour at the nearest point of the front bearings for different oil-air mist pressures

Chapter 3 and Chapter 4 focused on the design and development of the HSPM generator and the analysis of the of the HSPM generator, respectively. Detailed design drawings were produced for every part of the generator, considering the required specifications of the generator such as physical size, maximum speed (30000 RPM), power generated (10 kW), rigidity and preload, and cooling of the bearings through the use of oil-air mist lubrication and the housing cooling by means of cooling jackets. The design and development of the generator was supported by the analysis performed in Chapter 4. Ultimately, a surface mounted HSPM generator was designed. The rotor and stator were made from thin silicon steel laminations (M19, 29 gauge) which were stacked together to reduce the losses in the rotor and stator interface. To achieve the desired output power and speed, the stator had 24 slots, while the selected permanent magnets (NdFeB) were mounted on the rotor laminations and held by the retaining sleeve. Litz wire was used for the star connected stator winding. The selection of the bearings was dependent on the permissible rigidity and high precision of the generator. High precision angular contact ball bearings were selected for the front (drive end) and rear (non-drive end). The bearings assumed a back-to-back configuration, for preload purposes as well as the implementation of a lubricating and cooling system for the bearings which used oil-air mist lubrication. A brass cooling cartridge was also introduced to increase the heat transfer from the rotor and stator interface to the housing. The housing was designed with cooling jackets, which uses forced convection for heat transfer to the coolant. Chapter 4, presented the analysis of the HSPM generator, mainly focusing on the rigidity of the shaft. The loads on the front and rear bearings were 302 N and 52 N, respectively. Furthermore, the minimum/critical diameter was determined and was 6mm. However, for practical reasons the shaft is expected to be much larger based on the bearing life and bearing selection. Thus, based on the high precision angular contact ball bearings selected, the shaft diameter of the drive end was 50 mm and the diameter of the non-drive end was 25 mm. The key was omitted from the rotor shaft design of the HSPM generator, instead, two flat surfaces and an interference fit was adopted to transmit power. The required preload for the bearings was determined using the NSK, bearing manufacturer, catalogue and was determined to be 300 N, 83 N/µm and 94 N, 43 N/µm, for the front and rear bearings, respectively. The initial tensile force on the locknut was also determined, 34500 N, while the maximum permissible torque was determined to be 166 Nm. Further analysis was also carried out on the retaining sleeve and a sleeve thickness of 1 mm was chosen in line with the limitations of the airgap between the rotor and the stator and the required power output and speed. Heat generation was also a key factor, in the design of the HSPM generator due to the high speeds (mechanical losses) and electromagnetic losses, which are further discussed and analysed in the next chapter. The HSPM generator was designed and developed with the main specifications of power output and speed in mind and was achieved through technical drawing design and analysis. The following chapters focus on testing and experimental results of the HSPM generator.

Chapter 5

NUMERICAL CALCULATIONS

5.1 Introduction

The analysed HSPM generator, is designed by the mechanical and electrical engineering department at UCT. The generator is built with a surface magnet rotor. The generator is coupled to a gas turbine and is used to produce power to serve a small industrial community with drinking water production of 1000 m^3/d.

Parameters of the designed SPM, HSPM generator are as follows:

Voltage	220 V
Current	15.8 A
Resistance	0.014 Ω
Torque	3.18 Nm
Speed	30000 RPM
Output power	10000 W
Number of pole pairs	2

5.1.1 Classification of HSPM generator

- Stator: designed of 24 slots
    - Dimensions:
        - The outer diameter: 120mm
        - The inner diameter: 74 mm
        - Length: 140 mm

- Solid rotor with PMs mounted on its surface (SPM)
    - Dimensions:
        - The outer diameter: 72 mm
        - The inner diameter: 40 mm

- Permanent magnets
    - Amount: 12
    - Length: 35 mm
    - Height: 2.92 mm
    - Magnet angle: 120.06°E

- Air gap:
    - Width: 2 mm

The developed HSPM generator and its cross-section are presented in Figure 5.1 and Figure 5.2, respectively.

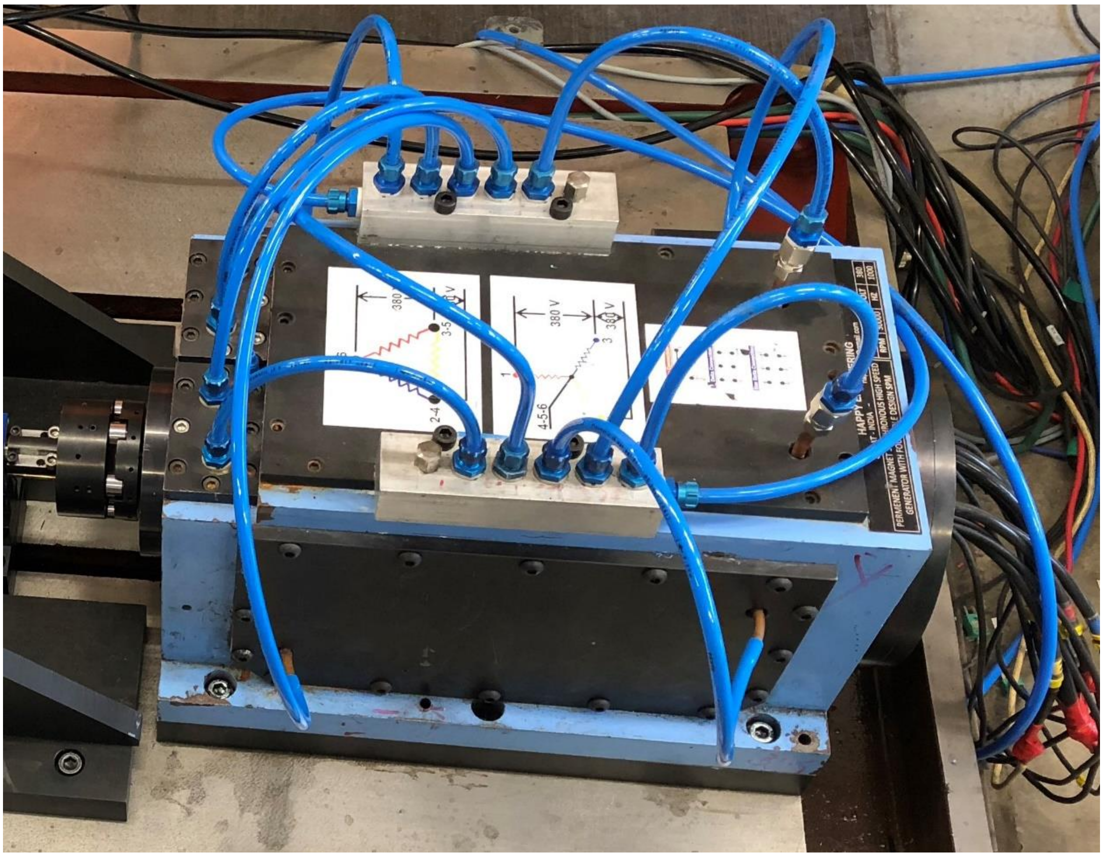

Figure 5.1: Developed HSPM generator

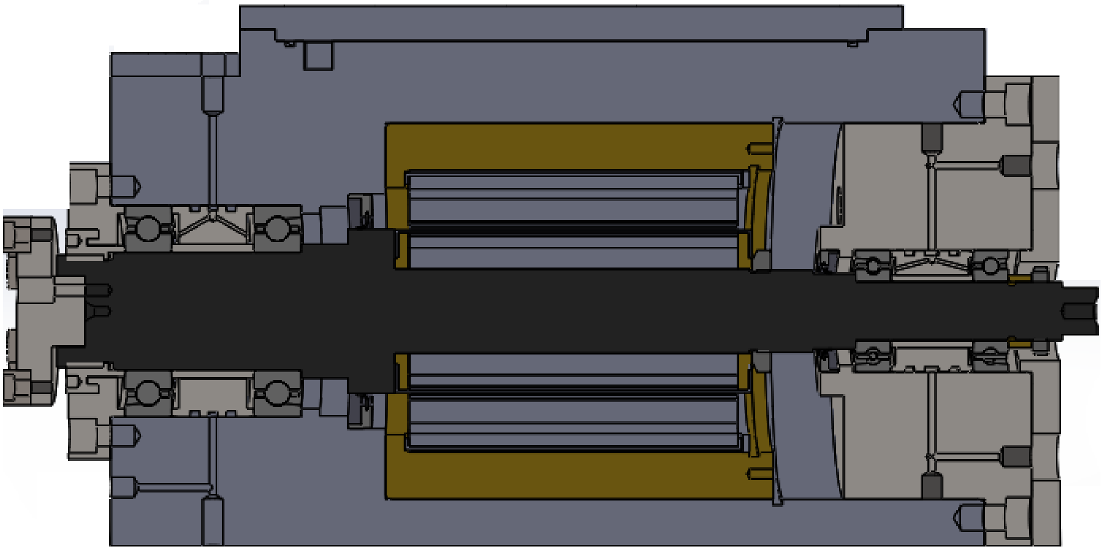

Figure 5.2: Solidworks cross-section of HSPM generator

5.1.2 Permanent magnets used in the HSPM generator

Permanent magnets of NdFeB type are applied to the analysed HSPM generator. This material belongs to the rare-earth permanent magnets. The main properties of this material are high remnant magnetic flux density, high coercive force, high energy product, and linear demagnetization curve. Properties of the applied NdFeB are presented as follows:

Table L: Properties of applied NdFeB magnet material

Density	7600 kg/m^3
Thermal Conductivity	8 W/mK
Specific Heat	440 J/kgK
Relative Permeability μ_{rec}	1.1
Resistivity (ρ_m)	1.6 X 10^{-6}Ωm
Remanence (B_r, type, 20°C)	1.11 T
Coercivity (H_c, type, 20°C)	850 kA/m
Coercivity (H_c, type, 150°C)	740 kA/m
Energy product $(BH)_{max}$, type, 20°C)	230 kJ/m^3
Curie Temperature	350 °C
Max. operation temperature	190 °C

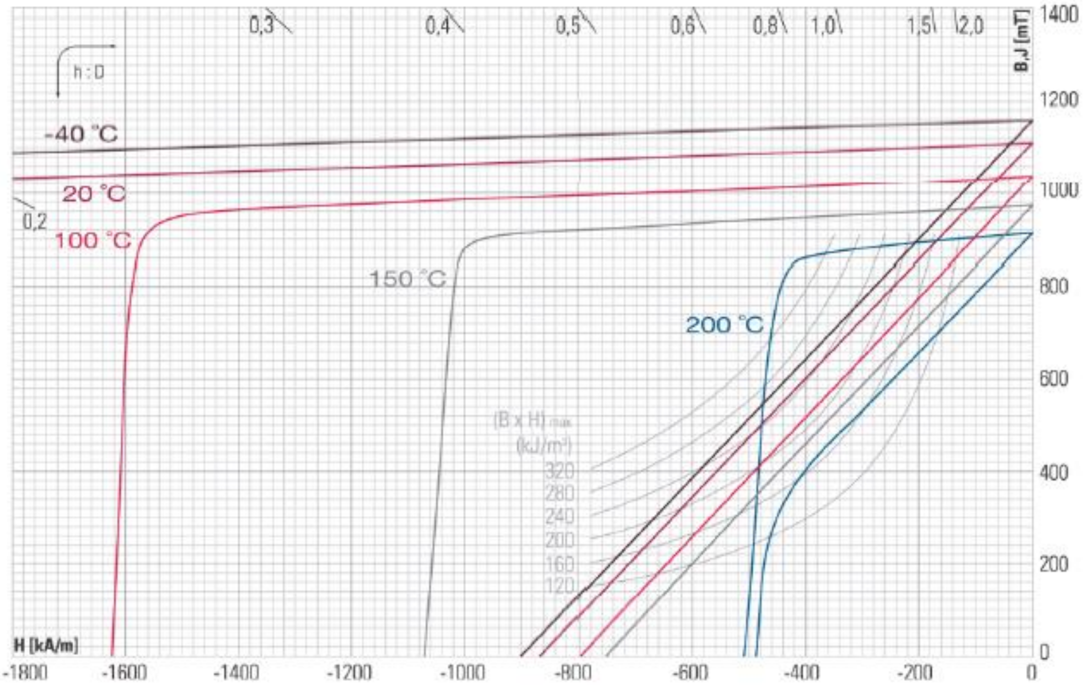

Figure 5.3: Demagnetization curve of applied NdFeB magnet material

5.1.3 Insulation Class

Insulation for wires have been standardized and graded by their resistance to thermal aging and failure. Four insulation classes are commonly used. For simplicity, they are designated by the letters A, B, F, and H. The temperature capabilities of these classes are separated from each other by 25 °C increments. The temperature capabilities of each insulation class are defined as being the maximum temperature at which the insulation can be operated to yield an average life of 20 000 hours.

The thermal design should make sure that the HSPM generator windings temperatures do not exceed the limit for the pertinent insulation class, in the worst situation. Finding the highest winding temperature spots is crucial to insulation (and machine) working life. Insulation systems are rated y IEC (International Electro technical commission) and NEMA (National Electrical Manufacturers Association) classification according to maximum allowable temperatures:

Table M: Insulation class

Insulation Class	Temperature rating [°C]
A	105
B	130
F	155
H	180

Practice has shown that increasing the winding temperature over the insulation class limit reduces the insulation life. There is a lot of insulating components used in the process of building generators. The obvious ones are the enamel coating on the magnet wire and the insulation on the leads that come to the conduit box. Some less obvious components are the sleevings used over joints, where leads connect to the magnets wire, and the lacing string that is used to bind the end turns of the generator. Other components are the slot liners that are used in the stator laminations to protect the wire from chafing. Also, top sticks are used to hold the wire down in place inside the stator slots.

Another important component of the generator system is the varnish in which the completed assembly is dipped prior to being baked. The dipping varnish is used for sealing nicks or scratches that may occur during the winding process. The varnish also binds the entire winding together into a solid mass so that it does not vibrate and chafe when subjected to the high magnetics forces that exist in the generator.

5.2 Heat Transfer Theory

Theory of heat transfer predicts the energy transfer that takes place between material bodies as a result of temperature difference. This energy transfer is defined as heat. Three modes of heat transfer exist in which heat can be transferred from one place to another and they are conduction, convection and radiation.

5.2.1 Conduction Heat Transfer

In conduction, heat is carried by means of collisions between rapidly moving molecules closer to the region with the highest temperature and the molecules closer to the region of the body with lower temperature. Some of the kinetic energy of the fast-moving molecules passes to the slow molecules, and as a result of successive collisions, heat flows through the body from the high temperature region to the low temperature region. Since the design of the HSPM generator assumes a cylindrical cross-section from the rotor to the housing, the rate at which heat is conducted through a cylindrical slab of a particular material, as shown in Figure 5.4, is proportional to the area of each material and to the temperature difference (ΔT) between the different materials and inversely proportional to the length of the HSPM generator. The amount of heat ‘$Q_{cond,\ cyl}$’ that flows through the generator is in the normal direction to the wall surface (no significant heat transfer occurs in other directions) and is given by [96]:

$$Q_{cond,cyl} = 2\pi kL \frac{T_1 - T_2}{\ln\left(\frac{r_2}{r_1}\right)} \tag{5.1}$$

Where k is the thermal conductivity [W/mK], and L [m] is the length of the generator.

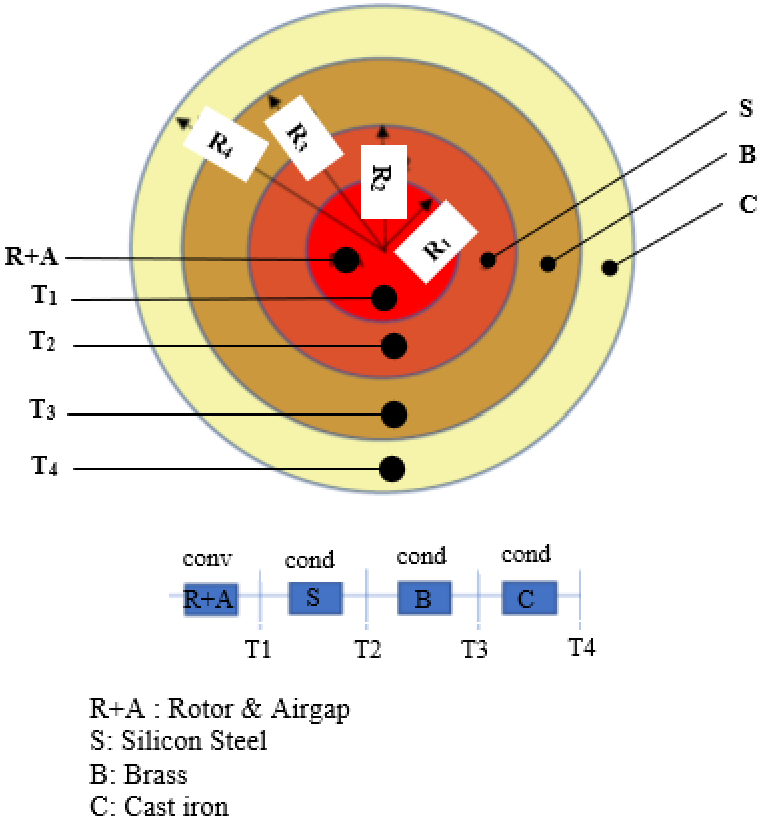

Figure 5.4: Conduction heat transfer through a cylindrical cross section (HSPM generator)

5.2.2 Forced Convection Heat Transfer

Forced convection heat transfer is the mechanism of heat transfer through a fluid in the presence of a bulk fluid motion [97]. In forced convection, the fluid is forced to flow over a surface or in a tube by external means such as a pump or fan. Forced convection is complicated since it involves fluid motion as well as heat conduction. The fluid motion enhances heat transfer (the higher the velocity the higher the heat transfer rate). The rate of convection heat transfer is expressed by Newton's law of cooling given by [Forced Convection]:

$$Q_{conv} = hA(T_s - T_\infty) \tag{5.2}$$

Where h is the convective heat transfer coefficient, which strongly depends on the fluid properties and roughness of the solid surface, and the type of the fluid (laminar or turbulent). It also assumed that the velocity of the fluid is zero at the surface as shown in Figure 5.5, this is called no-slip condition. Due to this assumption, the heat transfer from the solid surface to the fluid adjacent to the surface is by pure conduction, since the fluid is motionless. Thus, the convection heat transfer coefficient. in general, varies along the flow direction.

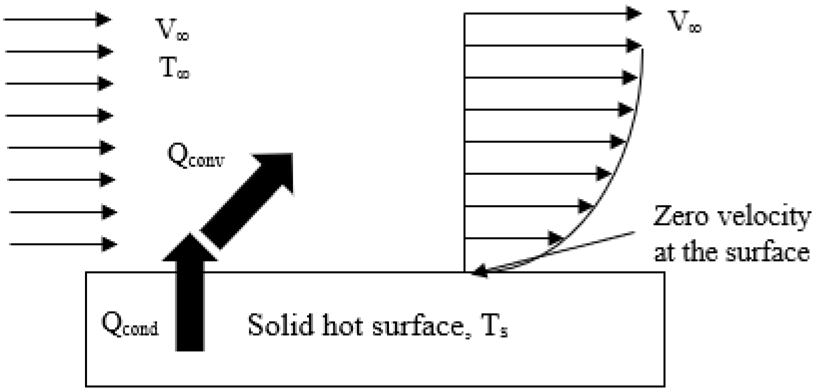

Figure 5.5: Forced convection of fluid flowing over a solid surface

The theory of heat transfer, in particular conduction and convection (forced), is a key feature of ANSYS Fluent which is used to analyse the effect of coolant velocity on the HSPM generator, which is developed from ANSYS Maxwell which determines the losses in the generator from the rotor and stator interface to the dissipation of heat by the cooling jackets through forced convection.

5.3 ANSYS – Maxwell Familiarization

In this thesis, the analysis of the HSPM generator was computed both 2-dimensionally (2D) and 3-dimensionally using ANSYS, which is an American Computer-aided engineering software. Ansys publishes engineering analysis software across a range of disciplines like finite element analysis, structural analysis, computational fluid dynamics, explicit/implicit methods, and heat transfer.

Ansys Maxwell is a high-performance, low frequency electromagnetic field simulation interactive software package that uses finite element analysis (FEA) to solve electromagnetic problems by solving *Maxwell's equations* in a finite region of space with appropriate boundary and user-specified initial conditions for 2D/3D electromagnetic and electromechanical devices, including motors, actuators, transformers, sensors and coils. Maxwell uses the accurate finite element method to solve static, frequency-domain, and time-varying electromagnetic and electric fields. The software can only use a triangular/tetrahedral element to mesh the domain and linear interpolation functions to approximate the solution [98].

The physical equations that describe the electromagnetic field given by J. C. Maxwell are [98],

Gauss' law for Electricity:

$$\boldsymbol{\nabla} . \boldsymbol{D} = \boldsymbol{p} \tag{5.3}$$

Gauss' Law for Magnetism:

$$\boldsymbol{\nabla} . \boldsymbol{B} = \boldsymbol{0} \tag{5.4}$$

Faraday's Law of Induction:

$$\boldsymbol{\nabla} \times \mathbf{E} = -\frac{\boldsymbol{\partial B}}{\boldsymbol{\partial t}} \tag{5.5}$$

Amperes' Law:

$$\boldsymbol{\nabla} \times \mathbf{H} = \boldsymbol{J} + \frac{\boldsymbol{\partial D}}{\boldsymbol{\partial t}} \tag{5.6}$$

$$D = \varepsilon_0 E + P$$

General case

$$D = \varepsilon_0 E$$ *Free space*

$$D = \varepsilon E$$ *Isotropic linear dielectric*

$$B = \mu_0 (H + M)$$

General case

$$B = \mu_0 H$$ *Free space*

$$B = \mu H$$ *Isotropic linear magnetic medium*

Figure 5.6: Physical equations describing electromagnetic field

Where,

$\mathbf{B}$: Magnetic field
$\mathbf{D}$: Electric displacement
$\mathbf{E}$: Electric field
$\mathbf{H}$: Magnetic field strength
$\mathbf{J}$: Current density
$\mathbf{M}$: Magnetization
$\mathbf{P}$: Polarization
ρ: Charge density
: Differential operator (“del”)
μ_0: Permeability
ε_0: Permittivity

Numerical techniques are necessary to solve the equations above.

5.4 ANSYS Maxwell

(RMxprt) Rotating Machine Expert is a template-based design tool of the ANSYS – Maxwell suite used to create a customized machine design flow to meet demand for higher efficiency. Using classical analytical motor theory and equivalent magnetic circuit methods, RMxprt calculates machine performance, makes initial sizing decisions and performs numerous "what if" analyses. RMxprt can automatically set up a complete Maxwell project (2-D/3-D) including geometry, materials and boundary conditions. The set up includes the appropriate symmetries and excitations with coupling circuit topology for electromagnetic transient analysis. The analysed model of RMxprt can be exported to create Maxwell 2D/3D models that include FE mesh modelling algorithms to solve the machine’s Magneto Static and Transient equations. Maxwell uses the Finite Element Method (FEM) to solve Maxwell ‘s electro-magnetic field equations. To obtain the set of algebraic equations to be solved, the geometry of the problem is discretized automatically into basic platonic solids (e.g. Triangle in 2D & Tetrahedron in 3D) as shown in Figure 5.7 and Figure 5.8 respectively. The assembly of all tetrahedra/triangles is referred to as the finite element mesh of the model or simply, the mesh.

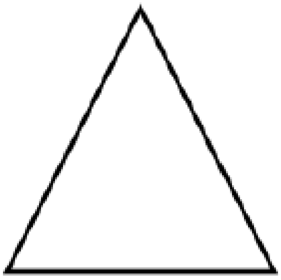

Figure 5.7: 2D FEM element Triangle

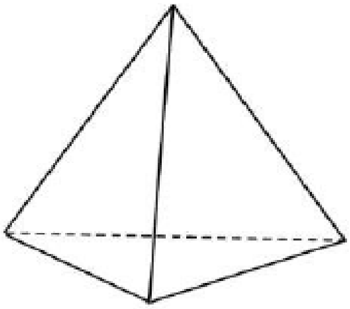

Figure 5.8: 3D FEM element Tetrahedron

The initial design on Maxwell was done by the Electrical Engineering Department. The model was simplified to a quarter of the entire model to save on computation and simulation time. Finite Element Analysis was performed in 2D, followed by 3D analysis for a more accurate simulation and representation of the machine model. Figure 5.9 shows a 2D model with a flux plot of the HSPM generator under no load.

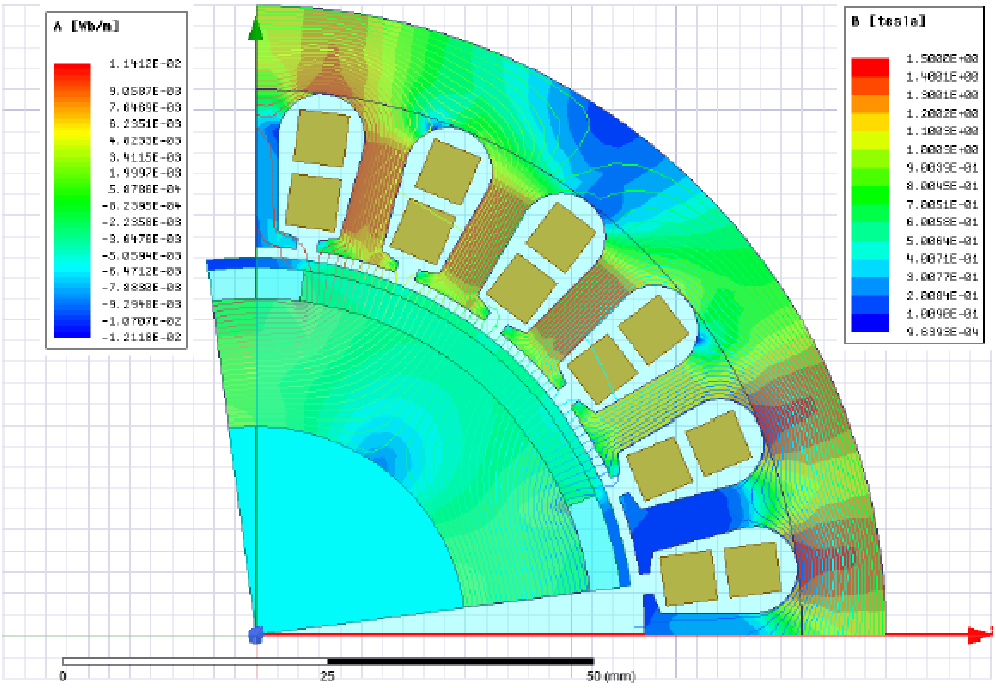

Figure 5.9: 2D Model of the HSPM Generator

5.5 Coupling Maxwell Designs with ANSYS Thermal via Workbench

To understand the severity of the rotor speed parameter on internal heat generation of the HSPM generator, ANSYS Maxwell simulation analysis was performed. The analysis was done by coupling Maxwell to Mechanical Steady State Thermal and importing the load generated by Maxwell for the thermal analysis. Coupling Maxwell2D/3D with ANSYS Thermal is supported via the Workbench schematic. The heat generated varies with the speed of the HSPM generator. The housing temperature boundary condition was 53°C, which was set based on a safety factor of 1.5 of the maximum allowable temperature for the coolant which is 80°C. Table N also shows the relationship between the operating speeds of the HSPM generator and the losses of the stator and rotor as well as the total loss.

Table N: Stator and Rotor Losses of the HSPM Generator and Total Losses

Speed (RPM)	Stator Loss (W)	Rotor (W)	Total Loss (W)
3000	1417.9	183.59	1601.49
5000	1375.07	155.70	1530.77
10000	1390.19	106.66	1496.85
15000	1421.87	68.41	1490.28
20000	1560.04	37.40	1597.44
25000	1603.69	15.16	1618.85
30000	1707.05	0.21	1707.26

5.6 Computational Fluid Dynamics-ANSYS Fluent

ANSYS Fluent is used to predict the flow and effect of coolant velocity on the HSPM generator. The ribbon, at the top of the Fluent Graphical User Interface (GUI), as shown in Figure 5.10, is the primary method for setting up and running the simulation. The ribbon is featured with tabs from left to right, which are; setting up domain, setting up physics, solving, and postprocessing. The ribbon guides the basic workflow, and this is shown in Figure 5.11.

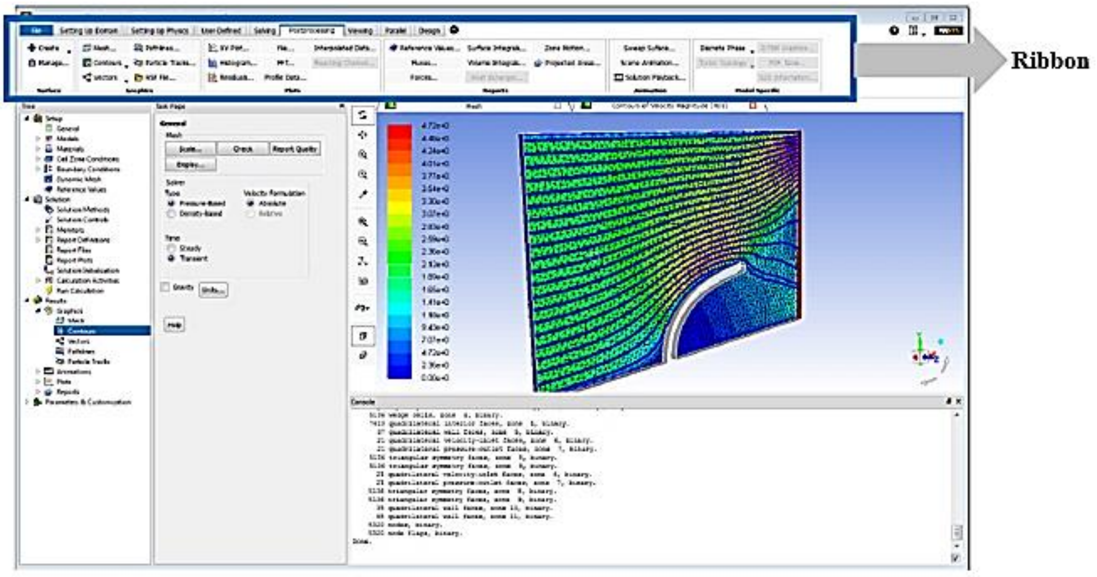

Figure 5.10: Fluent Graphical User Interface (Ribbon)

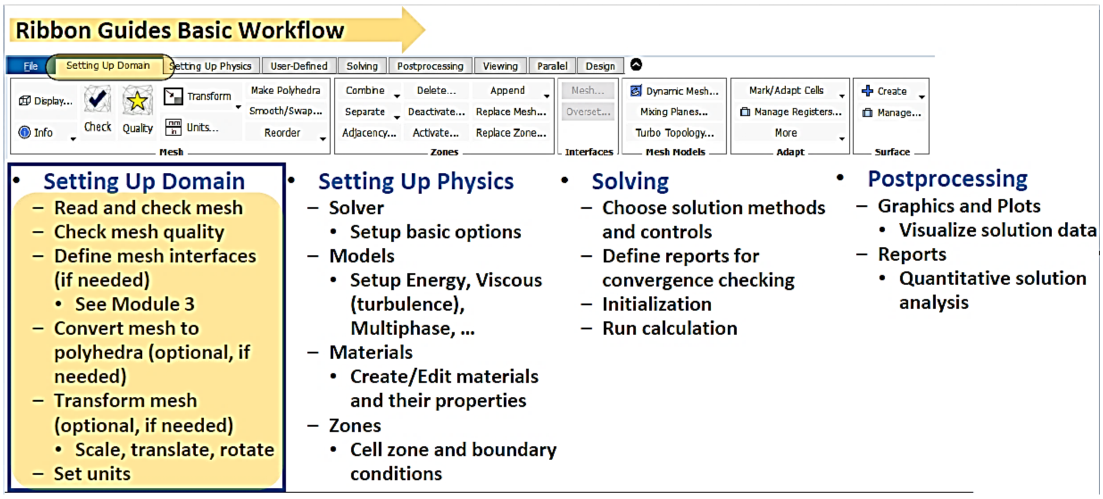

Ribbon Guides Basic Workflow

- Setting Up Domain
  - Read and check mesh
  - Check mesh quality
  - Define mesh interfaces (if needed)
    - See Module 3
  - Convert mesh to polyhedra (optional, if needed)
  - Transform mesh (optional, if needed)
    - Scale, translate, rotate
  - Set units
- Setting Up Physics
  - Solver
    - Setup basic options
  - Models
    - Setup Energy, Viscous (turbulence), Multiphase, …
  - Materials
    - Create/Edit materials and their properties
  - Zones
    - Cell zone and boundary conditions
- Solving
  - Choose solution methods and controls
  - Define reports for convergence checking
  - Initialization
  - Run calculation
- Postprocessing
  - Graphics and Plots
    - Visualize solution data
  - Reports
    - Quantitative solution analysis

Figure 5.11: Ribbon basic guide workflow for simulation

The first step in the analysis of HSPM generator and the effect of the coolant flowrate is setting up the domain. This step performs the mesh-related activities using the ‘Setting Up Domain’ ribbon tab (Mesh group), shown in Figure 5.12. The mesh was of the HSPM generator was checked by selecting the blue tick, shown in Figure 5.12, which ensures that each cell is in a correct format and connected to other cells as expected. No failures of the mesh were detected for the generator model which suggested that there were no badly formed or corrupted meshes that needed to be repaired prior to simulation

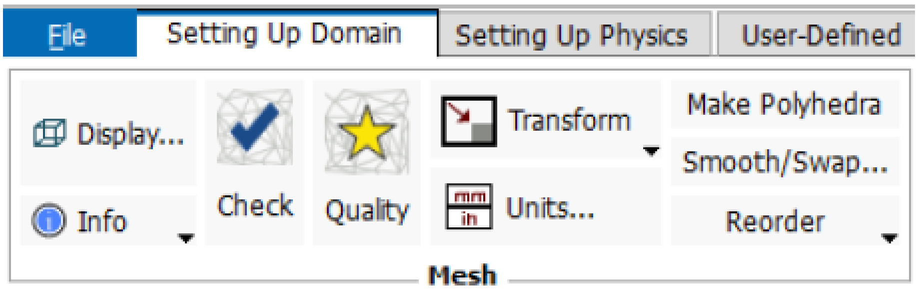

Figure 5.12: 'Setting Up Domain' ribbon tab, mesh group

The quality of the mesh plays a significant role in the accuracy and stability of the numerical computation of the generator, and thus the quality of the mesh was checked to perform a robust simulation. Minimum cell orthogonality is an important indicator of mesh quality and generally, values for orthogonality can very between 0 and 1, with lower values indicating poorer quality cells. The minimum orthogonality of the HSPM generator was above 0.01 and the average value was significantly larger. To adjust and display the mesh, the Faces option was disabled, and the Edges option was selected in the mesh display dialog box, as shown in Figure 5.13. The Temperature units were also changed to Celsius, by selecting temperature in the Quantities list in the Set Units dialog box, as shown in Figure 5.14, and selecting ‘c’.

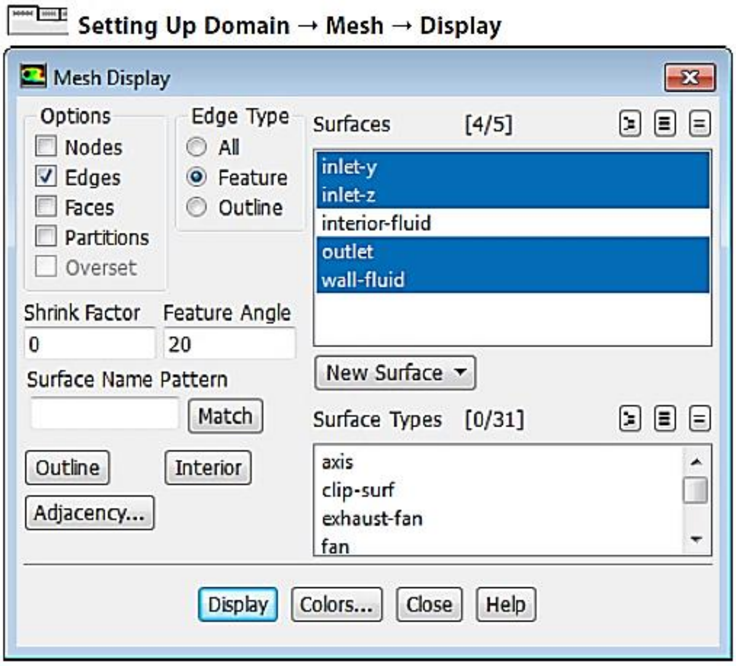

☐ Nodes
☑ Edges
☐ Faces
☐ Partitions
☐ Overset

Edge Type: ○ All ● Feature ○ Outline

Shrink Factor 0

Feature Angle 20

Surfaces [4/5]

- inlet-y
- inlet-z
- interior-fluid
- outlet
- wall-fluid

Figure 5.13: ANSYS Fluent mesh display

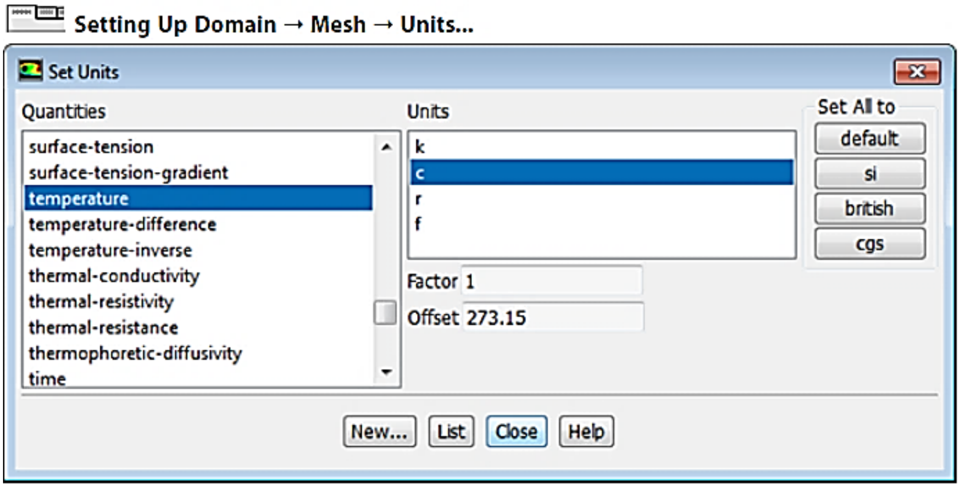

Quantities: temperature

Units: c

Factor 1

Offset 273.15

Figure 5.14: ANSYS Fluent Set Units display dialog box

The next step is setting up the physics. In this step, a solver was selected and physical models, material properties, and zone conditions for the simulation of the HSPM generator were specified, using the Setting Up Physics ribbon tab.

In the Solver group of the Setting Up Physics ribbon tab as shown in Figure 5.15, the default selection of the Steady, Pressure-Based solver was retained as shown in Figure 5.15.

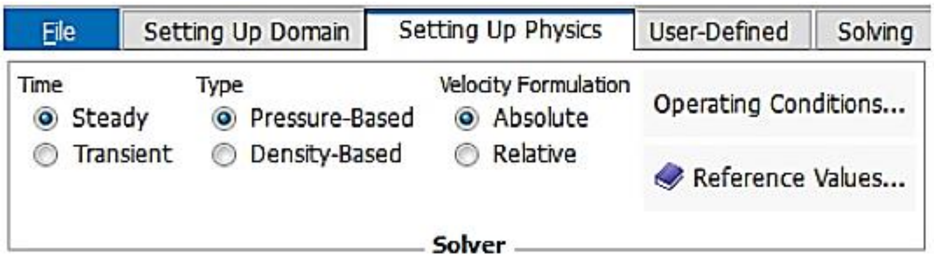

Time
● Steady
○ Transient

Type
● Pressure-Based
○ Density-Based

Velocity Formulation
● Absolute
○ Relative

Figure 5.15: Solver group of the ‘Setting Up Physics’ ribbon tab

Heat transfer was then enabled by activating the energy equation as shown in Figure 5.16, by selecting Energy (Models group). Activating the Energy equation allows temperature dependent problems to be solved. The realizable k-ε turbulence model was also enabled by clicking Viscous in the Models group of the Setting Up Physics ribbon tab and selecting k-epsilon in the Viscous Model dialog box, as shown in Figure 5.17. Turbulence modelling is a complex area. The choice of model depends on the application. For the HSPM generator, the realizable k-epsilon model was used, which is an improvement on the well-established standard k-epsilon model. The other default settings as shown in Figure 5.17 were retained. It is important to note that the Viscous…label in the ribbon is displayed in blue to indicate that the viscous model is enabled as shown in Figure 5.16.

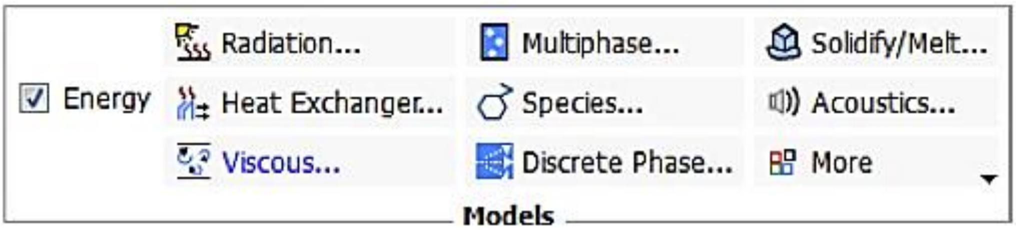

☑ Energy

Figure 5.16: Models group of the 'Setting Up Physics ' ribbon tab

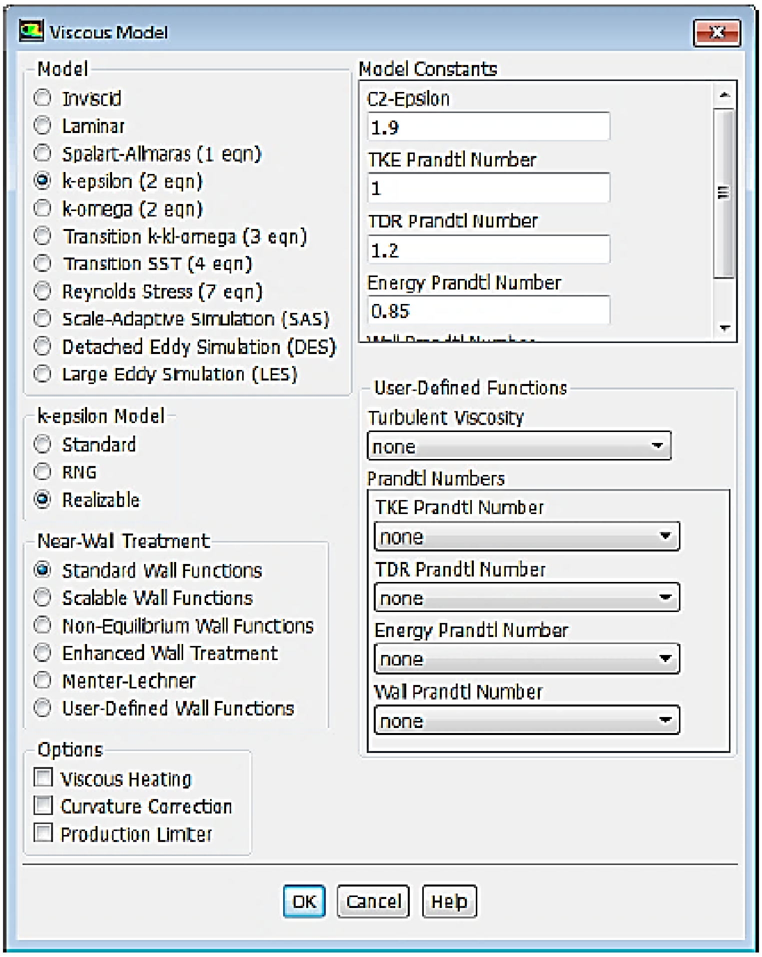

Viscous Model

Model
- ○ Inviscid
- ○ Laminar
- ○ Spalart-Allmaras (1 eqn)
- ● k-epsilon (2 eqn)
- ○ k-omega (2 eqn)
- ○ Transition k-kl-omega (3 eqn)
- ○ Transition SST (4 eqn)
- ○ Reynolds Stress (7 eqn)
- ○ Scale-Adaptive Simulation (SAS)
- ○ Detached Eddy Simulation (DES)
- ○ Large Eddy Simulation (LES)

k-epsilon Model
- ○ Standard
- ○ RNG
- ● Realizable

Near-Wall Treatment
- ● Standard Wall Functions
- ○ Scalable Wall Functions
- ○ Non-Equilibrium Wall Functions
- ○ Enhanced Wall Treatment
- ○ Menter-Lechner
- ○ User-Defined Wall Functions

Options
- ☐ Viscous Heating
- ☐ Curvature Correction
- ☐ Production Limiter

Model Constants

C2-Epsilon: 1.9

TKE Prandtl Number: 1

TDR Prandtl Number: 1.2

Energy Prandtl Number: 0.85

User-Defined Functions

Turbulent Viscosity: none

Prandtl Numbers

TKE Prandtl Number: none

TDR Prandtl Number: none

Energy Prandtl Number: none

Wall Prandtl Number: none

Figure 5.17: Fluent Viscous Model dialog box

The materials for the HSPM generator CFD simulation was set up using the Materials group of the Setting Up Physics ribbon tab as show in Figure 5.18. To create new materials, the Create/Edit Materials dialog box was used as shown in Figure 5.19 and Fluent Database was selected. In the Fluent Database Materials dialog box, as shown in Figure 5.20, the desired materials were selected from the Fluid Materials list. Since the Fluent Fluid Materials list is very long, materials can be located by using the slider bar at the right of the list by left-clicking on the slider bar to the list, typing the first letter of the desired material, and using the keyboard arrows or the mouse wheel to scroll to the required entry.

Figure 5.18:Materials group of the ‘Setting Up Physics ribbon tab

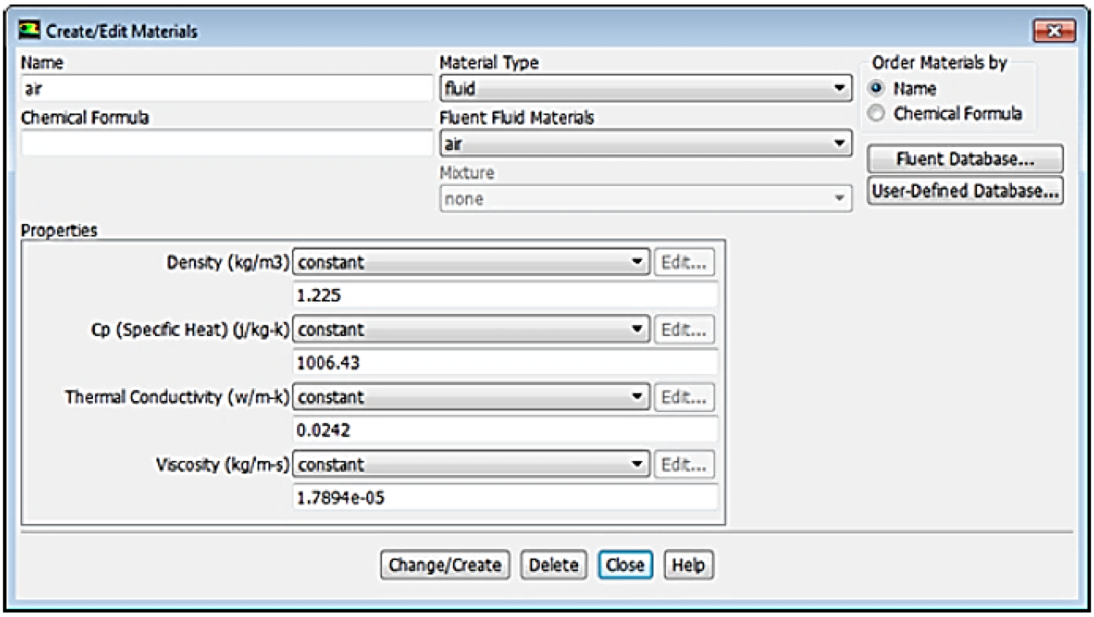

Name: air
Chemical Formula:
Material Type: fluid
Fluent Fluid Materials: air
Mixture: none
Order Materials by: ● Name ○ Chemical Formula

Properties
Density (kg/m3): constant — 1.225
Cp (Specific Heat) (j/kg-k): constant — 1006.43
Thermal Conductivity (w/m-k): constant — 0.0242
Viscosity (kg/m-s): constant — 1.7894e-05

Figure 5.19: Create/Edit Materials dialog box

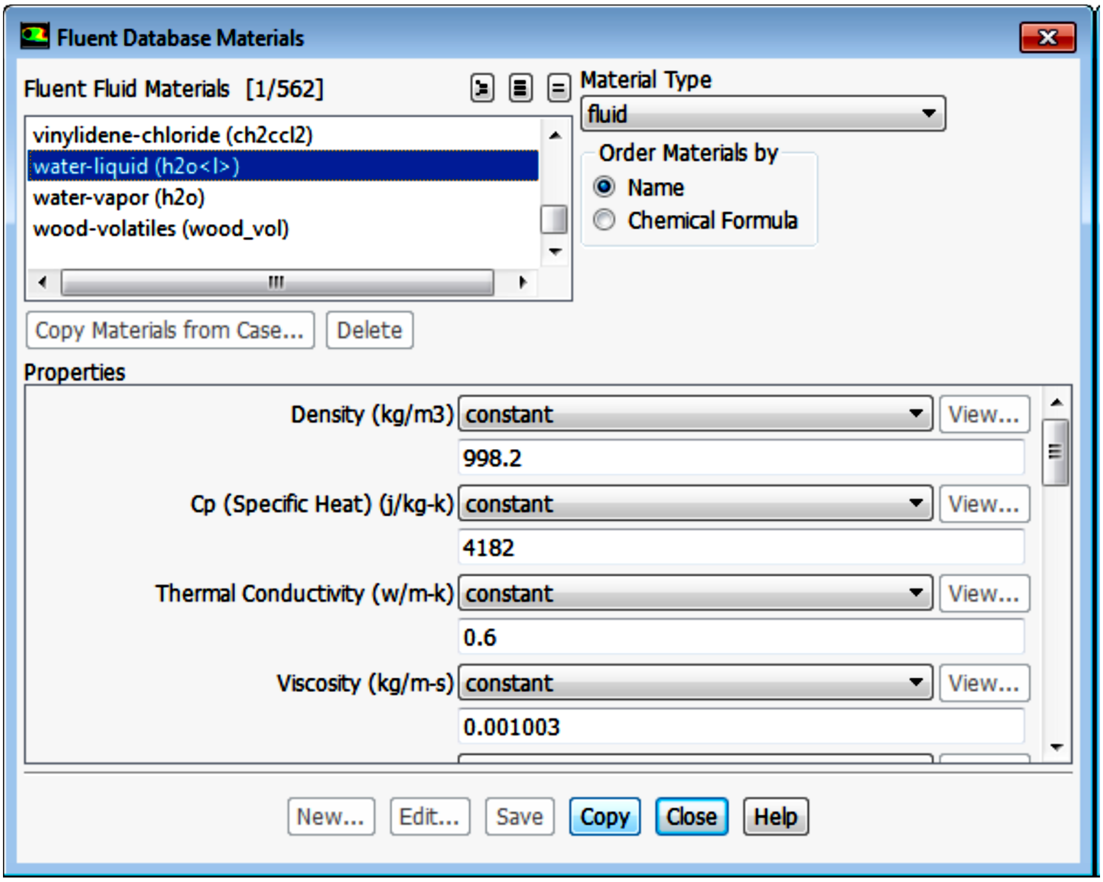

Fluent Fluid Materials [1/562]
vinylidene-chloride (ch2ccl2)
water-liquid (h2o<l>)
water-vapor (h2o)
wood-volatiles (wood_vol)

Material Type: fluid
Order Materials by: ● Name ○ Chemical Formula

Properties
Density (kg/m3): constant — 998.2
Cp (Specific Heat) (j/kg-k): constant — 4182
Thermal Conductivity (w/m-k): constant — 0.6
Viscosity (kg/m-s): constant — 0.001003

Figure 5.20: Fluent database Materials dialog box

The next step was to set up the cell zone conditions for the CFD simulation using the Zones group of the Setting Up Physics ribbon tab as shown in Figure 5.21. The cell zone conditions for the fluid zone was set by selecting fluid in the zone list of the Cell

Zone Conditions task page shown in Figure 5.22. In the Fluid dialog box, the desired material name can be selected from the Material Name drop-down list.

Figure 5.21: Zones group of the Setting Up Physics ribbon tab

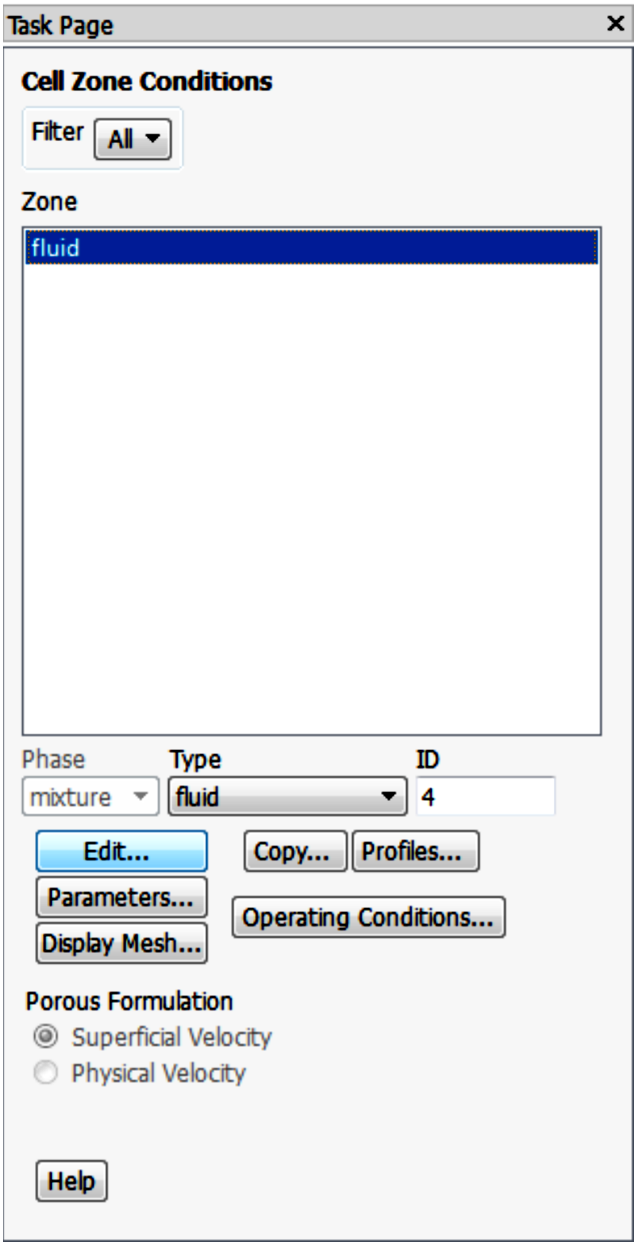

Cell Zone Conditions

Filter: All

Zone: fluid

Phase: mixture
Type: fluid
ID: 4

Porous Formulation
● Superficial Velocity
○ Physical Velocity

Figure 5.22: Cell Zone Conditions task page

The boundary conditions of the HSPM generator CFD analysis was set up using the Zones group of the Setting Up Physics ribbon tab, shown in Figure 5.21. In the boundary conditions task page any or all of the required zones can be selected, and the velocity inlet dialog box was opened by clicking on Edit…, as shown in Figure 5.23. In the Velocity Inlet dialog box, the Magnitude, Normal to Boundary was selected for the Velocity Specification Method. The Velocity Magnitude was also specified at no flow and maximum flow. Furthermore, Intensity and Hydraulic Diameter was selected from the Specification Method drop-down list in the Turbulence group. Inlet flows bring turbulence with them. The quantities depend on the upstream conditions, so they are user inputs. For flow in pipes, turbulent intensity is typically 5 to 10%. The length-scale of the turbulence can be deducted from the pipe diameter. For HSPM generator simulation, the Turbulent Intensity was retained at its default of 5% and the hydraulic diameter was also entered as shown in Figure 5.24. The hydraulic diameter D_h is defined as

$$D_h = \frac{4A}{P_w} \qquad (5.7)$$

Where A is the cross-sectional area and P_w is the wetted perimeter.

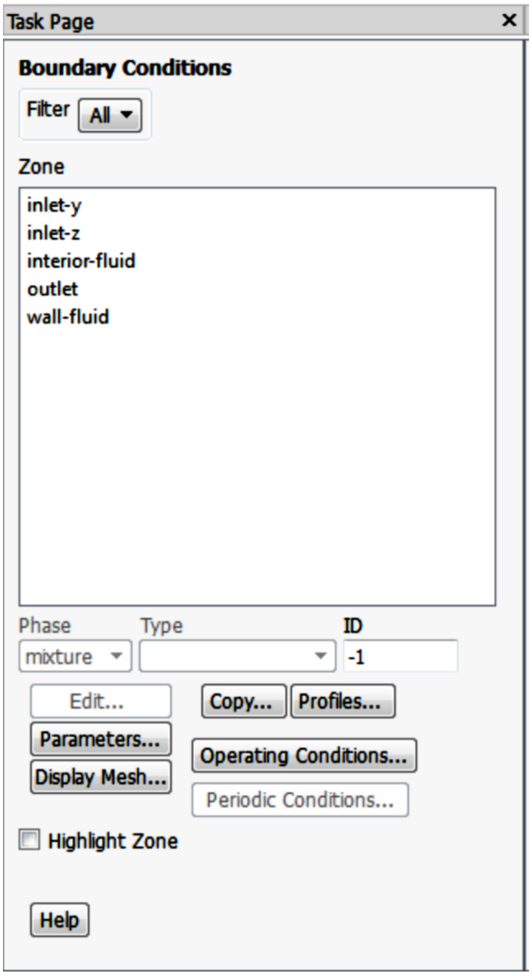

Task Page

Boundary Conditions

Filter: All

Zone

inlet-y
inlet-z
interior-fluid
outlet
wall-fluid

Phase: mixture

Type:

ID: -1

Figure 5.23: Fluent Boundary Conditions task page

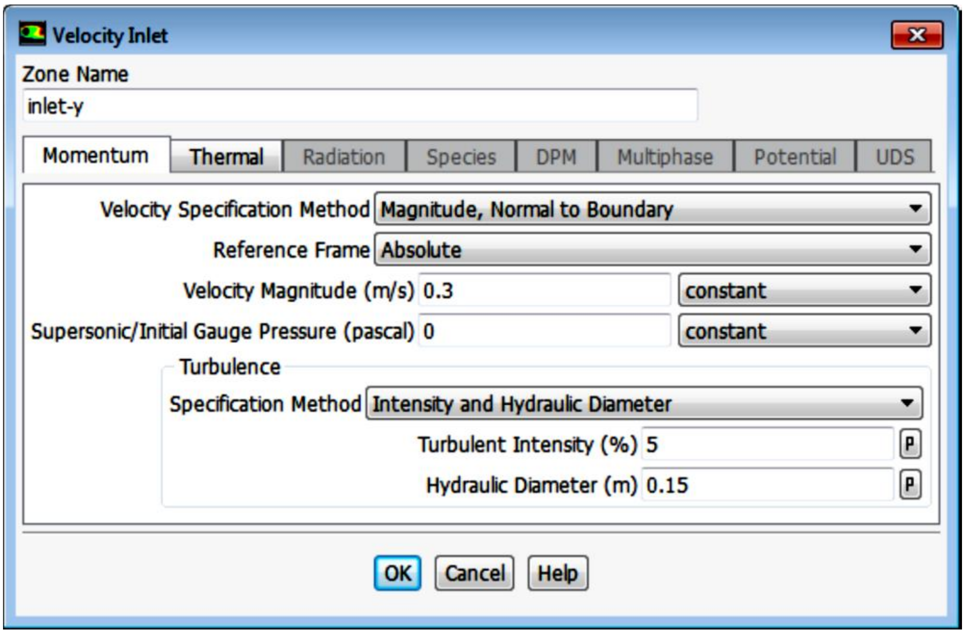

Zone Name: inlet-y

Velocity Specification Method: Magnitude, Normal to Boundary

Reference Frame: Absolute

Velocity Magnitude (m/s): 0.3 constant

Supersonic/Initial Gauge Pressure (pascal): 0 constant

Specification Method: Intensity and Hydraulic Diameter

Turbulent Intensity (%): 5

Hydraulic Diameter (m): 0.15

Figure 5.24: Velocity inlet dialog box

The inlet temperature was then specified by opening the Thermal tab in the Velocity Inlet dialog box. In the analysis of the HSPM generator many of the options are left to default settings as they are not relevant to this particular type of analysis. The same process is followed for the other inlets as well as the outlets of the cooling jackets of the HSPM generator. It is possible that during the solution process, material may flow back into the domain through an outlet boundary. This could either be a genuine feature of the flow, or just a short-lived state reached during the convergence process. Either way, ANSYS Fluent needs to know realistic conditions at this boundary. ANSYS Fluent will use the backflow conditions only if the fluid is flowing into the computational domain through the outlet. Since backflow might occur at some point during the solution procedure, a reasonable backflow condition needs to be set as shown in Figure 5.25 to prevent the convergence from being adversely affected. If, the converged model has flow leaving only at the outlet boundary, then these values are not used and do not affect the final answer. For the HSPM generator analysis, the analysis was selected such that flow enters the model only at well-defined inlets, with no backflow occurring.

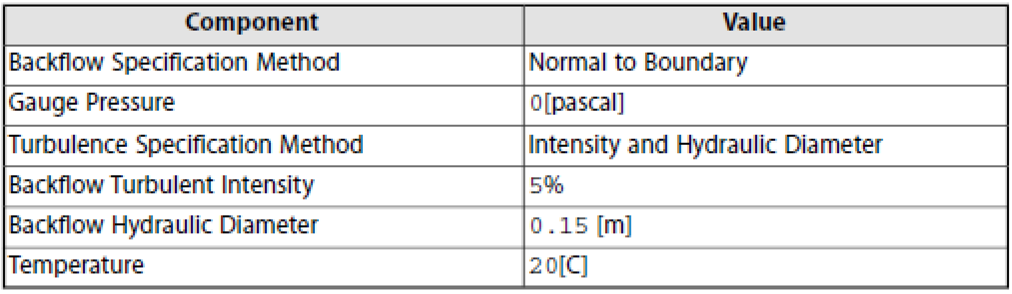

Component	Value
Backflow Specification Method	Normal to Boundary
Gauge Pressure	0[pascal]
Turbulence Specification Method	Intensity and Hydraulic Diameter
Backflow Turbulent Intensity	5%
Backflow Hydraulic Diameter	0.15 [m]
Temperature	20[C]

Figure 5.25:Set up for backflow conditions

The result of the heat distribution of the HSPM generator at varying speeds, which was generated using the ANSYS software is shown in the Figures below. Figure 5.26 shows the sectioned isometric view of the thermal behaviour of the HSPM Generator, this figure shows the general layout of the generated temperature results. The temperature bar is located on the left from maximum (Max) temperature to minimum (Min) temperature at the top and bottom of the bar, respectively. The sectioned model showing the temperature distribution is located at the centre. The Max temperature of the HSPM generator is generally developed at the rotor and stator interface and the Min temperature is at the housing where forced convection takes place in the cooling jackets. The temperature distribution for the HSPM generator at varying speeds is shown in Figure 5.27 to Figure 5.38. The Min temperature for the analysis of the HSPM generator at maximum coolant flowrate was maintained at 53°C and for no coolant flowrate condition it was maintained at 69°C.

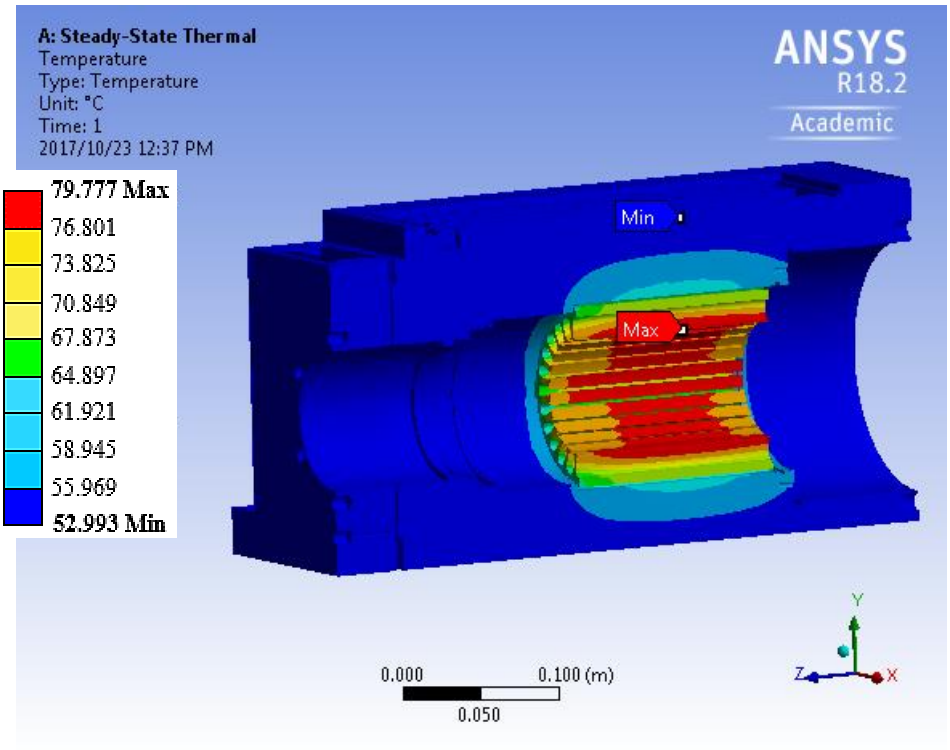

Figure 5.26: Sectioned Isometric View of the Thermal Behaviour of the HSPM Generator

In Figure 5.27, the Max temperature was 76 °C, while the Min temperature was 53 °C. The Max temperature is located at the rotor and stator interface as previously stated. The Max temperature recorded for the rest of the analysis, 5000 RPM, 10000 RPM, 15000 RPM, 20000 RPM, and 25000 RPM was 78 °C, 79 °C, 88 °C, and 93 °C, respectively. Figure 5.33 to Figure 5.38, shows the temperature distribution at no flowrate, which includes the Max and Min temperatures at varying speeds of the HSPM generator. The Max temperatures recorded for this condition, from 3000 RPM to 25000 RPM, was 92 °C, 94 °C, 102 °C, 104 °C, and 108 °C, respectively.

Hot spots are a result of the heat generated by the rotor-stator configuration as well as the reduced housing thickness for allowance of the stator. Furthermore, shown in Figure 5.27 to 5.38 are the hot spots marked in red for both the maximum and no flow flowrates which have similar temperature distribution patterns. The reason for the similarity in patterns is that the cooling jacket design/configuration was not changed, it is only the coolant flowrates that were changed, which is evident in the temperature values recorded. While there are still hotspots in the maximum flow condition, the temperatures recorded for these are significantly lower for this condition than in the no flow rate condition (The difference at 25000 RPM is 108°C minus 93°C, which is a 15°C difference). a Flowrate of 3.5 m3/hr reduces the recorded temperature of the hotspots by 15 deg due to the design of the cooling jacket which specifically targets the hotspot areas as shown in section 4.6, in Figure 4.23. Thus, the hotspot temperature is significantly reduced as a result of the cooling jacket configuration and the increased velocity coolant velocity (3.5 m3/hr). Utilizing the theory of heat transfer, forced convection and the finding in Section 4.13, Figure 4.36, maximizing the coolant flowrate was leveraged to reduce the hotspot temperature developed at the rotor-stator interface/configuration.

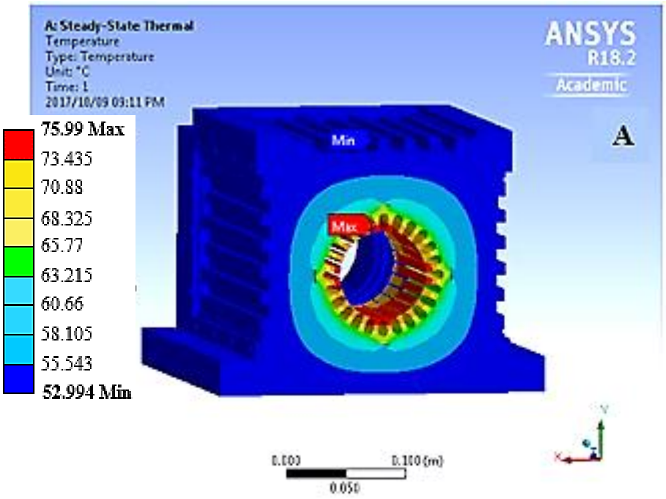

Figure 5.27: Thermal Behaviour of the HSPM Generator at 3000 RPM, at max flow

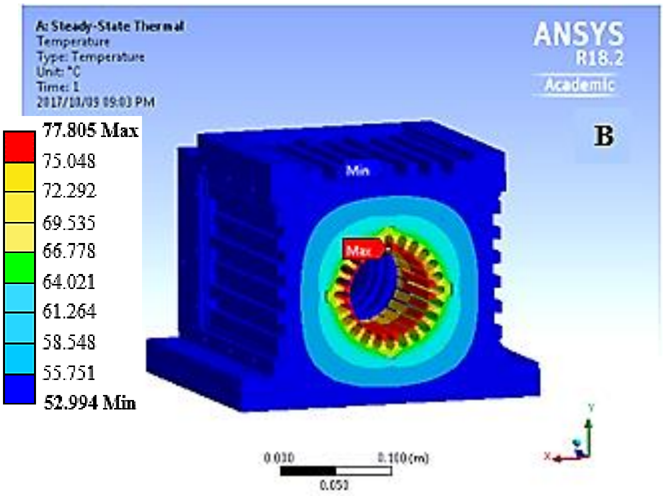

Figure 5.28: Thermal Behaviour of the HSPM Generator at 5000 RPM, at max flow

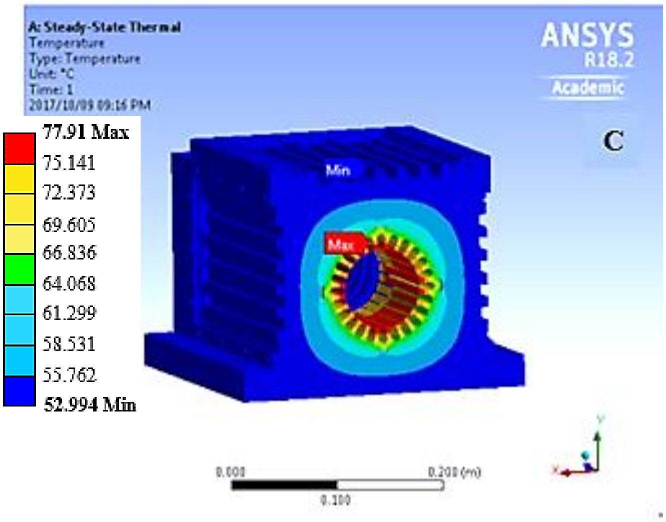

Figure 5.29: Thermal Behaviour of the HSPM Generator at 10000 RPM, at max flow

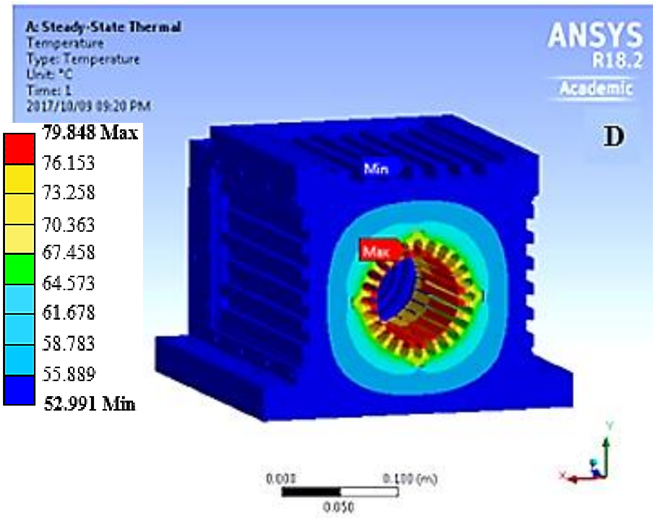

Figure 5.30: Thermal Behaviour of the HSPM Generator at 15000 RPM, at max flow

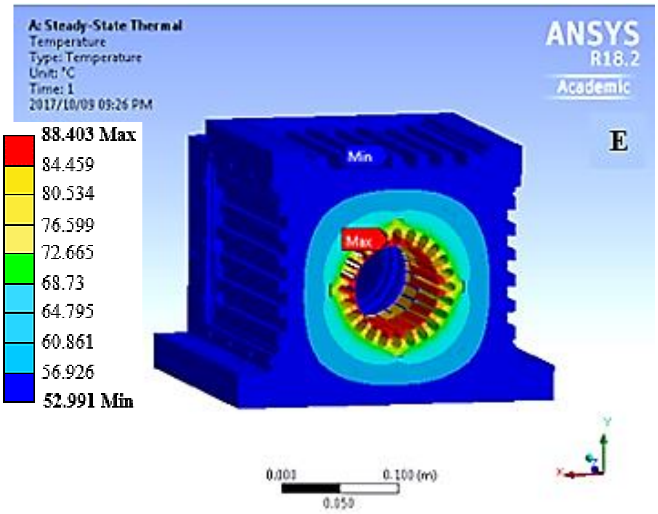

Figure 5.31: Thermal Behaviour of the HSPM Generator at 20000 RPM, at max flow

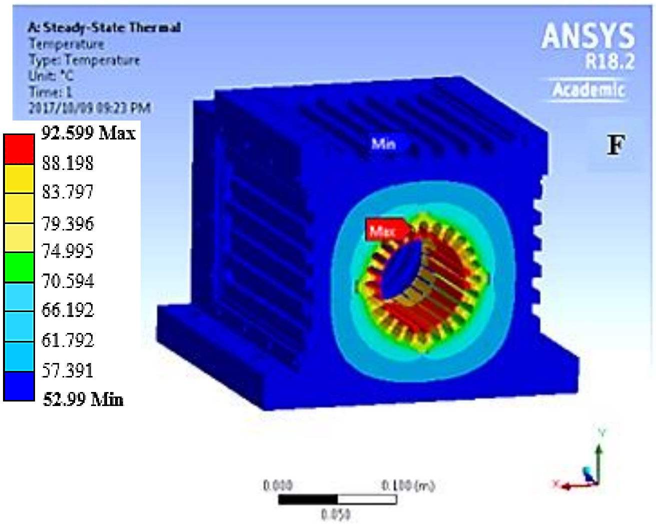

Figure 5.32: Thermal Behaviour of the HSPM Generator at 25000 RPM, at max flow

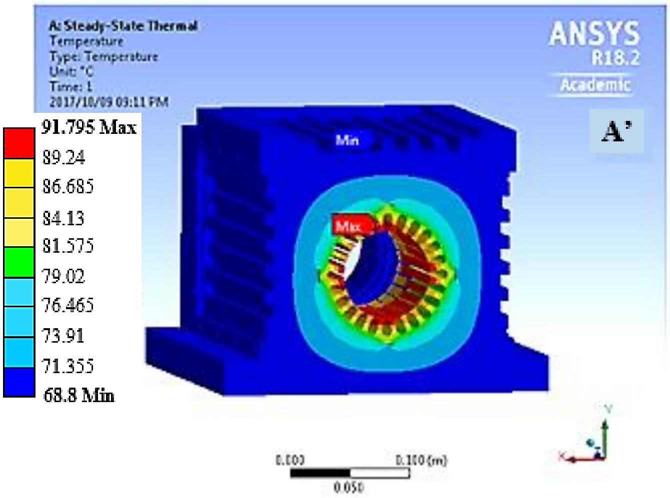

Figure 5.33: Thermal Behaviour of the HSPM Generator at 3000 RPM, at no flow

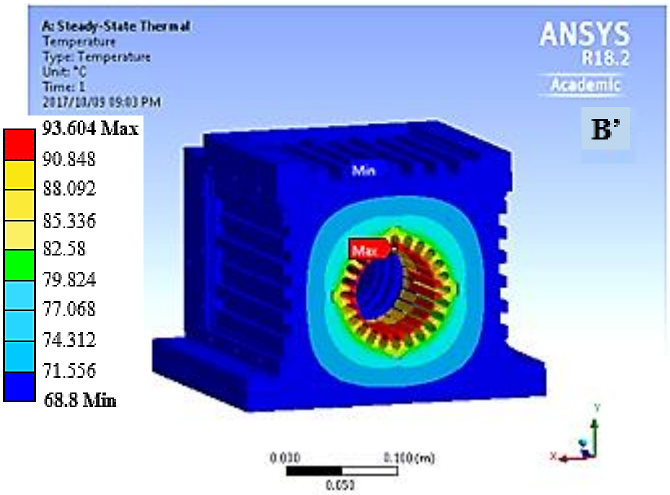

Figure 5.34: Thermal Behaviour of the HSPM Generator at 5000 RPM, at no flow

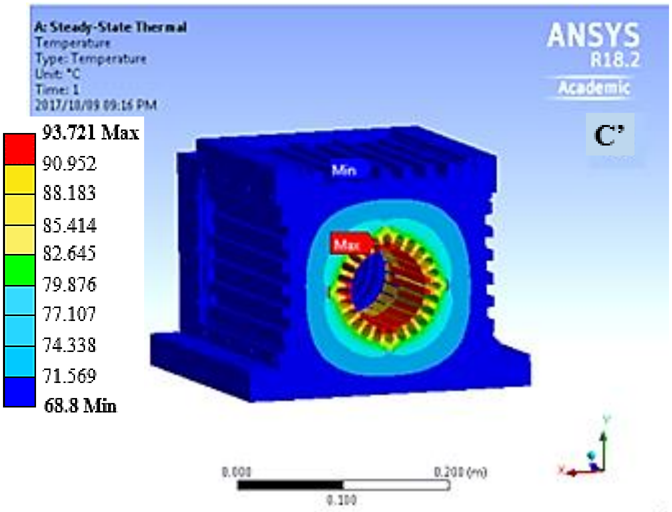

Figure 5.35: Thermal Behaviour of the HSPM Generator at 10000 RPM, at no flow

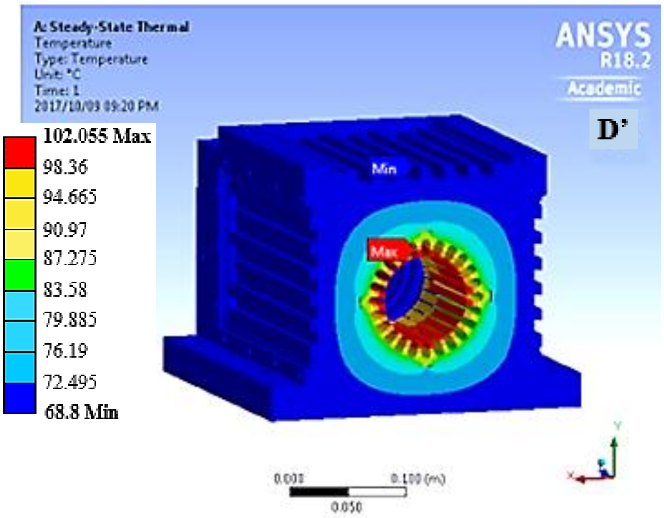

Figure 5.36: Thermal Behaviour of the HSPM Generator at 15000 RPM, at no flow

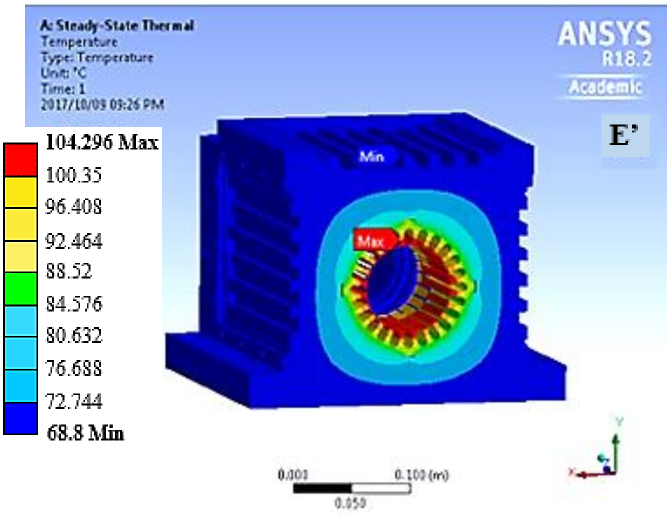

Figure 5.37: Thermal Behaviour of the HSPM Generator at 20000 RPM, at no flow

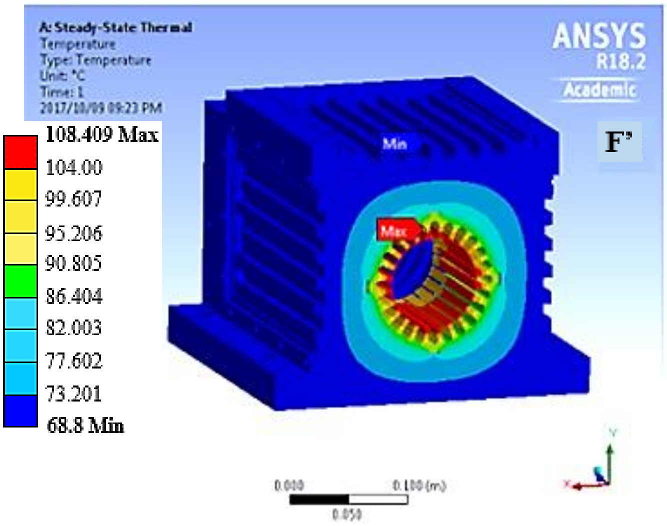

Figure 5.38: Thermal Behaviour of the HSPM Generator at 25000 RPM, at no flow

Chapter 6

EXPERIMENTAL RESULTS AND DISCUSSSION

6.1 Test Setup

An overview of the experimental test setup is given in Figure 6.1. As can be seen from the figure, an aircraft motor was used to drive the HSPM generator, with a limiting speed of 10000 RPM. The aircraft motor used is supplied with air from a blower which regulates the temperature rise in the aircraft motor. A water chiller is used to pump the water throughout the cooling jackets of the HSPM generator. An inlet and outlet manifold are used to channel the flow of the coolant between the HSPM generator and the chiller into the inlets and outlets of each cooling jacket. The cooling jackets of the HSPM generator, regulates the temperature rise of the generator. An oil-air mist lubrication unit (Supplied by Producut) is used to lubricate the drive and non-drive end bearings of the HSPM generator. The oil-air mist lubrication unit utilizes a specially designed mixing valve and performs cooling of the bearings through intermittent feeding of 0.03~0.05 cc of VG68 oil every 8 minutes into a stream of compressed air from the compressor. During the experiment the temperature at the front (drive end) and rear bearing (non-drive end) as well as in different locations of the winding and stator core were measured. Thermocouples were used to record the temperature readings and recorded on a data logger, which was connected to a computer. DeweSoft, a leading provider of high-end data acquisition hardware, software and provides total test and measurement solutions is used for the vibration test of the HSPM generator at different speeds.

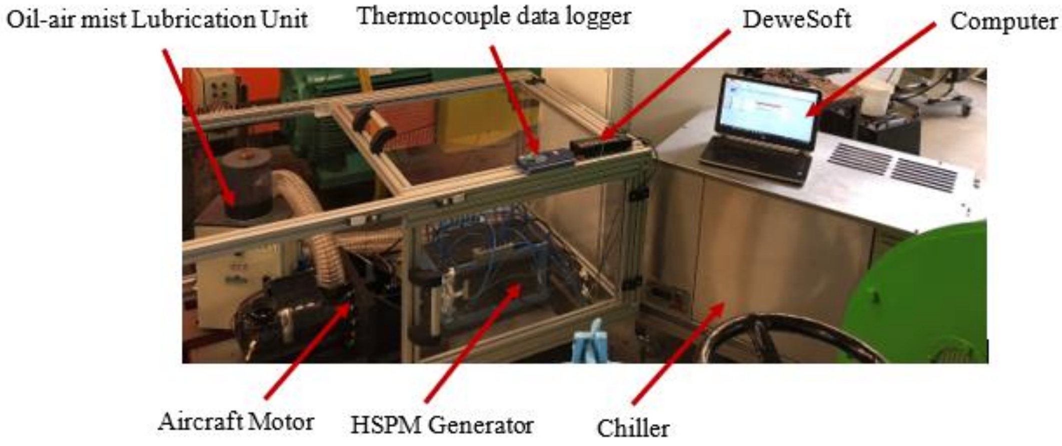

Figure 6.1: Overview of the experimental setup in the lab

Table O: Description of data acquisition equipment

Equipment	Description
Thermocouple data logger	PICO, TC-08
DeweSoft data acquisition	
Computer	HP Pavilion 15 Notebook PC

6.2 Procedure and data acquisition

The HSPM generator was designed to operate at 30000 RPM and deliver a power output of 10 kW. However, due to the speed limitation and temperature rise of the aircraft motor, testing on the HSPM generator was limited to 10000 RPM.

There were two tests that were performed on the HSPM generator. The first test was the vibration test and the second test performed was the Temperature (heat generation and effect of coolant flowrate) test. The tests were conducted at different speeds and for the temperature test only two coolant flowrates were considered which were no coolant flow and maximum coolant flow. This was due to the limitation presented by the ball valve to accurately adjust the flowrate of the coolant at each speed.

6.2.1 Vibration Test Procedure

As first step of each measurement, the setup shown in Figure 6.2 was used. The accelerometer was placed on the housing of the HSPM generator in line with the front bearing as shown in Figure 6.3. The oil-air mist lubrication unit and the chiller were switched on for the lubrication of the front and rear bearings and cooling of the HSPM generator, respectively. 2 minutes after the oil-air mist lubrication unit and chiller were switched on, the HSPM generator starts up. The Dewe Software on the computer was opened and the HSPM generator speed was adjusted to the desired speed. The Dewe Software recorded readings for 12 seconds for the different speeds ranging from 3000 RPM to 10000 RPM. The data was then analysed.

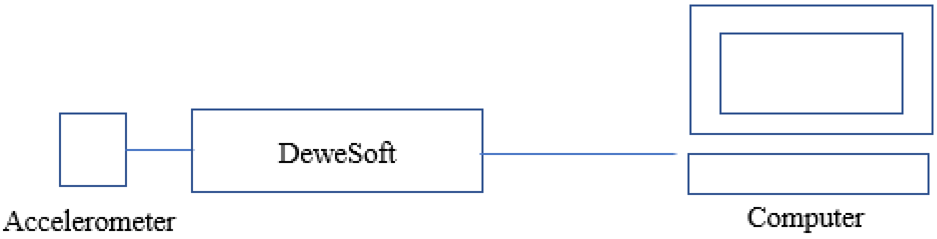

Figure 6.2: Vibration Test Set up

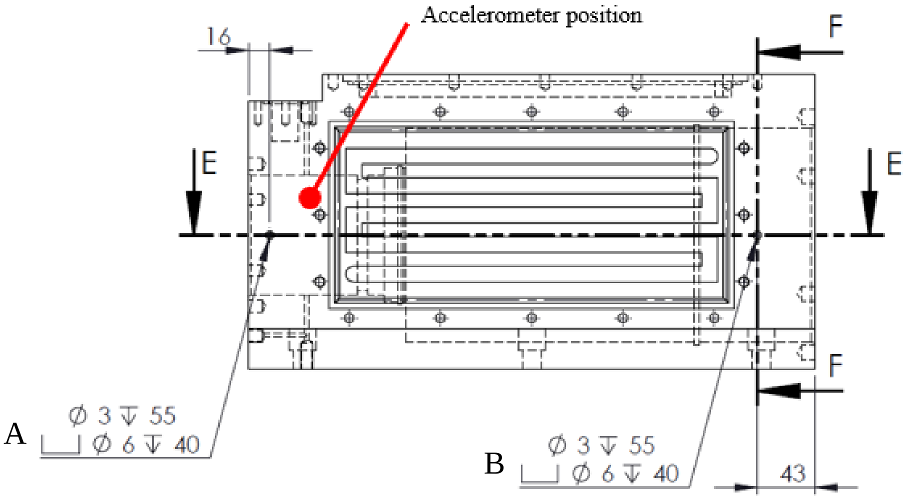

Figure 6.3: Accelerometer position on the housing of the HSPM generator

6.2.2 Temperature Test Procedure

As first step of each measurement, the setup shown in Figure 6.4 was used. The Thermocouples were inserted in the holes A and B located on the housing of the HSPM generator, in line with the front and rear bearings as shown in Figure 6.3. The other thermocouples were placed on the stator core outer surface and end windings, located in coil number 17, 19, and 21 as shown in Figure 6.5 by the manufacturer. The oil-air mist lubrication unit and the chiller were switched on for the lubrication of the front and rear bearings and cooling of the HSPM generator, respectively. 2 minutes after the oil-air mist lubrication unit and chiller were switched on, the HSPM generator starts up. The Pico TC-08 thermocouple data logger was used to capture the temperature readings of the HSPM generator at different speeds ranging from 3000 RPM to 10000RPM. Two sets of temperature readings were recorded, the first set considered no coolant flow and the second set considered maximum coolant flow.

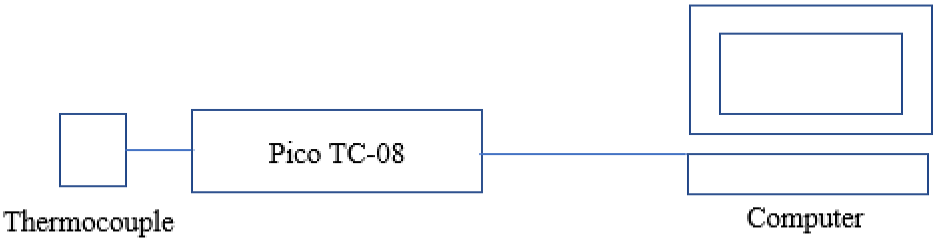

Figure 6.4: Temperature Test Setup

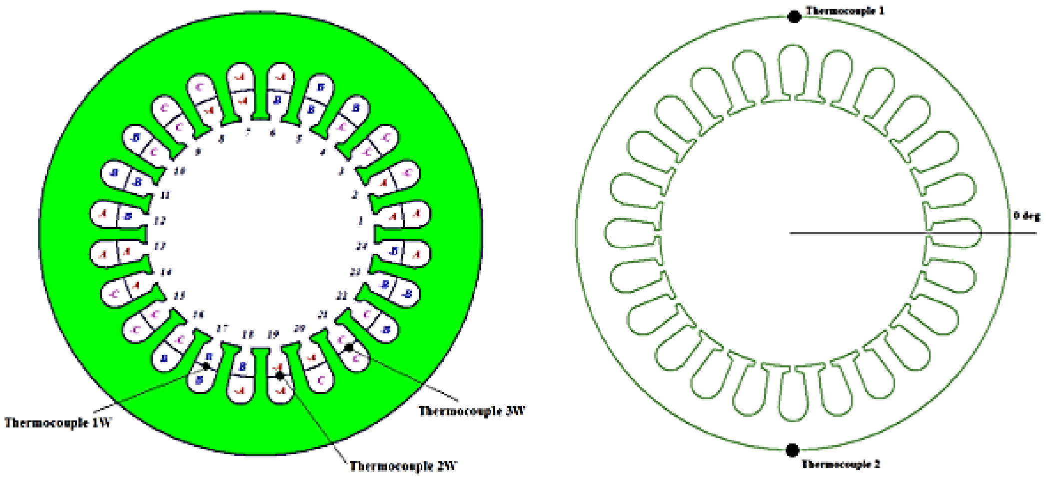

Figure 6.5: Thermocouple position on the stator core outer surface and end windings

This section presents the HSPM generator results from the vibration test and temperature test performed up to 8000 RPM. Testing was limited to a third of the rated speed due to the limitations presented earlier in Section 1.5.2, which outlines the test setup and its limitations.

6.3 Vibration Test

The vibration test was conducted to ensure that the HSPM generator was still acceptable to operate at elevated speeds. The vibration test was conducted from 3000 RPM to 8000 RPM using DeweSoft to analyse the data. The next section explains how the data was analysed and finally presents the data from the tests.

6.3.1 Vibration Test Data Analysis

DeweSoft interface was used to record the data as shown in Figure 6.6. The data was analysed by manipulating the two white vertical lines and the yellow vertical line to zoom into the data as shown in Figure 6.7. The average of three readings were taken, each reading is the summation of the peak and trough as shown in Figure 6.8, for all the speeds from 1000 RPM to approximately 8000 RPM.

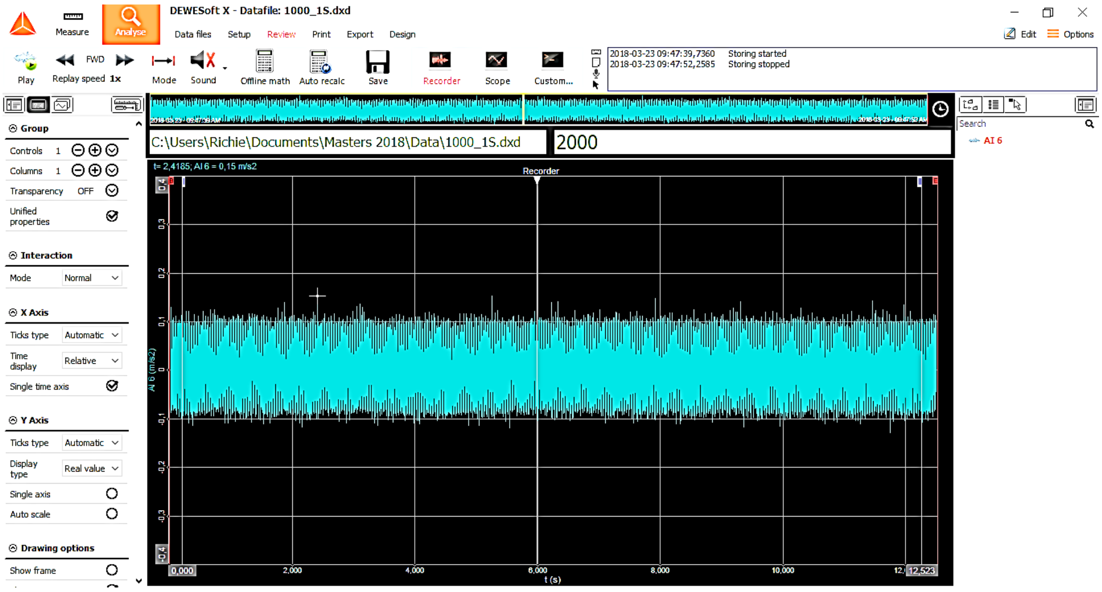

2018-03-23 09:47:39,7360 Storing started
2018-03-23 09:47:52,2585 Storing stopped

C:\Users\Richie\Documents\Masters 2018\Data\1000_1S.dxd

2000

t= 2,4185; AI 6 = 0,15 m/s2

Group
Controls 1
Columns 1
Transparency OFF
Unified properties ☑

Interaction
Mode Normal

X Axis
Ticks type Automatic
Time display Relative
Single time axis ☑

Y Axis
Ticks type Automatic
Display type Real value
Single axis ○
Auto scale ○

Drawing options
Show frame ○

Figure 6.6: DeweSoft interface used to record and analyse the vibration test data

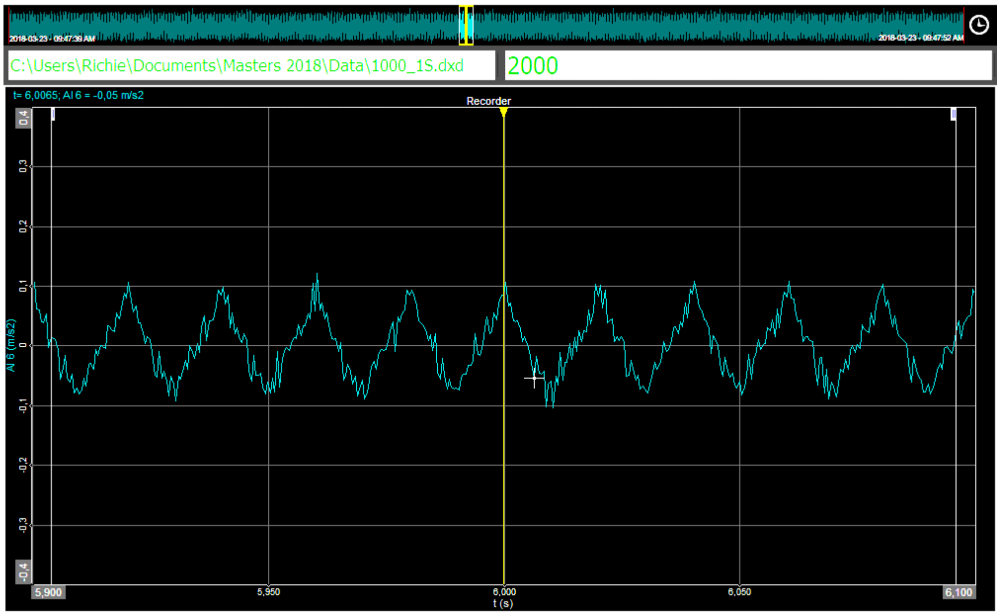

C:\Users\Richie\Documents\Masters 2018\Data\1000_1S.dxd

2000

t= 6,0065; AI 6 = -0,05 m/s2

Figure 6.7: Zoomed-in data analysis

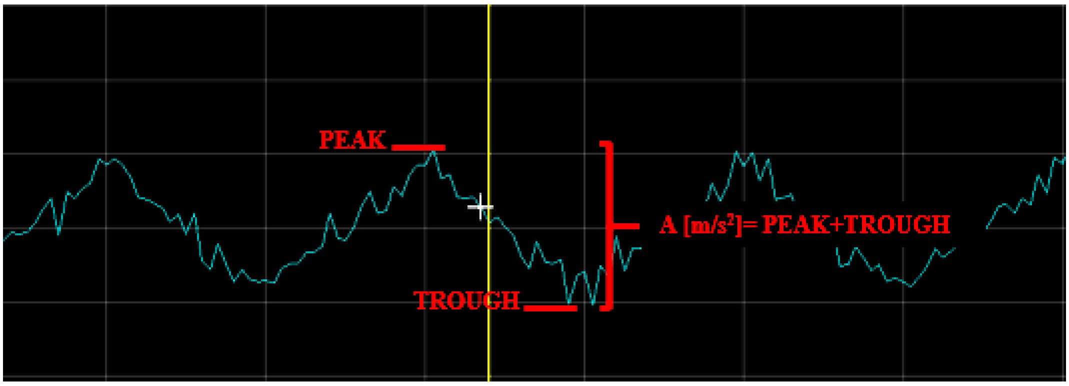

Figure 6.8: Total acceleration reading for the vibration test

6.3.2 Vibration Results

The averaged values of the vibration test were plotted against the speed of the HSPM generator. This test was used to best understand the integrity of the machine with increasing speed, based on the vibrations generated. The vibration data was compared to the vibration reading of the high speed milling machine situated at UCT's Advanced Manufacturing Lab in the Mechanical Engineering Department. The vibration reading of the high speed milling machine was found to be greater than 1 m/s^2, operating at 3000 RPM. Furthermore, the acceptable vibration for motors by General Motors [96] and Welkon [97] was found to be 0.35 g's, which is approximately 3.4 m/s^2 (1 g = 9.80665 m/s^2), and 3.5 m/s^2, respectively. Thus, the vibration of the HSPM was deemed to be satisfactory from 1000-8990 RPM to proceed with the temperature tests.

The results of the vibration test are shown in Figure 6.9. As the speed of the HSPM generator increases the vibration measured also increases. This could be due to a low precision of rotor balancing, resulting in a higher runout.

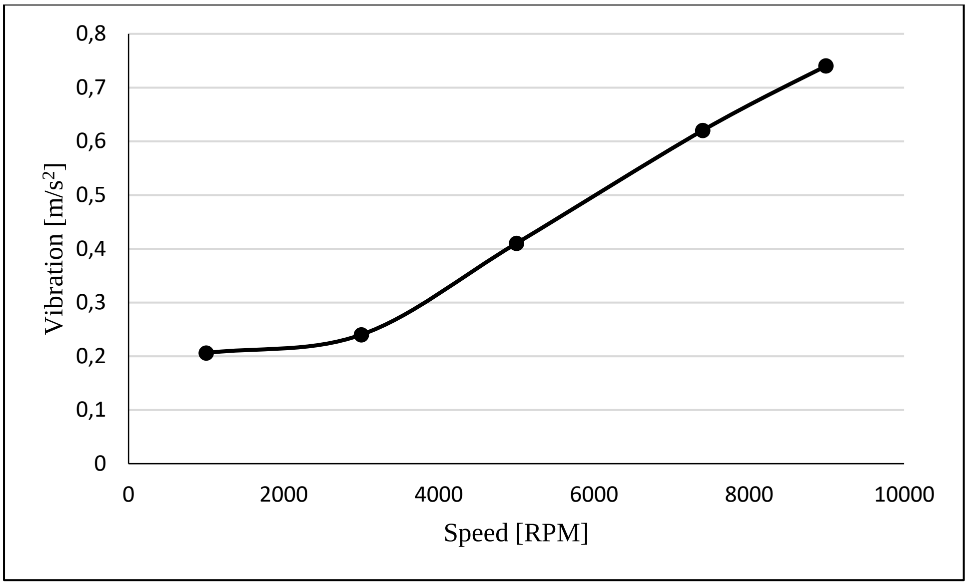

Figure 6.9: Vibration test data at varying speeds of the HSPM generator

6.4 Temperature Test

The Temperature test was conducted after the vibration test. The temperature test measures the effect of the coolant velocity on the cooling of the HSPM generator. The Temperature test was limited to two flowrates, no flow and maximum flowrate. This was conducted from 3000 RPM to approximately 8000 RPM. The data was collected using the PICO TC-08 thermocouple data logger. The next section explains how the data was analysed and finally presents the data from the tests.

6.4.1 Temperature Test Data Analysis

The PICO TC-08 thermocouple data logger was used to record the data as shown in Figure 6.10. The thermocouples are inserted into the slots (1-8) on the data logger and these slots correspond to the selected thermocouple which can be easily read off the PLW recorder on any PC once the freeware has been installed. To keep consistency in the recorded values a waiting period of 2 minutes was employed for the Temperature readings to stabilize for all the speeds from 3000 RPM to approximately 8000 RPM.

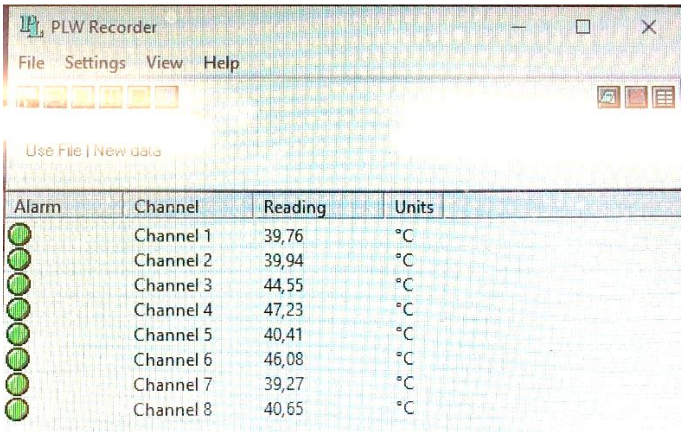

Alarm	Channel	Reading	Units
●	Channel 1	39,76	°C
●	Channel 2	39,94	°C
●	Channel 3	44,55	°C
●	Channel 4	47,23	°C
●	Channel 5	40,41	°C
●	Channel 6	46,08	°C
●	Channel 7	39,27	°C
●	Channel 8	40,65	°C

Figure 6.10: PICO TC-08 data logger, PLW recorder

6.4.2 Temperature Results

The recorded temperature readings of the HSPM generator housing located near the front and rear bearings were plotted against the speed of the HSPM generator. Figure 6.11 shows the temperature comparison of the housing located at the front and rear bearings when there is no flow of the coolant through the cooling jacket. T1, represents the location of the front bearing and T2, the location of the rear bearing. In Figure 6.11, as the rotor speed of the HSPM generator increases the housing temperature also increases. The logarithmic trendline is also plotted for T1 and T2. It can be seen that while T1 and T2 have a similar shape, the temperature readings recorded for T1 are higher than that of T2. Figure 6.12 shows the temperature comparison of the housing located at the front and rear bearings when there is maximum flow of the coolant through the cooling jacket. In Figure 6.12, the logarithmic trendline is also plotted for T1 and T2, and the housing temperature also increases with increasing rotor speed. Temperature, T1 is also higher than T2, and the temperature difference between, T1 and T2 is much bigger compared to Figure 6.11. This trend is seen in both cases when there is no flowrate and when there is maximum coolant flow and the reason for this is because the front bearing is located at the driving end, where the HSPM generator is coupled to the aircraft motor and because of the high torque and forces experienced by the front bearing more heat is generated. The rear bearing is located at the non-drive end and does not experience excess forces resulting in lower heat generated.

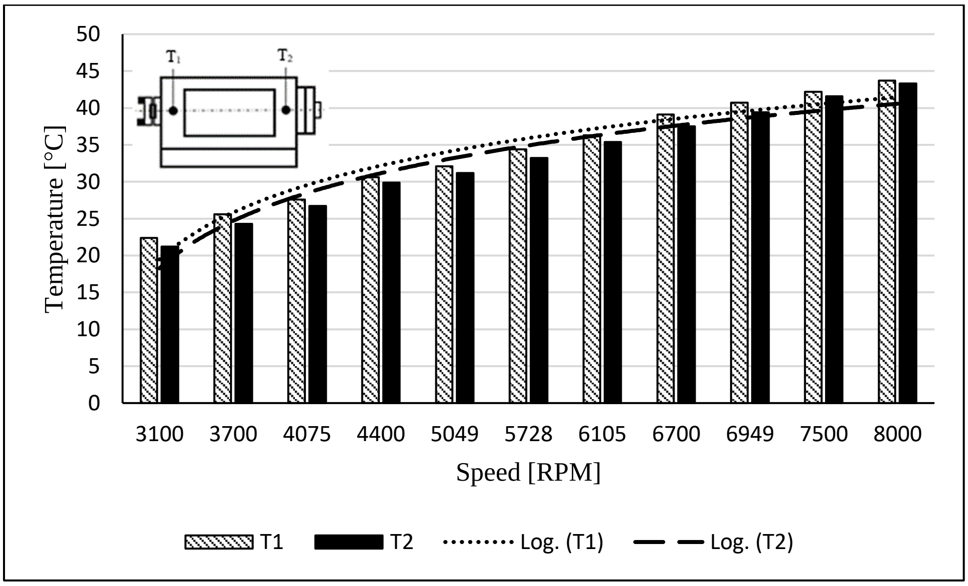

Figure 6.11: Temperature comparison of front and rear bearings at no coolant flowrate

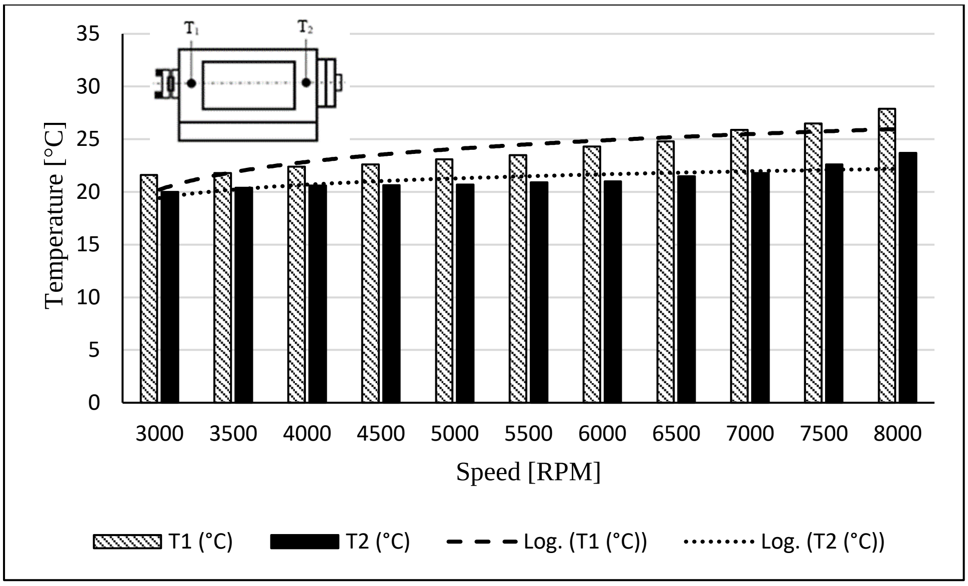

Figure 6.12: Temperature comparison of front and rear bearing at maximum flowrate

Figure 6.13 shows the temperature comparison of the housing located at the front bearing when there is no coolant flow and at maximum flow through the cooling jacket. In Figure 6.13, the general trend of the housing temperature located at the front bearing increases, at no coolant flow and maximum coolant flow, as the rotor speed of the HSPM generator increases from approximately 3000 RPM to 8000 RPM. However, at maximum coolant flow, the housing temperatures at the front bearing are significantly lower than when there is no coolant flow in the cooling jackets. In Figure 6.14 the housing temperature located at the rear bearing also increases as the rotor speed increases for both cases of no coolant flow and maximum coolant flow through the cooling jackets. In Figure 6.14 it is also observed that the temperature readings recorded when the HSPM generator operates with maximum coolant flow through the cooling jackets is drastically lower than when there is no coolant flow. This trend is clearly visible in both cases, The HSPM generator experiences lower housing temperatures when maximum coolant flowrate is employed through the cooling jackets. This agrees with the theory of heat transfer, forced convection and the analytical calculations done in Section 3.13, ‘coolant flow rate on heat transfer characteristics of the HSPM generator’, which showed that as the coolant flowrate increases, the convection heat transfer coefficient also increases, shown in Figure 4.36. This results in more heat removed from the HSPM generator. Furthermore, since the experimental tests were performed up to a speed of 8000 RPM, comparison with the ANSYS simulations conducted was done at 10000 RPM for both the maximum flow and no flow conditions and the difference in the temperature generated at position T1, as shown in Figure 6.13 was, 68.8°C – 52.99°C, approximately 16°C. The experimental results validate these findings since the experimental temperature difference was found to be, 43.7°C -27.9°C, approximately 16°C at 8000 RPM taken at position T1. The ANSYS simulation temperatures are higher than those of the experimental temperatures due the different speeds that were considered for the simulation and temperature experimental tests, 10000 RPM and 8000 RPM, respectively. This is consistent with the trendlines in Figure 6.13 and Figure 6.14, which shows that temperature increases with increasing rotor speed.

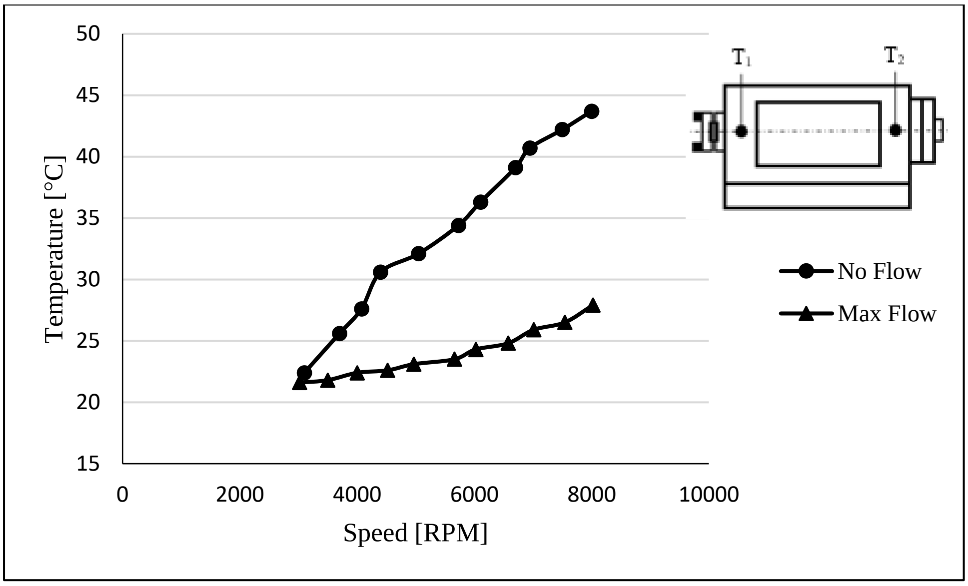

Figure 6.13: Temperature comparison of front bearing at No flow and maximum flow

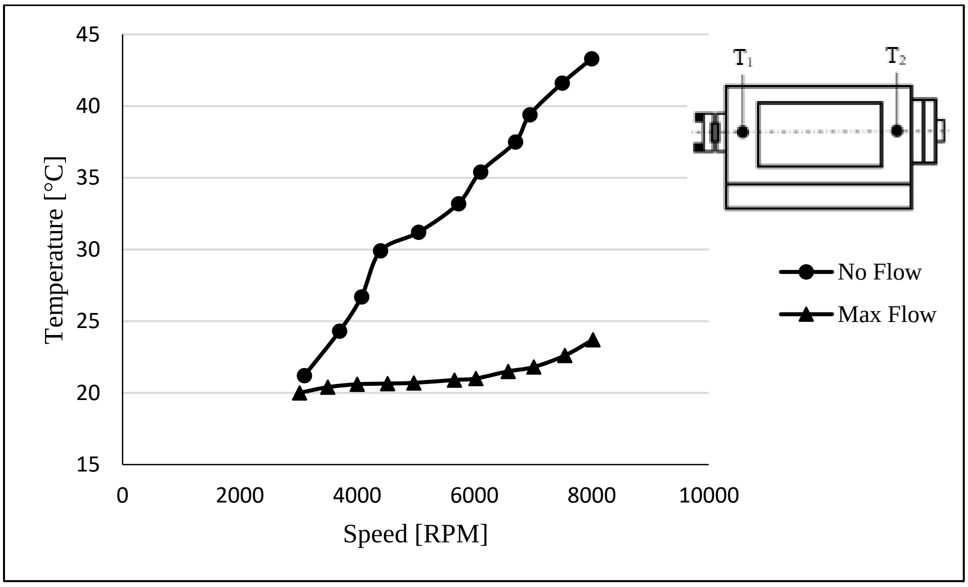

Figure 6.14: Temperature comparison of rear bearing at no flow and maximum flow

Chapter 7

CONCLUSIONS AND RECOMMENDATIONS

7.1 Conclusions

This dissertation discussed the design of the HSPM generator and the effect of the coolant velocity to enhance the machine performance through analytical and numerical simulations done through ANSYS.

Based on the findings of this dissertation, the following conclusions are deduced:

7.1.1 The development of the HSPM generator has seen an advancement in several research areas related to the design and development of the generator. This was due to the specifications presented for the HSPM generator such as high operational frequencies, which exposed the generator to various mechanical constraints. Thus, research that has been spear-headed by the design and development of the HSPM generator is in bearing cooling technology, coolant cooling methods, and optimization of the cooling jackets through analytical calculations and Numerical analysis.

7.1.2 In this thesis, a study on the role of oil-air mist lubrication on the HSPM generator was conducted. Idle power analysis using the theory of hydraulics and thermal analysis using ANSYS Maxwell simulation study confirms the severity of thermal damage and associated power losses. Furthermore, the ANSYS mechanical thermal steady state makes it possible to determine the temperature distribution of the high speed of the HSPM generator, given a set of boundary conditions which was imported from Maxwell. The HSPM generator was designed and developed to operate at a maximum speed of ~30000 RPM and expected to exhibit 92% temperature rise and ~ 2kW idle power consumption to cause a severe impact to the rolling elements of the bearing. However, the built-in oil-air mist lubrication controls the temperature rise at the rolling element and ensures the use of high speed conditions for the generator.

7.1.3 The analytical calculations for the role of coolant flow rate on heat transfer characteristics for a high speed generator, showed that the convection heat transfer coefficient increases with an increase in flowrate (0.3 to 3.5 m^3/hr), which would result in the longevity of the critical components, in particular the bearings.

7.1.4 The numerical simulations on the effect of coolant velocity to enhance HSPM generator efficiency was performed using ANSYS Fluent. Two coolant flowrates were considered, no flowrate and maximum flowrate (3.5 m^3/hr). Maximum coolant flowrate conditions showed lower temperature generation throughout the generator compared to no coolant flowrate through the cooling jackets. The lower temperatures achieved, ensure that the magnets, winding insulation, and bearings are not affected by the heat generated.

7.1.5 A HSPM generator was constructed, with an emphasis on the need for high precision machining, tolerances and balancing throughout the development process. As a basis for future work which is beyond the scope of this thesis, basic no-load tests were conducted on the generator, that validated the analytical calculations and numerical simulations.

7.2 Recommendations

The following recommendation is made based on the findings of this dissertation:

7.2.1 To further validate the design of the HSPM generator, a drive motor with a specification of 30000 RPM needs to be procured, since the aircraft motor that was used to drive the HSPM generator was limited to a speed of 8000 RPM, alternatively the IPM generator (with an operating speed of 30000 RPM) is to be converted to a motor and drive the HSPM generator, to establish results of the generator at no load and full load conditions at continuous duty.

7.2.2 To successfully validate the design of the HSPM generator at speeds greater than 8000 RPM, a high-speed test rig should be built, with provision made for all rotating components to be encased using suitable material for high-speed/ballistic impact. The design of the casing should also make provision for a rotating speed sensor

7.2.3 To further improve the design of the HSPM generator and achieve speeds greater than 8000 RPM, the rotor sleeve needs to be redesigned by considering FEA using ANSYS, and stronger material selection for a thickness of 1mm. A thorough runout test also needs to be conducted on the generator using a capacitive sensor, Keyence-Ex-110. Further balancing is also required as the speed further increases from 8000 RPM to 30000 RPM.

7.2.4 The accurate estimation of losses in the HSPM generator needs to be done using MATLAB, which can be extended to the development of a thermal/mathematical model for the accurate prediction of temperatures within the machine. This will also allow for more efficient designs of the cooling system.

7.2.5 There is a need to thoroughly investigate coolant flowrate speeds between 0-3.5 m^3/hr to better understand the thermal behaviour of the HSPM generator. The optimum coolant flowrate for the current cooling jacket also needs to be determined.

REFERENCES

[1] L. Dong Hyun *et al.*, “Performance Evaluation of an In-Wheel Motor Cooling System in an Electric Vehicle/Hybrid Electric Vehicle,” *Energies*, pp 961-971, 2014.

[2] P. Jaen-Sola *et al.*, “Dynamic structural design of Offshore Direct-Drive Wind Turbine Electrical Generators,” *Ocean Engineering 161*, pp 1-19, 2018

[3] D. Trajkovski, and G. Cvetkovski, “Performance Analysis of Different Rotor Topologies in Permanent Magnet Motor,” *IEEE EUROCON*, Orchid, R. Macedonia, 2017

[4] A. Munteanu *et al*., “Influence of the Stator Winding on the Performance of a Five-Phase PMSG,” *Buletinul Agir nr. 3*, 2013

[5] R. L. Stoll, “The Analysis of Eddy Currents,” *Oxford University Press*, 1974

[6] D. Hong *et al*., “Development of an Ultra High Speed Permanent Magnet Synchronous Motor,” *International Journal of Precision engineering and Manufacturing Vol 14*, pp 493-499, 2012

[7] Z. Huang *et al*., “Loss Calculation and Thermal Analysis of Rotors Supported by Active Magnetic Bearings for High-Speed Permanent-Magnet Electrical Machines”, *IEEE Transactions on Industrial Electronics*, Vol 63, No. 4, 2016

[8] A. Tenconi *et al*., “Electrical Machines for High-Speed Applications: Design Considerations and Tradeoffs”, *IEEE Transactions on Industrial Electronics*, Vol 61, No. 6, 2014

[9] E. Uhlmann, J. Hu, “Thermal Modelling of a High Speed Motor Spindle”, *Procedia CIRP 1*, pp 313-318, 2012

[10] W. Tong, *Mechanical Design of Electric Motors*, CRC Press, Boca Raton, 2014

[11] M. Benhaddadi, G. Olivier, R. Ibtiouen, J. Yelle, J. Tremblay, “Premium Efficiency Motors,” *Electric Machines and Drives*, 2011

[12] General Electric, “Evaluation and Application of Energy Efficient Motors,” e-GEA-M1019, *GE Industrial Systems*, Fort Wayne, Indiana, 2002

[13] M. Murugesan, R. Balasubramanian, “The Effect of Mass flow Rate on the Enhanced Heat Transfer Characteristics in A Corrugated Plate Type Heat Exchanger,” *Res. J. Engineering sci.*, Vol. 1(6), pp 22-26, 2016

[14] H. Hu *et al.*, “Effect of Cooling Water Flow Rates on Local Temperatures and Heat Transfer of Casting Dies,” *J. Mat. Proc. Tech. 148*, pp 57-67, 2004

[15] Z. Rehman, K. Seong, “Three-D Numerical Thermal Analysis of Electric Motor with Cooling Jacket,” *Energies*, 2018

[16] S. Li *et al.*, “High-Speed Electric Machines: Challenges and Design Considerations,” *IEEE Transactions on Transportation Electrician*, Vol. 2, No. 1, 2016

[17] J. Schultz, “Examining How Cooling Impacts the Torque and Power of PMAC Motors,” *Parker Hannifin*

[18] R. R. Moghaddam, “High Speed Operation of Electrical Machines, a Review on Technology, Benefits and Challenges,” *2014 IEEE Energy Convers. Congr. Expo. ECCE 2014*, pp. 5539-5546, 2014

[19] E. W. Fairall, S. Member, B. Bilgan, and A. Emadi, “State-of-the-Art High-Speed Switched Reluctance Machines,” pp. 1-7, 2015.

[20] J. F. Gieras, “Comparison of High-Power High-Speed Machines: Cage Induction versus Switched Reluctance Motors,” *1999 IEEE Africon. 5th Africon Conf. Africa (Cat. No.99CH36342)*, vol. 2, pp. 675-678, 1999.

[21] T. J. Miller, *Brushless Permanent-Magnet and Reluctance Motor Drives (Monographs in Electrical and Electronic Engineering 21)*, no. 21. 1989.

[22] F. Cupertino, M. Palmieri, and G. Pellegrino, “Design of high-speed synchronous reluctance machines,” in *2015 IEEE Energy Conversion Congress and Exposition (ECCE)*, 2015, pp. 4828-4834.

[23] J. Ikaheimo, J. Kolehmainen, T. Kansakangas, V. Kivela, and R. R. Moghaddam, “Synchronous high-speed reluctance machine with novel rotor construction,” *IEEE Trans. Ind. Electron.*, vol. 61. No. 6, pp. 2969-2975, 2014.

[24] H. Hofmann and S. R. Sanders, “High-speed synchronous reluctance machine with minimized rotor losses,” *IEEE Trans. Ind. Appl.*, vol. 36, no. 2, pp. 531-539, 200.

[25] M. -I. Lamghari-Jamal, J. Fouladgar, E. -H. Zaim, and D. Trichet, “A magneto-thermal study of a high -speed synchronous reluctance machine,” *IEEE Trans. Magn.*, vol. 42, no. 4, pp. 1271-1274, Apr. 2006.

[26] M. Palmieri, M. Perta, and F. Cupertino, “Design of a 50 000 rpm Synchronous Reluctance Machine for an Aeronautic Diesel Engine Compressor,” *IEEE Energy Convers. Congr. Expo.*, vol. 52, no. 5, pp. 5138–5143, 2014.

[27] P. Tsao, M. Senesky, and S. Sanders, “A synchronous homopolar machine for high-speed applications,” *Conf. Rec. 2002 IEEE Ind. Appl. Conf. 37th IAS Annu. Meet. (Cat. No.02CH37344)*, vol. 1, pp. 406–416, 2002.

[28] W. Li, K. T. Chau, T. W. Ching, Y. Wang, and M. Chen, “Design of a highspeed superconducting bearingless machine for flywheel energy storage systems,” *IEEE Trans. Appl. Supercond.*, vol. 25, no. 3, pp. 5–8, 2015.

[29] J. R. Bumby, E. Spooner, and M. Jagiela, “Solid Rotor Induction Machines for Use in Electrically-Assisted Turbochargers,” *PEMD*, pp. 341–345, 2006.

[30] D. Gerada, A. Mebarki, N. L. Brown, C. Gerada, A. Cavagnino, and A. Boglietti, “High-speed electrical machines: Technologies, trends, and developments,” *IEEE Trans. Ind. Electron.*, vol. 61, no. 6, pp. 2946–2959, 2014.

[31] J. Lahteenmaki, “Design and voltage supply of high-speed induction machines,” Helsinki Univ. Technol, 2002.

[32] H. Zhou and F. Wang, “Comparative Study on High speed Induction Machine with Different Rotor Structures,” no. c, pp. 1009–1012, 2007.

[33] A. Binder and T. Schneider, “High-speed inverter-fed AC drives,” *Int. Aegean Conf. Electr. Mach. Power Electron. Electromotion ACEMP’07 Electromotion’07 Jt. Conf.*, pp. 9–16, 2007.

[34] A. Arkkio, T. Jokinen, and E. Lantto, “Induction and permanent-magnet synchronous machines for high-speed applications,” *2005 International Conference on Electrical Machines and Systems*, vol. 2. pp. 1–6, 2005.

[35] Y. Honda, S. Yokote, T. Higaki, and Y. Takeda, “Using the Halbach magnet array to develop an ultrahigh-speed\nspindle motor for machine tools,” *IAS ’97. Conf. Rec. 1997 IEEE Ind. Appl. Conf. Thirty-Second IAS Annu. Meet.*, vol. 1, no. mm, 1997.

[36] A. Borisavljevic, *Limits, Modeling and Design of High-Speed Permanent Magnet Machines*. Berlin, Heidelberg: Springer Berlin Heidelberg, 2013.

[37] P. Chudi, A. Malmquist, “Development of a Small Gas Turbine-driven High-speed Permanent Magnet Generator.” *Licentiate Thesis*, The Royal Institute of Technology. KTH 1989.

[38] Y. K. Kim, M. C. Choi, K. H. Suh, Y. C. Ji, and D. S. Wang, “High-Speed Induction Motor Development for Small Centrihgal Compressor,” in *Proc. of the Fifth Internutionul Conference on Electrical Machines and Systems*, pp. 891-894.

[39] W. Fengxiang, Z. Wenpeng, Z. Ming, W. Baoguo, “Design Considerations of High-Speed PM Generators for Micro Turbines,” *IEEE*, pp. 158-162, 2002

[40] R. Kuppuswamy, C. Richmond, A. Khan, “A study on the Role of Oil-Air Mist Lubrication On An Ultrahigh-Speed Generator,” *Procedia Manufacturing*, 33, pp 107-114, ISSN 2351-9789, 2019

[41] A. Binder, “Tutorial ‘High Speed Drives,’” in *ICEM*, 2014.

[42] S. Li, Y. Li, W. Choi, and B. Sarlioglu, “High speed electric machines - Challenges and design considerations,” *Electr. Mach. (ICEM), 2014 Int. Conf.*, pp. 2549 - 2555, 2014

[43] A. Looser and J. W. Kolar, “A Hybrid Bearing Concept for High-Speed Applications Employing Aerodynamic Gas-Bearings and a Self-Sensing Active Magnetic Damper,” pp. 1686–1691, 2011.

[44] M. Salehi, H. Heshmat, J. F. Walton, and M. Tomaszewski, “Operation of a Mesoscopic Gas Turbine Simulator at Speeds in Excess of 700,000 rpm on Foil Bearings,” *J. Eng. Gas Turbines Power*, vol. 129, no. 1, p. 170, 2007.

[45] B. Polajzer, “Design and analysis of an active magnetic bearing experimental system,” University of Maribor, 2002.

[46] T. Schneider and A. Binder, “Design and Evaluation of a 60000 rpm Permanent Magnet Bearingless High Speed Motor,” *J. Sci. Instrum.*, Mar. 2007.

[47] X. Sun, L. Chen, and Z. Yang, “Overview of bearingless permanent-magnet synchronous motors,” *IEEE Trans. Ind. Electron.*, vol. 60, no. 12, pp. 5528–5538, 2013.

[48] A. Salazar, A. Chiba, and T. Fukao, “A Review of Developments in Bearingless Motors,” in *7th International Symposium on Magnetic Bearings*, 2000.

[49] V. Kluyskens and B. Dehez, “Dynamic Electromechanical Model for Magnetic Bearings Subject to Eddy Currents,” *IEEE Trans. Magn.*, no. 4, pp. 1444 - 1452, 2013.

[50] M. Y. Chen, S. C. Huang, S. K. Hung, and L. C. Fu, “Design and implementation of a new six-DOF Maglev positioner with a fluid bearing,” *IEEE/ASME Trans. Mechatronics*, vol. 16, no. 3, pp. 449–458, 2011.

[51] M. Yoon, C. Jeon, S. Ken Kauh, “Efficiency Increase of an Induction Motor by Improving Cooling Performance,” *IEEE Transactions on Energy Conversion*, Vol. 17, No. 1, 2002

[52] T. Nakahama *et al*., “Improved Cooling Performance of Large Motors Using Fans,” *IEEE Transactions on Energy Conversion*, Vol. 21, No. 2, 2006

[53] A. Bonnett, “Operating Temperature Considerations and Performance Characteristics for IEEE 841 Motors,” *IEEE*, 2000

[54] J. Faiz, R. Iranpour, P. Pillay, “Thermal Model for a Switched Reluctance Motor TEFC Design During Steady and Transient Operation,” *Electr. Mach. Power Syst. 26 (1)*, pp 77–91, 1998

[55] M.J. Durán, J. Fernández, “Lumped-Parameter Thermal Model for Induction Machines,” *IEEE Trans. Energy Convers. 19 (4)*, pp 791–792., 2004

[56] K.N. Srinivas, R. Arumugam, “Thermal Characterization Through Finite Element Analysis of the Switched Reluctance Motor,” *TENCON 2001, in: Proceedings of IEEE Region 10, International Conference on Electrical and Electronic Technology*, pp. 819–823., 2001

[57] K.M. Rahman, B. Fahimi, G. Suresh, A.V. Rajarathnam, M. Ehsani, “Advantages of Switched Reluctance Motor Applications to EV and HEV: Design and Control Issues,” *IEEE Trans. Ind. Appl. 36*, pp 111–121., 2000

[58] C.C. Chang, Y.F. Kuo, J.C. Wang, S.L. Chen, "Air Cooling for a Large-Scale Motor," *Appl. Therm. Eng. 30,* pp 1360–1368., 2010

[59] Y. Bertin, E. Videcoq, S. Thieblin, D. Petit, "Thermal Behavior of an Electrical Motor Through a Reduced Model," *IEEE Trans. Energy Convers. 15 (2),* pp 129–134., 2000

[60] H. Li, "Cooling of a Permanent Magnet Electric Motor with a Centrifugal Impeller," *Int. J. Heat Mass Transf. 53,* pp 797–810., 2010

[61] D.A. Staton, A. Cavagnino, "Convection Heat Transfer and Flow Calculations Suitable for Electric Machines Thermal Models," *IEEE Trans. Industr. Electron. 55 (10),* pp 3509–3516., 2008

[62] Z. Huang, F. Marquez, A. Alakula, J. Yuan, "Characterization and Application of Forced Cooling Channels for Traction Motors in HEVs," *in: International Conference on Electrical Machines, Marseille, Sept 2012,* pp. 1212–1218., 2012

[63] D.H. Lim, S.C. Kim, "Thermal Performance of Oil Spray Cooling System for Inwheel Motor in Electric Vehicles," *Appl. Therm. Eng. 63,* pp 577–587., 2014

[64] M. Anibal, J. Tapia, "Heat Transfer and Thermal Design of Finned Frames for TEFC Variable-Speed Motors," *IEEE Trans. Industr. Electron. 55 (10),* pp 3500–3508., 2008

[65] M. Polikarpova *et al*., "Hybrid Cooling Method of Axial-Flux Permanent-Magnet Machines for Vehicle Applications," *IEEE Trans. Industr. Electron. 62 (12),* pp 7382-7390., 2015

[66] K. Lee, H. Cha, Y. Kim, "Development of an Interior Permanent Magnet Motor Through Rotor Cooling for Electric Vehicles," *Appl. Therm. Eng. 95,* pp 348–356., 2016

[67] F. Zhang, S. Song, G. Di, Y. Li, "Analysis of the 3D Steady Temperature Field of MW High Speed Permanent Magnet Motor," *in: International Conference on Electrical Machines and Systems, Busan, Oct 2013,* pp. 1351–1354., 2013

[68] P. Zheng *et al*., "Research on the Cooling System of a 4QT Prototype Machine Used for HEV," *IEEE Trans. Energy Conver 23 (1),* pp 61-67, 2008

[69] R. Pechanek, L. Bouzek, " Analyzing of Two Types Water Cooling Electric Motors Using Computational Fluid Dynamics," *in: International Power Electronics and Motion Control Conference, Europe,* 2012

[70] L. Cuiping *et al*., "Analysis of 3D Static Temperature Field of Water Cooling Induction Motor in Mini Electric Vehicle," *in: International Conference on Electrical Machines and Systems, Beijing, Aug 2011*

[71] A. Boglietti *et al*., "Evolution and Modern Approaches for Thermal Analysis of Electrical Machines," *IEEE Trans. Industr. Electron. 56 (3),* pp 871–882., 2009

[72] R. Kuppuswamy, "Design and Development of a Bio-Generator," University of Cape Town, South Africa, 2016.

[73] M. Katna, “Theories of Failure,” *Faculty of Engineering and Applied Science*, Memorial University of Newfoundland

[74] Mechanical Power Transmission (Hub Design), *EML 2322L-MAE Design and Manufacturing Laboratory*, Retrieved from http://www2.mae.ufl.edu/designlab/Lab%20Assignments/EML2322L-Mechanical%20Power%20Transmission.pdf

[75] M. Calistrat, “Hydraucally Fitted Hubs, Theory and Practice,” *Proceedings of the Ninth Turbomachiney Symposium*, pp 1-10, n.d.

[76] Oil Injection Method, *SKF*, Sweden, Publication No. 2930EW, 1976

[77] F. Cupertino *et al.,*” Design Procedure for High-Speed PM Motors Aided by Optimization Algorithms, *“Machines*, pp 1-17, 2018

[78] Lahne, H.C.; Gerling, D.; Staton, D.; Chong, Y.C. Design of a 50,000 rpm high speed high-power six-phase PMSM for use in aircraft applications. In Proceedings of the Eleventh International Conference on Ecological Vehicles and Renewable Energies (EVER), Monte Carlo, Monaco, 6–8 April 2016.

[79] S. Yoon *et al*., *Control of Surge in Centrifugal Compressors by Active Magnetic Bearings*. London, Heidelberg: Springer London Heidelberg New York Dordrecht, 2013

[80] S. Yoon *et al*., “Introduction to Rotor Dynamics,” In Book Control of Surge in Centrifugal Compressors by Active Magnetic Bearings: *Theory and Implementation*, London: Springer-Verlag

[81] M. Branagan *et al*., “Compliant Gas Foil Bearings and Analysis Tools,” *J. Eng. Gas Turbines Power 138(5)*, 2015

[82] S. Li *et al*., “High-Speed Electric Machines: Challenges and Design Considerations,” *IEEE Trans. Transportation Electrification 2(1)*, pp 2-13, 2016

[83] P. Bagiriski, G. Zywica, “The Influence of Temperature on Dynamics of the Rotor-Foil Bearing System,” *Transactions of the Institute of Fluid-Flow Machinery* (134), pp 11-28, 2016

[84] L. Andres, T. Chirathadam, “Measurements of Rotordynamic Response in a High Temperature Rotor Supported on Two Metal Mesh Foil Bearings,” *TAMU Turbomachinery Research Consortium*, pp 1-50, 2012

[85] G. Queitzsch, D. Fleming, “Rotordynamic Influence on Rolling Element Bearing Selection And Operation,” *International Symposium on Stability Control of Rotating Machinery*, 2001

[86] J. Shigley, “Mechanical Engineering Design: First Metric Edition”, pp 565-582, 1986

[87] Tojiro, Aoyama, Ichiro, Inasaki, Satoshi Tsutsui, and Tetsu Shimizu, “Development of oil air lubrication system with piezo electric nozzle for machine tool spindles,” *International journal of Japan society of mechanical engineers (JSME), 32(2)*, pp 259-263, 1989.

[88] Hermann, Schlichting, and K. Gersten, “Fundementals of Boundary-Layer Theory,” *In Book Boundary-Layer Theory*, 9th ed, Berlin: Springer Verlag, 2017

[89] D, Mazur, “Thermal Analysis of the Permanent Magnet Synchronous Generator with the Use of Ansys Fluent.” Paper presented at *International Symposium on Electrodynamic and Mechatronic Systems (SELM*), Opole-Zawiercie, Poland, May 2013

[90] H. Rouhani, J. Faiz, and C. Lucas. “Lumped Thermal Model for Switched Reluctance Motor Applied to Mechanical Design Optimization.” *Mathematical and Computer Modelling 45(5-6)*, pp 625-638, 2007

[91] J. Rucker, “Design and Analysis of a Permanent Magnet Generator for Naval Applications,” *Master’s Thesis*, Massachusetts Institute of Technology, 2005

[92] T. Stolarski, “Elements of Contact Mechanics.” In Book *Tribology in Machine Design*, Heinemann Newnes Publisher, Oxford, London, 1990

[93] Y. Inada, “Studies in Ultra High Speed Grinding”, *PhD Thesis,* Tohoku University, Japan, 1996

[94] C. Tso, “Basic Concepts of Heat Transfer,” NTU, Singapore

[95] J. Brändlein, P. Eschmann, L. Hasbargen, and K. Weigand, “Friction, Temperature and Lubrication,” in Book *Ball and Roller Bearings: Theory Design and Application. 3rd Edition,* John Wiley and sons, England, 1999

[96] M. Bahrami, “Steady Conduction Heat Transfer,” *ENSC 388 (F09),* Simon Fraser University, Canada, pp. 1-14.

[97] M. Bahrami, “Forced Convection Heat Transfer,” *ENSC 388 (F09),* Simon Fraser University, Canada, pp. 1-11

[98] ANSYS, ”Maxwell Online Help Release 18.2,” Canonsburg, PA, July 2017

[99] General Motors Corporation Vibration Standards Committee,” Vibration Standard for the Purchase of New and Rebuilt Machinery and Equipment,” GM Specification No. V1.0-1997, https://www.maintenance.org/fileSendAction/fcType/0/fcOid/399590942963972104/filePointer/399590942964810069/fodoid/399590942964810067/GMVibeStandard.pdf

[100] Welkon Limited,” Vibration-Electric Motors,” https://www.welkon.net/downloads/vibration.pdf

APPENDIX A

A.1. Mechanical Drawings

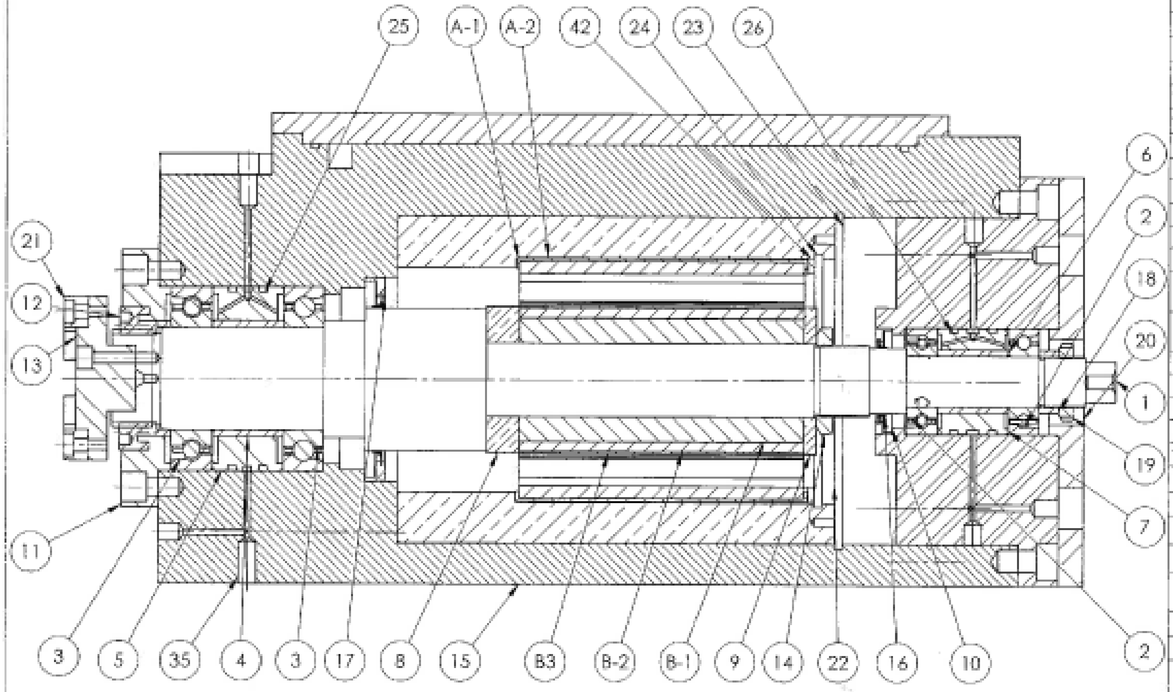

ITEM NO.	Name	DESCRIPTION	QTY.
1	Shaft	En24	1
2	High Precision Angular contact Ball Bearing	7205C SN24 TYNDBLP4	2
3	High Precision Angular contact Ball Bearing	7210C SN24 TYNDBLP4	2
4	Inner spacer	S45C	1
5	Outer spacer	S45C	1
6	Inner spacer-rear BRG S45C	S45C	1
7	Outer spacer rear brg	S45C	1
* 8	Front Brass Spacer	Bronze	1
* 9	Rear Brass Spacer	Bronze	1
10	Rear Housing	En24	1
11	Front labrinth	En24	1
12	Front brg Nut	En24	1
13	Clutch Plate	En24	1
14	Lock Nut	KM 7 (SKF)	1
15	Housing_rev1	FC20	1
16	Turcon varilp PDR seal (Trelleborg)	TJA3B0320-T251	1
17	Turcon varilp PDR seal (Trelleborg)	TJA3B0700-T251	1
18	Preload Rear Spacer	S45C	1
19	Lock Nut	KM 5 (SKF)	1
20	Rear cover	S45C	1
21	Clutch tooth	SKC43	6
*22	Brass cooling cartridge	Brass	1
23	Inner circlip	Dia 160	1
24	Inner circlip	Dia 120	1
25	O-ring	OD: 90 C/S Ø : 3	2
25	O-ring	OD: 52 C/S Ø : 3	2
A-1	Stator Spring Clamp (SMPMM)	SCM 420	4
A-2	Stator Stamping (SMPMM)	M19	400
B-1	Rotor Stamping (SMPMM)	M19	400
B-2	Rotor Magnet (IPMM)	Neodymium (NdFeB30)	4
B-3	Rotor Sleeve (SMPMM)	Epoxy	1
B-4	Rotor Clamp Rod	Nylon 66	4
B-5	Rotor Stamp Nut	Nylon 66	8
42	Spring Clamp Spacer	Bronze	1

Note:

Customer: Maxas

* Parts which differ to IPM Machine

Itm B-4 & B-5, are on Rotor Assly (drawing Number: B)

A3 Landscape	University of Cape Town Department of Mechanical Engineering			
	Title: Surface Mounted Permanent Magnet Machine (SMPMM)			
Assembly Drawing	Scale: 1:5	Date: 2016-12-02	Sheet 1	of 2
	Drawn By: CR	Checked By: RK	Drawing Number M1	

ITEM NO.	PART NUMBER	DESCRIPTION	QTY.
27	Hex socket Head cap screw	M6 x 10	16
28	Hex socket Head cap screw	M6 x 15	6
29	Hex socket Head cap screw	M6 x 20	3
30	Hex socket Head cap screw	M6 x 10	3
31	Hex socket Head cap screw	M8 x 12	32
32	Hex socket Head cap screw	M8 x12	18
33	Hex socket Head cap screw	M10 x 16	6
34	Hex socket Head cap screw	M12 x 15	6
35	Hex socket Head cap screw	M16 x30	6
36	Taper Pin	Ø 8 x 24	4
37	Front bearing cooling cover left	S15C	1
38	Front bearing cooling cover right	S15C	1
39	Cooling system cover_side_ left	S15C	1
40	Cooling system cover_side_ right	S15C	1
41	Cooling system cover	S15C	1

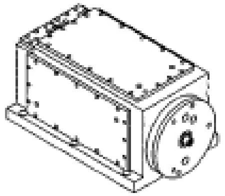

Note:

DETAIL	VALUE
Physical size	460mm x 280mm x 230mm
Maximum / Field Speed	30 000 RPM
Power generated	10 kW
Coolant	Water based coolant
Coolant pressure	15~20 bar
Coolant Flowarate	0.3 to 3.5 m3/s
Oil-air mist ratio	1:10 ~ 1:13
Mist Pressure	2~5 bar
Lock Nut KM5 Pre Load Torque	0.2 ~ 1.1 N.m
Front brg Nut Preload Torque	1.3 ~ 6.1 N.m

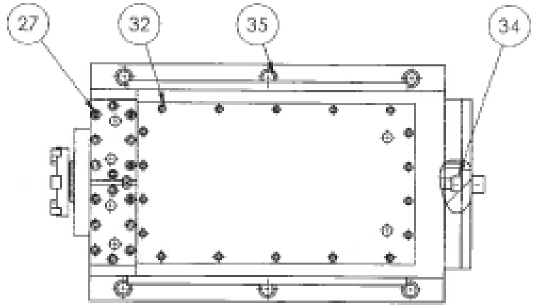

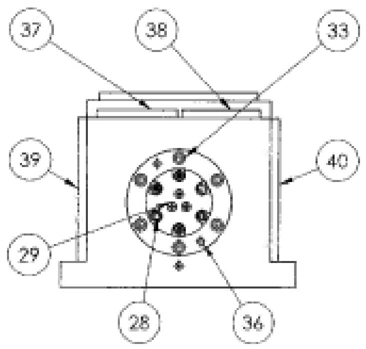

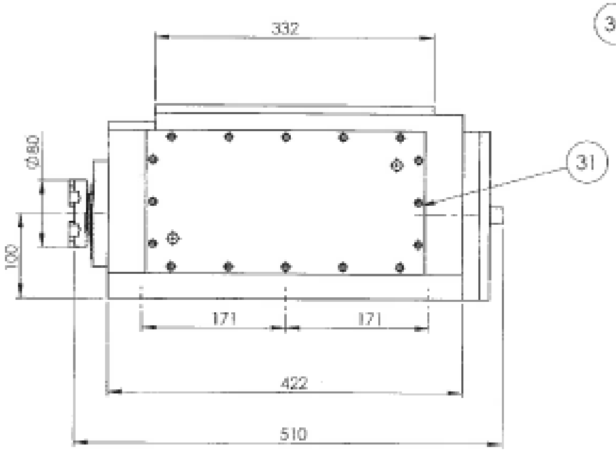

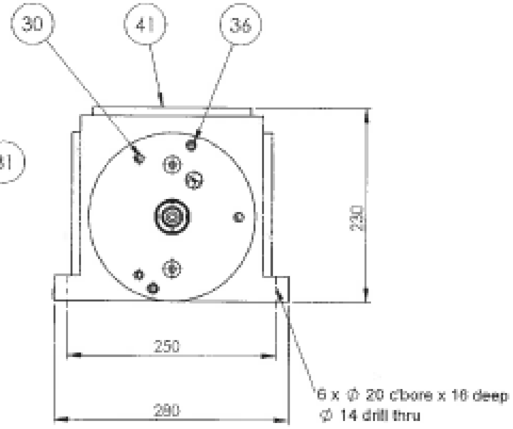

Note:

Customer: Maxas

A3 Landscape	University of Cape Town Department of Mechanical Engineering			
	Title: Surface Mounted Permanent Magnet Machine (SMPMM)			
Assembly Drawing	Scale: 1:5	Date: 2016-10-03	Sheet 2	of 2
	Drawn By: CR	Checked By: RK	Drawing Number M1	

SOLIDWORKS Student Edition.
For Academic Use Only.

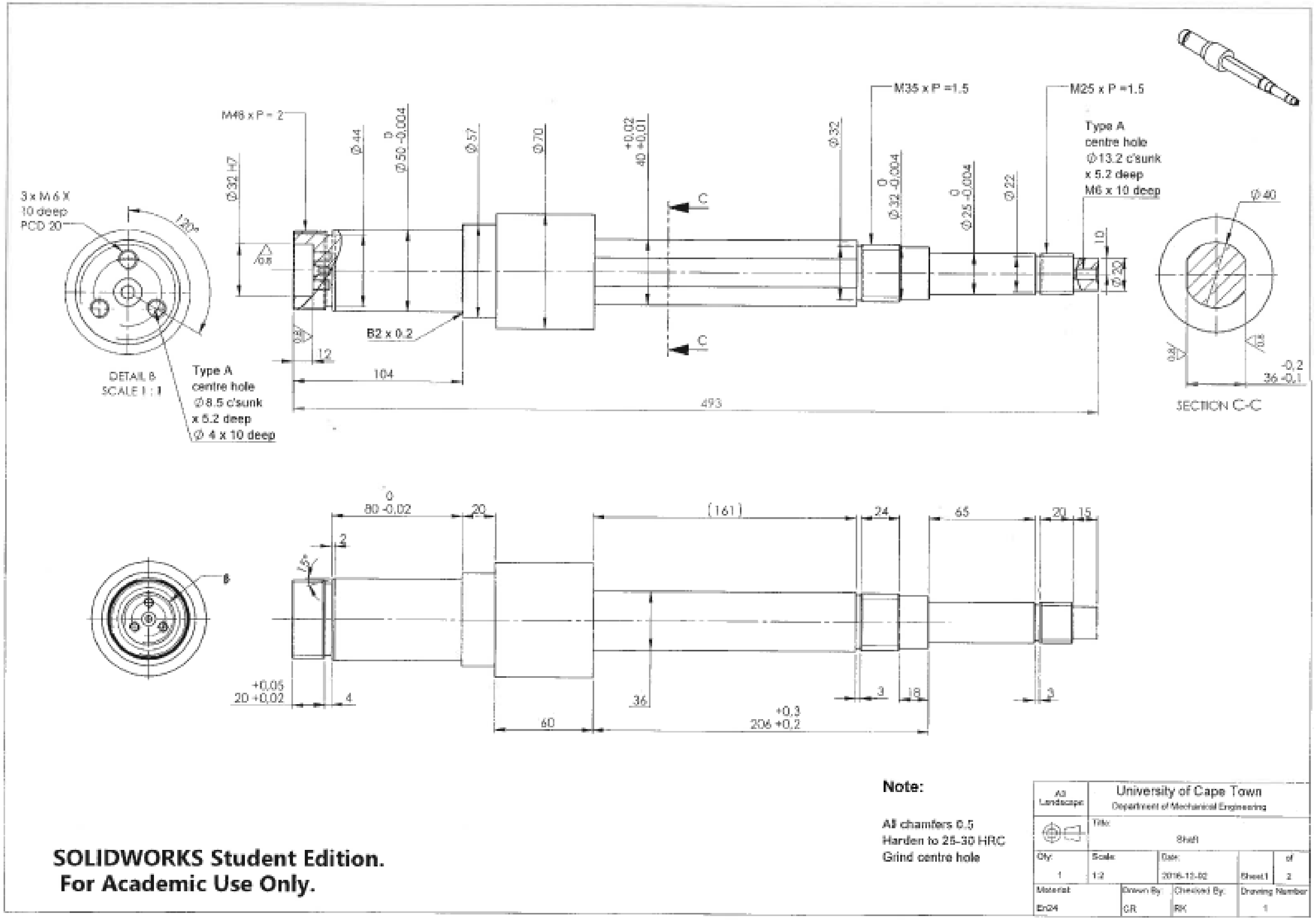
3 x M 6 X
10 deep
PCD 20
120°
DETAIL B
SCALE 1 : 1
Type A
centre hole
Ø 8.5 c'sunk
x 5.2 deep
Ø 4 x 10 deep
M48 x P = 2
Ø 32 H7
0.8
Ø 44
0
Ø 50 -0.004
Ø 57
Ø 70
+0.02
40 +0.01
Ø 32
0
Ø 32 -0.004
0
Ø 25 -0.004
Ø 22
M35 x P =1.5
M25 x P =1.5
Type A
centre hole
Ø 13.2 c'sunk
x 5.2 deep
M6 x 10 deep
10
Ø 20
C
C
B2 x 0.2
12
104
493
Ø 40
0.8
0.8
-0.2
36 -0.1
SECTION C-C
B
0
80 -0.02
20
(161)
24
65
20
15
2
15°
+0.05
20 +0.02
4
60
36
+0.3
206 +0.2
3
18
3
Note:
All chamfers 0.5
Harden to 25-30 HRC
Grind centre hole
SOLIDWORKS Student Edition.
For Academic Use Only.
A3
Landscape
University of Cape Town
Department of Mechanical Engineering
Title:
Shaft
Qty:
1
Scale:
1:2
Date:
2016-12-02
Sheet1
of
2
Material:
En24
Drawn By:
CR
Checked By:
RK
Drawing Number
1

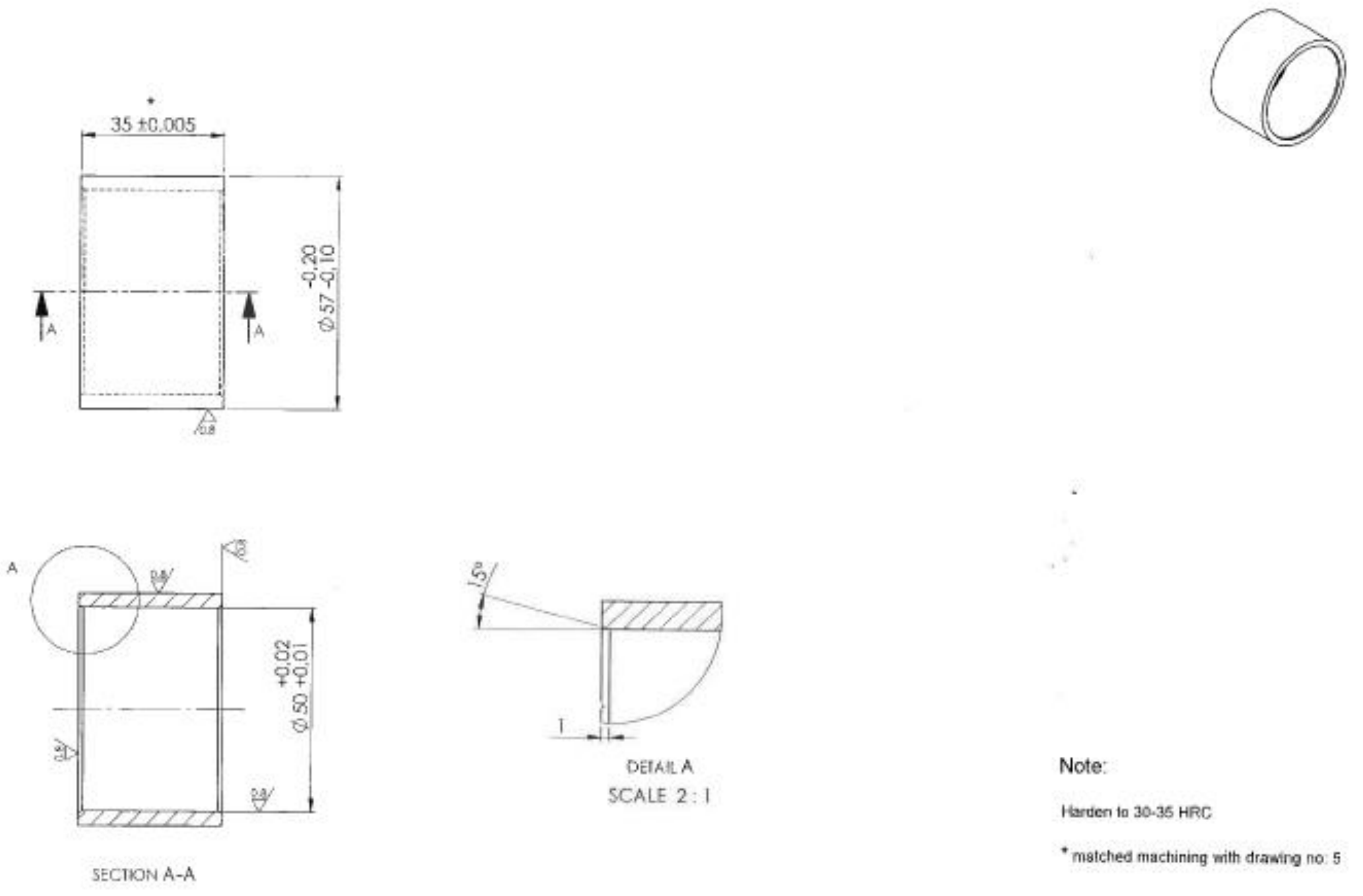

Note:

Harden to 30-35 HRC

* matched machining with drawing no: 5

A3 Landscape	University of Cape Town Department of Mechanical Engineering					
	Title: Inner spacer					
Qty 1	Scale: 1:1		Date: 2016-12-02		Sheet: 1	of 1
Material En24C		Drawn By CR		Checked By RK	Drawing Number 4	

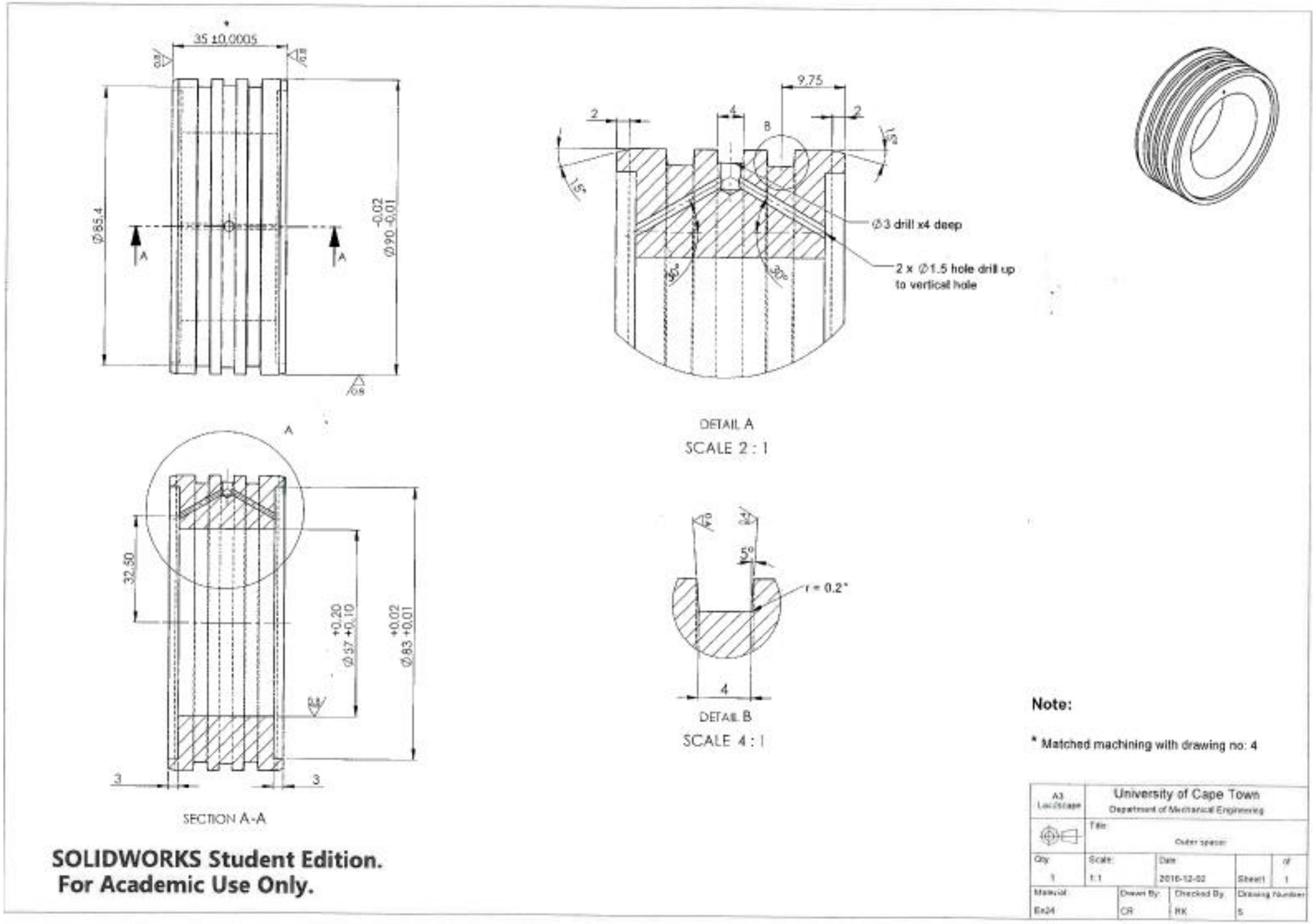

Note:

* Matched machining with drawing no: 4

A3 Landscape	University of Cape Town Department of Mechanical Engineering				
	Title: Outer spacer				
Qty: 1	Scale: 1:1	Date: 2016-12-02		Sheet	of 1
Material: En24		Drawn By: CR	Checked By: RK	Drawing Number: 5	

SOLIDWORKS Student Edition.
For Academic Use Only.

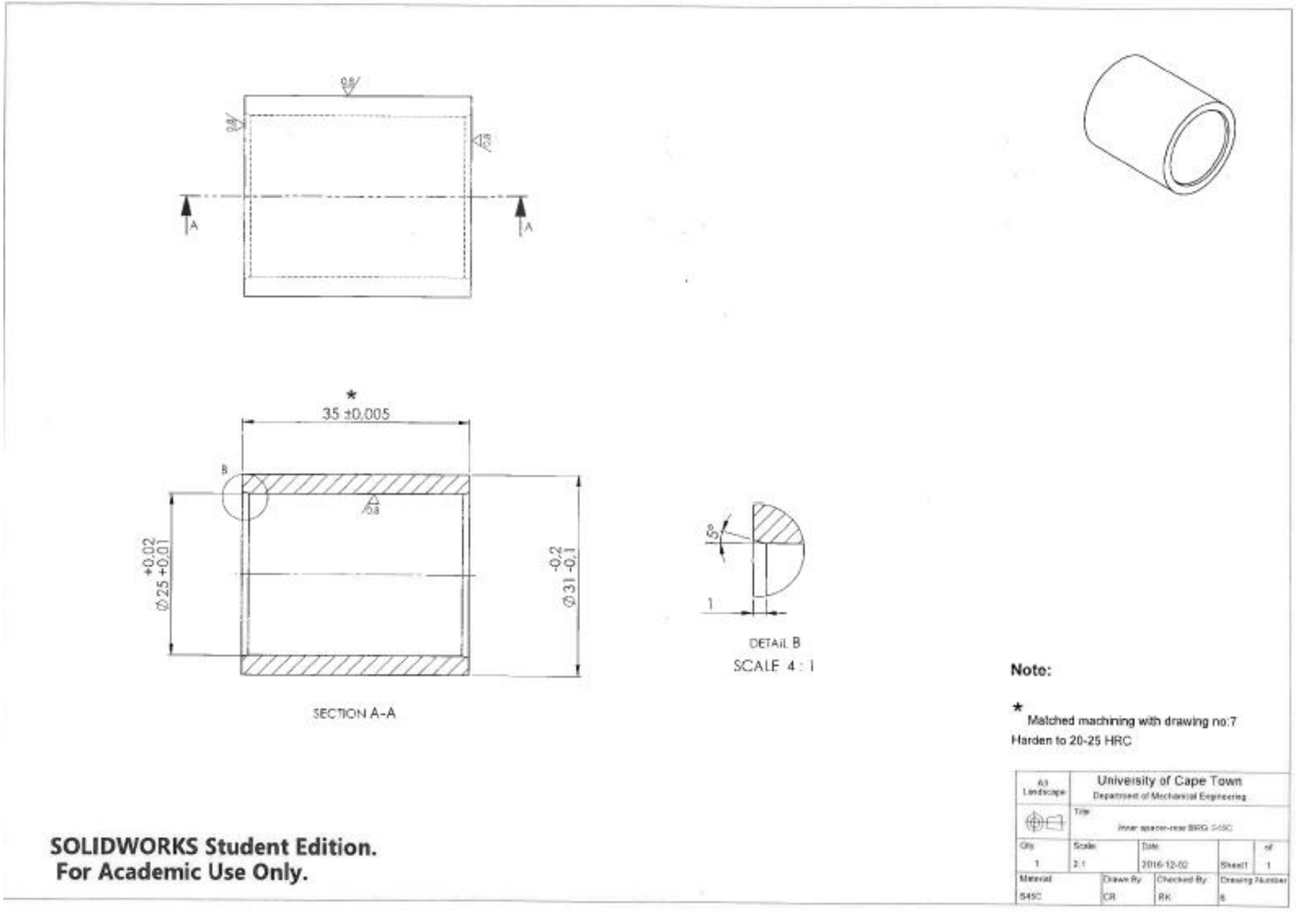
0.8
0.8
0.8
A
A
*
35 ±0,005
B
0.8
Ø25 +0,01 +0,02
Ø31 -0,1 -0,2
SECTION A-A
5°
1
DETAIL B
SCALE 4 : 1
Note:
*
Matched machining with drawing no:7
Harden to 20-25 HRC
A3 Landscape
University of Cape Town
Department of Mechanical Engineering
Title
Inner spacer-rear BRG S45C
Qty
1
Scale
2:1
Date
2016-12-02
Sheet1
of
1
Material
S45C
Drawn By
CR
Checked By
RK
Drawing Number
6
SOLIDWORKS Student Edition.
For Academic Use Only.

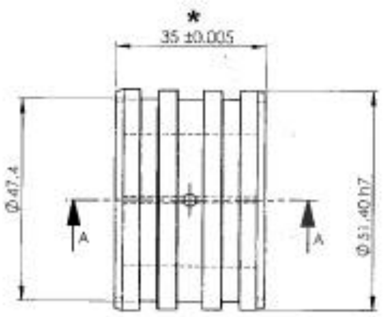

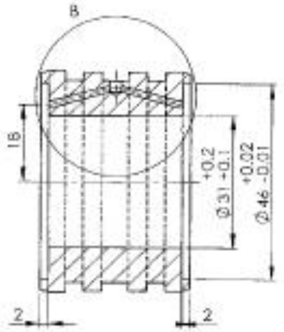

SECTION A-A

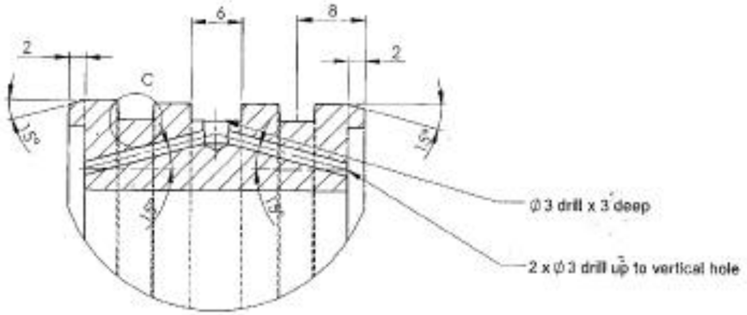

DETAIL B
SCALE 2 : 1

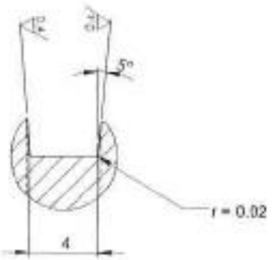

DETAIL C
SCALE 4 : 1

Note:

*Matched machining with drawing no: 6
Harden to 20-25 HRC

A3 Landscape	University of Cape Town Department of Mechanical Engineering			
	Title: Outer spacer bearing			
Qty: 1	Scale: 1:1	Date: 2016/11/30	Sheet1	of 1
Material: 845C	Drawn By: DR	Checked By: RH	Drawing Number 7	

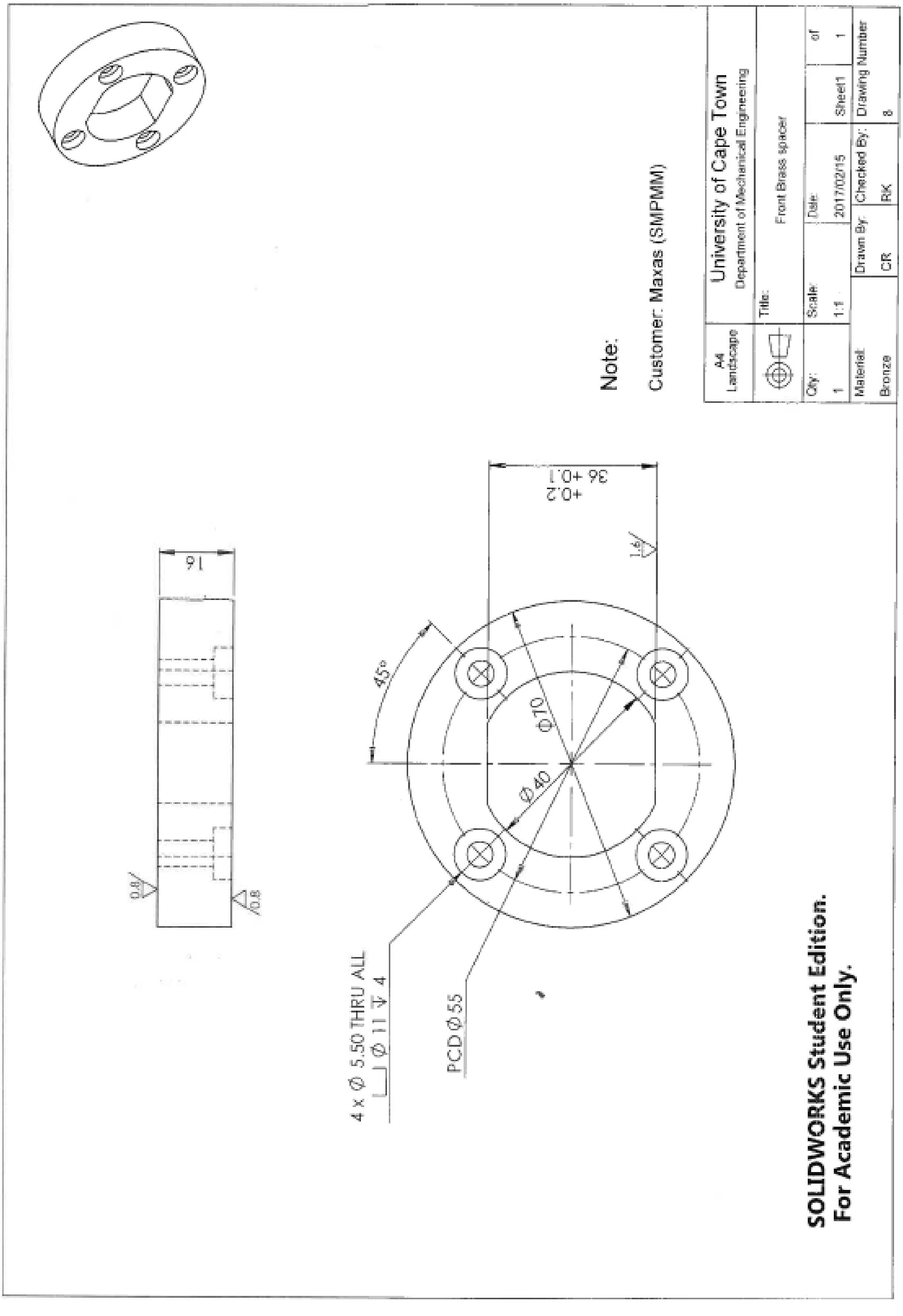
4 x Ø 5.50 THRU ALL
⌴ Ø 11 ↧ 4
PCD Ø 55
Ø 40
Ø 70
45°
16
36 +0.1
+0.2
0.8
0.8
1.6
Note:
Customer: Maxas (SMPMM)
A4
Landscape
University of Cape Town
Department of Mechanical Engineering
Title:
Front Brass spacer
Qty:
1
Scale:
1:1
Date:
2017/02/15
Sheet1
of
1
Material:
Bronze
Drawn By:
CR
Checked By:
RK
Drawing Number
8
SOLIDWORKS Student Edition.
For Academic Use Only.

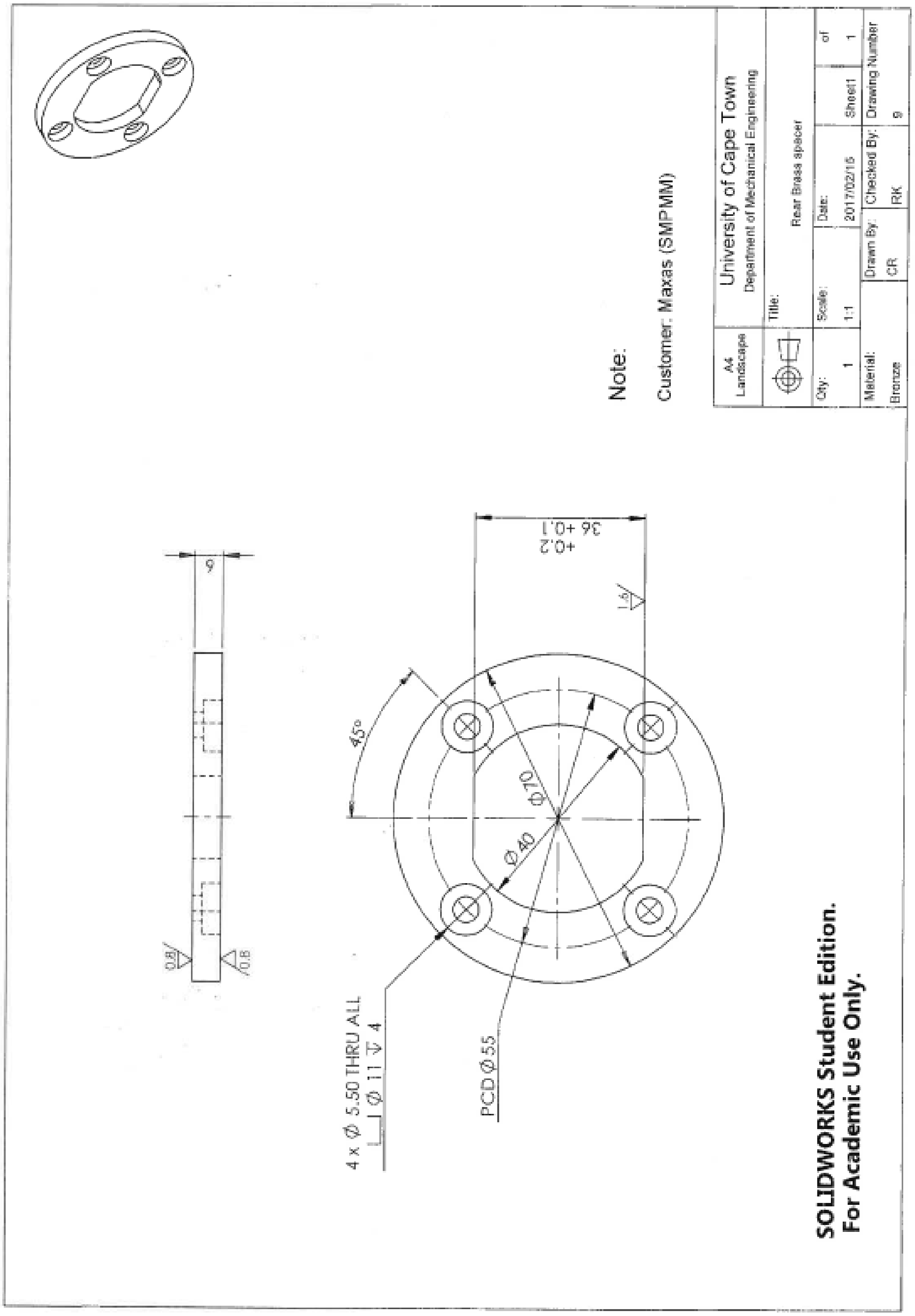
4 x Ø 5.50 THRU ALL
⌴ Ø 11 ↧ 4
PCD Ø 55
Ø40
Ø70
45°
36 +0.1 +0.2
9
1.6
0.8
0.8
SOLIDWORKS Student Edition.
For Academic Use Only.
Note:
Customer: Maxas (SMPMM)
A4 Landscape
University of Cape Town
Department of Mechanical Engineering
Title:
Rear Brass spacer
Qty:
1
Scale:
1:1
Date:
2017/02/16
Sheet1
of
1
Material:
Bronze
Drawn By:
CR
Checked By:
RK
Drawing Number
9

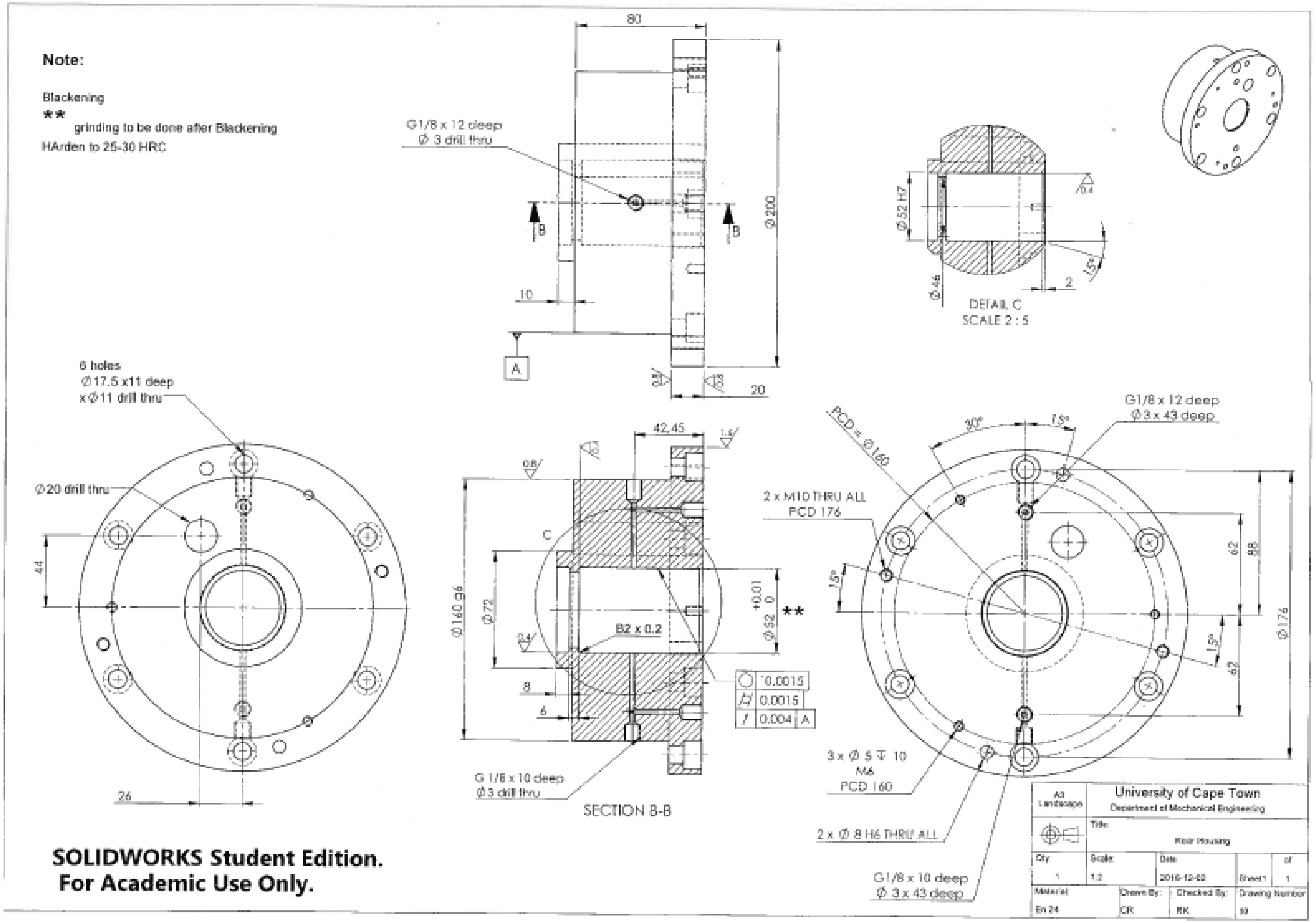
Note:
Blackening
**
grinding to be done after Blackening
HArden to 25-30 HRC
80
G1/8 x 12 deep
Ø 3 drill thru
B
B
Ø 200
10
A
20
Ø 52 H7
Ø 46
2
15°
DETAIL C
SCALE 2 : 5
6 holes
Ø17.5 x11 deep
x Ø11 drill thru
Ø20 drill thru
44
26
42.45
C
Ø160 g6
Ø72
B2 x 0.2
+0.01
Ø 52 0
**
8
6
0.0015
0.0015
0.004
A
G 1/8 x 10 deep
Ø3 drill thru
SECTION B-B
PCD = Ø160
30°
15°
G1/8 x 12 deep
Ø 3 x 43 deep
2 x M10 THRU ALL
PCD 176
62
98
62
Ø176
3 x Ø 5 ↧ 10
M6
PCD 160
2 x Ø 8 H6 THRU ALL
G1/8 x 10 deep
Ø 3 x 43 deep
A3
Landscape
University of Cape Town
Department of Mechanical Engineering
Title:
Weir Housing
Qty:
1
Scale:
1:2
Date:
2016-12-02
Sheet1
of
1
Material:
En 24
Drawn By:
CR
Checked By:
RK
Drawing Number
10
SOLIDWORKS Student Edition.
For Academic Use Only.

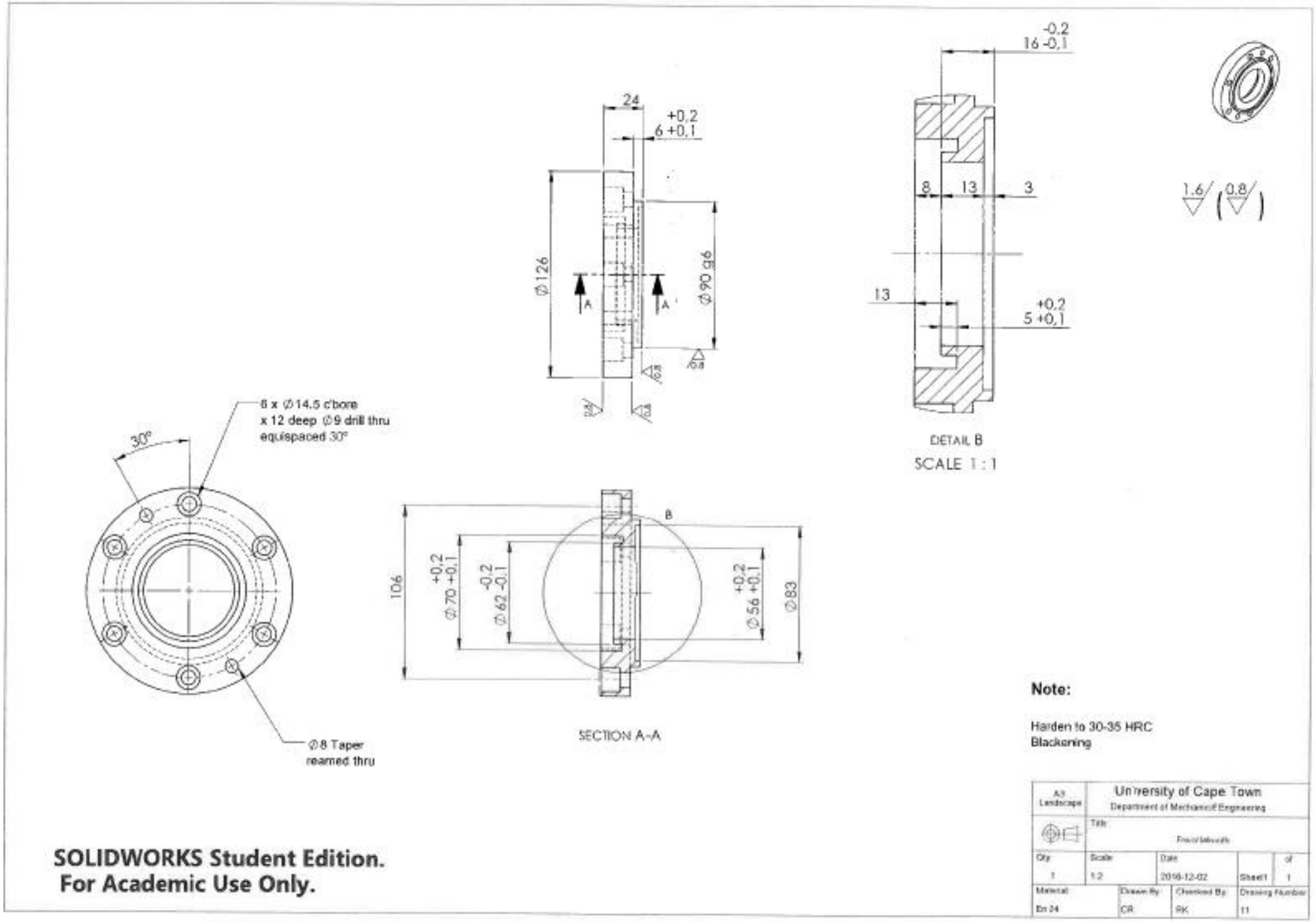
6 x Ø14.5 c'bore
x 12 deep Ø9 drill thru
equispaced 30°
30°
Ø8 Taper
reamed thru
24
6 +0,2 +0,1
Ø126
Ø90 g6
A
A
0.8
106
Ø70 +0,2 +0,1
Ø62 -0,2 -0,1
Ø56 +0,2 +0,1
Ø83
B
SECTION A-A
16 -0,2 -0,1
8
13
3
13
5 +0,2 +0,1
DETAIL B
SCALE 1 : 1
1.6
0.8
Note:
Harden to 30-35 HRC
Blackening
A3
Landscape
University of Cape Town
Department of Mechanical Engineering
Title
Qty
1
Scale
1:2
Date
2016-12-02
Sheet1
of
1
Material
En 24
Drawn By
CR
Checked By
RK
Drawing Number
11
SOLIDWORKS Student Edition.
For Academic Use Only.

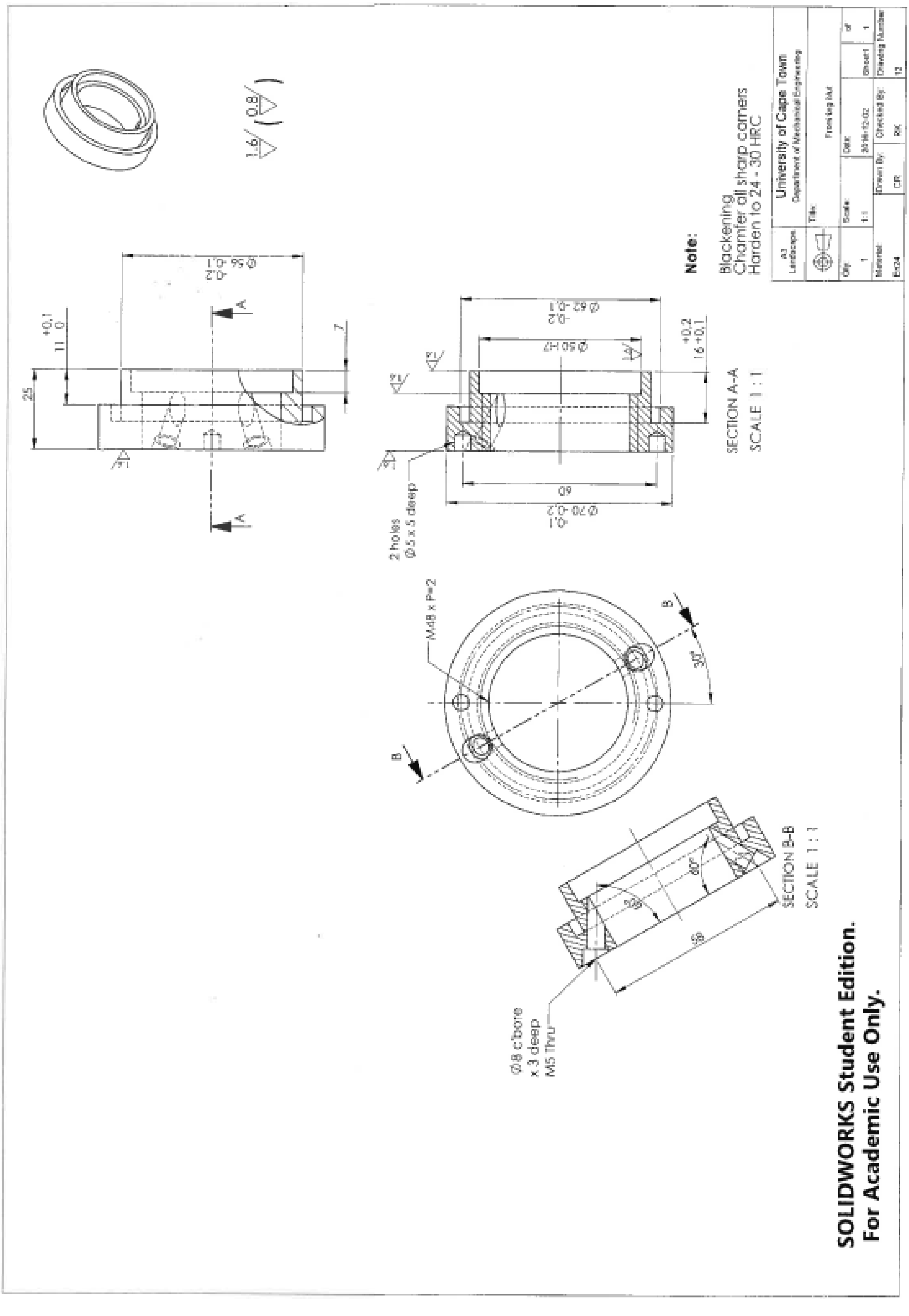Ø56 -0.1 -0.2
+0.1 11 0
25
7
A
A
Ø62 -0.1 -0.2
Ø50 H7
+0.2 16 +0.1
60
Ø70 -0.2 -0.1
2 holes Ø5 x 5 deep
SECTION A-A
SCALE 1 : 1
M48 x P=2
B
B
30°
60°
SECTION B-B
SCALE 1 : 1
Ø8 c'bore x 3 deep M5 Thru
Note:
Blackening
Chamfer all sharp corners
Harden to 24 - 30 HRC
A3 Landscape
University of Cape Town
Department of Mechanical Engineering
Title:
Qty: 1
Scale: 1:1
Date:
Sheet 1 of 1
Material: En24
Drawn By: CR
Checked By: RK
Drawing Number: 12
SOLIDWORKS Student Edition.
For Academic Use Only.

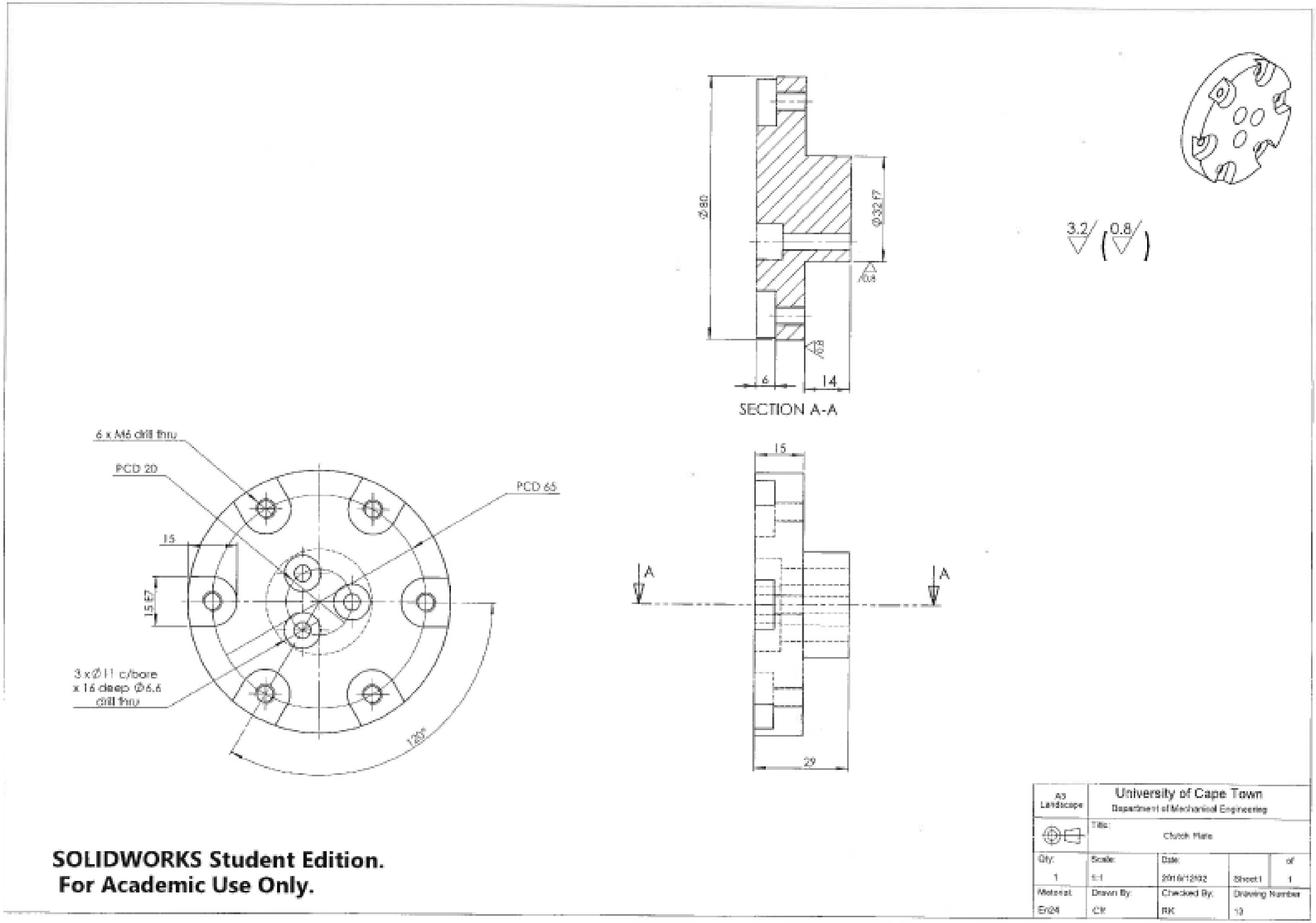
6 x M6 drill thru
PCD 20
PCD 65
15
15 E7
3 x Ø11 c/bore
x 16 deep Ø6.6
drill thru
120°
Ø80
Ø32 f7
0.8
0.8
6
14
SECTION A-A
15
A
A
29
3.2
0.8
A3
Landscape
University of Cape Town
Department of Mechanical Engineering
Title:
Clutch Plate
Qty:
1
Scale:
1:1
Date:
2016/12/02
Sheet 1
of
1
Material:
En24
Drawn By:
CY
Checked By:
RK
Drawing Number
13

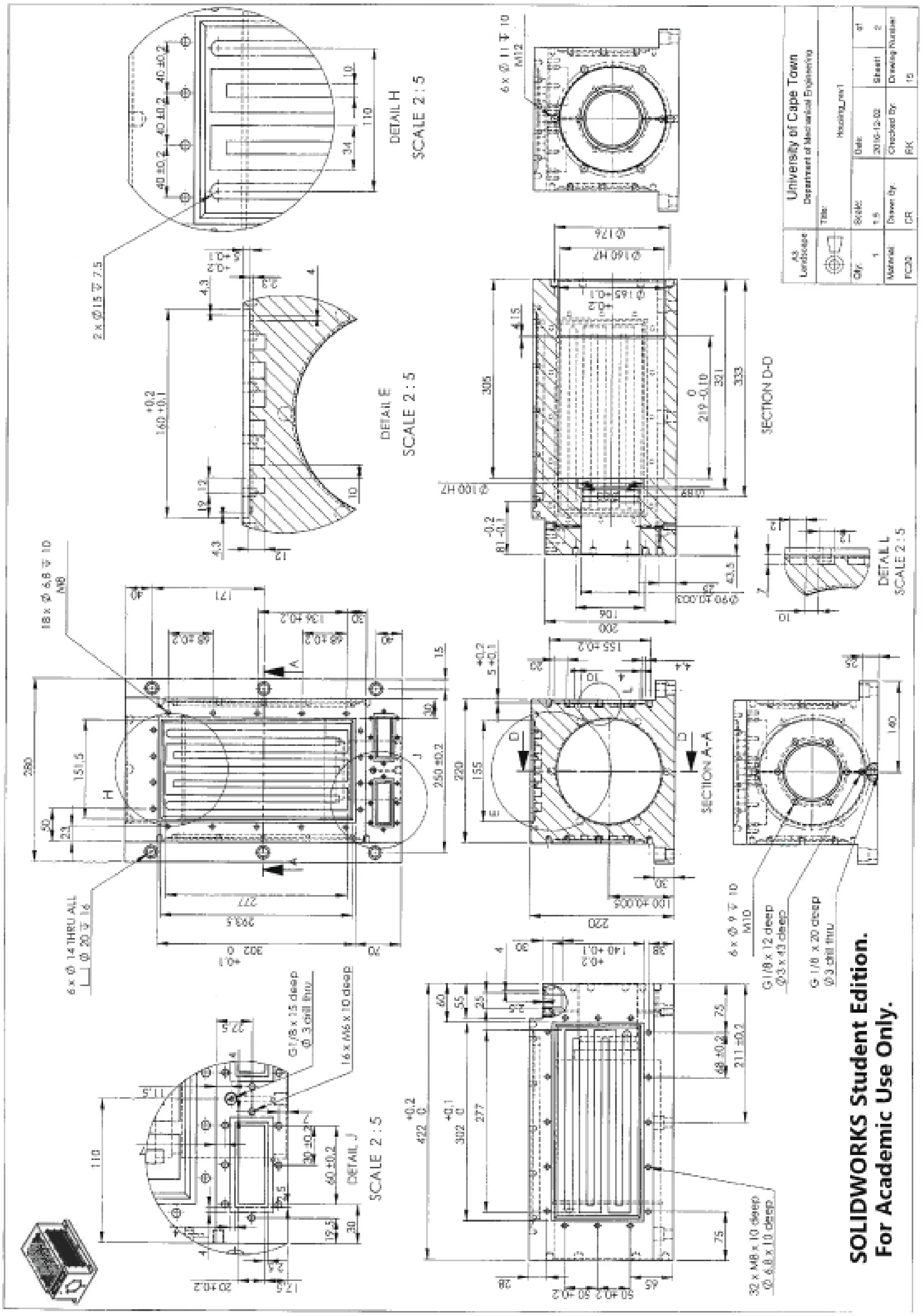
DETAIL H
SCALE 2 : 5
DETAIL E
SCALE 2 : 5
SECTION D-D
SECTION A-A
DETAIL J
SCALE 2 : 5
DETAIL L
SCALE 2 : 5
University of Cape Town
Department of Mechanical Engineering
Housing_rev1
A3 Landscape
SOLIDWORKS Student Edition.
For Academic Use Only.

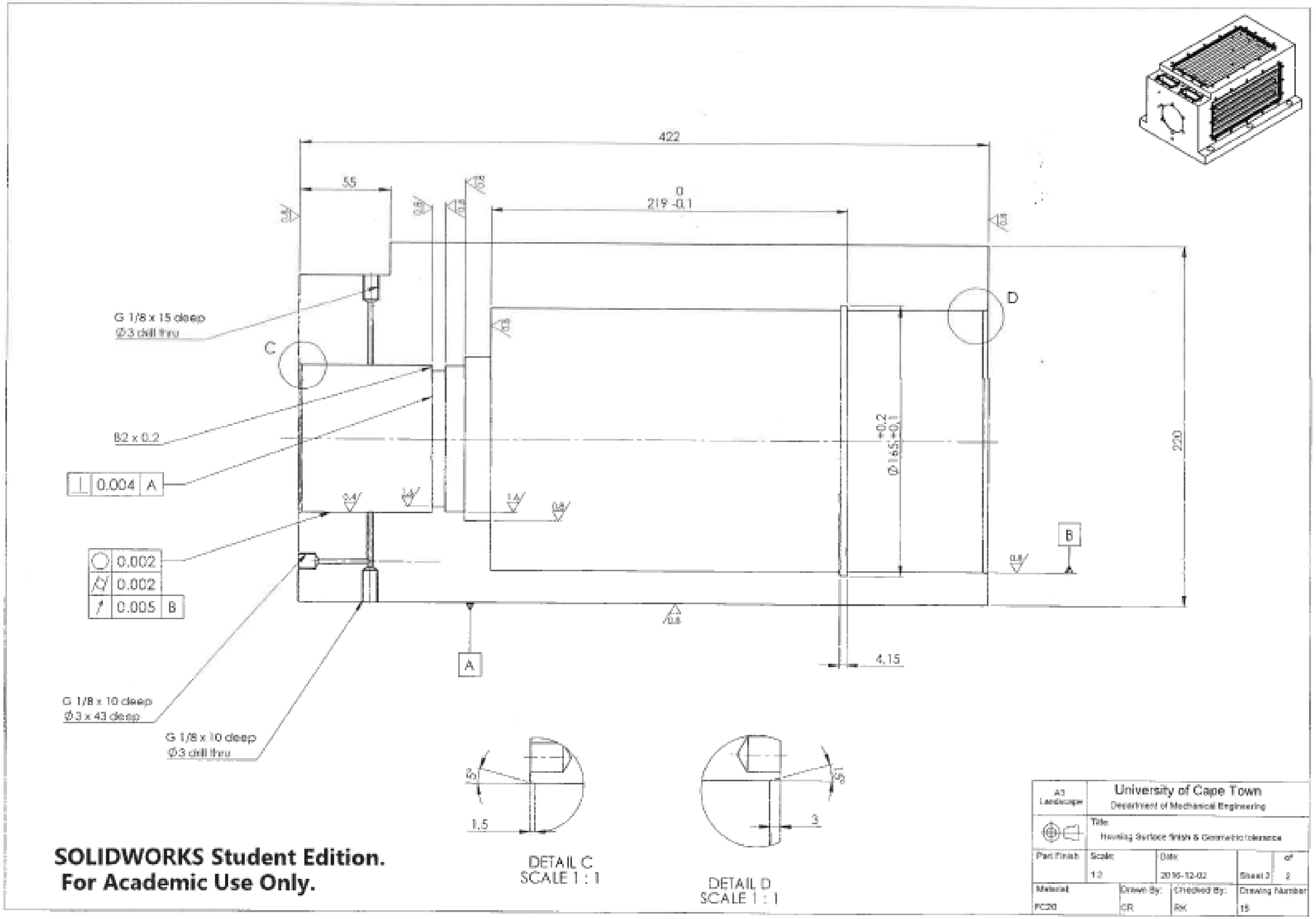
422
55
0
219 -0.1
220
+0.2
Ø165+0.1
4,15
G 1/8 x 15 deep
Ø3 drill thru
C
D
B2 x 0.2
⊥ 0.004 A
○ 0.002
⌭ 0.002
↗ 0.005 B
G 1/8 x 10 deep
Ø3 x 43 deep
G 1/8 x 10 deep
Ø3 drill thru
A
B
0.4
1.6
0.8
1.5
3
DETAIL C
SCALE 1 : 1
DETAIL D
SCALE 1 : 1
SOLIDWORKS Student Edition.
For Academic Use Only.
A3 Landscape
University of Cape Town
Department of Mechanical Engineering
Title:
Housing Surface finish & Geometric tolerance
Part Finish
Scale:
1:2
Date:
2016-12-02
Sheet 2
of
2
Material
PC20
Drawn By:
CR
Checked By:
RK
Drawing Number
15

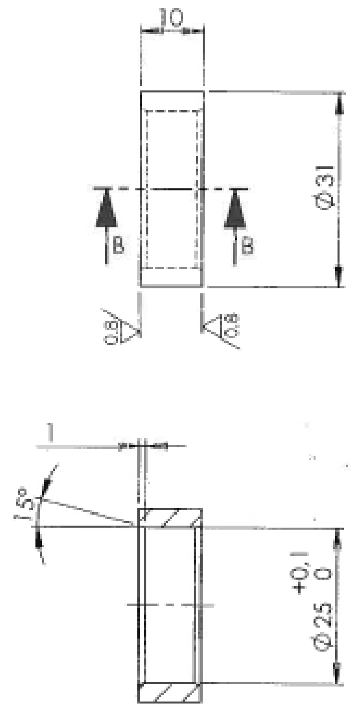

SECTION B-B

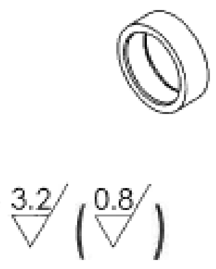

Note:

Harden to 20-25 HRC

A4 Landscape	University of Cape Town Department of Mechanical Engineering			
	Title: Preload Rear Spacer			
Qty: 1	Scale: 1:1	Date: 2016-12-02	Sheet1	of 1
Material: S45C	Drawn By: CR	Checked By: RK	Drawing Number 18	

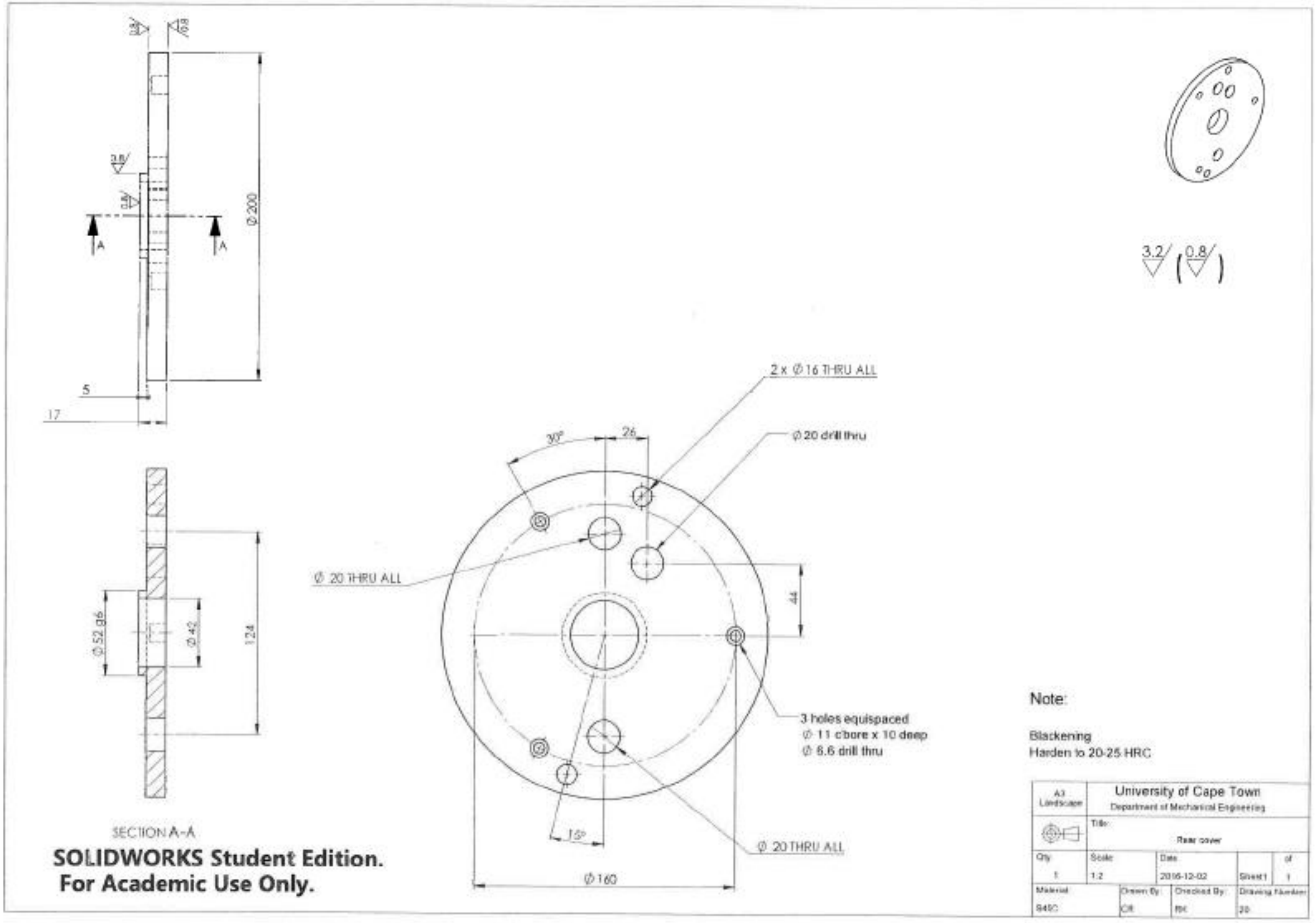
3.2
0.8
A
A
Ø 200
5
17
SECTION A-A
Ø 52 g6
Ø 42
124
SOLIDWORKS Student Edition.
For Academic Use Only.
3.2 (0.8)
2 x Ø 16 THRU ALL
Ø 20 drill thru
30°
26
44
Ø 20 THRU ALL
3 holes equispaced
Ø 11 c'bore x 10 deep
Ø 6.6 drill thru
15°
Ø 20 THRU ALL
Ø 160
Note:
Blackening
Harden to 20-25 HRC
A3 Landscape
University of Cape Town
Department of Mechanical Engineering
Title:
Rear cover
Qty
1
Scale
1:2
Date
2016-12-02
Sheet1
of
1
Material
S45C
Drawn By:
CR
Checked By:
RK
Drawing Number
20

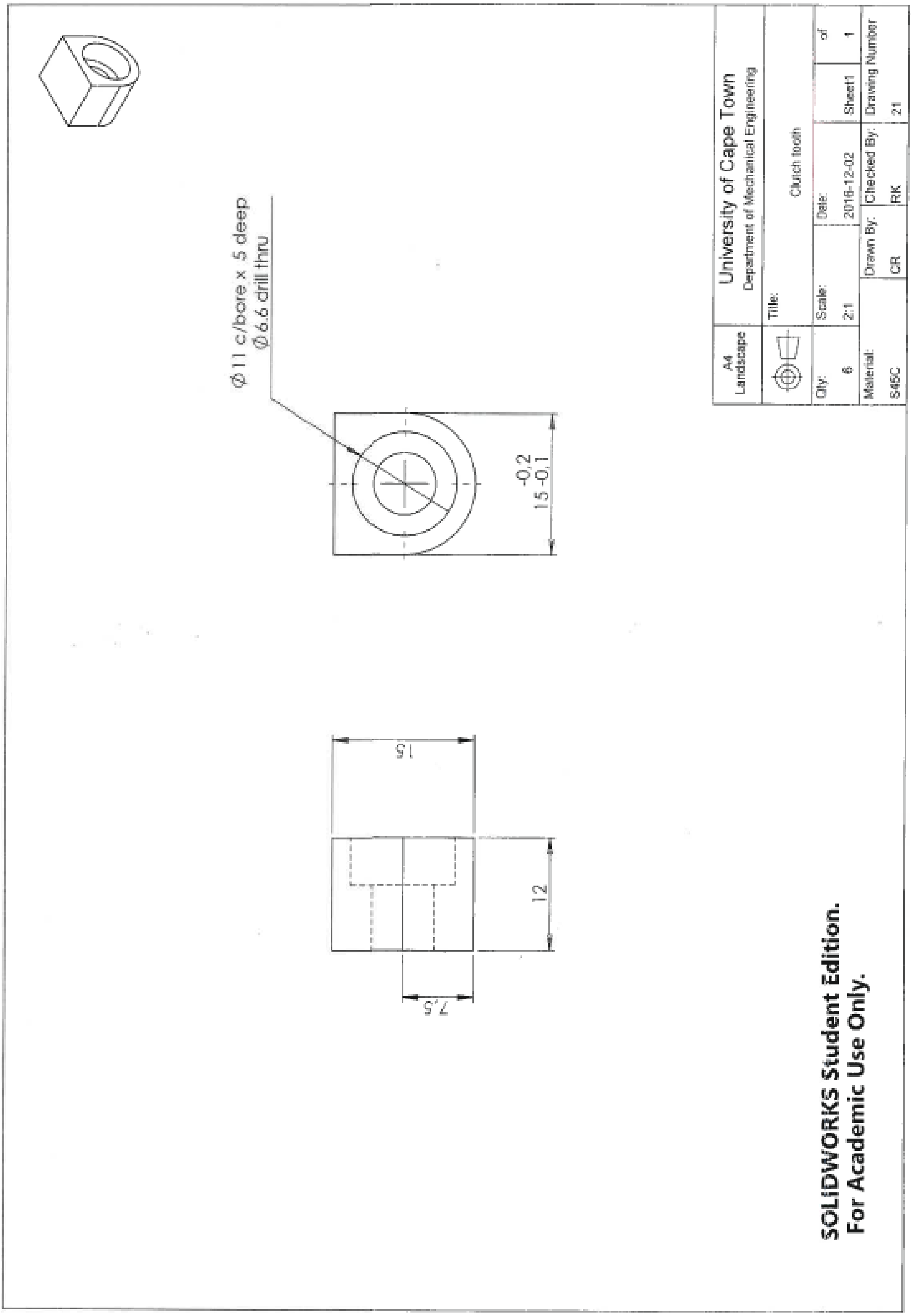
Ø11 c/bore x 5 deep
Ø6.6 drill thru
15 -0,2 -0,1
15
12
7,5
SOLIDWORKS Student Edition.
For Academic Use Only.
A4 Landscape
University of Cape Town
Department of Mechanical Engineering
Title:
Clutch tooth
Qty:
6
Scale:
2:1
Date:
2016-12-02
Sheet1
of
1
Material:
S45C
Drawn By:
CR
Checked By:
RK
Drawing Number
21

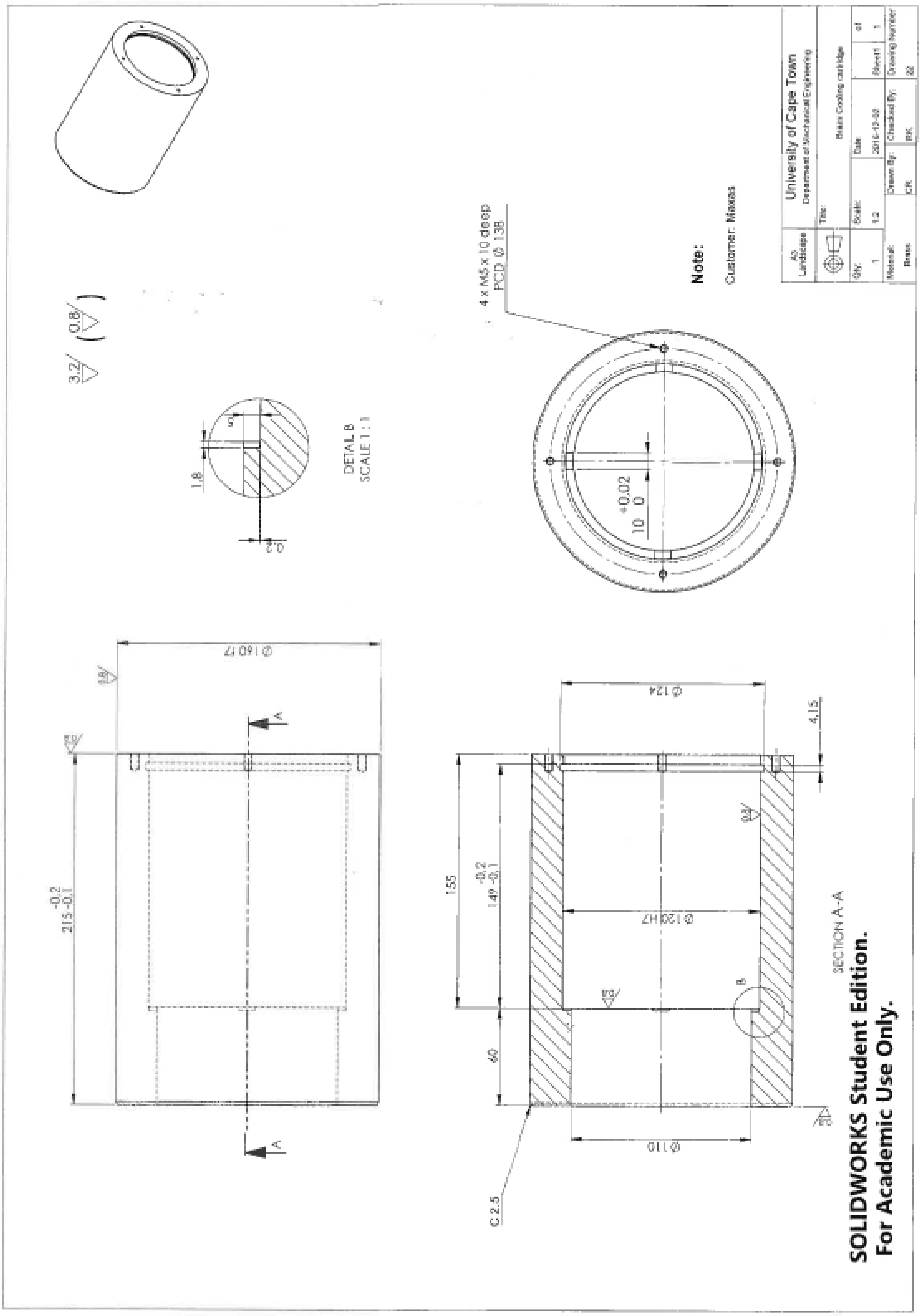
University of Cape Town
Department of Mechanical Engineering
A3 Landscape
Title:
Brass Cooling cartridge
Qty: 1
Scale: 1:2
Date: 2016-12-02
Sheet 1 of 1
Material: Brass
Drawn By: CR
Checked By: RK
Drawing Number 22
Note:
Customer: Maxas
4 x M5 x 10 deep
PCD Ø 138
+0.02
10 0
DETAIL B
SCALE 1 : 1
1.8
5
0.2
3.2
0.8
Ø 160 f7
215 -0.2 -0.1
A
A
155
149 -0.2 -0.1
60
Ø 124
Ø 120 H7
Ø 110
4.15
B
C 2.5
SECTION A-A
SOLIDWORKS Student Edition.
For Academic Use Only.

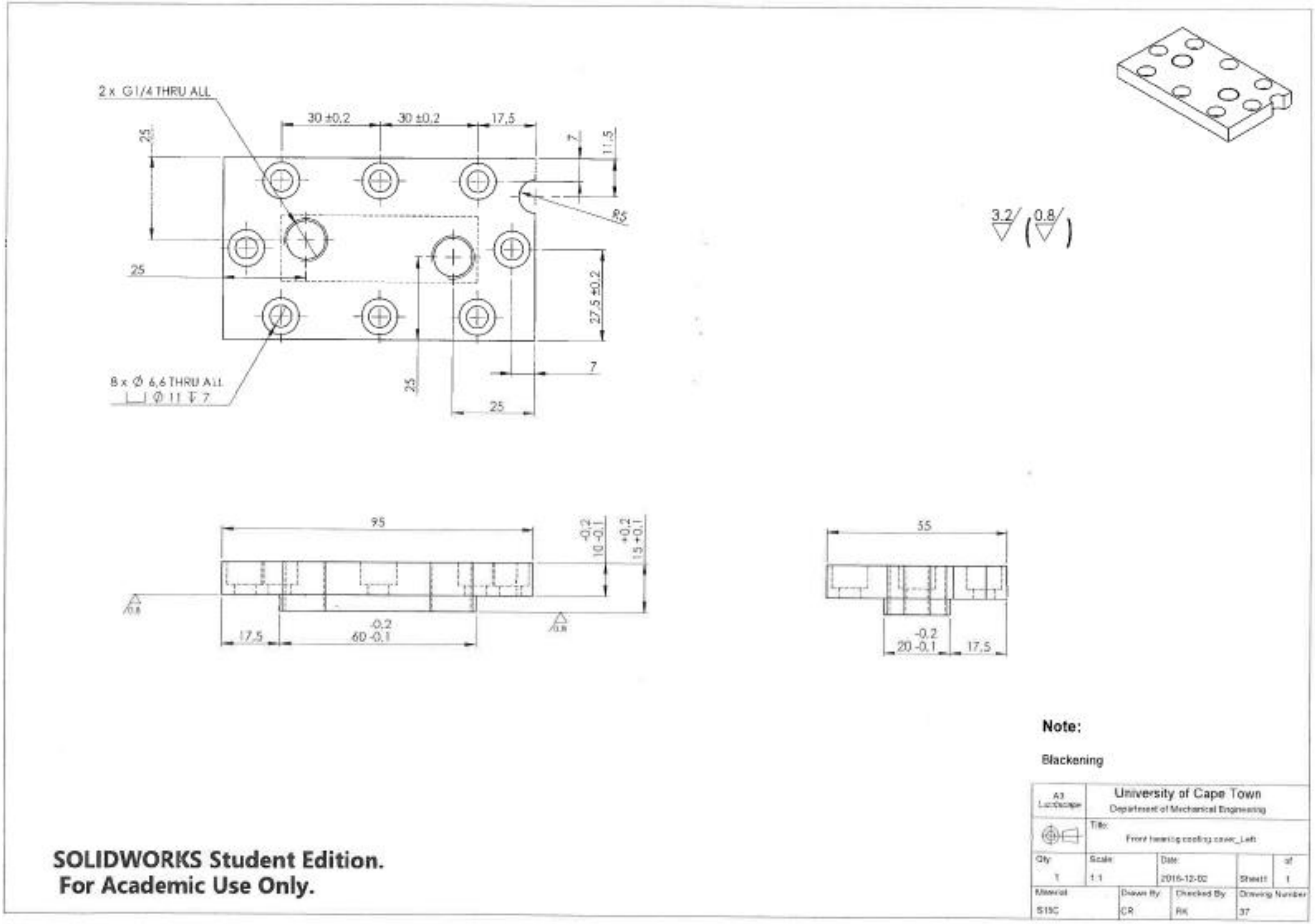

Note:

Blackening

A3 Landscape	University of Cape Town Department of Mechanical Engineering				
	Title: Front bearing cooling cover_Left				
Qty: 1	Scale: 1:1	Date: 2016-12-02		Sheet1	of 1
Material S15C	Drawn By: CR	Checked By RK	Drawing Number 37		

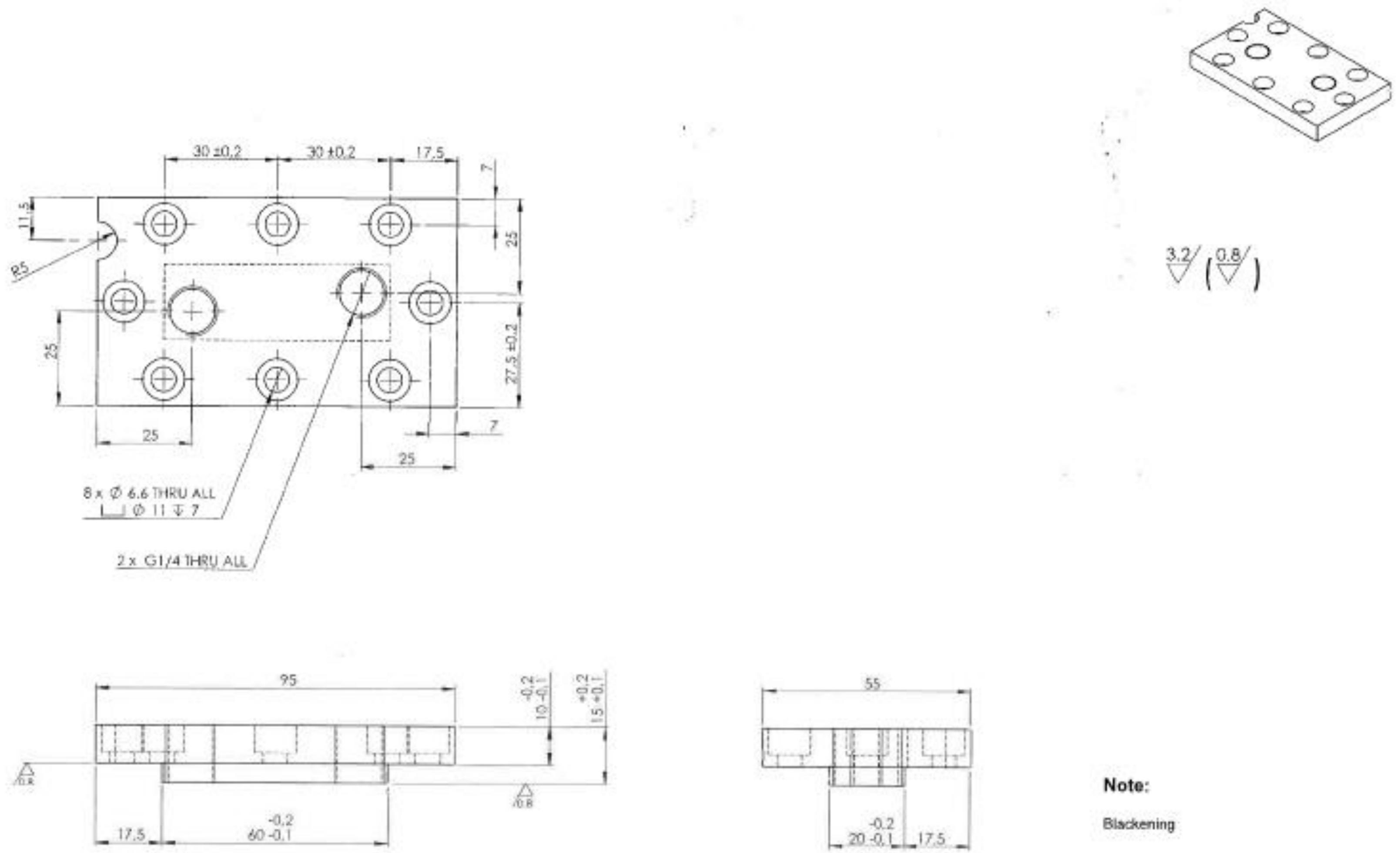

Note:

Blackening

A3 Landscape	University of Cape Town Department of Mechanical Engineering			
	Title: Front bearing cooling cover_Right			
Qty: 1	Scale: 1:1	Date: 2019-12-02	Sheet1	of 1
Material: S15C	Drawn By: CR	Checked By: RK	Drawing Number: 38	

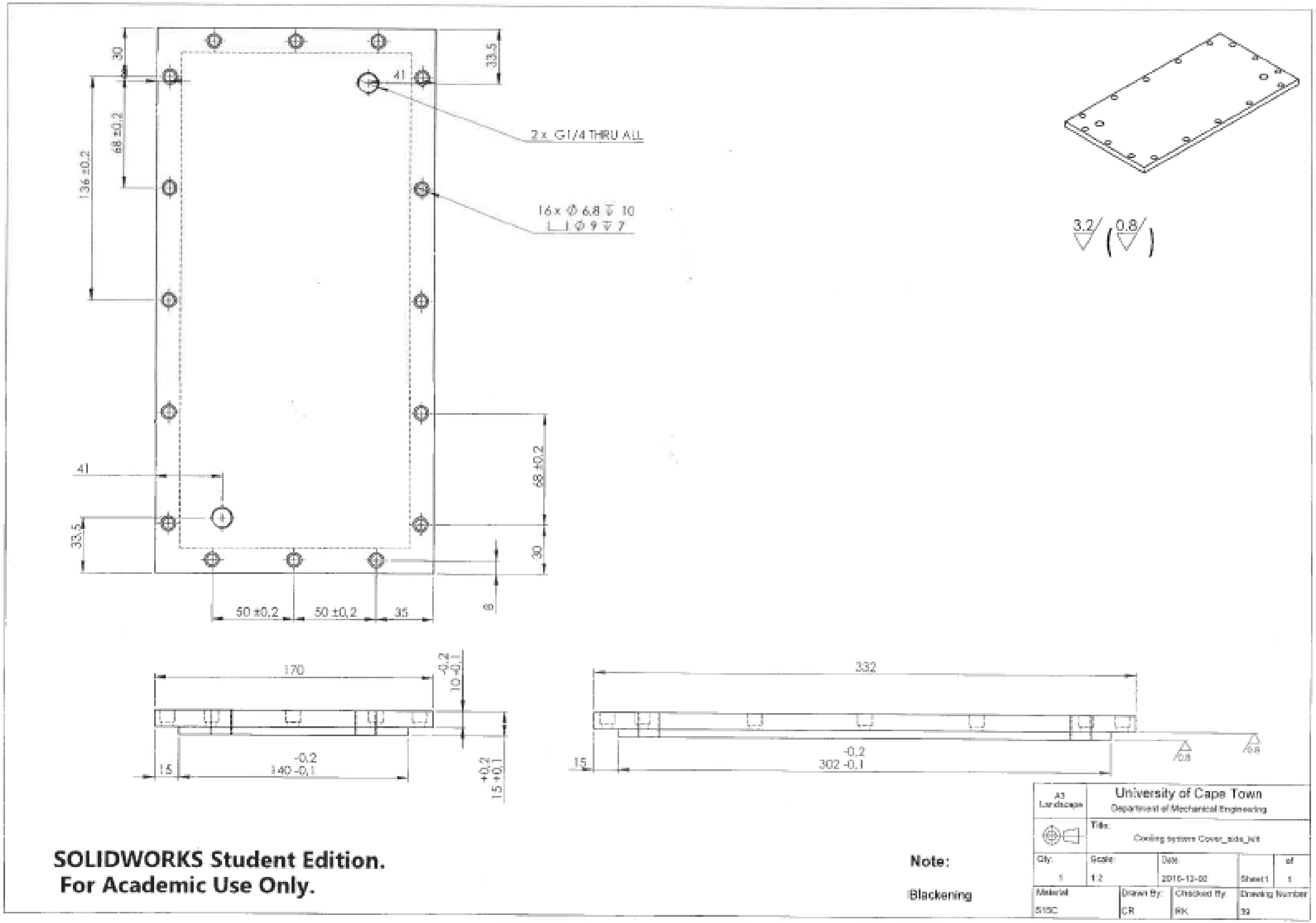
2 x G1/4 THRU ALL
16 x Φ 6.8 ↧ 10
⌴ Φ 9 ↧ 7
3.2/ (0.8/)
30
33.5
41
68 ±0.2
136 ±0.2
41
33.5
68 ±0.2
30
8
50 ±0.2
50 ±0.2
35
170
10 -0.2 -0.1
15
140 -0.2 -0.1
15 +0.2 +0.1
332
15
302 -0.2 -0.1
0.8
0.8
SOLIDWORKS Student Edition.
For Academic Use Only.
Note:
Blackening
A3 Landscape
University of Cape Town
Department of Mechanical Engineering
Title:
Cooling system Cover_side_left
Qty:
1
Scale:
1:2
Date:
2016-12-02
Sheet1
of
1
Material
S15C
Drawn By:
CR
Checked By:
RK
Drawing Number
39

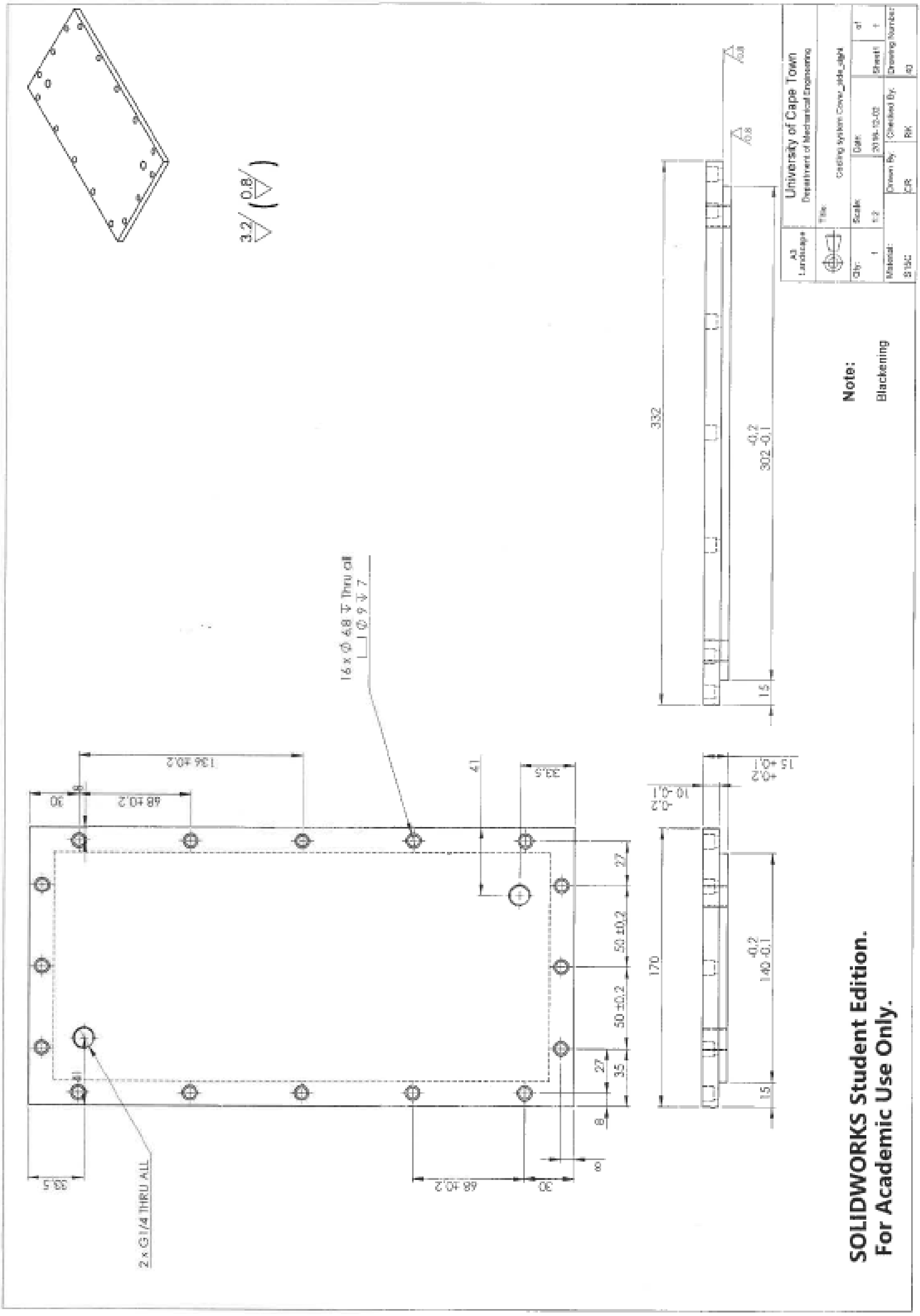
University of Cape Town
Department of Mechanical Engineering
A3 Landscape
Title:
Cooling system Cover_side_right
Qty: 1
Scale: 1:2
Date: 2018-12-02
Sheet 1 of 1
Material: S16C
Drawn By: CR
Checked By: RK
Drawing Number: 40
Note:
Blackening
3.2 (0.8)
16 x ∅ 6.8 ⊽ Thru all
⌴ ∅ 9 ⊽ 7
2 x G1/4 THRU ALL
136 ±0.2
68 ±0.2
30
8
33.5
41
27
50 ±0.2
50 ±0.2
27
35
8
170
68 ±0.2
30
8
10 -0.1 -0.2
15 +0.2 +0.1
140 -0.1 -0.2
15
332
302 -0.1 -0.2
15
0.8
0.8
SOLIDWORKS Student Edition.
For Academic Use Only.

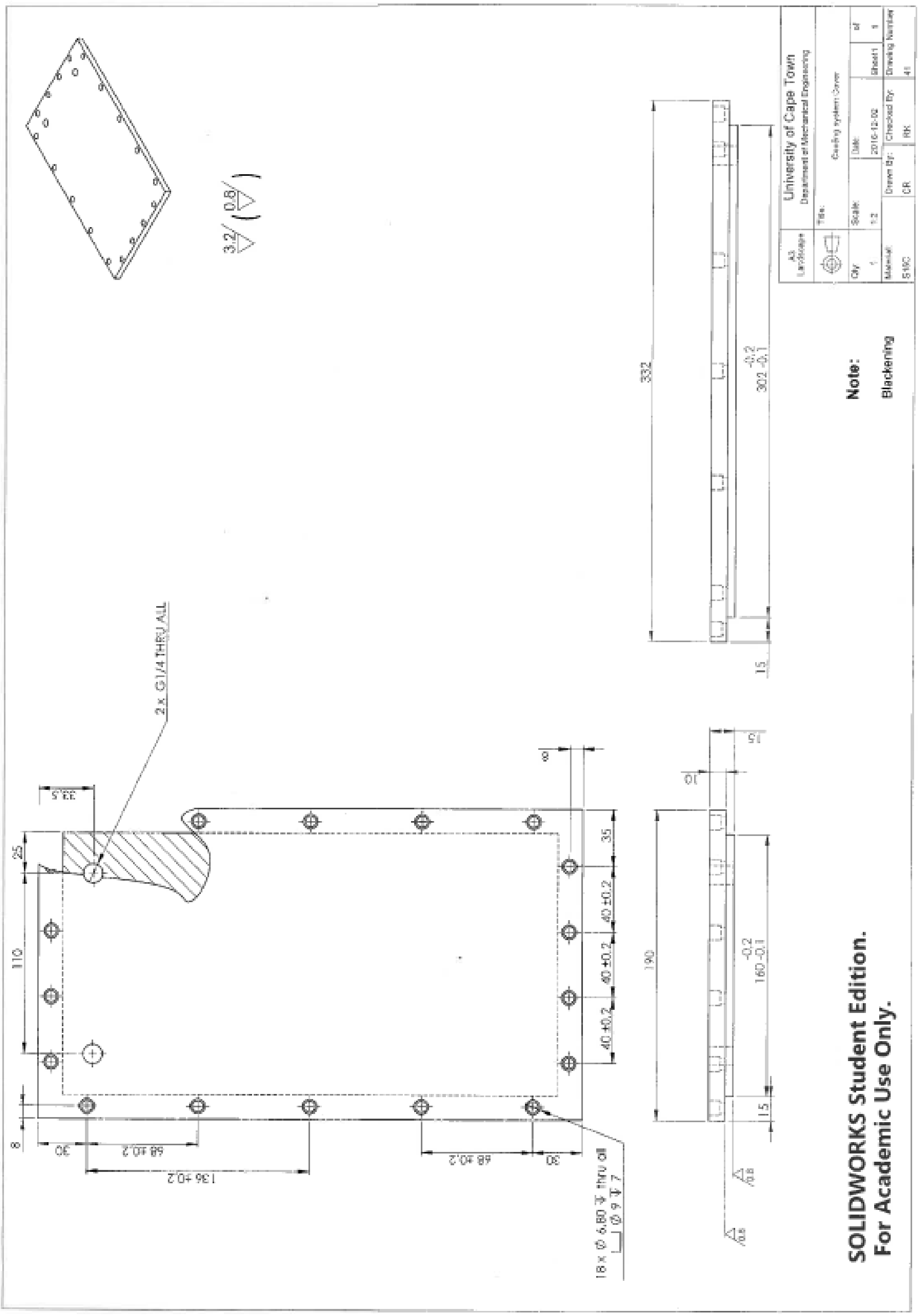
2 x G1/4 THRU ALL
33.5
25
110
8
30
68 ±0.2
136 ±0.2
30
68 ±0.2
18 x Ø 6.80 ⇂ thru all
⌴ Ø 9 ⇂ 7
35
40 ±0.2
40 ±0.2
40 ±0.2
9
190
-0.2
160 -0.1
15
10
15
0.8
0.8
332
-0.2
302 -0.1
15
3.2
0.8
SOLIDWORKS Student Edition.
For Academic Use Only.
Note:
Blackening
A3 Landscape
University of Cape Town
Department of Mechanical Engineering
Title:
Cooling system Cover
Qty
1
Scale:
1:2
Date:
2016-12-02
Sheet 1
of
1
Material:
S16C
Drawn By:
CR
Checked By:
RK
Drawing Number
41

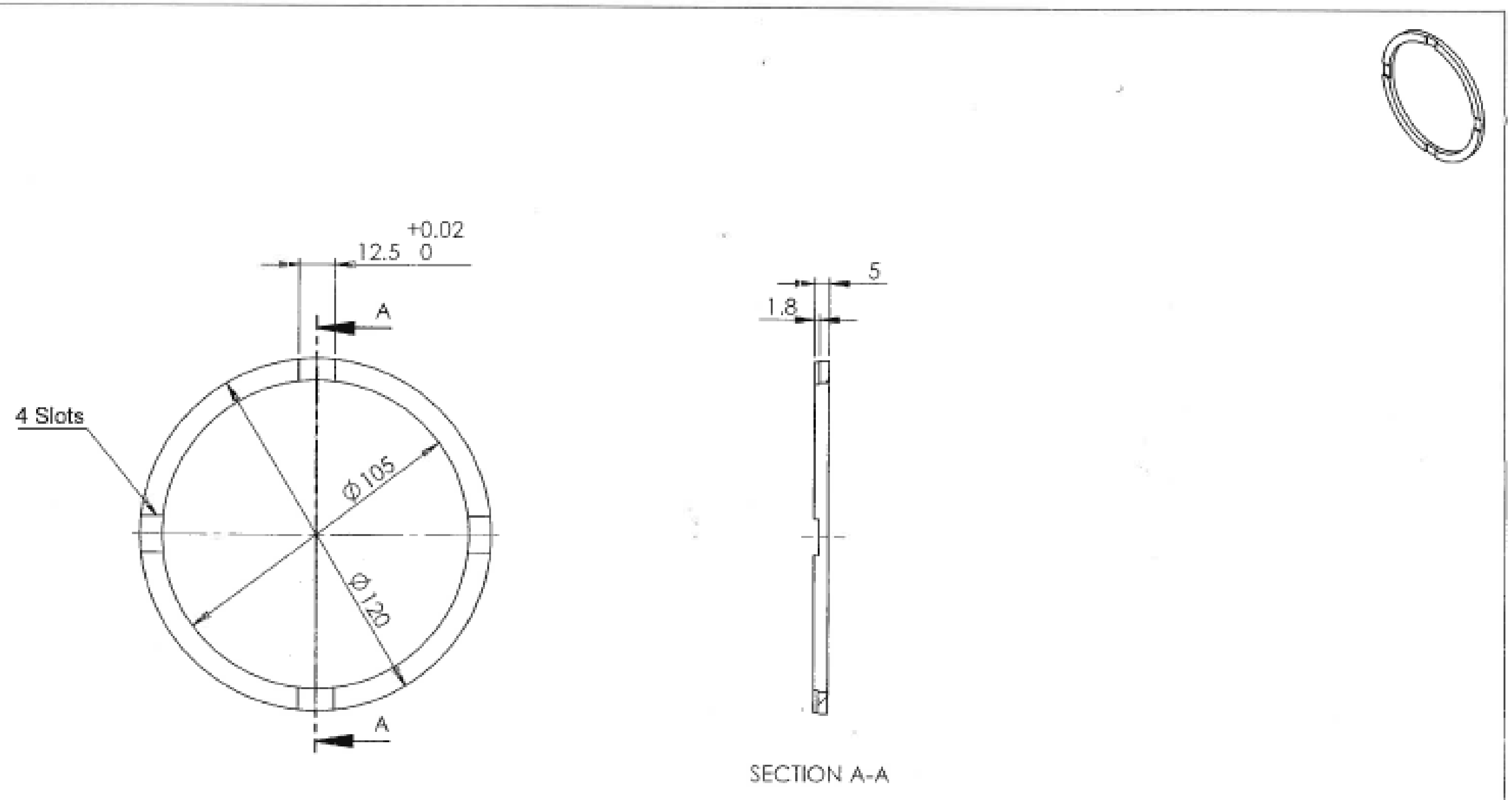

A4 Landscape	University of Cape Town Department of Mechanical Engineering			
	Title: Spring Clamp Spacer (SMPMM)			
Qty: 1	Scale: 1:2	Date: 2017/02/14	Sheet1	of 1
Material: Bronze	Drawn By: CR	Checked By: RK	Drawing Number 42	

Machine Dimensions	
Machine Diameter	120 mm
Rotor Radius	70 mm
Slot Avg Width	7.45 mm
Back Iron Thick.	8 mm
Machine Length	140 mm
Active Length	193 mm
Slot Height	15.01
Tooth Width	4.2 mm

Machine Ratings	
Power Rating	10 kW
Va (RMS)	220 V
Ea (RMS)	218.83 V
Synch Reactance	0.857 ohm
Stator Cur Den	3000 A/cm2
Phases	3
Speed	30000 RPM
Current (RMS)	15.8 A
Arm Resistance	0.014 ohm
Synch Induct	0.152 mH
Tip Speed	110 m/s
Frequency	1000 Hz

Stator Parameters	
Number of Slots	24
Winding Factor	0.933
Slots/pole/phase	2
Num turns per coil	2
Num Arm turns	16

Rotor Parameters	
Magnet Height	2.92 mm [NdFeB30]
Air gap	2 mm
Magnet Angle	120.06°
Pole Pairs	2

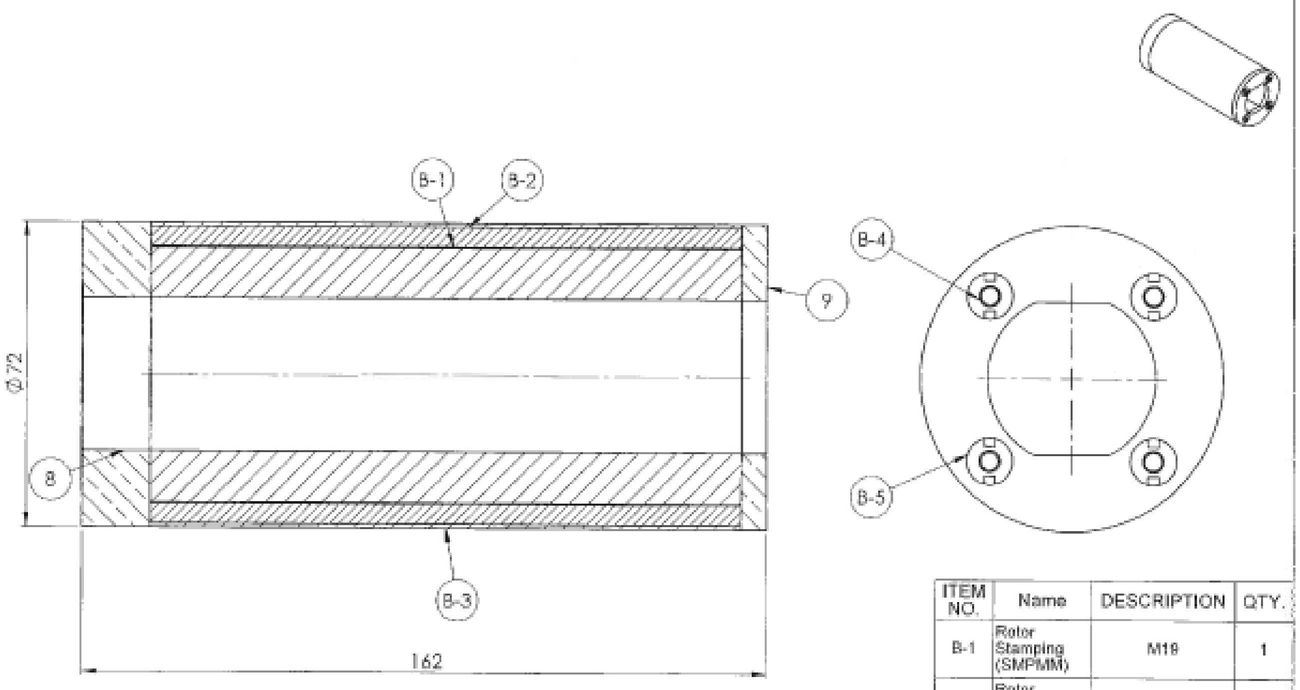

ITEM NO.	Name	DESCRIPTION	QTY.
B-1	Rotor Stamping (SMPMM)	M19	1
B-2	Rotor Magnet (IPMM)	Neodymium (NdFeB30)	4
B-3	Rotor Sleeve (SMPMM)	Epoxy	1
B-4	Rotor Clamp Rod (SMPMM)	Nylon 66	4
B-5	Rotor Stamp Nut (SMPMM)	Nylon 66	8
8	Front Brass spacer	Bronze	1
9	Rear Brass spacer	Bronze	1

A3 Landscape	University of Cape Town Department of Mechanical Engineering			
	Title: Rotor Assembly (SMPMM)			
Assembly Drawing	Scale: 1:1	Date: 2016-12-02	Sheet1	of 1
	Drawn By: CR	Checked By: RK	Drawing Number: B	

Note:

To be balanced to G1-6 Level 2, RPM 30000

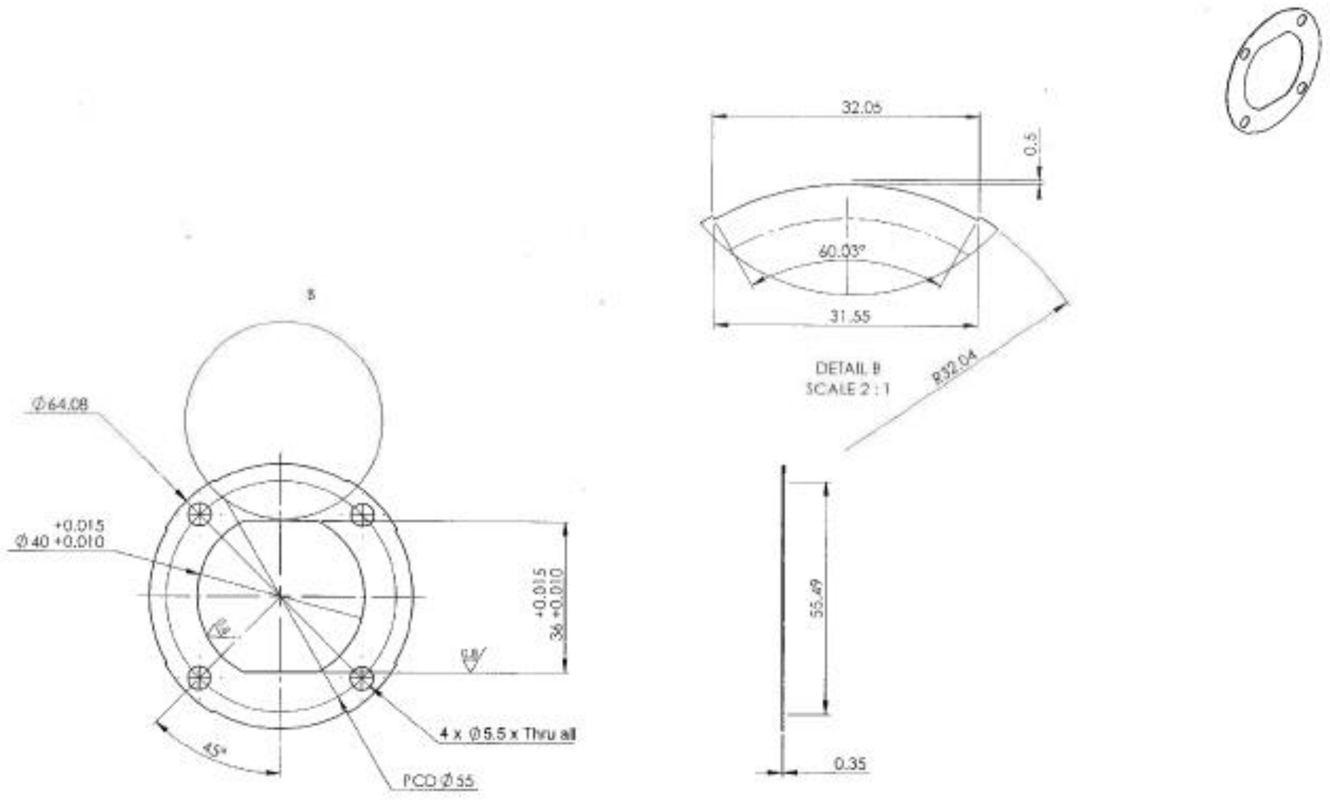

Note:

Slot to be honed after chemical Machining
(In assembled stack condition). Refer to B

A3 Landscape	University of Cape Town Department of Mechanical Engineering			
	Title: Roto Stamping ([illegible])			
Qty 400	Scale: 1:1	Date 2017/02/14	Sheet1	of 1
Material M19	Drawn By CR	Checked By RK	Drawing Number B-1	

SOLIDWORKS Student Edition.
For Academic Use Only.

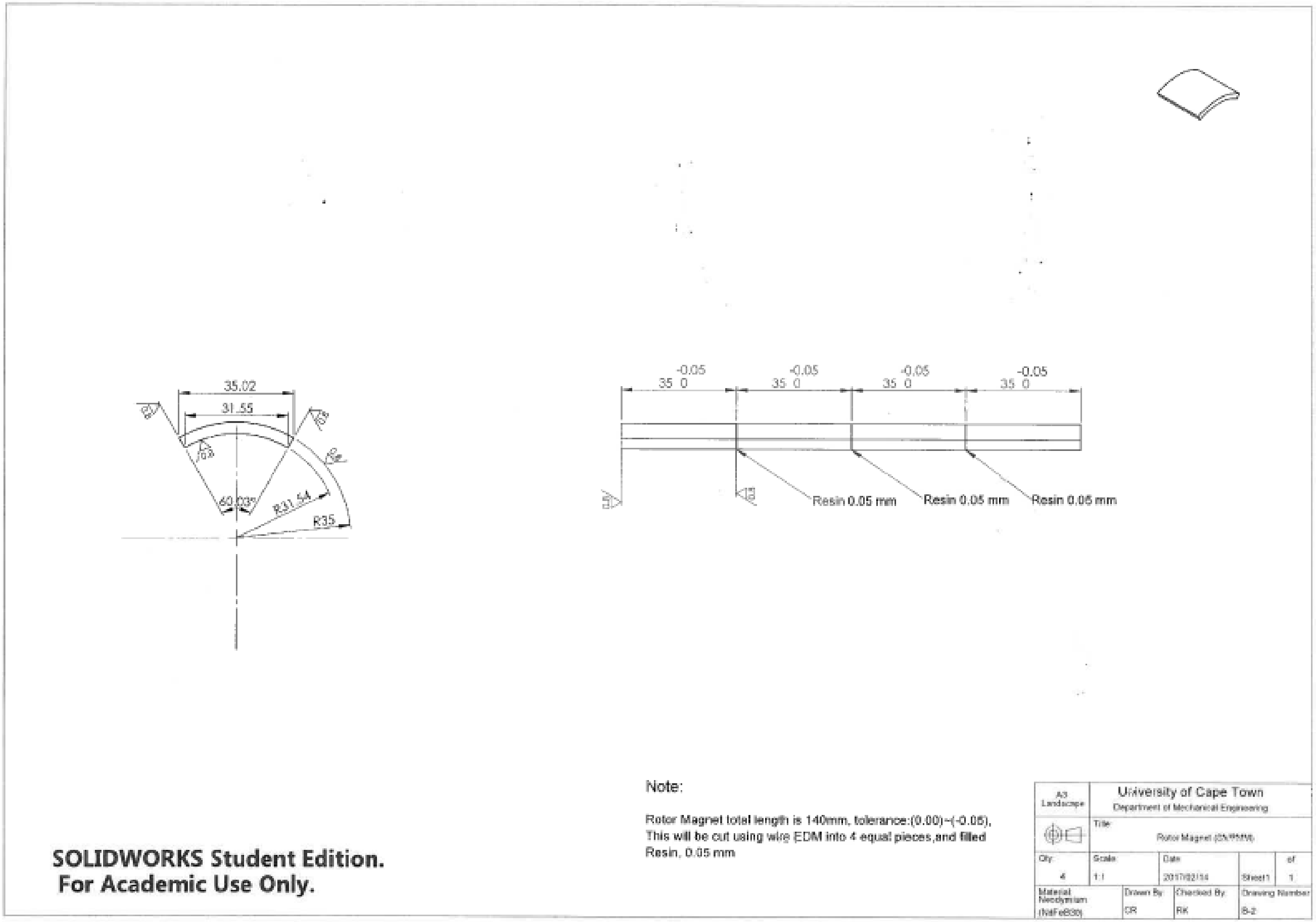

Note:

Rotor Magnet total length is 140mm, tolerance:(0.00)~(-0.05),
This will be cut using wire EDM into 4 equal pieces,and filled
Resin, 0.05 mm

A3
Landscape

University of Cape Town
Department of Mechanical Engineering

Title:
Rotor Magnet [illegible]

Qty: 4
Scale: 1:1
Date: 2017/02/14
Sheet1 of 1

Material: Neodymium (NdFeB30)
Drawn By: CR
Checked By: RK
Drawing Number: B-2

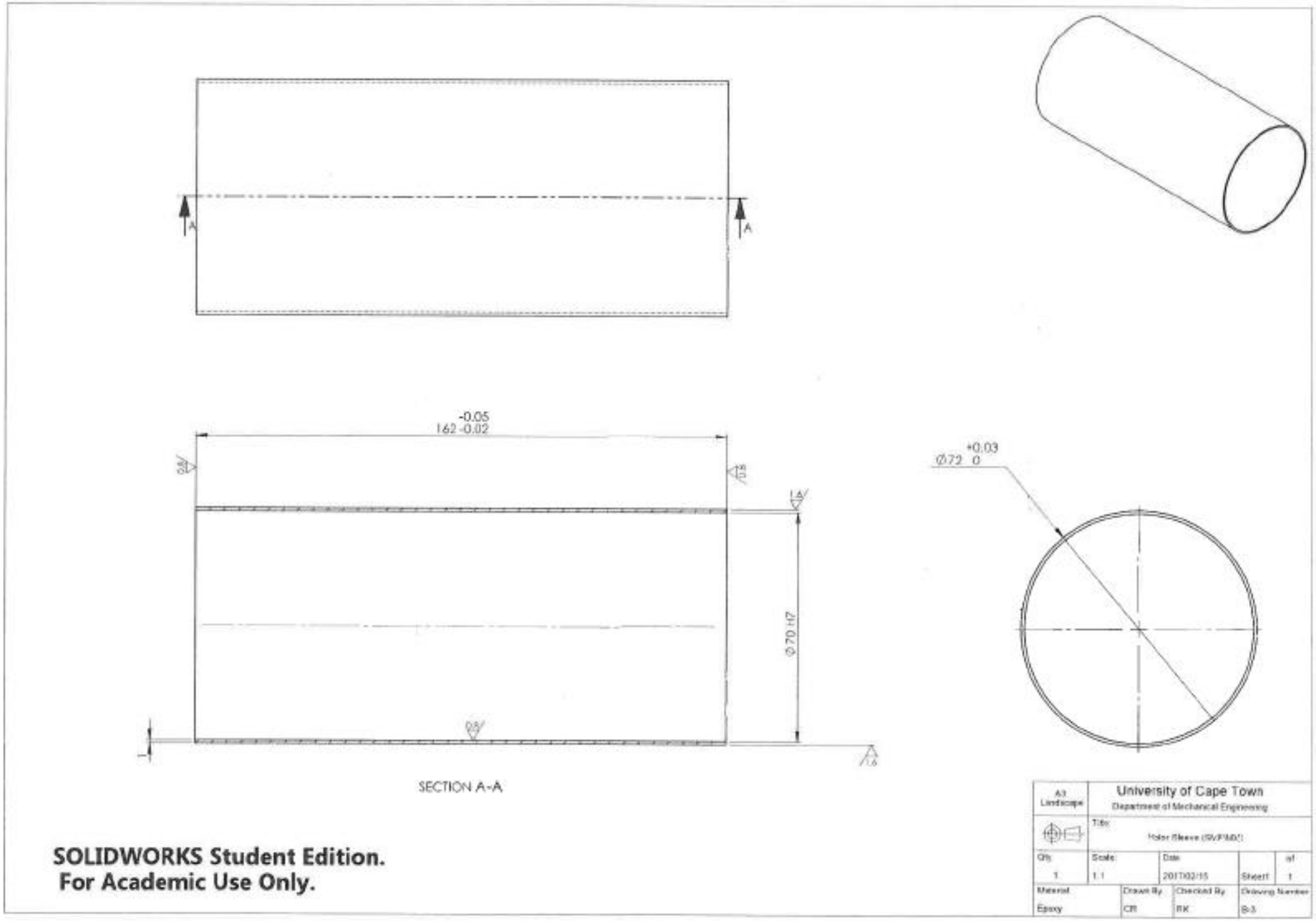A
A
-0.05
162 -0.02
0.8
0.8
1.6
Ø70 H7
0.8
1
1.6
SECTION A-A
+0.03
Ø72 0
A3
Landscape
University of Cape Town
Department of Mechanical Engineering
Title:
Rotor Sleeve (SVPMM)
Qty
1
Scale:
1:1
Date
2017/02/15
Sheet
1
of
1
Material
Epoxy
Drawn By
CR
Checked By
RK
Drawing Number
B-3

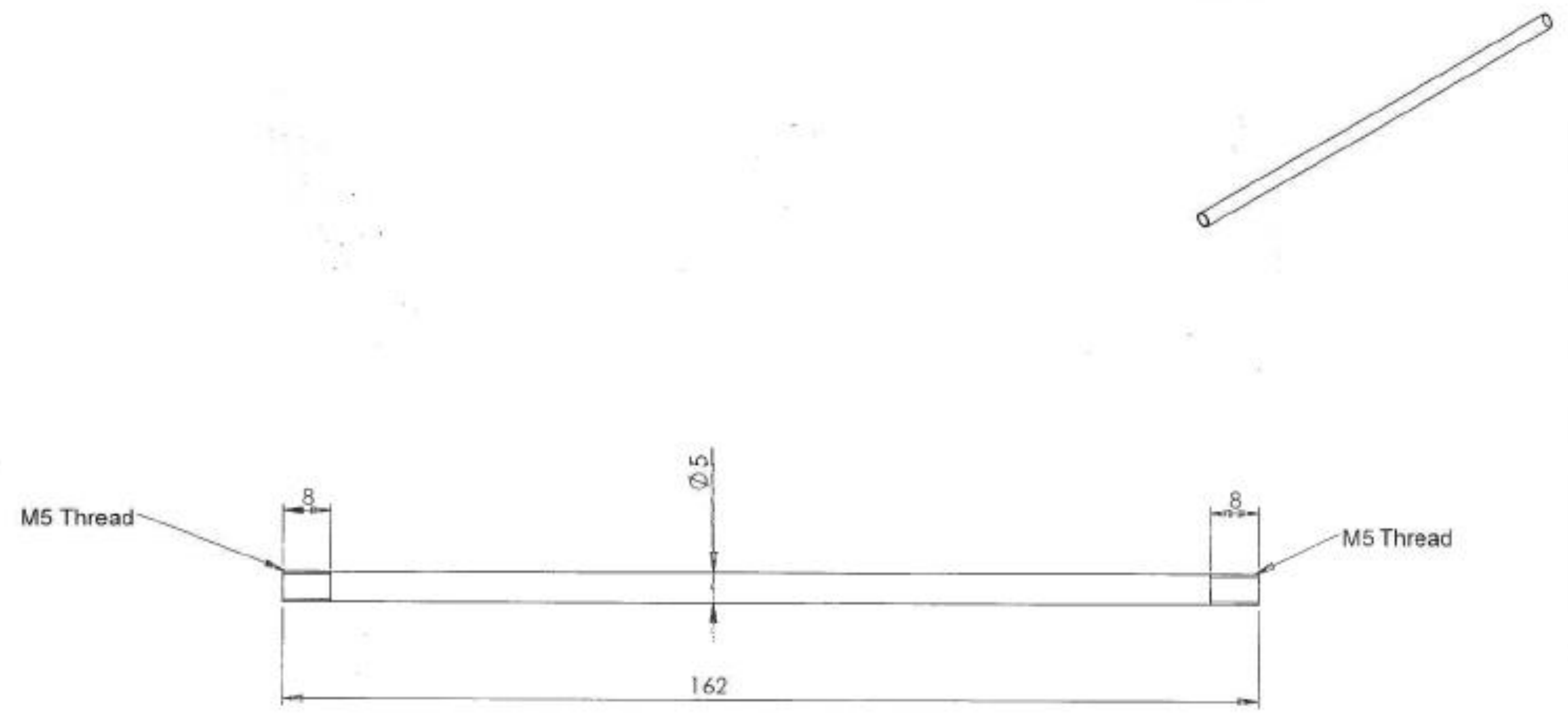

A4 Landscape	University of Cape Town Department of Mechanical Engineering				
	Title: Rotor Clamp Rod (SMPMM)				
Qty: 4	Scale: 1:1	Date: 2017/02/14		Sheet1	of 1
Material: Peek Plastic	Drawn By: CR	Checked By: RK	Drawing Number B-4		

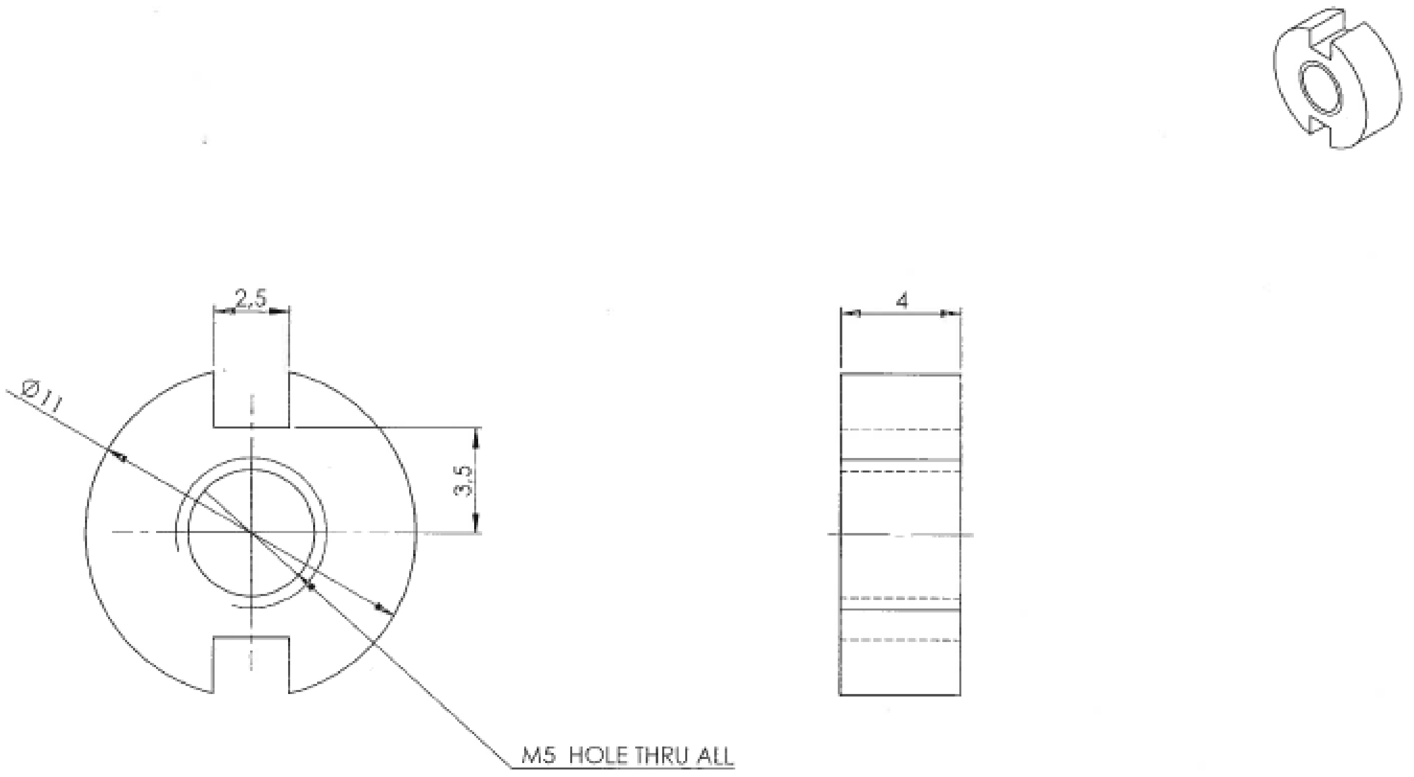

A4 Landscape	University of Cape Town Department of Mechanical Engineering			
	Title: Rotor Stamp Nut			
Qty: 8	Scale: 5:1	Date: 2016-12-02	Sheet1	of 1
Material: Nylon 66	Drawn By: CR	Checked By: RK	Drawing Number B-5	

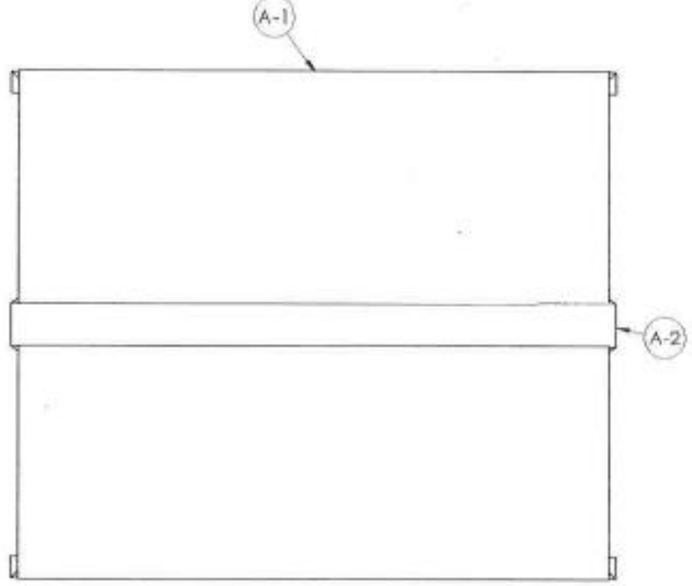

Note:

Stator Spring Clamp (A-2) to becrimped into the stator pack

All slots to be skewed by 15°

ITEM NO.	NAME	DESCRIPTION	QTY.
A-1	Stator Stamping	M19	400
A-2	Stator Spring Clamp (IPMM)	SCM 420	4

A3 Landscape	University of Cape Town Department of Mechanical Engineering			
	Title Stator Assembly (SMPMM)			
Assembly Drawing	Scale 1:1	Date 2016-12-02	Sheet1	of 1
	Drawn By CR	Checked By RK	Drawing Number A	

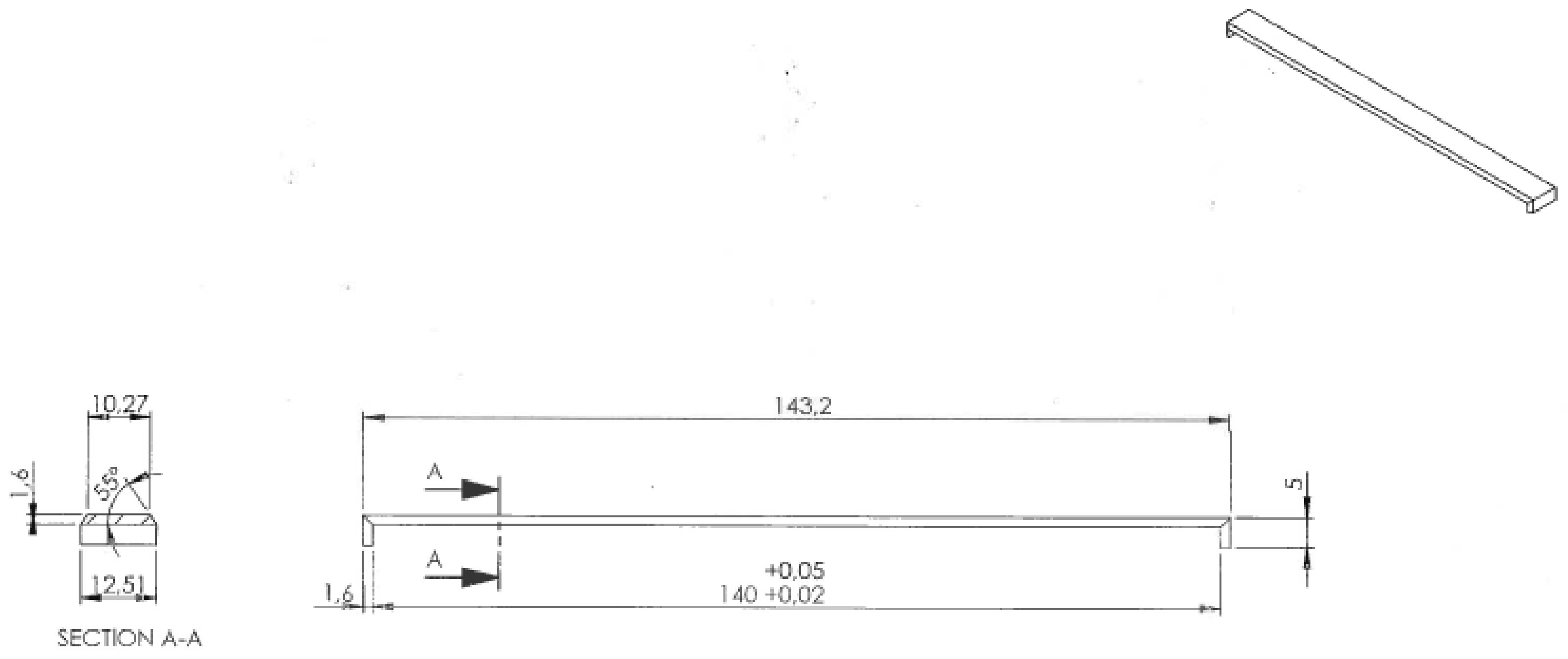

SOLIDWORKS Student Edition.
For Academic Use Only.

Note:

Chamfer all sharp corners

To be crimped into 15° skewed slots

A4 Landscape	University of Cape Town Department of Mechanical Engineering				
	Title: Stator Spring Clamp (SMPMM)				
Qty: 4	Scale: 1:1		Date: 2016-12-02	Sheet1	of 1
Material: SCM 420		Drawn By: CR	Checked By: RK	Drawing Number A-1	

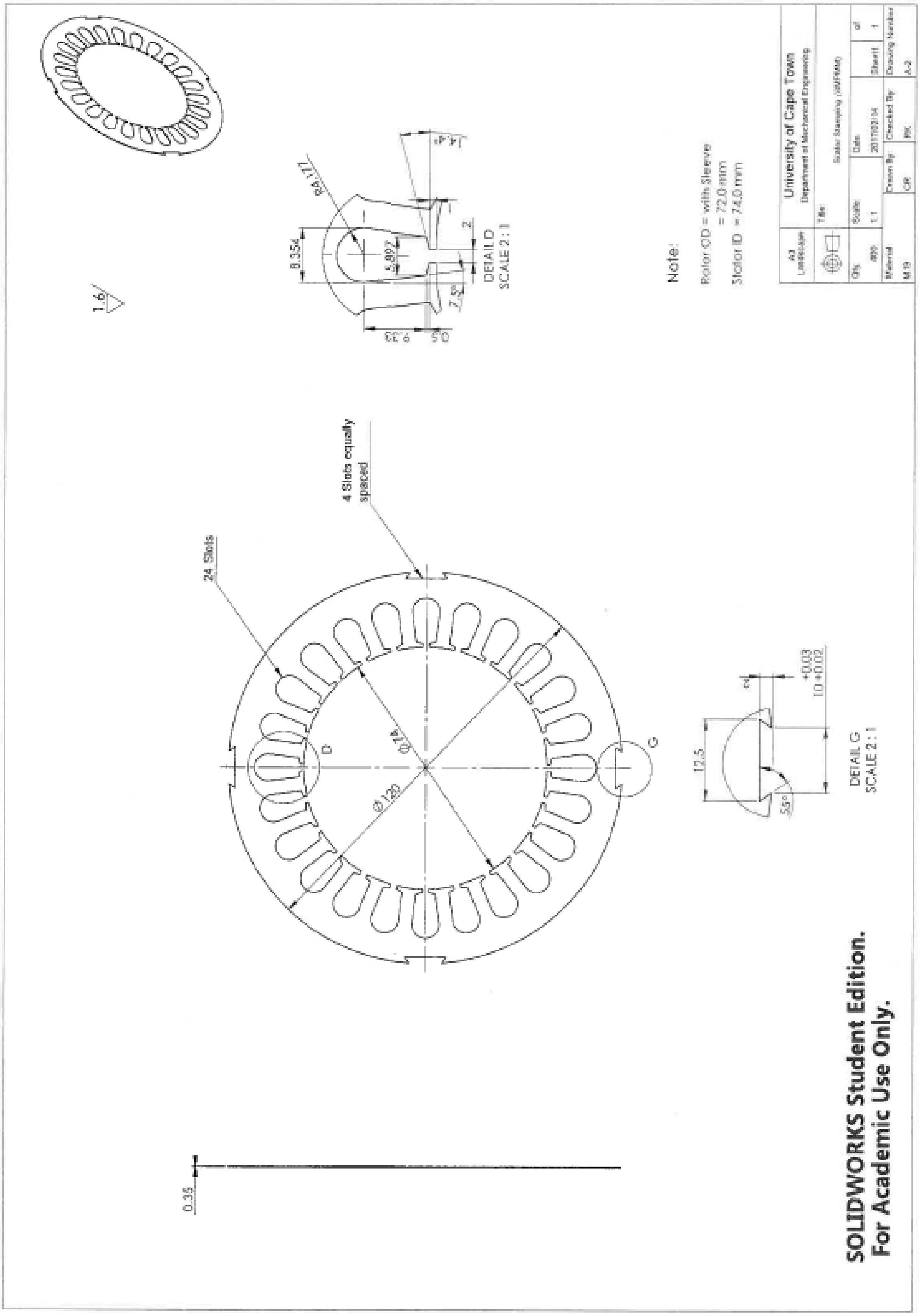
24 Slots
4 Slots equally spaced
Ø120
Ø74
D
G
DETAIL D
SCALE 2 : 1
R4.177
8.354
5.892
7.5°
9.33
0.5
2
14.4°
DETAIL G
SCALE 2 : 1
12.5
55°
2
10 +0.03 +0.02
1.6
0.35
Note:
Rotor OD = with Sleeve
= 72.0 mm
Stator ID = 74.0 mm
A3
Landscape
Title:
Qty.
400
Scale:
1:1
Date:
2017/02/14
Sheet 1
of
1
Material
M19
Drawn By:
CR
Checked By:
RK
Drawing Number
A-2
University of Cape Town
Department of Mechanical Engineering

APPENDIX B

B.1. Retaining Sleeve Calculations

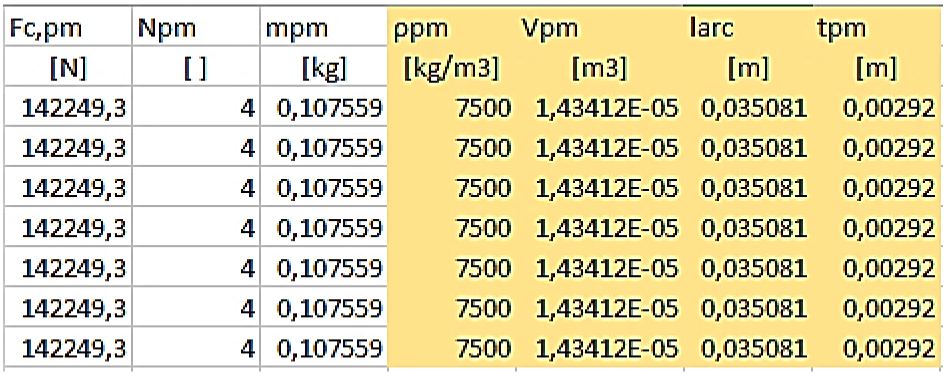

Fc,pm	Npm	mpm	ρpm	Vpm	larc	tpm
[N]	[ ]	[kg]	[kg/m3]	[m3]	[m]	[m]
142249,3	4	0,107559	7500	1,43412E-05	0,035081	0,00292
142249,3	4	0,107559	7500	1,43412E-05	0,035081	0,00292
142249,3	4	0,107559	7500	1,43412E-05	0,035081	0,00292
142249,3	4	0,107559	7500	1,43412E-05	0,035081	0,00292
142249,3	4	0,107559	7500	1,43412E-05	0,035081	0,00292
142249,3	4	0,107559	7500	1,43412E-05	0,035081	0,00292
142249,3	4	0,107559	7500	1,43412E-05	0,035081	0,00292

Figure B- 1: Calculation of Centrifugal Force, $F_{c,PM}$ for the Retaining Sleeve

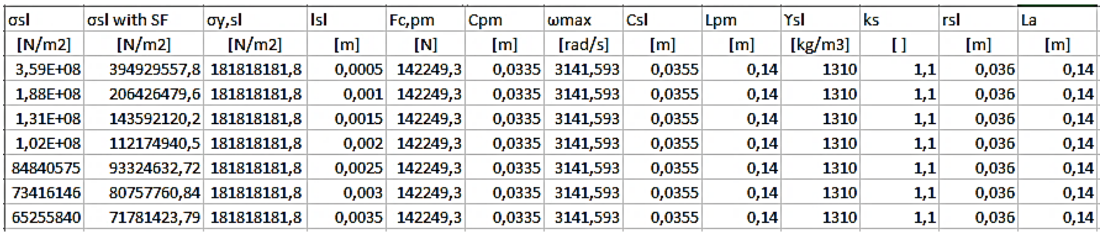

σsl	σsl with SF	σy,sl	lsl	Fc,pm	Cpm	ωmax	Csl	Lpm	Ysl	ks	rsl	La
[N/m2]	[N/m2]	[N/m2]	[m]	[N]	[m]	[rad/s]	[m]	[m]	[kg/m3]	[ ]	[m]	[m]
3,59E+08	394929557,8	181818181,8	0,0005	142249,3	0,0335	3141,593	0,0355	0,14	1310	1,1	0,036	0,14
1,88E+08	206426479,6	181818181,8	0,001	142249,3	0,0335	3141,593	0,0355	0,14	1310	1,1	0,036	0,14
1,31E+08	143592120,2	181818181,8	0,0015	142249,3	0,0335	3141,593	0,0355	0,14	1310	1,1	0,036	0,14
1,02E+08	112174940,5	181818181,8	0,002	142249,3	0,0335	3141,593	0,0355	0,14	1310	1,1	0,036	0,14
84840575	93324632,72	181818181,8	0,0025	142249,3	0,0335	3141,593	0,0355	0,14	1310	1,1	0,036	0,14
73416146	80757760,84	181818181,8	0,003	142249,3	0,0335	3141,593	0,0355	0,14	1310	1,1	0,036	0,14
65255840	71781423,79	181818181,8	0,0035	142249,3	0,0335	3141,593	0,0355	0,14	1310	1,1	0,036	0,14

Figure B- 2: Calculation of Hoop Stress σ_{SL} and Sleeve Thickness, l_{SL}, for the Retaining Sleeve

APPENDIX C

C.1. Bearing Selection Catalogue

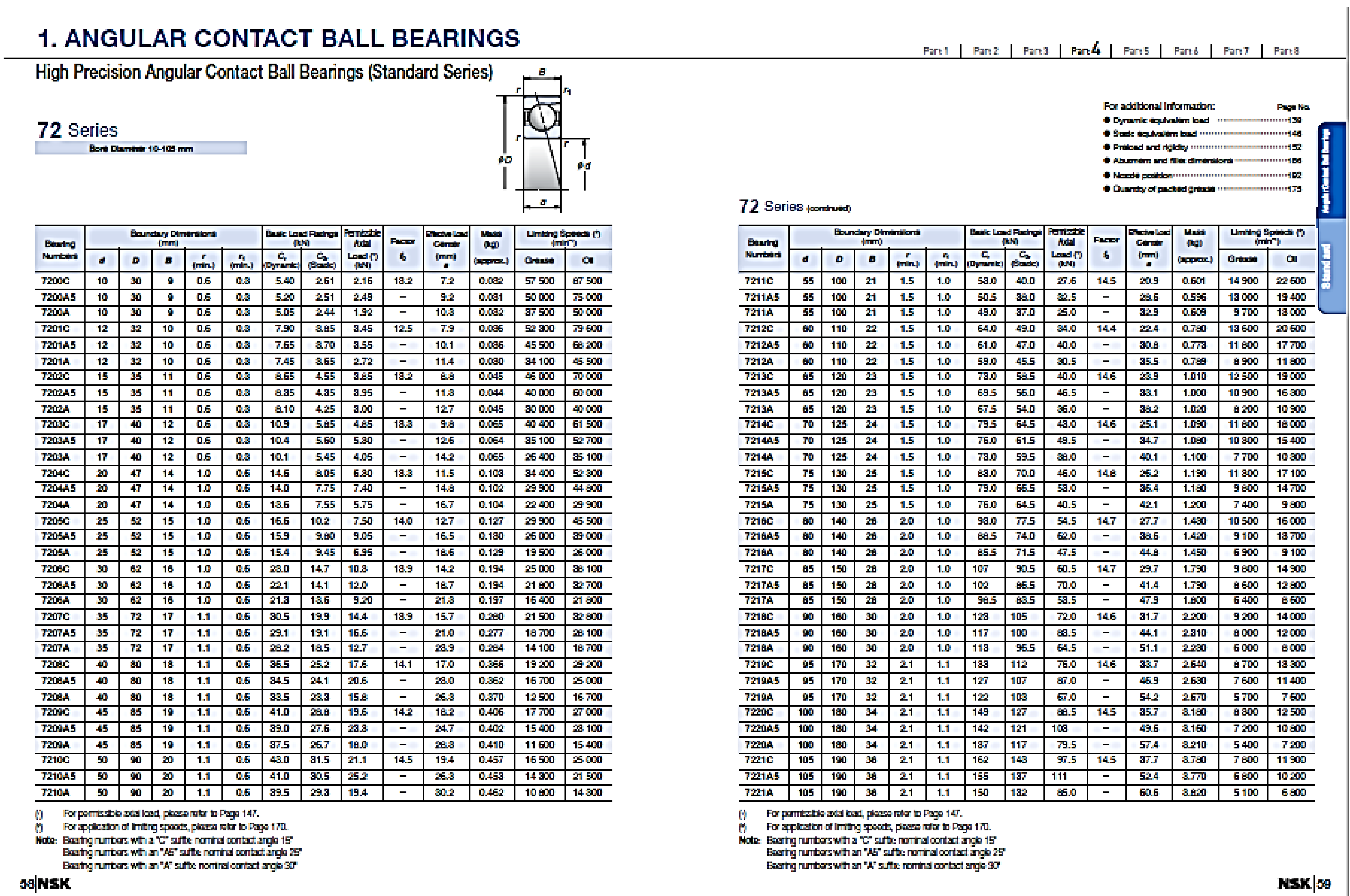

Part 1 | Part 2 | Part 3 | Part 4 | Part 5 | Part 6 | Part 7 | Part 8

1. ANGULAR CONTACT BALL BEARINGS

High Precision Angular Contact Ball Bearings (Standard Series)

72 Series

Bore Diameter 10-105 mm

Bearing Numbers	Boundary Dimensions (mm)					Basic Load Ratings (kN)		Permissible Axial Load (1) (kN)	Factor f_0	Effective Load Center (mm) a	Mass (kg)	Limiting Speeds (2) (min^{-1})	
	d	D	B	r (min.)	r_1 (min.)	C_r (Dynamic)	C_{0r} (Static)				(approx.)	Grease	Oil
7200C	10	30	9	0.6	0.3	5.40	2.61	2.16	13.2	7.2	0.032	57 500	87 500
7200A5	10	30	9	0.6	0.3	5.20	2.51	2.49	–	9.2	0.031	50 000	75 000
7200A	10	30	9	0.6	0.3	5.05	2.44	1.92	–	10.3	0.032	37 500	50 000
7201C	12	32	10	0.6	0.3	7.90	3.85	3.45	12.5	7.9	0.036	52 300	79 600
7201A5	12	32	10	0.6	0.3	7.65	3.70	3.55	–	10.1	0.036	45 500	68 200
7201A	12	32	10	0.6	0.3	7.45	3.65	2.72	–	11.4	0.030	34 100	45 500
7202C	15	35	11	0.6	0.3	8.65	4.55	3.85	13.2	8.8	0.045	46 000	70 000
7202A5	15	35	11	0.6	0.3	8.35	4.35	3.95	–	11.3	0.044	40 000	60 000
7202A	15	35	11	0.6	0.3	8.10	4.25	3.00	–	12.7	0.045	30 000	40 000
7203C	17	40	12	0.6	0.3	10.9	5.85	4.85	13.3	9.8	0.065	40 400	61 500
7203A5	17	40	12	0.6	0.3	10.4	5.60	5.30	–	12.6	0.064	35 100	52 700
7203A	17	40	12	0.6	0.3	10.1	5.45	4.05	–	14.2	0.065	26 400	35 100
7204C	20	47	14	1.0	0.6	14.6	8.05	6.30	13.3	11.5	0.103	34 400	52 300
7204A5	20	47	14	1.0	0.6	14.0	7.75	7.40	–	14.8	0.102	29 900	44 800
7204A	20	47	14	1.0	0.6	13.6	7.55	5.75	–	16.7	0.104	22 400	29 900
7205C	25	52	15	1.0	0.6	16.6	10.2	7.50	14.0	12.7	0.127	29 900	45 500
7205A5	25	52	15	1.0	0.6	15.9	9.80	9.05	–	16.5	0.130	26 000	39 000
7205A	25	52	15	1.0	0.6	15.4	9.45	6.95	–	18.6	0.129	19 500	26 000
7206C	30	62	16	1.0	0.6	23.0	14.7	10.3	13.9	14.2	0.194	25 000	38 100
7206A5	30	62	16	1.0	0.6	22.1	14.1	12.0	–	18.7	0.194	21 800	32 700
7206A	30	62	16	1.0	0.6	21.3	13.6	9.20	–	21.3	0.197	16 400	21 800
7207C	35	72	17	1.1	0.6	30.5	19.9	14.4	13.9	15.7	0.280	21 500	32 800
7207A5	35	72	17	1.1	0.6	29.1	19.1	16.6	–	21.0	0.277	18 700	28 100
7207A	35	72	17	1.1	0.6	28.2	18.5	12.7	–	23.9	0.284	14 100	18 700
7208C	40	80	18	1.1	0.6	36.5	25.2	17.6	14.1	17.0	0.366	19 200	29 200
7208A5	40	80	18	1.1	0.6	34.5	24.1	20.6	–	23.0	0.362	16 700	25 000
7208A	40	80	18	1.1	0.6	33.5	23.3	15.8	–	26.3	0.370	12 500	16 700
7209C	45	85	19	1.1	0.6	41.0	28.8	19.6	14.2	18.2	0.406	17 700	27 000
7209A5	45	85	19	1.1	0.6	39.0	27.6	23.3	–	24.7	0.402	15 400	23 100
7209A	45	85	19	1.1	0.6	37.5	26.7	18.0	–	28.3	0.410	11 600	15 400
7210C	50	90	20	1.1	0.6	43.0	31.5	21.1	14.5	19.4	0.457	16 500	25 000
7210A5	50	90	20	1.1	0.6	41.0	30.5	25.2	–	26.3	0.453	14 300	21 500
7210A	50	90	20	1.1	0.6	39.5	29.3	19.4	–	30.2	0.462	10 800	14 300

(1) For permissible axial load, please refer to Page 147.
(2) For application of limiting speeds, please refer to Page 170.
Note: Bearing numbers with a "C" suffix: nominal contact angle 15°
Bearing numbers with an "A5" suffix: nominal contact angle 25°
Bearing numbers with an "A" suffix: nominal contact angle 30°

58 | NSK

For additional information: Page No.
- Dynamic equivalent load ………… 139
- Static equivalent load ………… 146
- Preload and rigidity ………… 152
- Abutment and fillet dimensions ………… 186
- Nozzle position ………… 192
- Quantity of packed grease ………… 175

72 Series (continued)

Bearing Numbers	Boundary Dimensions (mm)					Basic Load Ratings (kN)		Permissible Axial Load (1) (kN)	Factor f_0	Effective Load Center (mm) a	Mass (kg)	Limiting Speeds (2) (min^{-1})	
	d	D	B	r (min.)	r_1 (min.)	C_r (Dynamic)	C_{0r} (Static)				(approx.)	Grease	Oil
7211C	55	100	21	1.5	1.0	53.0	40.0	27.6	14.5	20.9	0.601	14 900	22 600
7211A5	55	100	21	1.5	1.0	50.5	38.0	32.5	–	28.6	0.596	13 000	19 400
7211A	55	100	21	1.5	1.0	49.0	37.0	25.0	–	32.9	0.609	9 700	13 000
7212C	60	110	22	1.5	1.0	64.0	49.0	34.0	14.4	22.4	0.780	13 600	20 600
7212A5	60	110	22	1.5	1.0	61.0	47.0	40.0	–	30.8	0.773	11 800	17 700
7212A	60	110	22	1.5	1.0	59.0	45.5	30.5	–	35.5	0.789	8 900	11 800
7213C	65	120	23	1.5	1.0	73.0	58.5	40.0	14.6	23.9	1.010	12 500	19 000
7213A5	65	120	23	1.5	1.0	69.5	56.0	46.5	–	33.1	1.000	10 900	16 300
7213A	65	120	23	1.5	1.0	67.5	54.0	36.0	–	38.2	1.020	8 200	10 900
7214C	70	125	24	1.5	1.0	79.5	64.5	43.0	14.6	25.1	1.090	11 800	18 000
7214A5	70	125	24	1.5	1.0	76.0	61.5	49.5	–	34.7	1.080	10 300	15 400
7214A	70	125	24	1.5	1.0	73.0	59.5	38.0	–	40.1	1.100	7 700	10 300
7215C	75	130	25	1.5	1.0	83.0	70.0	46.0	14.8	26.2	1.190	11 300	17 100
7215A5	75	130	25	1.5	1.0	79.0	66.5	53.0	–	36.4	1.180	9 800	14 700
7215A	75	130	25	1.5	1.0	76.0	64.5	40.5	–	42.1	1.200	7 400	9 800
7216C	80	140	26	2.0	1.0	93.0	77.5	54.5	14.7	27.7	1.430	10 500	16 000
7216A5	80	140	26	2.0	1.0	88.5	74.0	62.0	–	38.6	1.420	9 100	13 700
7216A	80	140	26	2.0	1.0	85.5	71.5	47.5	–	44.8	1.450	6 900	9 100
7217C	85	150	28	2.0	1.0	107	90.5	60.5	14.7	29.7	1.790	9 800	14 900
7217A5	85	150	28	2.0	1.0	102	86.5	70.0	–	41.4	1.790	8 600	12 900
7217A	85	150	28	2.0	1.0	98.5	83.5	53.5	–	47.9	1.800	6 400	8 600
7218C	90	160	30	2.0	1.0	128	105	72.0	14.6	31.7	2.200	9 200	14 000
7218A5	90	160	30	2.0	1.0	117	100	88.5	–	44.1	2.310	8 000	12 000
7218A	90	160	30	2.0	1.0	118	96.5	64.5	–	51.1	2.230	6 000	8 000
7219C	95	170	32	2.1	1.1	133	112	76.0	14.6	33.7	2.640	8 700	13 300
7219A5	95	170	32	2.1	1.1	127	107	87.0	–	45.9	2.630	7 600	11 400
7219A	95	170	32	2.1	1.1	122	103	67.0	–	54.2	2.670	5 700	7 600
7220C	100	180	34	2.1	1.1	149	127	88.5	14.5	35.7	3.160	8 300	12 500
7220A5	100	180	34	2.1	1.1	142	121	108	–	49.6	3.160	7 200	10 800
7220A	100	180	34	2.1	1.1	137	117	79.5	–	57.4	3.210	5 400	7 200
7221C	105	190	36	2.1	1.1	162	143	97.5	14.5	37.7	3.780	7 800	11 900
7221A5	105	190	36	2.1	1.1	155	137	111	–	52.4	3.770	6 800	10 200
7221A	105	190	36	2.1	1.1	150	132	85.0	–	60.6	3.820	5 100	6 800

(1) For permissible axial load, please refer to Page 147.
(2) For application of limiting speeds, please refer to Page 170.
Note: Bearing numbers with a "C" suffix: nominal contact angle 15°
Bearing numbers with an "A5" suffix: nominal contact angle 25°
Bearing numbers with an "A" suffix: nominal contact angle 30°

NSK | 59

Figure C- 1: 72 Series Angular Contact Ball Bearing Catalogue

C.1. Bearing Life Calculation

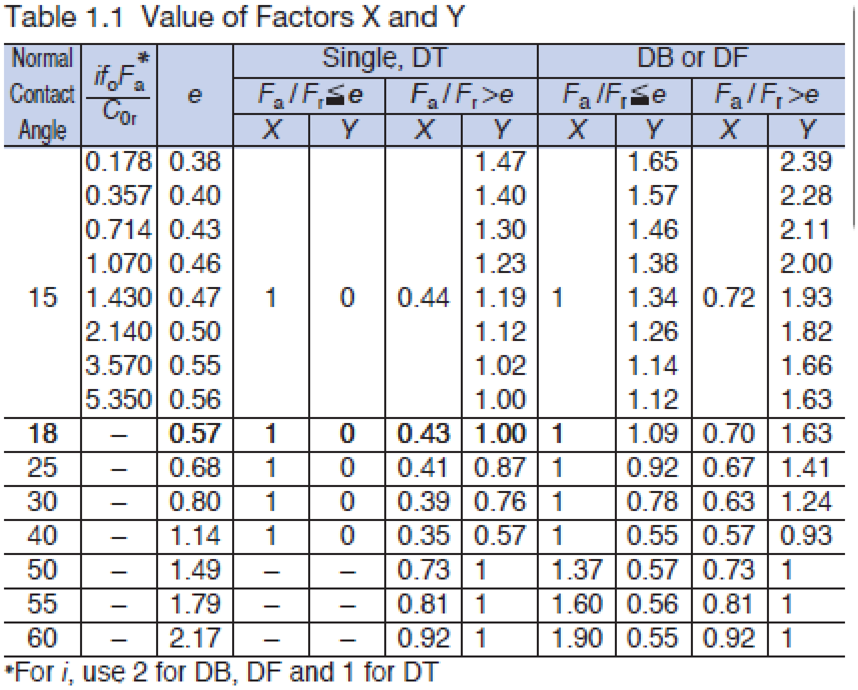

Table 1.1 Value of Factors X and Y

Normal Contact Angle	$\frac{if_o F_a}{C_{0r}}$*	*e*	Single, DT				DB or DF			
			$F_a/F_r \leqq e$		$F_a/F_r > e$		$F_a/F_r \leqq e$		$F_a/F_r > e$	
			X	*Y*	*X*	*Y*	*X*	*Y*	*X*	*Y*
15	0.178	0.38	1	0	0.44	1.47	1	1.65	0.72	2.39
	0.357	0.40				1.40		1.57		2.28
	0.714	0.43				1.30		1.46		2.11
	1.070	0.46				1.23		1.38		2.00
	1.430	0.47				1.19		1.34		1.93
	2.140	0.50				1.12		1.26		1.82
	3.570	0.55				1.02		1.14		1.66
	5.350	0.56				1.00		1.12		1.63
18	–	**0.57**	**1**	**0**	**0.43**	**1.00**	**1**	1.09	0.70	1.63
25	–	0.68	1	0	0.41	0.87	1	0.92	0.67	1.41
30	–	0.80	1	0	0.39	0.76	1	0.78	0.63	1.24
40	–	1.14	1	0	0.35	0.57	1	0.55	0.57	0.93
50	–	1.49	–	–	0.73	1	1.37	0.57	0.73	1
55	–	1.79	–	–	0.81	1	1.60	0.56	0.81	1
60	–	2.17	–	–	0.92	1	1.90	0.55	0.92	1

*For *i*, use 2 for DB, DF and 1 for DT

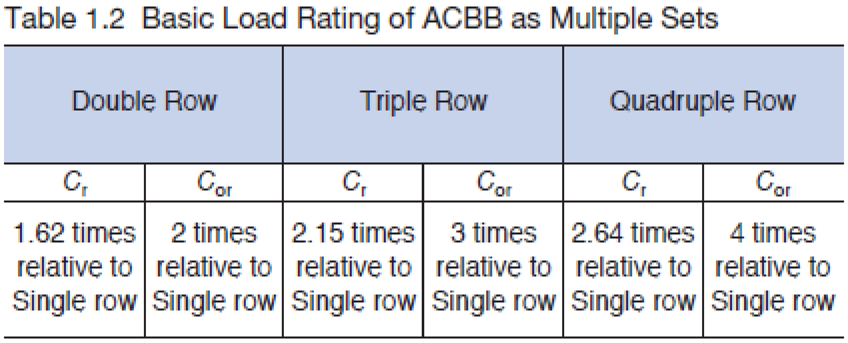

Table 1.2 Basic Load Rating of ACBB as Multiple Sets

Double Row		Triple Row		Quadruple Row	
C_r	C_{or}	C_r	C_{or}	C_r	C_{or}
1.62 times relative to Single row	2 times relative to Single row	2.15 times relative to Single row	3 times relative to Single row	2.64 times relative to Single row	4 times relative to Single row

Figure C- 2: Tables used to Calculate Bearing Life

APPENDIX D

D.1. MagWeb Core Loss Data

AK Steel	M-19 14 mil	50	1000			a040
Manufacturer		*Hz min*	*Hz Max*	*g/cm3*	*μΩcm*	*Curve*

Table D- 1: Table used to Plot M-19 Material Core Loss, Sourced from: MagWeb Free Core Loss Curves, Electrical Steel NGO – AK Steel's M-19

Core Loss

B	*50Hz*	*60 Hz*	*150Hz*	*400 Hz*	*1000Hz*	*2000 Hz*
Tesla	**w/kg**	**w/kg**	**w/kg**	**w/kg**	**w/kg**	**w/kg**
0,00	0,00	0,00	0,00	0,00	0,00	0,00
0,10	0,02	0,02	0,06	0,25	1,02	3,20
0,20	0,07	0,09	0,26	0,99	3,94	11,70
0,30	0,15	0,19	0,60	2,30	8,97	26,25
0,40	0,24	0,30	0,93	3,60	14,00	40,80
0,50	0,36	0,45	1,44	5,67	22,37	66,87
0,60	0,48	0,60	1,94	7,74	30,73	92,93
0,70	0,60	0,75	2,44	9,81	39,10	119,00
0,80	0,77	0,95	3,13	12,84	52,73	165,00
0,90	0,93	1,16	3,81	15,87	66,37	211,00
1,00	1,09	1,36	4,50	18,90	80,00	257,00
1,05	1,20	1,49	4,95	20,90	90,00	291,50
1,10	1,30	1,63	5,40	22,90	100,00	326,00
1,15	1,41	1,76	5,85	24,90	110,00	360,50
1,20	1,51	1,89	6,30	26,90	120,00	395,00
1,25	1,65	2,06	6,86	29,35	131,50	447,50
1,30	1,79	2,23	7,41	31,80	143,00	500,00
1,35	1,97	2,45	8,12	34,65		
1,40	2,14	2,66	8,82	37,50		
1,45	2,35	2,93	9,66	40,95		
1,50	2,56	3,19	10,50	44,40		
1,55	2,77	3,44	11,40	47,60		
1,60	2,96	3,67	12,00	50,80		

1,65	**3,13**	**3,89**	**12,80**
1,70	**3,29**	**4,08**	**13,40**
1,75		**4,24**	**13,70**
1,80		**4,40**	**14,00**

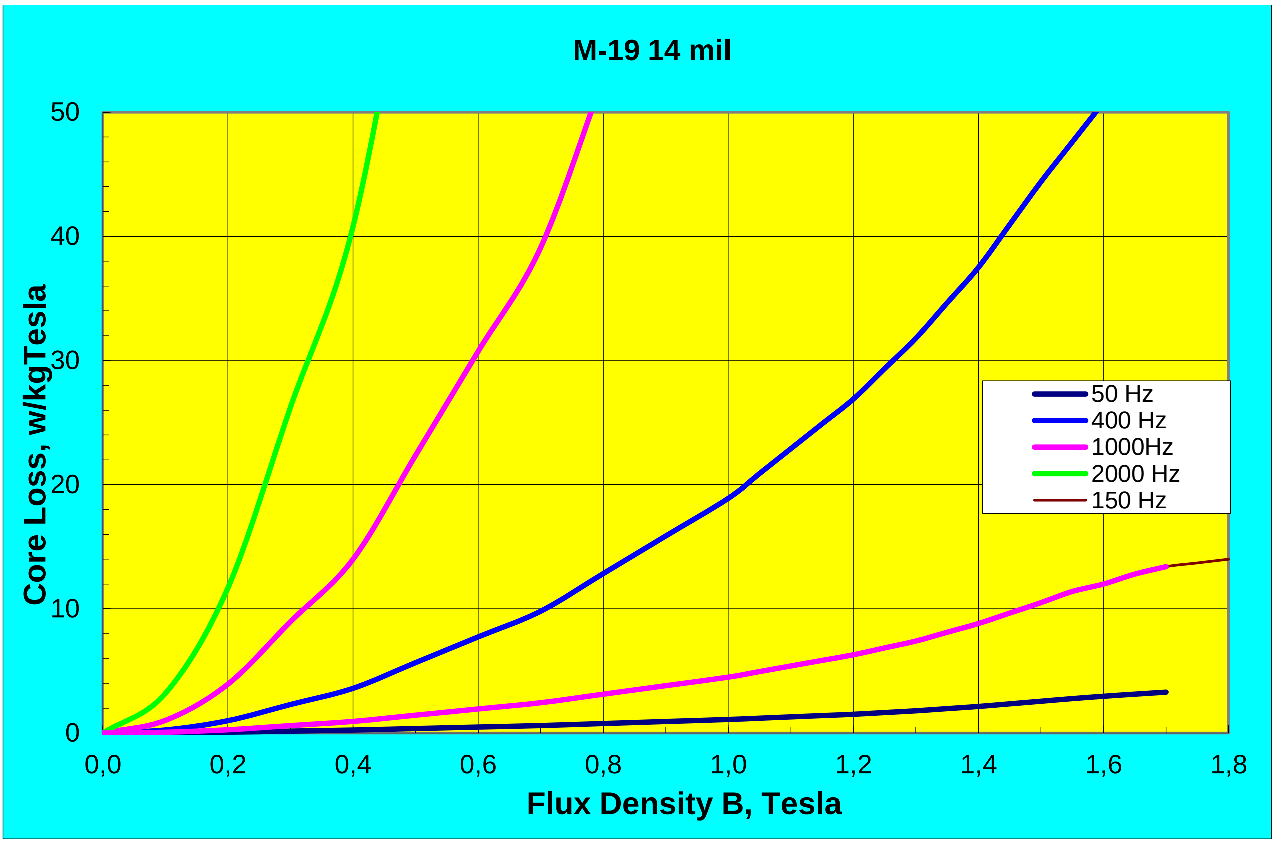

Figure D- 1: M-19 Material Core Loss Plot, Sourced from: MagWeb Free Core Loss Curves, Electrical Steel NGO – AK Steel's M-19